



ISSN 1605-2730

# **MATERIALS PHYSICS AND MECHANICS**

**Vol. 32, No. 3, 2017**

# MATERIALS PHYSICS AND MECHANICS

## Principal Editors:

**Dmitrii Indeitsev**  
*Institute of Problems of Mechanical Engineering  
of the Russian Academy of Science (RAS), Russia*

**Andrei Rudskoi**  
*Peter the Great St.Petersburg Polytechnic University, Russia*

## Founder and Honorary Editor: Ilya Ovid'ko (1961-2017)

*Institute of Problems of Mechanical Engineering  
of the Russian Academy of Sciences (RAS), Russia*

## Staff Editors:

**Anna Kolesnikova**  
*Institute of Problems of Mechanical Engineering  
of the Russian Academy of Sciences (RAS), Russia*

**Alexander Nemov**  
*Peter the Great St.Petersburg Polytechnic University, Russia*

## Editorial Board:

**E.C. Aifantis**  
*Aristotle University of Thessaloniki, Greece*

**K.E. Aifantis**  
*University of Florida, USA*

**U. Balachandran**  
*Argonne National Laboratory, USA*

**A. Bellosi**  
*Research Institute for Ceramics Technology, Italy*

**A.K. Belyaev**  
*Institute of Problems of Mechanical Engineering (RAS), Russia*

**S.V. Bobylev**  
*Institute of Problems of Mechanical Engineering (RAS), Russia*

**A.I. Borovkov**  
*Peter the Great St.Petersburg Polytechnic University, Russia*

**G.-M. Chow**  
*National University of Singapore, Singapore*

**Yu. Estrin**  
*Monash University, Australia*

**A.B. Freidin**  
*Institute of Problems of Mechanical Engineering (RAS), Russia*

**Y. Gogotsi**  
*Drexel University, USA*

**I.G. Goryacheva**  
*Institute of Problems of Mechanics (RAS), Russia*

**D. Hui**  
*University of New Orleans, USA*

**G. Kiriakidis**  
*IESL/FORTH, Greece*

**D.M. Klimov**  
*Institute of Problems of Mechanics (RAS), Russia*

**G.E. Kodzhaspirov**  
*Peter the Great St.Petersburg Polytechnic University, Russia*

**S.A. Kukushkin**  
*Institute of Problems of Mechanical Engineering (RAS), Russia*

**T.G. Langdon**  
*University of Southampton, U.K.*

**V.P. Matveenko**  
*Institute of Continuous Media Mechanics (RAS), Russia*

**A.I. Melker**  
*Peter the Great St.Petersburg Polytechnic University, Russia*

**Yu.I. Meshcheryakov**  
*Institute of Problems of Mechanical Engineering (RAS), Russia*

**N.F. Morozov**  
*St.Petersburg State University, Russia*

**R.R. Mulyukov**  
*Institute for Metals Superplasticity Problems (RAS), Russia*

**Yu.V. Petrov**  
*St.Petersburg State University, Russia*

**N.M. Pugno**  
*Politecnico di Torino, Italy*

**B.B. Rath**  
*Naval Research Laboratory, USA*

**A.E. Romanov**  
*Ioffe Physico-Technical Institute (RAS), Russia*

**A.M. Sastry**  
*University of Michigan, Ann Arbor, USA*

**A.G. Sheinerman**  
*Institute of Problems of Mechanics (RAS), Russia*

**N.V. Skiba**  
*Institute of Problems of Mechanics (RAS), Russia*

**R.Z. Valiev**  
*Ufa State Aviation Technical University, Russia*

**K. Zhou**  
*Nanyang Technological University, Singapore*

## “Materials Physics and Mechanics” Editorial Office:

**Phone:** +7(812)591 65 28 **E-mail:** mpmjournal@spbstu.ru **Web-site:** <http://www.mpm.spbstu.ru>

International scientific journal "Materials Physics and Mechanics" is published by Peter the Great St.Petersburg Polytechnic University in collaboration with Institute of Problems of Mechanical Engineering of the Russian Academy of Sciences in both hard copy and electronic versions.

The journal provides an international medium for the publication of reviews and original research papers written in English and focused on the following topics:

- Mechanics of nanostructured materials (such as nanocrystalline materials, nanocomposites, nanoporous materials, nanotubes, quantum dots, nanowires, nanostructured films and coatings).
- Physics of strength and plasticity of nanostructured materials, physics of defects in nanostructured materials.
- Mechanics of deformation and fracture processes in conventional materials (solids).
- Physics of strength and plasticity of conventional materials (solids).

Owner organizations: Peter the Great St. Petersburg Polytechnic University; Institute of Problems of Mechanical Engineering RAS.

*Materials Physics and Mechanics is indexed in Chemical Abstracts, Cambridge Scientific Abstracts, Web of Science Emerging Sources Citation Index (ESCI) and Elsevier Bibliographic Databases (in particular, SCOPUS).*

© 2017, Peter the Great St. Petersburg Polytechnic University  
© 2017, Institute of Problems of Mechanical Engineering RAS



# **МЕХАНИКА И ФИЗИКА МАТЕРИАЛОВ**

**Materials Physics and Mechanics**

**Том 32, номер 3, 2017 год**

Учредители:

ФГАОУ ВО «Санкт-Петербургский политехнический университет Петра Великого»  
ФГБУН «Институт проблем машиноведения Российской Академии Наук»

## Редакционная коллегия журнала

### Главные редакторы:

д.ф.-м.н., чл.-корр. РАН **Д.А. Индейцев**  
Институт проблем машиноведения Российской Академии Наук  
(РАН)

д.т.н., академик РАН **А.И. Рудской**  
Санкт-Петербургский политехнический университет  
Петра Великого

**Основатель и почетный редактор:** д.ф.-м.н. **И.А. Овидько (1961-2017)**  
Институт проблем машиноведения Российской Академии Наук (РАН)

### Ответственные редакторы

д.ф.-м.н. **А.Л. Колесникова**  
Институт проблем машиноведения Российской Академии Наук  
(РАН)

к.т.н. **А.С. Немов**  
Санкт-Петербургский политехнический университет Петра  
Великого

### Международная редакционная коллегия:

д.ф.-м.н., проф. **А.К. Беляев**  
Институт проблем машиноведения РАН, Россия  
д.ф.-м.н. **С.В. Бобылев**  
Институт проблем машиноведения РАН, Россия  
к.т.н., проф. **А.И. Боровков**  
Санкт-Петербургский политехнический у-т Петра Великого, Россия  
д.ф.-м.н., проф. **Р.З. Валиев**  
Уфимский государственный технический университет, Россия  
д.ф.-м.н., академик РАН **И.Г. Горячева**  
Институт проблем механики РАН, Россия  
д.ф.-м.н., академик РАН **Д.М. Климов**  
Институт проблем механики РАН, Россия  
д.т.н., проф. **Г.Е. Коджаспиров**  
Санкт-Петербургский политехнический у-т Петра Великого, Россия  
д.ф.-м.н., проф. **С.А. Кукушкин**  
Институт проблем машиноведения РАН, Россия  
д.ф.-м.н., академик РАН **В.П. Матвеев**  
Институт механики сплошных сред РАН, Россия  
д.ф.-м.н., проф. **А.И. Мелькер**  
Санкт-Петербургский политехнический у-т Петра Великого, Россия  
д.ф.-м.н., проф. **Ю.И. Мещеряков**  
Институт проблем машиноведения РАН, Россия  
д.ф.-м.н., академик РАН **Н.Ф. Морозов**  
Санкт-Петербургский государственный университет, Россия  
д.ф.-м.н., чл.-корр. РАН **Р.Р. Мулюков**  
Институт проблем сверхпластичности металлов РАН, Россия  
д.ф.-м.н., чл.-корр. РАН **Ю.В. Петров**  
Санкт-Петербургский государственный университет, Россия  
д.ф.-м.н., проф. **А.Е. Романов**  
Физико-технический институт им. А.Ф. Иоффе РАН, Россия  
д.ф.-м.н. **Н.В. Скиба**  
Институт проблем машиноведения РАН, Россия  
д.ф.-м.н., проф. **А.Б. Фрейдин**  
Институт проблем машиноведения РАН, Россия  
д.ф.-м.н. **А.Г. Шейнман**  
Институт проблем машиноведения РАН, Россия

Prof., Dr. **E.C. Aifantis**  
Aristotle University of Thessaloniki, Greece  
Dr. **K.E. Aifantis**  
University of Florida, USA  
Dr. **U. Balachandran**  
Argonne National Laboratory, USA  
Dr. **A. Bellosi**  
Research Institute for Ceramics Technology, Italy  
Prof., Dr. **G.-M. Chow**  
National University of Singapore, Singapore  
Prof., Dr. **Yu. Estrin**  
Monash University, Australia  
Prof., Dr. **Y. Gogotsi**  
Drexel University, USA  
Prof., Dr. **D. Hui**  
University of New Orleans, USA  
Prof., Dr. **G. Kiriakidis**  
IESL/FORTH, Greece  
Prof., Dr. **T.G. Langdon**  
University of Southampton, UK  
Prof., Dr. **N.M. Pugno**  
Politecnico di Torino, Italy  
Dr. **B.B. Rath**  
Naval Research Laboratory, USA  
Prof., Dr. **A.M. Sastry**  
University of Michigan, Ann Arbor, USA  
Prof. Dr. **K. Zhou**  
Nanyang Technological University, Singapore

Тел.: +7(812)591 65 28 E-mail: mpmjournal@spbstu.ru Web-site: <http://www.mpm.spbstu.ru>

### Тематика журнала

Международный научный журнал "Materials Physics and Mechanics" издается Санкт-Петербургским политехническим университетом Петра Великого в сотрудничестве с Институтом проблем машиноведения Российской Академии Наук в печатном виде и электронной форме. Журнал публикует обзорные и оригинальные научные статьи на английском языке по следующим тематикам:

- Механика наноструктурных материалов (таких как нанокристаллические материалы, нанокомпозиты, нанопористые материалы, нанотрубки, наноструктурные пленки и покрытия, материалы с квантовыми точками и проволоками).
- Физика прочности и пластичности наноструктурных материалов, физика дефектов в наноструктурных материалах.
- Механика процессов деформирования и разрушения в традиционных материалах (твердых телах).
- Физика прочности и пластичности традиционных материалов (твердых тел).

Редколлегия принимает статьи, которые нигде ранее не опубликованы и не направлены для опубликования в другие научные издания. Все представляемые в редакцию журнала "Механика и физика материалов" статьи рецензируются. Статьи могут отправляться авторам на доработку. Не принятые к опубликованию статьи авторам не возвращаются.

Журнал "Механика и физика материалов" ("Materials Physics and Mechanics") включен в систему цитирования Web of Science Emerging Sources Citation Index (ESCI), SCOPUS и РИНЦ.

© 2017, Санкт-Петербургский политехнический университет Петра Великого  
© 2017, Институт проблем машиноведения Российской Академии Наук

## Contents

|   |                |
|---|----------------|
| <b>Investigation of the influence of strain induced junction disclinations on hardening and nucleation of cracks during plastic deformation of polycrystals.....</b>                  | <b>237-242</b> |
| V.V. Rybin, V.N. Perevezentsev, J.V. Svirina  |                |
| <b>Micropolar media with structural transformations – theory illustrated by an example problem.....</b>   | <b>243-252</b> |
| W. H. Müller, E.N. Vilchevskaya   |                |
| <b>Mechanical properties of nanostructured titanium with bioactive titanium-organic nanocoating.....</b>  | <b>253-257</b> |
| E.G. Zemtsova, N.F. Morozov, B.N. Semenov, R.Z. Valiev, V.M. Smirnov  |                |
| <b>Dynamic strength properties of an ultra-fine-grained aluminum alloy under tension conditions.....</b>  | <b>258-261</b> |
| A.D. Evstifeev, A.A. Chevrychkina, Y.V. Petrov  |                |
| <b>Nucleation and growth mechanisms of CdTe thin films on silicon substrates with silicon carbide buffer layers.....</b>  | <b>262-271</b> |
| A.A. Koryakin, S.A. Kukushkin, A.V. Redkov  |                |
| <b>On influence of shear traction on hydraulic fracture propagation.....</b>  | <b>272-277</b> |
| A. M. Linkov  |                |
| <b>Elastomer composites based on filler with negative coefficient of thermal expansion: experiments and numerical simulations of stress-strain behaviour.....</b>                     | <b>278-287</b> |
| S.N. Shubin, A.G. Akulichev, A.B. Freidin   |                |
| <b>Fabrication of p-type transparent oxide films with delafossite structure by sol-gel processing.....</b>  | <b>288-292</b> |
| E.V. Shirshneva-Vaschenko, L.A. Sokura, T.G. Liashenko, E. Podlesnov, V.E. Bougrov, A.E. Romanov  |                |
| <b>Application of quantum-chemical modeling results in experimental investigations of silicone composites.....</b>  | <b>293-297</b> |
| H.H. Valiev, V.V. Vorobyev, Yu.N. Karnet, Yu.V. Kornev, O.B. Yumashev   |                |
| <b>Experimental verification of postulate of isotropy and mathematical modeling of elastoplastic deformation processes following the complex angled nonanalytic trajectories.....</b> | <b>298-304</b> |
| V.G. Zubchaninov, A.A. Alekseev, E.G. Alekseeva, V.I. Gultiaev  |                |
| <b>Testing of steel 45 under complex loading along the cylindrical screw trajectories of deformation....</b>  | <b>305-311</b> |
| V.G. Zubchaninov, V.I. Gultiaev, A.A. Alekseev, V.V. Garanikov, S.L. Subbotin   |                |
| <b>Validation of the mathematical model of isotropic material using parametric optimization of its physical and mechanical characteristics.....</b>                                   | <b>312-320</b> |
| A.I. Borovkov, O.I. Klyavin, O.I. Rozhdestvenskiy, M.V. Aleshin, A.N. Leontev, S.P. Nikulina, K.S. Ivanov, A.P. Okunev  |                |
| <b>On using quasi-random lattices for simulation of isotropic materials.....</b>  | <b>321-327</b> |
| Vadim A. Tsaplin, Vitaly A. Kuzkin  |                |
| <b>Review of the computational approaches to advanced materials simulation in accordance with modern advanced manufacturing trends.....</b>   | <b>328-352</b> |
| A.V. Shymchenko, V.V. Tereshchenko, Y.A. Ryabov, S.V. Salkutsan, A.I. Borovkov  |                |
| <b>On one class of applied gradient models with simplified boundary problems.....</b>   | <b>353-369</b> |
| S.A. Lurie, P. A. Belov, Y.O. Solyaev, E.C. Aifantis  |                |
| <b>Comparison of adaptive algorithms for solving plane problems of classical and cosserat elasticity....</b>  | <b>370-382</b> |
| M.A. Churilova, M.E. Frolov   |                |
| <b>Finite element modelling of the mitral valve repair using an implantable leaflet plication clip.....</b>   | <b>383-392</b> |
| M. D. Stepanov, O.S. Loboda, Y. V. Novozhilov, N. V. Vasilyev   |                |

## Содержание

|   |                |
|---|----------------|
| <b>Investigation of the influence of strain induced junction disclinations on hardening and nucleation of cracks during plastic deformation of polycrystals.....</b>                  | <b>237-242</b> |
| V.V. Rybin, V.N. Perevezentsev, J.V. Svirina  |                |
| <b>Micropolar media with structural transformations – theory illustrated by an example problem.....</b>   | <b>243-252</b> |
| W. H. Müller, E.N. Vilchevskaya   |                |
| <b>Mechanical properties of nanostructured titanium with bioactive titanium-organic nanocoating.....</b>  | <b>253-257</b> |
| E.G. Zemtsova, N.F. Morozov, B.N. Semenov, R.Z. Valiev, V.M. Smirnov  |                |
| <b>Dynamic strength properties of an ultra-fine-grained aluminum alloy under tension conditions.....</b>  | <b>258-261</b> |
| A.D. Evstifeev, A.A. Chevrychkina, Y.V. Petrov  |                |
| <b>Nucleation and growth mechanisms of CdTe thin films on silicon substrates with silicon carbide buffer layers.....</b>  | <b>262-271</b> |
| A.A. Koryakin, S.A. Kukushkin, A.V. Redkov  |                |
| <b>On influence of shear traction on hydraulic fracture propagation.....</b>  | <b>272-277</b> |
| A. M. Linkov  |                |
| <b>Elastomer composites based on filler with negative coefficient of thermal expansion: experiments and numerical simulations of stress-strain behaviour.....</b>                     | <b>278-287</b> |
| S.N. Shubin, A.G. Akulichev, A.B. Freidin   |                |
| <b>Fabrication of p-type transparent oxide films with delafossite structure by sol-gel processing.....</b>  | <b>288-292</b> |
| E.V. Shirshneva-Vaschenko, L.A. Sokura, T.G. Liashenko, E. Podlesnov, V.E. Bougrov, A.E. Romanov  |                |
| <b>Application of quantum-chemical modeling results in experimental investigations of silicone composites.....</b>  | <b>293-297</b> |
| H.H. Valiev, V.V. Vorobyev, Yu.N. Karnet, Yu.V. Kornev, O.B. Yumashev   |                |
| <b>Experimental verification of postulate of isotropy and mathematical modeling of elastoplastic deformation processes following the complex angled nonanalytic trajectories.....</b> | <b>298-304</b> |
| V.G. Zubchaninov, A.A. Alekseev, E.G. Alekseeva, V.I. Gultiaev  |                |
| <b>Testing of steel 45 under complex loading along the cylindrical screw trajectories of deformation....</b>  | <b>305-311</b> |
| V.G. Zubchaninov, V.I. Gultiaev, A.A. Alekseev, V.V. Garanikov, S.L. Subbotin   |                |
| <b>Validation of the mathematical model of isotropic material using parametric optimization of its physical and mechanical characteristics.....</b>                                   | <b>312-320</b> |
| A.I. Borovkov, O.I. Klyavin, O.I. Rozhdestvenskiy, M.V. Aleshin, A.N. Leontev, S.P. Nikulina, K.S. Ivanov, A.P. Okunev  |                |
| <b>On using quasi-random lattices for simulation of isotropic materials.....</b>  | <b>321-327</b> |
| Vadim A. Tsaplin, Vitaly A. Kuzkin  |                |
| <b>Review of the computational approaches to advanced materials simulation in accordance with modern advanced manufacturing trends.....</b>   | <b>328-352</b> |
| A.V. Shymchenko, V.V. Tereshchenko, Y.A. Ryabov, S.V. Salkutsan, A.I. Borovkov  |                |
| <b>On one class of applied gradient models with simplified boundary problems.....</b>   | <b>353-369</b> |
| S.A. Lurie, P. A. Belov, Y.O. Solyaev, E.C. Aifantis  |                |
| <b>Comparison of adaptive algorithms for solving plane problems of classical and cosserat elasticity....</b>  | <b>370-382</b> |
| M.A. Churilova, M.E. Frolov   |                |
| <b>Finite element modelling of the mitral valve repair using an implantable leaflet plication clip.....</b>   | <b>383-392</b> |
| M. D. Stepanov, O.S. Loboda, Y. V. Novozhilov, N. V. Vasilyev   |                |

# INVESTIGATION OF THE INFLUENCE OF STRAIN INDUCED JUNCTION DISCLINATIONS ON HARDENING AND NUCLEATION OF CRACKS DURING PLASTIC DEFORMATION OF POLYCRYSTALS

V.V. Rybin, V.N. Perevezentsev, J.V. Svirina\*

Mechanical Engineering Research Institute of RAS, 85 Belinsky str., 603024 Nizhny Novgorod, Russia

\*e-mail: j.svirina@mail.ru

**Abstract.** An influence of elastic field of strain induced junction disclinations on hardening and nucleation of a micro-crack in a head of edge lattice dislocations pile-up is considered. Computer simulation method is used to calculate critical external stress for plastic shear propagation through a force barrier induced by junction disclination. A qualitative explanation is given for the experimentally observed essential growth of the flow stress at sufficiently large plastic deformations. It is shown that the appearance of junction disclinations suppress nucleation of micro-cracks according to the mechanism of pile-up head dislocations confluence proposed by Stroh [1].

**Keywords:** strain induced junction disclination, plastic deformation, hardening, crack nucleation

## 1. Introduction

The difference in crystallographic orientations of polycrystal grains leads to their unequal plastic strains under loading. As a consequence it leads to the appearance of rotational type linear mesodefects in triple junctions and on the ledges of grain boundaries [2,3]. These mesodefects, called strain induced junction disclinations, generate powerful field of elastic stresses that essentially influences on plastic flow and fracture of polycrystals. However, up to now the main attention of researchers has been focused on the study of the role of strain induced junction disclinations in fragmentation phenomenon (i. e. subdivision of uniformly oriented initial grains of polycrystal into strongly misoriented regions, viz., fragments during large plastic deformation) [3,4]. The influence of strain induced junction disclinations on strain hardening and fracture of polycrystals remains less investigated [5,6].

In the framework of classical physics of dislocations, an increase of flow stress during plastic deformation is usually associated with an increase of a density of lattice dislocations distributed over the volume of grains, as well as with the interaction of dislocations with high angle grain boundaries and dislocation subboundaries [7]. However, physical models of hardening based on these assumptions do not explain the essential growth of plastic flow stresses up to values of  $\sim 10^{-3} \div 10^{-2} G$  ( $G$  is the shear modulus) at the true strain values  $\varepsilon > 0.2$ . In our opinion, it is possible to explain this experimental fact taking into account that the elastic fields of junction disclinations retard the motion of lattice dislocations providing plastic deformation of the body of grains. In present paper computer simulation method is used to investigate the conditions for the propagation of plastic shear carried out by both individual dislocations and pile-up of edge dislocations motion through a force barrier of junction disclination.

Besides, experimental studies show that at large plastic strains the change of fracture mechanisms take place. The nucleation of microcracks occurs according to the disclination mechanism [8], while classical Stroh's mechanism [1] of microcrack initiation in the head of a retarded pile-up of edge dislocations take no place. In this work the limitation of Stroh's model for large plastic deformations is explained by the influence of strain induced junction disclination.

## 2. Description of the model

Let us consider a junction of three grains plastically deformed up to a strain  $\varepsilon_i$  ( $i = 1, 2, 3$ ) (See Fig. 1). The difference of plastic strains of adjacent grains leads to the appearance of additional misorientations on the grain boundaries  $\Delta\Theta_j = N_j \times \Delta\varepsilon_j \cdot N_j$  ( $j = 1, 2, 3$ ). Their values are determined by the values of plastic deformation jumps  $\Delta\varepsilon_j$  at the  $j$ -th grain boundary and the orientation of the unit vector of the normal to the boundary  $N_j$ .

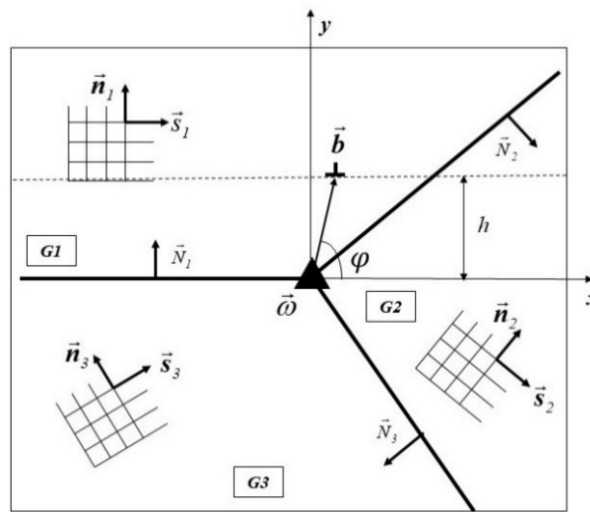


Fig. 1. Schematic plot of grain boundary triple junction.

The difference of additional misorientations on different grain boundaries leads to the appearance of a linear defect of the rotational type, i.e. junction disclination with a strength  $\omega = \sum_j \Delta\Theta_j$ , in the triple junction. Strain induced junction disclination generate field of elastic stresses that influences on the motion of lattice dislocations providing plastic deformation of the grains body. Further consideration of the model will be performed for two dimensional (2D) case for simplification.

Let edge dislocation with the Burgers vector  $\mathbf{b} = bs_1 = bi$  move in a slip plane placed at some distance  $y=h$  from the wedge junction disclination in the grain  $G1$ .

The disclination act on a probe dislocation in a given slip plane  $n_1$  with a force  $f_x^A = \sigma_{xy}^A b$ , where

$$\sigma_{xy}^A = -D\omega \frac{xy}{(x^2 + y^2)} = -\frac{D\omega \sin(2\varphi)}{2}, \quad (1)$$

$D = G/2\pi(1-\nu)$ ,  $\nu$  is a Poisson ratio,  $\varphi$  is an angle in polar coordinate system [9].

As seen from (1), this force is positive to the left of the disclination ( $x < 0$ ) and negative to the right of it ( $x > 0$ ). Thus, in the region  $x < 0$  the external stress force  $f_x^{ext} = \sigma_{xy}^{ext} b$  and disclination force acting on the dislocation are co-directed, and in the region  $x > 0$  these forces

are directed oppositely. Therefore in the region  $x > 0$  the moving dislocation is retarded by the elastic field of disclination. It is easy to note that a stable equilibrium takes place only if  $\sigma^{ext} < \sigma_c^*$ , where  $\sigma_c^* = D\omega/2$  is equal to maximum shear stress of the disclination (on the ray  $\varphi=45^\circ$  in polar coordinates). Thus, the condition for plastic shear propagation carried out by the motion of a single dislocation takes a form  $\sigma^{ext} \geq \sigma_c^*$ . Basing on this result, for typical values of the disclination strength  $\omega \approx 0.017 \div 0.034$  rad, the flow stress should be of the order of  $(2 \div 4) \cdot 10^{-2} G$ . However, this value can be smaller if plastic shear is carried out by a motion of group of dislocations.

In the case  $\sigma^{ext} < \sigma_c^*$  a single dislocation is stopped by the force barrier of junction disclination, but the emission of new dislocations by a source located in the slip plane leads to the formation of the dislocation pile-up, which creates an additional force acting on the head dislocation facilitating the shear propagation. Let us analyze the conditions for the plastic shear propagation through the disclination force barrier using computer simulation method [10].

The motion of dislocations was considered in a quasi-viscous approximation. The equation of motion for k-th dislocation of the pile-up in the slip plane  $y = h$  was written in the form:

$$\mathbf{V}^{(k)} = M\mathbf{b}^{(k)}\sigma_{xy}^\Sigma \quad (2)$$

Here:  $\mathbf{V}^{(k)}$  is the dislocation velocity,  $\sigma_{xy}^\Sigma = \sigma_{xy}^{ext} + \sigma_{xy}^A + \sigma_{xy}^{disl}$  is a total field of elastic stress including external stress  $\sigma_{xy}^{ext}$ , internal stresses caused by disclination  $\sigma_{xy}^A = -D\omega(xh/x^2 + h^2)$  and dislocations pile-up  $\sigma_{xy}^{disl} = Db \sum_{i \neq k} (x_k - x_i)^{-1}$  ( $1 \leq i \leq N_p - 1$ ),  $N_p$  is a number of dislocations in the pile-up,  $M$  is a dislocation mobility.

The formation of the pile-up were performed by sequential emission of positive dislocations by a source located on the left side of the grain  $GI$ . Each subsequent  $m + 1$  dislocation was emitted when other previously emitted  $m$  dislocations of the pile-up reach equilibrium state in order to avoid the influence of the dynamic effects [11] on the motion of dislocations and the configuration of the pile-up.

After emitting of the  $m + 1$  dislocation a new equilibrium pile-up configuration was calculated. Calculation of each configuration (the coordinates of the dislocations) was carried out by the method of sequential time iteration providing sufficiently small dislocation displacements for a given mobility  $M$ . The equilibrium configuration of the pile-up was determined from the condition that the forces acting on each dislocation of the pile-up were equal to zero. The condition for the plastic shear propagation were determined as the conditions under which the pile-up loss stability and its head dislocation leaves the pile-up and moves to a sink on the right side of the grain.

### 3. Results and discussion

Let us consider the influence of the external stress on the equilibrium configuration of the pile-up containing a given number of dislocations. The results of numerical calculation of the pile-up configuration for ten dislocations in the slip plane located at a distance  $h = 1 \mu\text{m}$  from the junction dislocation for different values of the external stress are shown in Fig. 2. The axial symmetry of the elastic stresses field of wedge disclination leads to the fact that in the absence of the external stresses ( $\sigma^{ext} = 0$ ) the dislocation pile-up is located symmetrically with respect to the plane passing through the disclination line perpendicular to the slip plane of the dislocations (Fig. 2a). As the external stress  $\sigma^{ext}$  increases, the dislocation pile-up displaces as a whole and its shape becomes more asymmetric (Fig. 2b). Finally, when the external stress

$\sigma^{ext}$  becomes greater than a certain critical one  $\sigma_c = 0.0145D$ , the pile-up becomes unstable, its head dislocation leaves the crystal.

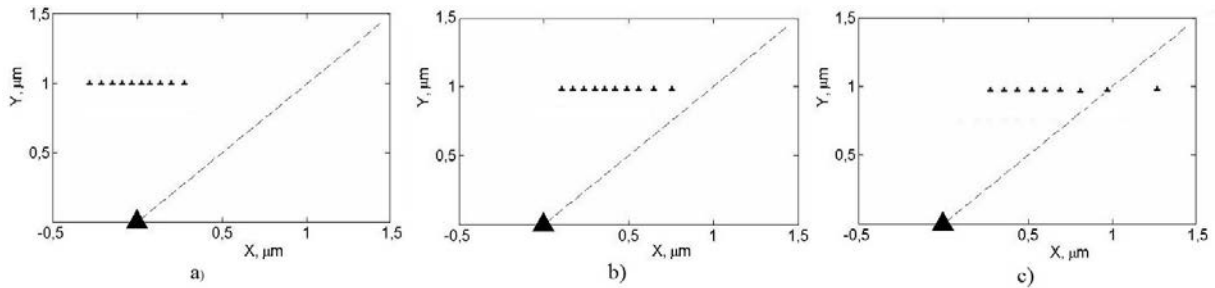


**Fig. 2.** Equilibrium configuration of the edge dislocations pile-up near disclination  $\omega = 0.04 \text{ rad}$ : (a)  $\sigma^{ext} = 0$ ; (b)  $\sigma_c = 0.01D$ ; (c) remaining part of the pile-up when the head dislocation left the crystal at  $\sigma^{ext} = 0.015D$ .

At the same time, the remaining dislocations of the pile-up rearrange into a new equilibrium configuration (Fig. 2c). It is obvious that an emission of a new dislocation by dislocation source will lead to the repeating of this process.

The results of calculations for the dependence of the critical shear stress on the number of dislocations in the pile-up for various values of  $h$  are shown in Fig. 3.

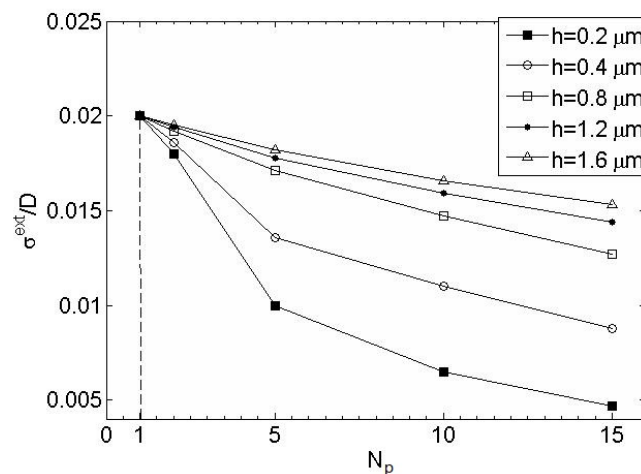


**Fig. 3.** The dependence of the critical external shear stress on the number of dislocations in the pile-up.

It is seen that for a fixed number of dislocations in the pile-up the value  $\sigma_c$  increases with the increase of the distance between the slip plane and disclination. Thus, when the plastic deformation is localized in certain slip planes, the greatest hardening effect from the elastic fields of disclination is achieved not near the grain boundary, but far from it.

It follows from the analysis that this type of dislocation pile-ups caused by junction disclinations accumulating during plastic deformation may exist in the body of grains in the absence of any visible physical barriers located in the slip plane.

One of the distinguishing features of this type of pile-ups is that they do not disappear under unloading.

Let us consider now the influence of junction disclinations on the nucleation of cracks at the head of the pile-up of edge dislocations stopped by the grain boundary oriented at an angle of  $30^\circ$  to the  $x$  axis (Fig.4). In the absence of disclinations ( $\omega = 0$ ) the classical scheme for

crack initiation according to the Stroh's model takes place. In this model the crack nucleation occurs at  $\sigma > \sigma_c$  where  $\sigma_c$  is the value of stress at which two head dislocations of the pile-up come to a distance  $d < 2r_c$ , where  $r_c \sim b$  is the radius of the dislocation core.

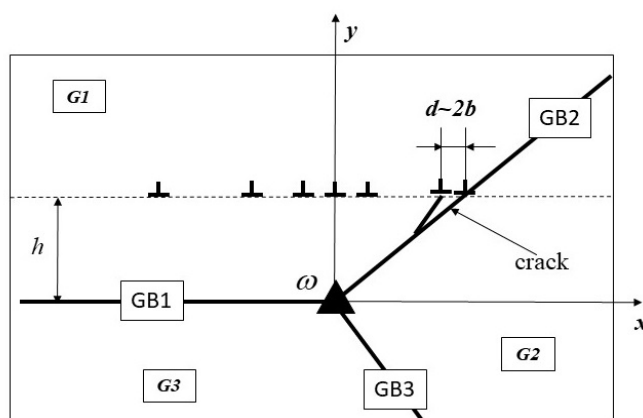


**Fig. 4.** Schematic plot of the crack nucleation at the head of edge dislocations pile-up.

For a given external stress, the crack nucleation is possible only when the number of dislocations in the pile-up is greater than a certain critical one (curve 2 in Figure 5.) Note that, as Stroh showed, at  $\sigma > \sigma_c$  the action of the external stress is sufficient to move the largest part of the remaining dislocations of pile-up into a crack that makes possible the initiation of a Griffith's crack.

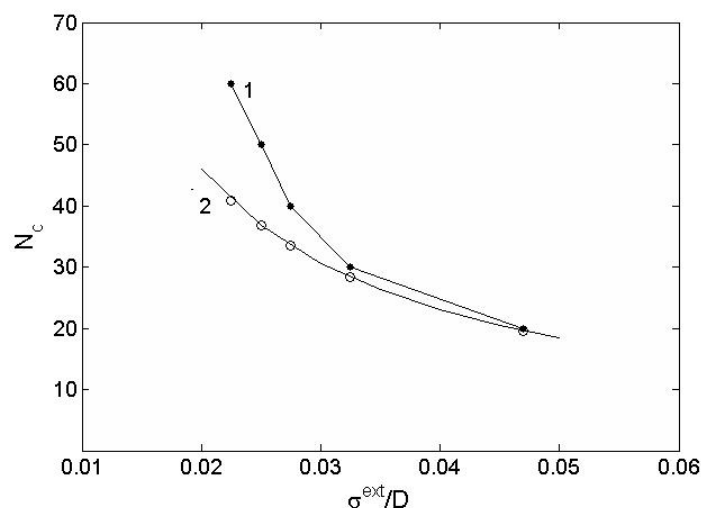


**Fig. 5.** The dependence of critical number of dislocations in the pile-up on the external stress at junction disclination strength  $\omega = 0.01$  (curve 1) and at  $\omega = 0$  (curve 2),  $h = 1 \mu\text{m}$ .

The results of computer simulation show that junction disclination suppress the crack nucleation. The confluence of the head dislocations of pile-up occurs at a greater number of dislocations than in the Stroh model. The dependence of the critical number of dislocations at the typical disclination strength  $\omega = 0.01$  rad is shown in curve 1 in Fig. 5 for  $h = 1 \mu\text{m}$ . Obviously, this effect can be neglected only for very large external stress values  $\sigma^{ext} \gg D\omega/2$ .

#### 4. Conclusion

Basing on the results of the analysis the following conclusion can be summarized:

- A physical mechanism of hardening associated with the accumulation of disclination in triple junctions of high angle grain boundaries at large plastic deformation is developed.
- An existence of special type dislocation pile-ups forming at large plastic deformation in the absence of any visible physical barriers in the body of grains is predicted.
- Strain induced junction disclinations suppress cracks nucleation in the head of dislocations pile-up.

#### *Acknowledgment*

*This work was supported by the Russian Science Foundation, project No. 15-13-20030.*

#### References

- [1] A.N. Stroh // *Proceedings of the Royal Society of London. Series A, Mathematical and Physical Sciences* **223(1154)** (1954) 404.
- [2] V.V. Rybin, A.A. Zisman, N.Yu. Zolotarevsky // *Acta Metallurgica et Materialia* **41(7)** (1993) 2211.
- [3] V.V. Rybin // *Problems of materials science* **1(33)** (2003) 9.
- [4] A.E. Romanov, A.L. Kolesnikova // *Progress in Materials Science* **54** (2009) 740.
- [5] M. Seefeldt // *Reviews on advanced materials science* **2** (2001) 44.
- [6] A.E. Romanov // *European Journal of Mechanics A/Solids* **22** (2003) 727.
- [7] J. Friedel, *Dislocations* (Pergamon, London 1964) p. 391.
- [8] V.N. Perevezentsev, G.F. Sarafanov // *Technical Physics Letters* **41(10)** (2015) 968.
- [9] A.E. Romanov, V.I. Vladimirov, In: *Dislocations in Solids*, ed. by F.R.N. Nabarro (North Holland, Amsterdam, 1992), Vol. 9, p. 191.
- [10] E. Van der Giessen and A. Needleman // *Modelling and Simulation in Materials Science and Engineering* **3(5)** (1995) 689.
- [11] E.A. Rzhavtsev, M.Y. Gutkin // *Scripta Materialia* **100** (2015) 102.

# MICROPOLAR MEDIA WITH STRUCTURAL TRANSFORMATIONS – THEORY ILLUSTRATED BY AN EXAMPLE PROBLEM

W. H. Müller<sup>1\*</sup>, E.N. Vilchevskaya<sup>2</sup>

<sup>1</sup>Institute of Mechanics, Chair of Continuum Mechanics and Constitutive Theory,  
Technische Universität Berlin, Einsteinufer 5, 10587 Berlin, Germany

<sup>2</sup>Institute for Problems in Mechanical Engineering of the Russian Academy of Sciences,  
Bol'shoy pr. 61, V.O., 199178 St. Petersburg, Russia and Peter the Great Saint-Petersburg Polytechnic  
University, Politekhnikeskaja 29, 195251 St.-Petersburg, Russia

\*e-mail: whmueller1000@gmail.com

**Abstract.** This paper is concerned with a model for an extended theory of micropolar media. The extension concerns the balance for the tensor field of the moment of inertia, which in contrast to previous theories contains a production term. This term becomes important if the micropolar material undergoes structural changes. In the present case we consider an assemblage of hollow spheres, which due to a transient temperature field contract or expand. This leads to a true field for the tensor of the moment of inertia varying in space and time. For this situation the production term can be calculated numerically. In addition, the temporal and spatial change of the macroscopic inertia field influences rotational motion. Based on a numerical solution for the balance of spin we study the evolution of angular velocity in space and time. The importance of the presence of a volume couple density is stressed and its physical realization will be discussed.

**Keywords:** micropolar media, production of microinertia, balances of angular momentum and spin, volume couple.

## 1. Introduction and outline to the paper

Generalized Continuum Theories (GCTs) have gained the attention of the materials science community for a long time. Their idea is to capture the behavior of high performance materials with an inner structure and internal degrees of freedom. Applications range from the small to the large scale and involve solids as well as liquids. Concrete examples are manifold and can be found in light-weight aerospace and automotive structures, liquid crystal panels, and well as micromechanics and microelectronic gadgets. One of the GCTs is the so-called micropolar theory, which emphasizes the aspect of inner rotational degrees of freedom of a material [1]. This theory seems particularly promising for applications to soils, polycrystalline and composite matter, granular and powder-like materials, and even to porous media and foams.

Continuum mechanics of solids is typically formulated in the Lagrangian way, a.k.a. material description, where the concept of an indestructible “material particle” prevails, identifiable by its reference position. Hence a bijective mapping for describing the particle's path through three-dimensional space in time uniquely can be used. Note that this requires the neighboring material particles to remain “close” to each other during the motion. Furthermore note that a material particle in the continuum sense is composed of myriads of atoms or molecules, so that statistical fluctuations play no role in a macroscopic continuum. Furthermore

there is no exchange of the atoms and molecules between material particles: The mass of a material particle is conserved.

Traditionally this concept is also used in micropolar theory [1,2]. One may say that the corresponding material particle consists of a statistically significant number of subunits on a mesoscopic scale, for confusion often also called “particles.” Now, if the Lagrangian idea of a material particle is followed, the material particles must stay together during the motion and there should be no exchange of subunits between them. Also note that within the material description of a micropolar continuum, each material point is phenomenologically equivalent to a rigid body, such that its microinertia does not change [2].

However, there is a catch. As an example consider a granular medium which is milled. This effects the material particle, because its subunits will be crushed. They will change their mass and their moment of inertia and, what is more, during the milling process there might even be an exchange of crushed subunits between neighboring material particles, which are then no longer material in the original sense. Consequently, on a macroscopic scale the moments of inertia will change as well. It is for that reason that the authors of [3] have departed from the idea of following the Lagrangian way and turn to the Eulerian perspective (a.k.a. spatial description) instead. Originally the Eulerian description stems from fluid mechanics. It does not impose strict constraints on the motion of mass-conserved material points. Rather it embraces the idea of an open system, allowing a priori for exchange of mass, momentum, energy, moment of inertia, etc., between the cells of the Eulerian grid.

Moreover, the authors in [3] proposed a kinetic equation for microinertia (the field of the local inertia tensor), which in contrast to former theories contains a production term. For a better understanding of this new concept they also present an underlying mesoscopic theory. Their idea is to connect information on a mesoscale by taking the intrinsic microstructure within a spatial grid cell into account with the macroscopic world, i.e., with the balances of micropolar continua in combination with suitable constitutive equations.

These new ideas have been illustrated by several examples in previous papers [3-5], in particular: (a) A homogeneous mix of pressurized hollow spherical particles undergoing a uniform change of external pressure so that their diameter and moment of inertia changes; (b) Particles of type (a) but initially inhomogeneously distributed in an isothermal atmosphere subjected to a barometric pressure distribution falling down and thereby transporting a flux of into new observational points; (c) Changes of anisotropy due to reorientation of initially randomly oriented ellipsoidal particles; (d) Fragmentation of spherical particles in a crusher, analytically as well as numerically. What has been missing so far were examples that show the impact of a changing moment of inertia onto rotational motion.

Therefore, in this paper we will, first, present the foundations of the extended continuum approach to micropolar media and make a few remarks regarding the underlying mesoscopic interpretation. In particular, we will motivate and explain the necessity for a kinetic equation describing the temporal development of the field for the moment of inertia. Second, we will study the change of the state of rotation of a homogeneous mix of pressurized hollow spherical particles undergoing a nonuniform change of external temperature affecting their moment of inertia. Note that within the classical framework of micropolar theory a change of temperature would not influence rotation. However, within the to-be-presented theory changes in temperature will influence the inertia tensor and hence couple to rotational speed.

The paper will conclude with an outlook of how the developed models can be used for complex engineering applications, which will require a fully numerical investigation. In this context the problems studied so far may provide a first orientation.

## 2. Theoretical background

If we refrain from taking an interaction between linear and angular kinetic energies into account, the objective of micropolar theory is to determine the following thirteen primary fields: (a) the scalar field of mass density,  $\rho(\mathbf{x}, t)$ ; (b) the vector field of linear velocity,  $\mathbf{v}(\mathbf{x}, t)$ ; (c) the symmetric, second rank, positive definite specific moment of inertia tensor field,  $\mathbf{J}(\mathbf{x}, t)$ , in units of  $\text{m}^2$ ; and (d) the spin (a.k.a. angular velocity) field,  $\boldsymbol{\omega}(\mathbf{x}, t)$ , in all points,  $\mathbf{x}$ , and at all times,  $t$ , within a region of space,  $\mathcal{B}$ , which can be either a material volume, *i.e.*, it consists of the same matter at all times, or be a region through which matter is flowing.

The determination of these fields relies on field equations for the primary fields. The field equations are based on balance laws and need to be complemented by suitable constitutive relations. In regular points these macroscopic balances read as follows:

- balance of mass:

$$\frac{\delta \rho}{\delta t} + \rho \nabla \cdot \mathbf{v} = 0, \quad (1)$$

- balance of momentum:

$$\rho \frac{\delta \mathbf{v}}{\delta t} = \nabla \cdot \boldsymbol{\sigma} + \rho \mathbf{f}, \quad (2)$$

- balance of moment of inertia and coupling moment of inertia tensors:

$$\frac{\delta \mathbf{J}}{\delta t} + \mathbf{J} \times \boldsymbol{\omega} - \boldsymbol{\omega} \times \mathbf{J} = \boldsymbol{\chi}_J, \quad (3)$$

- balance of spin:

$$\rho \mathbf{J} \cdot \frac{\delta \boldsymbol{\omega}}{\delta t} + \boldsymbol{\omega} \times \mathbf{J} \cdot \boldsymbol{\omega} = \nabla \cdot \boldsymbol{\mu} + \boldsymbol{\sigma}_\times + \rho \mathbf{m}, \quad (4)$$

with

$$\frac{\delta(\cdot)}{\delta t} = \frac{d(\cdot)}{dt} + (\mathbf{v} - \mathbf{w}) \cdot \nabla(\cdot), \quad (5)$$

denoting the substantial (a.k.a. material) derivative of a field quantity, and  $d(\cdot)/dt$  being the total time derivative including the mapping velocity  $\mathbf{w}$  of the observational point. Moreover,  $\boldsymbol{\sigma}$  is the (non-symmetric) Cauchy stress tensor,  $\mathbf{f}$  is the specific body force,  $\boldsymbol{\chi}_J$  (a second rank symmetric tensor) is the production related to the moment of inertia tensor,  $\mathbf{J}$ ;  $\boldsymbol{\mu}$  is the couple stress tensor,  $\boldsymbol{\sigma}_\times := \boldsymbol{\varepsilon} \bullet \boldsymbol{\sigma}$  is the Gibbsian cross applied to the (non-symmetric) Cauchy stress tensor (where “ $\bullet$ ” is supposed to denote the outer double scalar product),  $\boldsymbol{\varepsilon}$  being the Levi-Civita tensor, and  $\mathbf{m}$  refers to the specific volume couple density.

Additional information on this extended set of equations can be found in [3-5]. Nevertheless, since Eq. (3) is non-standard several comments are in order. In its present form it was introduced for the first time in [3]. There is a precedent relation to it called “conservation of microinertia” in [2], pg.15. Note that this equation does not contain a production term,  $\boldsymbol{\chi}_J$ . On the macroscopic continuum level this new term must be interpreted suitably. In [3] it was referred to as a constitutive quantity characteristic of the to-be-processed material. However, a deeper analysis shows that this is not as clear cut as we would wish it to be. Indeed, in [4] evidence was provided that it also takes process characteristics into account. On a more general note it must be asked as to whether Eq. (3) is truly a balance equation, because its counterpart in [2] is a purely kinematic relation. Therefore, one could be tempted to characterize it as a kinetic equation for  $\mathbf{J}$ , which would turn all of Eq. (3) into a constitutive relation. On the other hand, in view of Eq. (1), which balances translational inertia, *i.e.*, mass, it is equally tempting to interpret (3) as a balance of rotational inertia.

One of the purposes of this and other of our papers [4,5] is to present explicit relations for  $\chi_j$ , always in context with illustrative problems. Typically such relations are based on a mesoscopic model which is then applied on the macroscopic level. We shall illustrate this approach in the next sections. It should also be said that for certain situations it is possible to give additional explanations for the necessity of occurrence of a production of inertia. For example in [5] it was embedded in a mixture theory and related to reaction rates and excess velocities. In [7] statistical mechanics based on the transfer equation procedure introduced by Irving and Kirkwood was used in order to relate it to the effect of the non-material transport of rotational inertia on a microscopic scale through an open system. May it suffice to say that situations where the particle number and the associated moment of inertia (but not the mass) change require us to look at the problem from the Eulerian point-of-view (a.k.a. spatial description) and not from the Lagrangian one (a.k.a. material description). An example (the crusher) is presented in [4]. However, in the case study of this paper, this distinction is not necessary. Here the change of rotational inertia is based on internal shape changes as we shall now proceed to explain.

### 3. A model problem: Turning heat conduction into space-varying rotational motion

The general problem is as follows. We consider a medium consisting of empty hollow elastic spheres homogeneously distributed within a one-dimensional region  $x \in [0, L]$ . Their initial inner and outer radii are  $R_i$  and  $R_o$ , respectively. However, the temperature of this medium changes within time from an initially constant value  $T_{ini}$  because reservoirs kept at temperatures  $T_0$  and  $T_l$  are attached at positions  $x=0$  and  $x=l$  of the region, respectively. The development of temperature,  $T$ , is therefore governed by the following initial boundary value problem:

$$\frac{\partial T}{\partial t} = D \frac{\partial^2 T}{\partial x^2}, \quad D = \frac{\kappa}{\rho_0 c_v}, \quad T(x, t=0) = T_{ini}, \quad T(x=0, t) = T_0, \quad T(x=l, t) = T_l, \quad (6)$$

where  $D$  is thermal diffusivity,  $\kappa$  thermal conductivity,  $\rho_0$  the (constant) mass density of the medium, and  $c_v$  specific heat at constant volume. According to [8], Sect. 3.4 the solution to this problem in dimensionless form is given by:

$$\bar{T}(\bar{x}, \bar{t}) = \bar{T}_0 + (\bar{T}_l - \bar{T}_0)\bar{x} + \frac{2}{\pi} \sum_{n=1}^{\infty} \frac{\bar{T}_l \cos(n\pi) - \bar{T}_0}{n} \sin(n\pi\bar{x}) \exp(-n^2\pi^2\bar{t}) + \quad (7)$$

$$\frac{2}{\pi} \sum_{n=1}^{\infty} \frac{1 - \cos(n\pi)}{n} \sin(n\pi\bar{x}) \exp(-n^2\pi^2\bar{t}),$$

with  $\bar{x} = x/l$ ,  $\bar{t} = D/l^2 t$ ,  $\bar{T} = T/T_{ini}$ . It is assumed that the temperature is instantaneously adopted by the linear elastic spheres. In order to find the current inner and outer radii,  $r_i$  and  $r_o$ , respectively we have to solve the problem of thermal expansion of a hollow linear elastic sphere when subjected to a uniform temperature change. The solution for a free, fully radially symmetric expansion is:

$$r_i = [1 + \alpha T_{ini}(\bar{T} - 1)] R_i, \quad r_o = [1 + \alpha T_{ini}(\bar{T} - 1)] R_o. \quad (8)$$

Now recall that the current specific moment of inertia tensor of a hollow sphere with corresponding inner and outer radii is isotropic and given by:

$$\mathbf{J} = J \mathbf{I}, \quad J = \frac{2}{5} \frac{r_o^5 - r_i^5}{r_o^3 - r_i^3}. \quad (9)$$

Hence:

$$J = J_0 \left[ 1 + \alpha T_{\text{ini}} (\bar{T} - 1) \right]^2, \quad J_0 := \frac{2}{5} R_0^2 \frac{1 - \beta^5}{1 - \beta^3}, \quad \beta := \frac{R_1}{R_0}. \quad (10)$$

We now argue that after homogenization the macroscopic field for the tensor of inertia stays isotropic,  $\mathbf{J}(\mathbf{x}, t) = J(\mathbf{x}, t) \mathbf{I}$  (hence the second term on the left of Eq. (4) vanishes), and is given by the last relation where the normalized temperature  $\bar{T}$  is replaced by the expression shown in Eq. (7). Turning to Eq. (3) we are now in a position to specify the production for the moment of inertia, if we assume that the translational velocity vanishes,  $\mathbf{v} = \mathbf{0}$  (see Eq. (5)):

$$\chi_J = \chi_J \mathbf{I}, \quad \chi_J \equiv \frac{\partial J}{\partial t} = \chi_0 \left[ 1 + \alpha T_{\text{ini}} (\bar{T}(\bar{x}, \bar{t}) - 1) \right] \frac{\partial \bar{T}(\bar{x}, \bar{t})}{\partial \bar{t}}, \quad \chi_0 := 2 \alpha T_{\text{ini}} J_0 \frac{D}{l^2}. \quad (11)$$

How does this affect the development of translational and angular velocities? For an answer we turn to the macroscopic balances of linear and angular momentum shown in Eqs. (2/4). There are no body forces (we ignore gravity),  $\mathbf{f} = \mathbf{0}$ , the stress tensor is zero (we consider the medium to be “dust”),  $\boldsymbol{\sigma} = \mathbf{0}$ , the translational velocity is initially zero. Then Eq. (2) is telling us that it stays zero,  $\mathbf{v} = \mathbf{0}$ . Regarding the balance of angular momentum (4) we assume that the couple stress tensor vanishes,  $\boldsymbol{\mu} = \mathbf{0}$ , and initially start with a constant volume couple density different from zero,  $\mathbf{m} = m_0 \mathbf{e}_z$ ,  $m_0 = \text{const.}$ ,  $\mathbf{e}_z$  being the unit normal in  $z$ -direction.

Hence  $\boldsymbol{\omega} = \omega(x, t) \mathbf{e}_z$  and

$$\frac{\partial \omega}{\partial t} = \frac{m_0}{J(x, t)}. \quad (12)$$

This differential equation can be solved numerically so that we obtain an angular velocity field  $\omega = \omega(x, t)$  different from zero decreasing or increasing in space and time. We conclude that if the temperature changes in space and time due to the presence of external heat reservoirs, the moment of inertia will change accordingly, and we may harvest “good” macroscopic rotational energy by using this “heat engine,” provided there is an agent of transfer in terms of a non-vanishing (constant) specific volume couple density  $m_0$ . Note that even if the temperature remained totally constant we would obtain a homogeneously distributed angular velocity increasing linearly in time as follows,

$$\omega(t) = \frac{m_0}{J_0} t, \quad (13)$$

if we assume it initially to be zero.

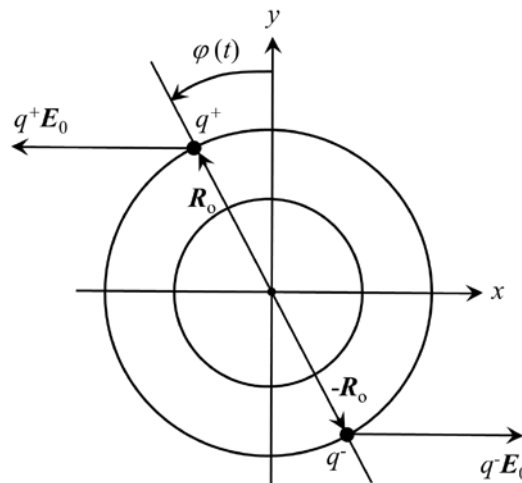


Fig. 1. Model of an electrically polarized sphere.

But how do we realize specific volume couples, at least theoretically? Unfortunately the pertinent literature on micropolar solids is rather taciturn regarding this issue. In [9] we read “Ordinarily, we expect gravitational or electromagnetic fields to produce the forces  $[\mathbf{f}]$  and  $[\mathbf{m}]$  ... The question of how best to describe the effects of electromagnetic fields is not so easily settled. It is of some importance since they are observed to influence the orientation of liquid crystals.” And in [10] we hear: “But the modern notion of volume couple, a continuum density of torque, is more elusive having, it is true, no direct physically visible realization ... But what about a density of magnetic couple, a thing that also played an important role in the construction of wide classes of GCM [Generalized Continuum Mechanics] with nonsymmetric Cauchy stress tensor? ...” Indeed, the theory of nematic crystals, which are perceived as electric dipoles, provides a clue. Imagine, we manage to polarize the spheres electrically as indicated in Fig. 1. The net charge,  $q^+ + q^-$ , would be zero. Now we apply a constant external electric field,  $\mathbf{E}_0 = E_0 \mathbf{e}_x$ , in negative  $x$ -direction. The total Coulomb force, and therefore (after homogenization) the body force (in  $x$ -direction), would vanish. However, the moment couple acting on the sphere would not. Rather it points in  $z$ -direction and is given by:

$$\mathbf{M} = q^+ \mathbf{R}_0 \times \mathbf{E}_0 - q^- \mathbf{R}_0 \times \mathbf{E}_0 = 2qR_0 E_0 \cos \varphi(t) \mathbf{e}_z, \quad (14)$$

$q$  being the magnitude of the dipole charge. Similar reflections can be found in [11]. Hence in this model the volume moment couple density is time-dependent as follows:

$$\mathbf{m} = m_0 \cos \int_{\bar{t}=0}^{\bar{t}=\bar{t}} \omega(\bar{t}) d\bar{t} \mathbf{e}_z, \quad m_0 = 2 \frac{q}{m_p} R_0 E_0 \quad (15)$$

provided  $\varphi(0) = 0$ .  $m_p$  is the mass of one particle. In this case the balance of angular momentum (12) would change to:

$$J(x, t) \frac{\partial \omega(x, t)}{\partial t} = m_0 \cos \int_{t'=0}^{t'=t} \omega(x, t') dt'. \quad (16)$$

This can be rewritten as

$$\frac{\partial}{\partial t} \left[ \frac{J}{m_0} \frac{\partial \omega}{\partial t} \right] = -\omega \sqrt{1 - \left( \frac{J}{m_0} \frac{\partial \omega}{\partial t} \right)^2}, \quad (17)$$

a differential equation leading to oscillating motion as to-be-expected.

In summary we may say that the harvesting of rotational energy becomes possible because of the presence of a specific volume couple density, i.e., because of an electric field, and the amount of harvesting in a point of space depends on the development of the temperature field therein.

#### 4. Results and discussion

We choose the following normalized temperature values for our numerical simulations of the developing temperature profile:  $\bar{T}_0 = 0.5$ ,  $\bar{T}_l = 2.0$ . Fig. 2 shows the development of temperature at three dimensionless times,  $\bar{t} = 0.001$  (blue),  $\bar{t} = 0.01$  (red), and  $\bar{t} = 1.0$  (green), according to Eq. (7) where infinity was replaced by  $n_{\max} = 100$ . The transition to the stationary linear temperature profile becomes quite obvious. These profiles are then used in Eq. (10) in order to calculate the temporal development of the moment of inertia,  $\bar{J}$ , for  $\alpha T_{\text{ini}} = 0.5$ . For this large value we get a certain departure from linearity, even at  $\bar{t} = 1.0$ : Fig. 3. The two plots are very similar. As to-be-expected the moment of inertia decreases if temperature goes down and vice versa.

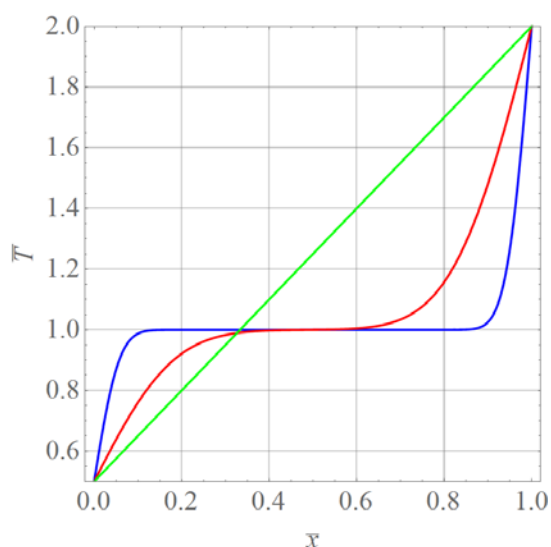


**Fig. 2.** Temperature profiles.

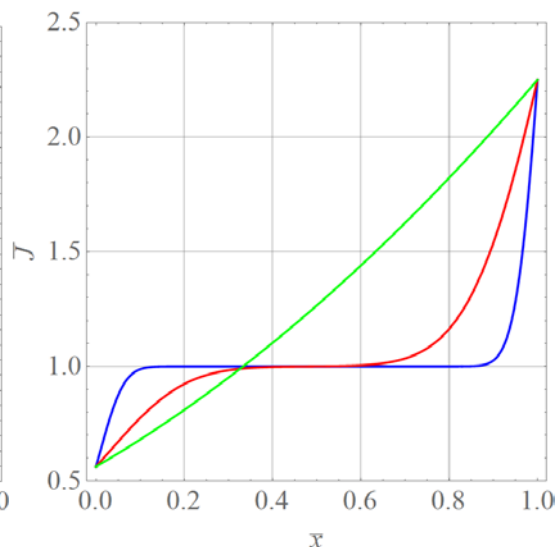


**Fig. 3.** Development of local moment of inertia.

The reason for the changing moment of inertia is presented in Fig. 4. It shows the temporal development of the normalized productions of moment of inertia,  $\bar{\chi} = \chi/\chi_0$ . Four positions are examined at  $\bar{x} = 0.1$  (blue),  $\bar{x} = 0.5$  (red),  $\bar{x} = 0.9$  (green), and  $\bar{x} = 1/3$  (magenta). The latter is the position for which  $\bar{T} = 1$  after an infinite time (see Eq. (7)). As demonstrated in Fig. 3 the spheres shrink for small values of  $\bar{x}$  (and expand for large ones), so that the moment of inertia decreases (and increases) accordingly, first fast and, as time goes on, slower and slower. The production behaves accordingly. The effect is less pronounced around the position  $\bar{x} = 1/3$  where the normalized temperature is close to one and only little change of moment of inertia occurs. For all cases the effect vanishes completely for  $\bar{t} \rightarrow \infty$  when the size of the spheres hardly changes any more.

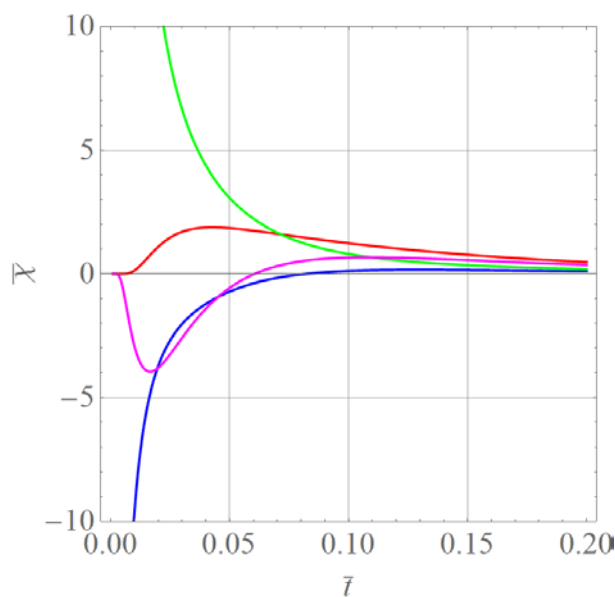


**Fig. 4.** Productions of moment of inertia at various positions (see text) over time.

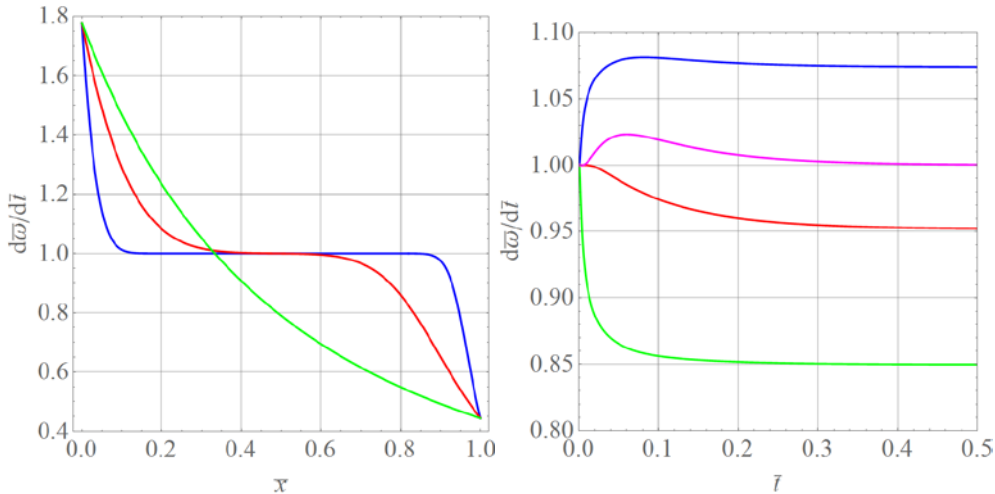


**Fig. 5.** Angular accelerations at various times over position and vice versa.

Now we turn to the balance of angular velocity for the case of a constant volume couple density,  $m_0$ , as shown in Eq. (12). In normalized form it reads:

$$\frac{\partial \bar{\omega}}{\partial \bar{t}} = \frac{1}{\bar{J}(x, \bar{t})}, \quad \bar{\omega} = \frac{\omega}{\omega_0}, \quad \omega_0 = \frac{m_0 l^2}{J_0 D}, \quad \bar{J} = \frac{J}{J_0} = [1 + \alpha T_{ini} (\bar{T} - 1)]^2. \tag{18}$$

The angular accelerations are shown in Fig. 5. On the left they are presented in normalized form as a function of position at times  $\bar{t} = 0.001$  (blue),  $\bar{t} = 0.01$  (red), and  $\bar{t} = 1.0$  (green). On the right they are shown as a function of time for various positions at  $\bar{x} = 0.1$  (blue),  $\bar{x} = 0.5$  (red),  $\bar{x} = 0.9$  (green), and  $\bar{x} = 1/3$  (magenta). Several features are remarkable: (i) After a certain while the accelerations assume constant values no matter which position is studied. (ii) Positions left of  $\bar{x} = 1/3$  show normalized accelerations greater than one, because the temperatures and, correspondingly, the moments of inertia go down and vice versa. (iii) For positions left of 0.5 the accelerations reach a maximum. A numerical integration of Eq. (18) yields the angular velocities as functions of time shown in Fig. 6 for a temporally constant volume couple density. Again four positions are examined at  $\bar{x} = 0.1$  (blue),  $\bar{x} = 0.5$  (red),  $\bar{x} = 0.9$  (green), and  $\bar{x} = 1/3$  (magenta). It rotates slightly faster than the angular velocity obtained for the case of a constant moment of inertia, which according to Eq. (13) is  $\bar{\omega}(\bar{t}) = \bar{t}$ . This case is shown as a black dashed line. As it should be material points on the left of  $\bar{x} = 1/3$  rotate faster and those which are on the right rotate slower, because they gain a smaller or larger moment of inertia, respectively.

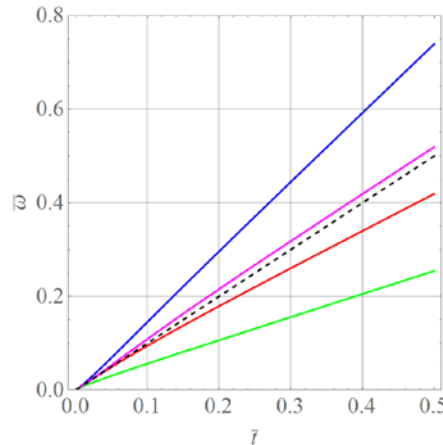


**Fig. 6.** Angular velocities at various positions.

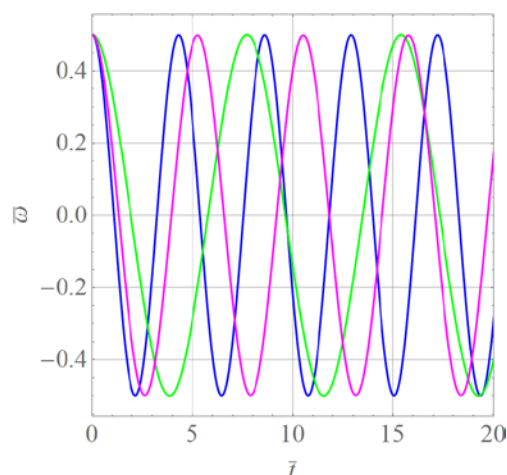


**Fig. 7.** Periodic movement of dipoles under a constant electric field at different locations.

Fig. 7 shows numerical solutions of the differential equation (17) in dimensionless form:

$$\frac{\partial}{\partial \bar{t}} \left[ \bar{J} \frac{\partial \bar{\omega}}{\partial \bar{t}} \right] = -\gamma \bar{\omega} \sqrt{1 - \left( \bar{J} \frac{\partial \bar{\omega}}{\partial \bar{t}} \right)^2}, \quad \gamma = \frac{m_0}{J_0} \left( \frac{l^2}{D} \right)^2, \quad (19)$$

with a periodically volume couple density at positions  $\bar{x} = 0.1$  (blue),  $\bar{x} = 0.9$  (green), and  $\bar{x} = 1/3$  (magenta). All curves were calculated with the same initial conditions,  $\bar{\omega}(\bar{x}, 0) = 0.4$ ,  $\partial \bar{\omega}(\bar{x}, 0) / \partial \bar{t} = 0.0$  and for  $\gamma = 1.5$ . The periodic motion is clearly visible. The durations of the period are influenced by location.

## 5. Conclusions and outlook

In this paper we first repeated the extended balance equations for a micropolar medium allowing for structural transformations. As a recently introduced feature these included a balance for the moment of inertia tensor with a production density. The case of hollow spheres was considered, which under the influence of a one dimensional temperature field would change their moment of inertia in space and time due to thermal expansion and contraction. This model of structural change allowed to calculate the production of the moment of inertia in the extended set of micropolar balance equations. Results for the moment of inertia varying in space and time were used to study the evolution of an angular velocity field. This necessitated a specific volume couple density to be present. An attempt was made to interpret this quantity based on a mesoscopic model of electrically polarized particles under the influence of an external electric field inducing a moment couple because of the Coulomb force.

In the future the authors will continue to explore the fully coupled set of equations for a micropolar medium. Whilst even the simplified one-dimensional examples presented so far required a numerical approach it is to be expected that the numerical effort for that will increase considerably.

**Acknowledgement.** *E.N.V. wishes to gratefully acknowledge support of her work by a grant from the Russian Foundation for Basic Research (16-01-00815).*

## References

- [1] V.A. Eremeyev, L.P. Lebedev, H. Altenbach, *Foundations of micropolar mechanics* (Springer Science & Business Media, Heidelberg, 2012).
- [2] A. Eringen, C. Kafadar, In: *Continuum Physics* (Academic Press, New York, 1976), vol. IV, pp. 33-63.
- [3] E.A. Ivanova, E.N. Vilchevskaya // *Continuum Mechanics and Thermodynamics* **28(6)**

- (2016) 1759.
- [4] W.H. Müller, E.N. Vilchevskaya, W. Weiss // *Phys. Mesomech.* **20(3)** (2017) 250.
- [5] W.H. Müller, E.N. Vilchevskaya // *Phys. Mesomech.* **20(3)** (2017) 263.
- [6] A. Kurganov, E. Tadmor // *Journal of Computational Physics* **160(1)** (2000) 241.
- [7] K.K. Mandadapu, B.E. Abali, P. Papadopoulos, *On the polar nature and invariance properties of a thermomechanical theory for continuum-on-continuum homogenization*. In: Proceedings of Royal Society, submitted.
- [8] H.S. Carslaw, J.C. Jaeger, *Conduction of heat in solids*. Second edition (Oxford, Clarendon Press, 1959).
- [9] J. L. Ericksen // *Archive for Rational Mechanics and Analysis* **9(1)** (1962) 371.
- [10] G.A. Maugin // *Mathematics and Mechanics of Solids* **20(3)** (2015) 280.
- [11] P.A. Zhilin, Ya.E. Kolpakov, *A micro-polar theory for piezoelectric materials*. Lecture (XXXIII Summer School - Conference “Advanced Problems in Mechanics”, St. Petersburg, Russia, 2005).

## MECHANICAL PROPERTIES OF NANOSTRUCTURED TITANIUM WITH BIOACTIVE TITANIUM-ORGANIC NANOCOATING

E.G. Zemtsova, N.F. Morozov, B.N. Semenov\*, R.Z. Valiev, V.M. Smirnov

Saint Petersburg State University, Universitetskaya nab.7/9, 199034, Saint Petersburg, Russia

\*e-mail: bsemenov@rambler.ru

**Abstract.** We present here the results of the study of mechanical properties of the nanostructured titanium samples fabricated by means of the severe plastic deformation that has titanium organic brush-like nanostructures on the surface. Based on the mechanical properties of the samples, we established for the first time that the gas-phase ALD synthesis at 200-400 °C of titanium organic nanocoatings with height of 220 nm and the distances between nanostructures up to 200 nm does not lead to deterioration of the mechanical properties of the nanostructured titanium.

**Keywords:** nanostructured titanium; equal channel angular pressing; brush-like nanostructure; titanium organic nanocoating; mechanical properties.

### 1. Introduction

The traditional metallic biomaterials reached the limit of the durability. These materials must correspond to the definitive requirements to be used as the medical pieces. They must be bioactive and biocompatible and also the materials should have high mechanical durability, especially under the cyclic loads that is important for the long-term usage of the produced medical pieces.

Currently, titanium and its alloys are known as the most successful materials for the fabrication of orthopedic and dental implants [1].

Currently, nanostructured metallic titanium (nanotitanium) is intensively studied [2, 3]. This material has better mechanical properties as compared with the pure titanium.

Particularly, severe plastic deformation of titanium and its alloys by means of equal channel angular pressing (ECAP) is used for the fabrication of nanotitanium with ultimate tensile strength higher than 1000 MPa [2, 4]. Due to the sufficiently high mechanical durability of pure titanium, we can avoid the addition of toxic additives. Titanium and nanotitanium are not toxic. However, additional surface modification is required for improvement of the biomedical properties of the titanium implant.

There are the several approaches for the improvement of survival rate of metal implant that are based on the application of the specific bioactive and biocompatible coatings [5-10]. However, chemical action of the reagents on the material surface at 200-400 °C can lead to the change of the mechanical properties of nanotitanium. Despite the fact that to date the mechanical properties of nanotitanium are studied in detail, there is no information about the influence of the chemically fabricated coatings (e.g. by Atomic Layer Deposition – ALD [11]) at high temperatures on the mechanical properties and the structure of nanotitanium.

The goal of this work was to study the influence of the brush-like titanium-organic nanocoatings on the titanium on the mechanical properties of the nanotitanium samples.

## 2. Experimental

The most important characteristics of the bulk material (metal) are its microstructure and mechanical properties. Given the above, certification of the microstructure of experimental samples was performed. The average size of nanotitanium grains was determined; mechanical tensile tests and fatigue tests were conducted.

To determine the effect of nanostructured brush-like coatings on the set of mechanical characteristics of experimental samples of nanotitanium, we prepared the samples with coatings and without coatings. Nanotitanium samples were prepared at the same conditions from the long ingot of the nanostructured Grade 4 titanium obtained by ECAP-Conform processing with subsequent drawing [2, 3].

Table 1. Structural characteristics of the nanotitanium samples with brush-like titanium-organic nanocoatings (samples 1-3) according to AFM and SEM.

| Name   | Sample       |        |        |        |
|--|--------------|--------|--------|--------|
|  | nanotitanium | 1      | 2      | 3      |
| Synthesis conditions                         |              |        |        |        |
| Temperature of the nanotitanium surface      | -            | 300    | 400    | 400    |
| Synthesis temperature, °C                    | -            | 200    | 200    | 200    |
| Number of the treatment cycles, n            | -            | 20     | 15     | 20     |
| Nanostructures size (width along X axis), nm | -            | 50-100 | 50-100 | 50-100 |
| Nanostructures height (Rz), nm               | -            | 7-36   | 15-35  | 50-220 |
| Distance between nanostructures (S), nm      | -            | 50-100 | 50-100 | 75-200 |

On the surfaces of the nanotitanium prepared for mechanical tests for stretching and fatigue strength, we synthesized brush-like titanium-organic nanocoatings [12].

The coatings were synthesized according to the conditions listed in the Table 1.

The nanostructures were coated using ALD - method [13-15].

According to Atomic Force microscopy (AFM) the surface of initial titanium support after such treatment is characterized by low roughness – average cluster height is ~1 nm.

The coatings were synthesized using the gas phase setup that provided the ALD reactions in the Ar gas stream.

Titanium tetrachloride (TiCl<sub>4</sub>) and propargyl alcohol (HC≡C-CH<sub>2</sub>-OH) were used as the reagents. Their vapors were transferred into the reactor by the argon stream at 200 °C. Before the synthesis, the nanotitanium plates were preheated in argon at 300 or 400 °C.

To be sure, in the repeatability of the results, five samples of each series were tested.

## 3. Results and discussion

The microstructure of nanotitanium samples without coating was analyzed by TEM (microscope JEOL JEM 2100) (Fig. 1).

We found that the structure is the mixture of the nanometer-sized grains. There are small grains of the size of 60-80 nm with the definitive boundaries with low dislocations density inside. Larger grains and fragments, 100-120 nm in size, contain high amount of dislocations. Average grains/subgrains size in nanotitanium samples was 100 nm.

All the mechanical tests were repeated for 5 samples of each series. The samples for the stretch tests (with diameter of 3 mm) were prepared according to the GOST 1497-84.

Strength characteristics of nanotitanium were tested using the universal testing machine Instron 5882 at room temperature with the speed of the crosshead of 1 mm/min. The fatigue life of the nanotitanium was tested using the universal testing machine Instron 8801.



**Fig. 1.** Nanotitanium microstructure.

**3.1. Mechanical properties of the nanostructured titanium.** In order to determine mechanical properties of nanotitanium, the tensile tests of cylindrical specimens have been carried out. The results of these tests are given in the Table 2, whereas the results of fatigue tests – in the Table 3.

Table 2. Mechanical properties of the nanostructured titanium samples.

| Sample       | Temperature T, °C | Conditional yield strength $\sigma_{0,2}$ , MPa | Tensile strength $\sigma_B$ , MPa | Relative elongation, $\delta$ , % |
|--------------|-------------------|---|-----------------------------------|-----------------------------------|
| nanotitanium | 20                | 1237  | 1290                              | 10.9                              |

Table 3. Fatigue life of the nano titanium experimental samples.

| Sample       | Temperature T, °C | Number of cycles | Endurance limit $\sigma_{-1}$ , MPa | Note          |
|--------------|-------------------|------------------|-------------------------------------|---------------|
| nanotitanium | 20                | $1 \times 10^6$  | 590                                 | Not destroyed |

At the initial stage of mechanical testing, extensive hardening of nanotitanium has been observed, that is related to increased dislocations density in the material. Further, when the deformation degree increases, after reaching of the maximum current, stress decrease is observed associated with the formation of neck in the region of strain localization.

According to the data given in the Table 3, nanotitanium samples without coatings withstood  $1 \cdot 10^6$  loading cycles at the load of 590 MPa without destroying.

Total load error during the test did not exceed  $\pm 3$  % at  $f = 50$  Hz.

In general, for the studied nanotitanium samples without coating the average values of the ultimate strength, conventional yield strength and elongation were equal to:  $\sigma_B = 1290$  MPa,  $\sigma_{0,2} = 1237$  MPa and  $\delta = 10,9$  %, endurance limit after  $10^6$  cycles is  $\sigma_{-1} = 590$  MPa.

**3.2. Mechanical properties of nanotitanium with brush-like titanium organic coatings on the surface.** TEM analysis of the microstructure of nanotitanium with brush-like titanium organic coatings is presented on Fig. 2.

Evidently, synthesis of coatings and thermal treatment of nanotitanium samples while coating, does not lead to a change in the size of grains and subgrains in the titanium structure. Average grains and subgrains size was 100 nm. However, boundaries for the most crystallites become more explicit and the dislocations density inside of the structure elements decreases. Such changes of the internal grains structure is called the return of the first kind [15]. It is characterized by the redistribution of the crystal lattice defects without formation and migration of the sub-boundaries.

To study the influence of coatings on mechanical properties of nanotitanium, we conducted mechanical tests of cylindrical samples of coated nanotitanium (Table 4). Five samples were tested for each series in order to be sure in the repeatability of the results.

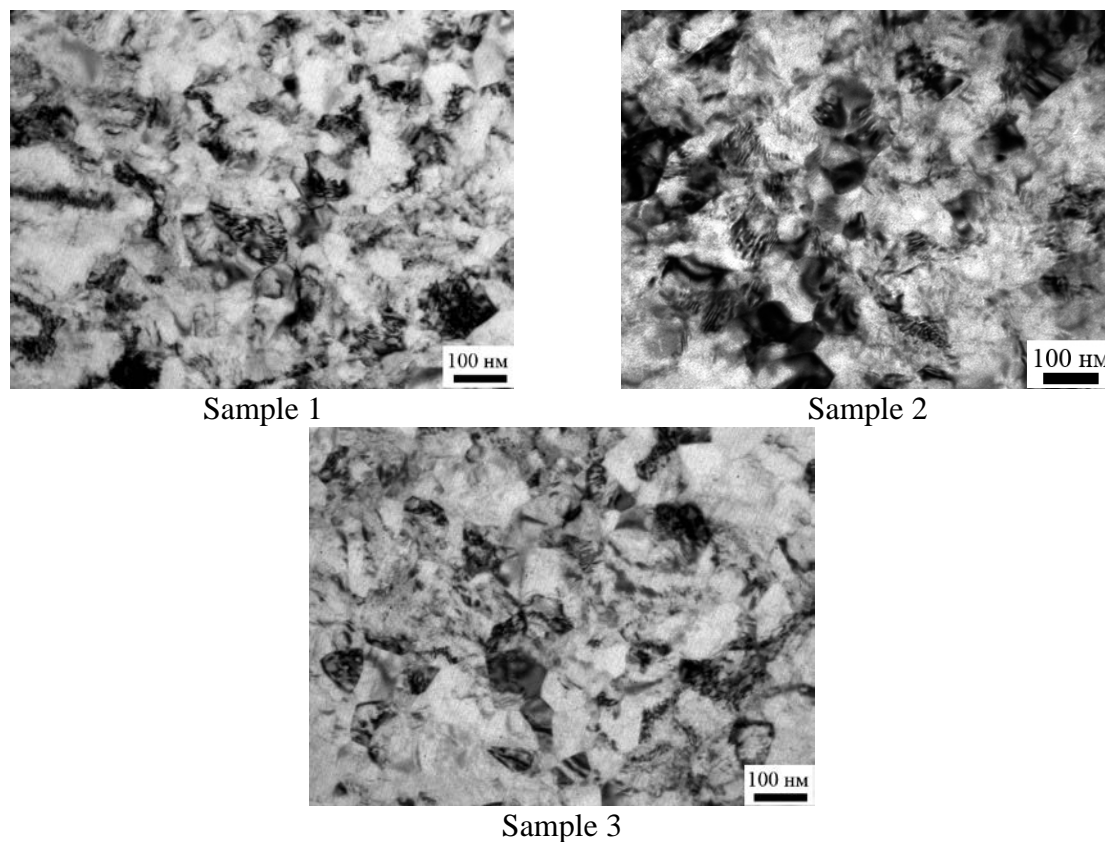


**Fig. 2.** Microstructure of nanotitanium samples with brush-like titanium organic coatings on the surface.

Evidently, the maximum current stress value in coated nanotitanium samples slightly decreased (in average, by 24 MPa), whereas relative elongation is increased.

Table 4. Mechanical properties of nanotitanium with brush-like titanium organic coatings on the surface.

| Sample | Temperature T, °C | Conditional yield strength $\sigma_{0,2}$ , MPa | Tensile strength $\sigma_B$ , MPa | Relative elongation $\delta$ , % |
|--------|-------------------|---|-----------------------------------|----------------------------------|
| HMT    | 20                | 1237  | 1290                              | 10.9                             |
| 1      | 20                | 1175  | 1266                              | 11,1                             |
| 2      | 20                | 1173  | 1255                              | 11,5                             |
| 3      | 20                | 1171  | 1253                              | 11,6                             |

Comparing to the non-coated nanotitanium, the mechanical behavior of titanium with brush-like coatings was rather similar. In all the samples, we observe hardening at the initial deformation stage, reaching of maximal yield strength with subsequent softening and destroying of the sample.

All the experimental samples survived after  $1 \cdot 10^6$  loading cycles (Table 5) at load of 590 MPa without destroying.

Table 5. Fatigue life of nano titanium samples with the brush-like titanium organic surface coatings.

| Sample | Temperature T, °C | Cycles number, N | Endurance limit $\sigma_{-1}$ , MPa | Note          |
|--------|-------------------|------------------|-------------------------------------|---------------|
| 1      | 20                | $1 \times 10^6$  | 590                                 | Not destroyed |
| 2      | 20                | $1 \times 10^6$  | 590                                 | Not destroyed |
| 3      | 20                | $1 \times 10^6$  | 590                                 | Not destroyed |

#### 4. Conclusions

In the present work, it was shown that the application of organic titanium nano-coating on the surface of nanostructured titanium in gas-phase in the temperature range 200-400 °C does not lead to deterioration of the mechanical properties of nanostructured titanium.

**Acknowledgements.** The work was done using equipment of resource centers of the Science Park of St. Petersburg State University "Methods of analysis of the substances composition", "Nanotechnology" and "Innovative technologies of composite nanomaterials".

This work was also supported in part by a grants from the St. Petersburg State University, No. 12.37.433.2015 and No. No. 6.38.337.2015.

#### References

- [1] D.M. Brunette, P. Tengvall, M. Textor, P. Thomsen, *Titanium in Medicine* (Springer-Verlag Berlin Heidelberg, Germany, 2001).
- [2] R.Z. Valiev, A.P. Zhilyaev, T.J. Landon, *Bulk nanostructured materials: fundamental backgrounds and applications* (Eco-Vector, St. Petersburg, 2017).
- [3] D.V. Nazarov, E.G. Zemtsova, A.Yu. Solokhin, R.Z. Valiev, V.M. Smirnov // *Nanomaterials* **7(1)** (2017) 15.
- [4] *Handbook of Mechanical Nanostructuring*, ed. by Mamood Aliofkhaezael (Wiley, 2015).
- [5] D.V. Shtansky, N.A. Gloushankova, I.A. Bashkova, M.A. Kharitonova, T.G. Moizhess, A.N. Sheveiko, F.V. Kiryukhantsev-Korneev, M.I. Petrzhik, E.A. Levashov // *Biomaterials* **27** (2006) 3519.
- [6] E.G. Zemtsova, A.Yu. Arbenin, R.Z. Valiev, V.M. Smirnov // *Materials* **9** (2016) 1010.
- [7] C.J. Brinker, G.C. Frye, A.J. Hurd, C.S. Ashley // *Thin Solid Films Preparation and Characterization* **201** (1991) 97.
- [8] D.V. Nazarov, E.G. Zemtsova, R.Z. Valiev, V.M. Smirnov // *Materials* **8** (2015) 8366.
- [9] E.A. Levashov, V.V. Kurbatkina, A.S. Rogachev, N.A. Kochetov, E.I. Patsera, N.V. Sachkova // *Russian Journal of Non-Ferrous Metals* **49** (2008) 404.
- [10] E.G. Zemtsova, A.Yu. Arbenin, N.M. Yuditseva, R.Z. Valiev, E.V. Orekhov, V.M. Smirnov // *Nanomaterials* **7** (2017) 323.
- [11] O.M. Osmolovskaya, I.V. Murin, V.M. Smirnov, M.G. Osmolovsky // *Reviews on Advanced Materials Science* **36** (2014) 70.
- [12] E.G. Zemtsova, P.E. Morozov, V.M. Smirnov // *Reviews on Advanced Materials Science* **45(1/2)** (2016) 59.
- [13] *Atomic Layer Deposition of Nanostructured Materials*, ed. by N. Pinna and M. Knez (Wiley, 2011).
- [14] A.A. Malygin, V.E. Drozd, A.A. Malkov, V.M. Smirnov // *Chemical Vapor Deposition* **21(10-12)** (2015) 216.
- [15] V.M. Smirnov, E.G. Zemtsova, E.B. Ivanov, M.G. Osmolovsky, V.G. Semenov, I.V. Murin // *Applied Surface Science* **195** (2002) 89.

# DYNAMIC STRENGTH PROPERTIES OF AN ULTRA-FINE-GRAINED ALUMINUM ALLOY UNDER TENSION CONDITIONS

A.D. Evstifeev<sup>1\*</sup>, A.A. Chevrychkina<sup>1,2</sup>, Y.V. Petrov<sup>1,2</sup>

<sup>1</sup>Saint Petersburg State University, Saint Petersburg, Universitetskaya Emb., 199034, Russia

<sup>2</sup>Institute of Problems of Mechanical Engineering, Russian Academy of Sciences, Saint Petersburg, Bolshoj 61, Vas.Ostrov, 199178, Russia

\*e-mail: ad.evstifeev@gmail.com

**Abstract.** Experimental and theoretical analysis of aluminum alloy 1230, subjected to static and dynamic tension is presented in the paper. The material was tested in two conditions - initial coarse-grained (CG) state and ultrafine-grained (UFG) state. Experimental results were processed using incubation time fracture criterion.

**Keywords:** dynamic impact, fracture, nanostructured material, strength criterion.

## 1. Introduction

Standard tests of construction materials for industrial applications include compression, tensile, bending, hardness, and fatigue tests. Such tests ensure, that the production satisfies existing safety and reliability rules. But in the case, when conditions are significantly different from quasistatic loads, additional tests and calculations are required. As a rule, such additional research is required, when material properties in high-rate loading conditions need to be assessed. Such loading conditions are typical for aerospace and military engineering applications, however high-rate testing is also used for civil construction in seismic regions.

In order to increase strength and reliability of products and parts, designed for use under high-rate loading one has to perform experimental and analytic studies of the strength characteristics of the material.

Research in this direction was initiated in the second half of the 20th century. A separate direction of science – fracture mechanics was formed. At the same time, despite the fact that a large number of experimental and theoretical works in this area was carried out, some crucial problems remain unsolved. New materials, such as bulk new nanostructured materials [1, 2, 3], generate new problems and require additional research. A lot of research results, presented in scientific literature, are aimed at studying of influence of the refined material structure on strength and performance properties of the material [4-7]. Data on the study of the behavior of the ultrafine-grained materials under dynamic conditions is less frequent. This is partly due to the dimensional features of the currently obtained samples of the UFG materials. For example, severe plastic deformation (SPD) technique is usually capable of production of disk specimens 20 mm in diameter and 1-2 mm in thickness. Standard test procedures for such small are not applicable.

Experimental results in this paper were received for a model material – aluminum alloy 1230 (ASTM).

## 2. Material

The aluminum alloy 1230 was modified using severe plastic deformation by torsion on the Walter-Klement high pressure torsion press in order to obtain the refined grain structure. Working parameters: pressure - 6 GPa, number of rotations - 10, processing speed - 1 revolution per minute. The samples were manufactured at room temperature.

Measurements of the Vickers microhardness of the samples demonstrated the uniformity of the specimens. On average, the microhardness of the samples increased by 87%.

Several studies of metals and alloys [8-9] have shown, that severe plastic deformation substantially increases hardness of the material and, as a rule, the strength characteristics of materials. However, the SPD treatment might lead to reduction of plasticity, which can have negative effect on the behavior of the material in the dynamic loading range. Thus, multiple dynamic experiments are needed in order to determine possible characteristics of the external loads.

## 3. Experimental Techniques

Experimental studies of the dynamic tension regime were performed on the drop tower machine Instron CEAST 9350 at a strain rate up to  $10^2$ - $10^3$  s<sup>-1</sup>. The main advantage of this equipment setup is certified signal capture techniques and an automated test procedure, which reduces the error of the experiment. Experiments with quasistatic loads were performed on Shimadzu AG-50kNX.

The tension experiments were carried out on an aluminum alloy for different geometric dimensions of flat samples. The first type of the sample geometry is shown in Fig. 1. The dimensions of the specimens correspond to ISO 8256 standard with the length and width of the working part equal to 10 mm and 3 mm respectively (Fig. 1, a). The second type of the sample geometry was developed considering the dimensional features of the samples obtained by SPD. The length and width of the working part are 5 mm and 2 mm respectively (Fig. 1, b). All the samples were cut using an electrical discharge machine ARTA 123 PRO with high accuracy and brought to a uniform roughness parameter using the polishing machine.

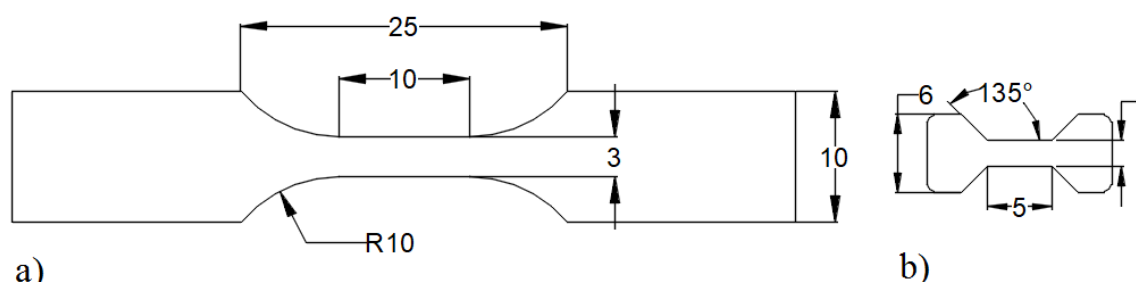


**Fig. 1.** Geometry size for samples of type "Sample I" a) and type "Sample II" b).

In Instron CEAST 9350 data signals are captured automatically using a force sensor and a velocity sensor. Fig. 2 shows examples of the stress chronograms for the "Sample II" type samples. The signals are quite stable and can be used to determine the threshold characteristics of the material under tension.

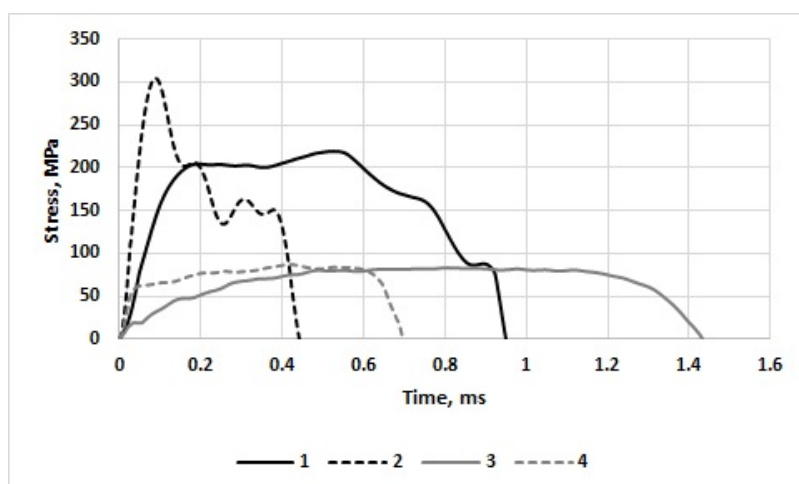


**Fig. 2.** Stress obtained during tensile test for samples of type «Sample II» for UFG and CG materials for different strain rate. 1 –  $\dot{\epsilon} = 304 \text{ s}^{-1}$  UFG alloy, 2 –  $\dot{\epsilon} = 642 \text{ s}^{-1}$  UFG alloy, 3 –  $\dot{\epsilon} = 328 \text{ s}^{-1}$  CG alloy, 4 –  $\dot{\epsilon} = 640 \text{ s}^{-1}$  CG alloy.

#### 4. Results and discussion

Dependence of the threshold stress values for the studied materials on the strain rate are shown in Fig. 3. The obtained results demonstrate that the CG alloy has lower strength than the UFG alloy. With an increase in the strain rate, a nonlinear increase in the maximum stress value is observed for both materials.

This feature of the behavior of the material at high strain rates can be explained using incubation time approach. Incubation time fracture criterion was used for the fracture analysis [10, 11]:

$$\frac{1}{\tau_c} \int_{t-\tau_c}^t \frac{\sigma(s)}{\sigma_c} ds \leq 1, \quad (1)$$

where  $t$  is time,  $\sigma$  is the applied stress (linearly increasing with time load),  $\sigma_c$  is the ultimate strength under static loads,  $\tau_c$  is the incubation time of fracture. The constants  $\sigma_c$  and  $\tau_c$  are the parameter of the material.

Correlation between maximum stress and strain rate under tension is shown on Fig.3. Theoretical lines are constructed using criterion (1) with the following parameters of the material: for the CG alloy  $E = 72 \text{ GPa}$ ,  $\tau_c = 0.8 \mu\text{s}$ ,  $\sigma_c = 80 \text{ MPa}$ ; for UFG alloy  $E = 72 \text{ GPa}$ ,  $\tau_c = 4.4 \mu\text{s}$ ,  $\sigma_c = 200 \text{ MPa}$ . A good agreement between the experimental data was obtained for different sample sizes and material states.

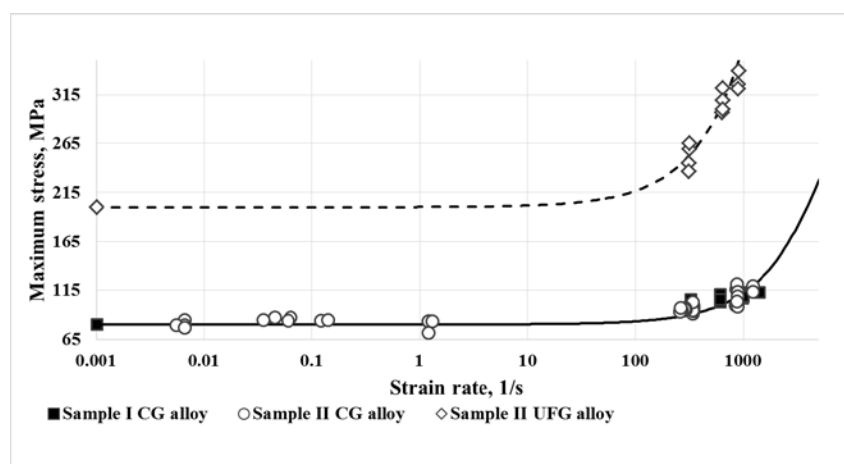


**Fig. 3.** Maximum tension stress versus strain rate. Lines constructed according (1) with material parameters: for CG alloy  $E = 72 \text{ GPa}$ ,  $\tau_c = 0.8 \mu\text{s}$ ,  $\sigma_c = 80 \text{ MPa}$ ; for UFG alloy  $E = 2 \text{ GPa}$ ,  $\tau_c = 4.4 \mu\text{s}$ ,  $\sigma_c = 200 \text{ MPa}$ .

A direct comparison of experimental data CG and UFG alloy makes it possible to determine a significant increase of the strength characteristics of the material after severe plastic deformation not only in the quasistatic range of the loading parameters but also in the dynamic one. Maximum stress in static regime of tension increased from 80 MPa to 200 MPa. The material parameter  $\tau_c$  (dynamic strength) increased from 0.8  $\mu\text{s}$  to 4.4  $\mu\text{s}$ .

The non-linear increase in strength with increasing of the strain rate and the significant change in the strength properties of the material after the SPD processing require a comprehensive experimental-theoretical investigation in order to assess applicability of a material for certain extreme conditions.

## 5. Conclusions

The performed experimental studies show that severe plastic deformation has a significant influence on the behavior of the material not only in quasistatic but also in dynamic loading regimes. A detailed study of the properties of the material in a wide range of parameters of the external action is required.

The effect of strain rate dependence of maximum stress under tension was investigated using incubation time approach. Parameters of materials were found and curves of maximum stress under tension were calculated. It was found that the SPD treatment has a great influence on strength characteristics of the material in static and dynamic regimes of loading. For the UFG aluminum alloy significant increase in strength was observed for a wide range of loads.

In addition to this, the use of the theoretical approach based on incubation time criterion makes it possible to predict behavior of the material for the regimes, that were not experimentally investigated. The proposed experimental-theoretical approach to testing of nanostructured materials for tensile strength has shown its robustness and can be recommended for complex testing of nanostructured materials, which are planned to be used under dynamic loads.

**Acknowledgement.** *The work has been done under financial support from the Russian Science Foundation (№17-79-10145). Experimental studies were carried out using the equipment of the resource center of the Science Park of St. Petersburg State University "Centre for Extreme States of Materials and Constructions" and the laboratory "Mechanics of Advanced Bulk Nanomaterials for Innovative Engineering Applications".*

## References

- [1] R.Z. Valiev // *Annales de Chimie. Science des Materiaux* **21(6)** (1996) 369.
- [2] R.Z. Valiev, A.V. Korznikov, R.R. Mulyukov // *Materials Science and Engineering: A* **186(2)** (1993) 141.
- [3] R. Z. Valiev // *Nature Materials* **3(8)** (2004) 511.
- [4] Q. Wei, H.T. Zhang, B.E. Schuster, K.T. Ramesh, R.Z. Valiev, L.J. Kecskes, R.J. Dowding, L. Magness, K. Cho // *Acta materialia* **54(15)** (2006) 4079.
- [5] Y. Estrin, A. Vinogradov // *International Journal of Fatigue* **32(6)** (2010) 898.
- [6] A. Mishra, M. Martin, N.N. Thadhani, B.K. Kad, E.A. Kenik, M.A. Meyers // *Acta materialia* **56(12)** (2008) 2770.
- [7] A.B. Witney, P.G. Sanders, J.R. Weertman, J.A. Eastman // *Scripta metallurgica et materialia* **33(12)** (1995) 2025.
- [8] R.Z. Valiev, I.V. Alexandrov, Y.T. Zhu // *Journal of Materials Research* **17(1)** (2002) 5.
- [9] S.V. Zherebtsov, G.A. Salishchev, R.M. Galejev, O.R. Valiakhmetov, S.Yu. Mironov, S.L. Semiatin // *Scripta materialia* **51(12)** (2004) 1147.
- [10] N.F. Morozov, Y.V. Petrov, *Dynamics of Fracture* (Springer, Berlin, 2000).
- [11] Y.V. Petrov // *Doklady Physics* **49(4)** (2004) 246.

# NUCLEATION AND GROWTH MECHANISMS OF CdTe THIN FILMS ON SILICON SUBSTRATES WITH SILICON CARBIDE BUFFER LAYERS

A.A. Koryakin<sup>1,2</sup>, S.A. Kukushkin<sup>1-3\*</sup>, A.V. Redkov<sup>1,3</sup>

<sup>1</sup>St. Petersburg Academic University RAS, Khlopina 8/3, St Petersburg, 194021, Russia

<sup>2</sup>ITMO University, Kronverkskii pr. 49, St. Petersburg, 197101, Russia

<sup>3</sup>Institute of Problems of Mechanical Engineering RAS,

Bolshoj pr., 61, V.O., St. Petersburg, 199178, Russia

\*e-mail: sergey.a.kukushkin@gmail.com

**Abstract.** The kinetics of the initial growth stages of cadmium telluride (CdTe) films on silicon substrates covered with silicon carbide (SiC) buffer layers grown by the method of topochemical substitution of atoms is investigated theoretically. The model based on the classical nucleation theory is proposed to depict the CdTe film growth by the method of thermal evaporation and condensation in vacuum. The model accounts for the mechanical stresses caused by the lattice mismatch and difference of thermal expansion coefficients of CdTe film and substrate. The influence of substrate and evaporator temperature on the nucleation mechanism and kinetics of the initial growth stages of CdTe film is estimated. The different growth regimes of CdTe films on the SiC/Si substrates are discussed, and the optimal growth conditions are found. It is shown that the elastic stresses in the CdTe/SiC/Si structure are approximately three times lower than the elastic stresses in the CdTe film grown coherently on the Si substrate without the SiC buffer layer. This leads to the large difference in the nucleation rates of the CdTe films on the SiC/Si substrate and Si substrate. The diagram of the nucleation rates of CdTe islands on the SiC/Si depending on the substrate and evaporator temperature is presented.

**Keywords:** thin film; CdTe; SiC; Si; silicon substrate; silicon carbide buffer layer; growth; nucleation; thermal evaporation.

## 1. Introduction

At present time considerable efforts of researchers are aimed at study of A<sup>II</sup>B<sup>VI</sup> group semiconductors and development of methods for growth of thin films of these materials [1-3]. Such semiconductors are of great practical interest and can be used for creation of various optoelectronic devices, solar batteries, photodetectors and ionizing radiation sensors [4, 5]. Cadmium telluride (CdTe) outstands among the semiconductors of this group, since it is widely applied in the solar batteries production [6]. CdTe is used as an absorbing layer because it is a direct-band semiconductor with a bandgap of 1.49 eV and has a high absorption coefficient in visible range. To create efficient solar batteries, thin CdTe films of high quality grown on conductive or semiconductive substrates are needed. This will greatly simplify the production of optoelectronic devices, since there is no need to add additional contacts. Materials such as indium tin oxide (ITO) [7], indium antimonide (InSb) [8], gallium arsenide (GaAs) [9], silicon (Si) [10], and many others [11] are often used as substrates. Silicon has a number of advantages, since silicon substrates are widely available and most well developed from a technological point

of view. However, various problems arise during the growth of CdTe directly on silicon. The film grows polycrystalline [12] often. In case of chemical deposition of thin CdTe films, the silicon reacts with precursors and forms  $\text{Si}_2\text{Te}_3$ , which significantly degrades the properties of the resulting structures. In this regard, it was proposed in [13] to use Si substrates with a buffer layer of silicon carbide (SiC) formed by the method of topochemical substitution of atoms [14] for deposition of CdTe. Silicon carbide does not interact with elements of group VI practically. In addition, SiC layer grown by the method of atoms substitution on Si substrate has a number of advantages over silicon carbide carved from SiC single crystals. According to [14], the feature of SiC epitaxial layer growth by the method of atoms substitution is that an ensemble of pores is being formed between the layer and the substrate during the synthesis. As a result, the contact area of the silicon substrate and the structure grown on SiC is being significantly reduced. Silicon substrates covered by SiC buffer layer that "hangs" above the pores in Si become elastically "compliant". They adapt well to growth conditions and nature of the films deposited on their surface. As a result, elastic stresses arising due to mismatch of the lattice parameters and difference in the thermal expansion coefficients of the substrate and the film materials are being significantly reduced. More details on the SiC/Si films obtained by the method of topochemical substitution of atoms, theoretical basis of this growth technology and the study of SiC/Si samples are presented in the review [14] and original paper [15].

There are various methods [16] for deposition of cadmium telluride films, such as magnetron sputtering [17], thermal evaporation and condensation in vacuum [18], chemical vapor deposition [19], etc. Thermal evaporation in vacuum has a number of advantages, since it ensures high deposition rate and does not require high material costs. However, to the best of our knowledge, despite a significant amount of experimental works on the growth of CdTe [20, 21], there is no quantitative theory describing the processes of CdTe formation, which would allow estimating of various parameters of the resulting films depending on growth conditions: pressures, temperatures. The present paper is a continuation of a series of papers on the growth of CdTe on SiC/Si substrates [13] by thermal evaporation and condensation in vacuum, and is devoted to the theoretical aspects of the growth of thin CdTe films. In the first part of the paper a model of the film growth is developed on the basis of the classical nucleation theory and estimates for the parameters necessary for calculations are made: the diffusion lengths of Cd and Te adatoms, their lifetimes, equilibrium concentrations and diffusion coefficients. In the second part, the calculation results within the framework of the model are compared with the experimental data [13] and growth regimes of CdTe under conditions other than in Ref. [13] are analyzed.

## 2. Model of the initial stages of CdTe thin film formation on Si/SiC substrate upon evaporation and condensation

Usually two-zoned reactor is being used for growth of CdTe films by the method of thermal evaporation and condensation in vacuum, in one of the zones of which the powdered cadmium telluride is being evaporated, and in the other one condensation of CdTe onto the substrate occurs. The principal scheme of the reactor, shown in Fig. 1, was proposed by I.P. Kalinkin and his group [22]. We note that this type of the reactor can be used both for the growth of films by the method of thermal evaporation in vacuum and for the growth in a quasi-closed volume. In the latter case, it is being lowered onto the substrate holder and it completely covers the substrate.

In the evaporation zone sufficiently high temperature  $T_g$  is maintained, so that the powdered CdTe evaporates by dissociating into Cd and  $\text{Te}_2$  chalcogen molecules as a result of the reaction:



We note that in the general case it is necessary to take into account the fact of the possible formation of individual tellurium atoms in vapor that can get onto the substrate. However, during thermal evaporation, this process is not very probable and in this study we will not take it into account. The mechanisms of evaporation of  $A^{II}B^{VI}$  compounds, to the group of which CdTe belongs, are mostly completely described in the monograph [22].

After evaporation of CdTe and formation of Cd and  $Te_2$  in vapor phase, the process of mass transfer through the gas phase towards the condensation zone (in which the substrate is located) begins. As a consequence, fluxes of Cd and  $Te_2$  onto the substrate appear. Since the substrate is maintained at temperature  $T_s$ , which is lower than  $T_g$ , the flux of material coming to the surface from the vapor exceeds the flux of material evaporating from the substrate. As a result, significant supersaturation appears on the substrate, which is sufficient to initiate the nucleation of CdTe islands. The nucleation is the main reason for the growth of CdTe film. The influence of the growth conditions, in particular, temperature of the evaporator and the substrate on possible growth regimes and conditions under which their change occurs will be estimated below.

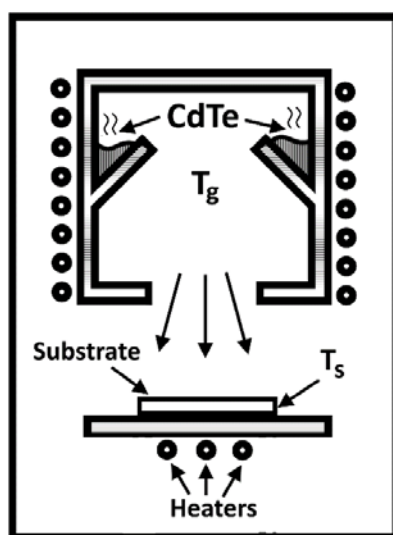


**Fig. 1.** Scheme of two-zoned reactor for the growth of CdTe by the method of thermal evaporation and condensation in vacuum [22].

We note that within the framework of the present model, it is believed that SiC film affects the nucleation of CdTe islands through three main parameters: the adsorption energy of Cd and Te (we suppose that  $Te_2$  molecules are being completely dissociated into atoms on the surface of the substrate); diffusion and, as a consequence, the mobility of Cd and Te adatoms; the field of mechanical stress  $\sigma$ , which arises due to the difference in lattice parameters of SiC and CdTe and which will be taken into account during calculation of the dependence of nucleation rate of CdTe islands on supersaturation. For simplicity in this paper we assume that diffusion lengths, lifetimes, and diffusion coefficients of adatoms during the growth of the first cadmium telluride layers directly on SiC surface coincide with these parameters on the surface of CdTe, although this is certainly not the case in real growth process. However, since the studies of evaporation processes of Cd and Te adatoms from the SiC surface are not available yet to the best of our knowledge, we are using this approximation, and in the future we will try to estimate these parameters from quantum-chemical calculations. We should also note, that increase in the thickness of the growing film, leads to rapid decrease in the influence of the existing differences in parameters, and since the films of thickness of the order of hundreds nanometers or more are of main practical interest, we believe that this assumption is quite reasonable.

### 3. The growth mechanism and nucleation rate of CdTe islands on the SiC/Si substrate

The nucleation rate of CdTe islands is determined by the equation [23]

$$I = N_0 W^+(n_c) Z \exp(-\Delta F(n_c)/kT), \quad (2)$$

where  $N_0$  is the number of adsorption sites on the substrate,  $N_0 \sim 1/l_0^2$ ;  $l_0$  is the lattice constant of SiC,  $n$  is the number of Cd atoms in the island (equals to the number of CdTe pairs);  $n_c$  is the critical size of island;  $W^+(n_c)$  is the diffusion coefficient in the size space for the island of the size  $n_c$ ;  $W^+(n_c)$  depends on the island growth mechanism and is of order of the number of CdTe pairs that attach to the critical island per second;  $\Delta F(i)$  is the free energy of the island formation without the entropy correction;  $k$  is the Boltzmann constant;  $T$  is the growth temperature;  $Z = \sqrt{-\Delta F''(n_c)/2\pi kT}$  denotes the Zeldovich factor. The free energy of the island formation  $\Delta F(i)$  equals [23]

$$\Delta F(i) = \alpha n^{1/2} - (\Delta\mu - w)n, \quad (3)$$

where  $\alpha = 2\pi^{1/2} \gamma(h\Omega)^{1/2}$  for the disk-shaped islands of the radius  $r$  and height  $H$ ;  $\gamma$  is the effective surface energy of the island sides,  $\Omega$  is the volume of the CdTe pair in solid state;  $\Delta\mu$  is the difference of chemical potential per CdTe pair between the two-dimensional gas of adatoms and bulk solid;  $\Delta\mu = kT \ln(C_{Cd}C_{Te}/K^{eq})$ ,  $C_i$  are the atomic concentrations of Cd and Te atoms on the surface of substrate;  $K^{eq} = C_{Cd}^{eq}C_{Te}^{eq}$  is the equilibrium constant of the chemical reaction  $Cd + Te \rightarrow CdTe$ ,  $C_i^{eq}$  is the equilibrium concentration of the  $i$ -th element;  $w$  is the elastic energy per CdTe pair produced by the lattice mismatch of the substrate and CdTe film. The difference  $\Delta\mu - w$  is the driving force of nucleation. The supersaturation of the two-dimensional gas of adatoms  $\xi$  relates to the difference of chemical potentials  $\Delta\mu$  by the formula  $\Delta\mu = kT \ln(\xi + 1)$  and, consequently,  $\xi = C_{Cd}C_{Te}/K^{eq} - 1$ . It is noteworthy that in our model we assume that the  $Te_2$  molecule absorbed on the substrate dissociates into two Te atoms. Therefore, the kinetics processes on the substrate (the island formation and growth) are governed by the diffusion of Te adatoms (not  $Te_2$  molecules) and their interaction with the Cd adatoms. We suppose that tellurium in molecular form desorbs easily from the substrate and is not involved in the nucleation process of CdTe islands. In the general case, the several possible growth mechanisms can be considered. Herein, we focus only on the mechanism mentioned above but, in the further studies, we will investigate other possible mechanisms. For instance, the  $Te_2$  molecule can interact with the Cd adatom and, as a result, the "free" Te adatom is produced on the surface. Also, one should consider the possibility of the reaction between the  $Te_2$  molecule in the vapor phase and two Cd adatoms on the surface [23]. Thus, we suppose that the following reaction on the substrate results in the formation of CdTe islands



where  $Cd(ad)$  и  $Te(ad)$  are the cadmium and tellurium adatoms,  $CdTe(s)$  is the cadmium telluride in solid state. It is well known that the critical size of island and nucleation barrier can be expressed by the formulas  $n_c = \alpha^2/4(\Delta\mu - w)^2$  and  $\Delta F(n_c) = \alpha^2/4(\Delta\mu - w)^2$ , correspondently. Following to Zeldovich [24], the diffusion coefficient in the size space  $W^+(n)$  can be defined by the formula

$$W^+(n) = - \frac{kT dn/dt}{\partial \Delta F / \partial n}, \quad (5)$$

where  $dn/dt$  is the island growth rate; it depends on the mechanism of material transport. In the general case, the different growth mechanisms of islands can be considered depending on the substrate temperature [25]. In this paper, we consider the most realistic mechanism that can occur at the growth conditions similar to those used in the work [13]. We assume that the island

has the shape of the thin disk of the radius  $r$  and height  $H$ . The height  $H$  equals to one monolayer and is a constant at the nucleation stage of the islands. Therefore, the radius of island, i.e. its lateral size, only changes during the growth. This assumption is reasonable because the number of atoms in the islands is usually about  $\sim 10$ -100 at the nucleation stage and the islands have the size of  $\sim 1$  nm [23]. At the initial growth stage, the average distance between islands is much larger than their sizes. Therefore, we assume that the island growth is limited by the surface diffusion of Cd and Te adatoms at the growth conditions [13]. In this case, we can use the following formula for the growth rate of island [25]

$$\frac{dn}{dt} = \frac{2\pi\gamma\Omega N_0 D_{\text{CdTe}}}{kT r} \left( \frac{r}{r_c} - 1 \right), \quad (6)$$

where

$$D_{\text{CdTe}} = \left( \sum_{i=\text{Cd,Te}} \frac{v_i^2 \ln \lambda_i / r_c}{D_i C_i^{\text{eq}}} \right)^{-1} \quad (7)$$

is the generalized diffusion coefficient;  $D_i$  and  $\lambda_i$  are the diffusion coefficient and diffusion length of the  $i$ -th element on the surface, correspondently, such that  $\lambda_i = \sqrt{D_i \tau_i}$ ,  $\tau_i$  is the adatom lifetime;  $v_i$  is the stoichiometric coefficient of the  $i$ -th element that corresponds to the reaction (4),  $v_{\text{Cd}} = 1$ ,  $v_{\text{Te}} = 1$ ;  $r_c = \gamma \Omega / \Delta \mu_c$  is the radius of the critical island. To calculate  $W^+(i_c)$ , we differentiate (3) with respect to  $n$  and substitute the derivative in (5) then simplify the result using the formula (6). Finally, we obtain the formula [26]

$$W^+(i_c) = 2\pi D_{\text{CdTe}} N_0, \quad (8)$$

where

$$D_{\text{CdTe}} = \frac{D_{\text{Cd}} D_{\text{Te}} C_{\text{Cd}}^{\text{eq}} C_{\text{Te}}^{\text{eq}}}{D_{\text{Te}} C_{\text{Te}}^{\text{eq}} \ln(\lambda_{\text{Cd}} / r_c) + D_{\text{Cd}} C_{\text{Cd}}^{\text{eq}} \ln(\lambda_{\text{Te}} / r_c)}. \quad (9)$$

Substituting (8) in (2) and calculating the Zeldovich factor, we rewrite the formula (2) for the nucleation rate of CdTe islands in the following form

$$I = \frac{N_0^2 D_{\text{CdTe}} (\Delta \mu - w)^{3/2}}{\gamma (h \Omega k T)^{1/2}} \exp \left( - \frac{\alpha^2}{4kT(\Delta \mu - w)} \right). \quad (10)$$

Let us estimate the values of the material constants of our model to use the formula (10). The adatom lifetime of Cd and Te can be found by means of the formula [25]

$$\tau_i = \tau_{0i} \exp \left( \frac{E_{a,i}}{kT} \right), \quad (11)$$

where  $\tau_{0i} \sim 1/\nu_{p,i}$ ,  $\nu_{p,i}$  is the frequency of normal vibrations of the  $i$ -th element on the substrate;  $\nu_{p,i}$  equals approximately  $\sim 10^{13} \text{ s}^{-1}$  [27];  $E_{a,i}$  is the activation energy of adsorption of the  $i$ -th element. The diffusion coefficient of the Cd and Te adatoms  $D_i$  is calculated using the equation

$$D_i = \frac{l_i^2 \nu_{t,i}}{z} \exp \left( - \frac{E_{d,i}}{kT} \right), \quad (12)$$

where  $E_{d,i}$  is the activation energy of the surface diffusion;  $l_i$  is the diffusion jump distance of the  $i$ -th element; we put  $l_i \sim l_0$  for simple estimates; the lattice constant of CdTe  $l_0$  equals to 0.648 nm [28];  $\nu_{t,i}$  is the frequency of tangential vibrations of the  $i$ -th element on the substrate,  $\nu_{t,i} \sim 10^{13} \text{ s}^{-1}$  [28];  $z$  is the number of neighboring sites which the adatom can hop to;  $z$  equals to 3 for the triangular lattice.

The activation energy of adsorption  $E_{a,i}$  is estimated using the results of the work [29],  $E_{a,\text{Cd}} \sim 0.5$  eV and  $E_{a,\text{Te}} \sim 1.5$  eV. The activation energy of diffusion  $E_{d,i}$  equals to  $E_{d,\text{Cd}} \sim 0.17$  eV and  $E_{d,\text{Te}} \sim 0.5$  eV [30]. After the activation energies were found, it easy to estimate the adatom lifetimes and diffusion coefficients according to the formulas (11) and (12). The calculated dependences of  $\tau_{\text{Cd}}$  and  $\tau_{\text{Te}}$  and, also,  $D_{\text{Cd}}$  and  $D_{\text{Te}}$  on the substrate temperature are presented in Fig. 2a. In order to estimate the temperature dependence of the evaporation and condensation fluxes of Cd and Te at the vapor-surface interface and, correspondently, the

equilibrium concentrations of adatoms, we use the data on the saturated vapor pressure of Cd and  $\text{Te}_2$  over the congruently sublimating crystal of CdTe [22, 31]. According to the work [31], the logarithm of the saturated vapor pressure of  $\text{Te}_2$  molecules equals to  $\log P_{\text{Te}_2} = -10^4/T + 6.346$ , where the temperature  $T$  is measured in degrees of Kelvin and the pressure  $P_{\text{Te}_2}$  is measured in atmospheres. The saturated vapor pressure of Cd is calculated by means of the equation  $P_{\text{Cd}} = 2P_{\text{Te}_2}$  [31]. The flux densities of Cd and Te atoms coming to the substrate from the vapor phase are equal to  $J_{\text{Cd}} = P_{\text{Cd}}/(2\pi m_{\text{Cd}}kT)^{1/2}$  and  $J_{\text{Te}} = 2P_{\text{Te}_2}/(2\pi m_{\text{Te}_2}kT)^{1/2}$ , correspondently, where  $m_{\text{Cd}}$  and  $m_{\text{Te}_2}$  are the mass of Cd and  $\text{Te}_2$ , correspondently.

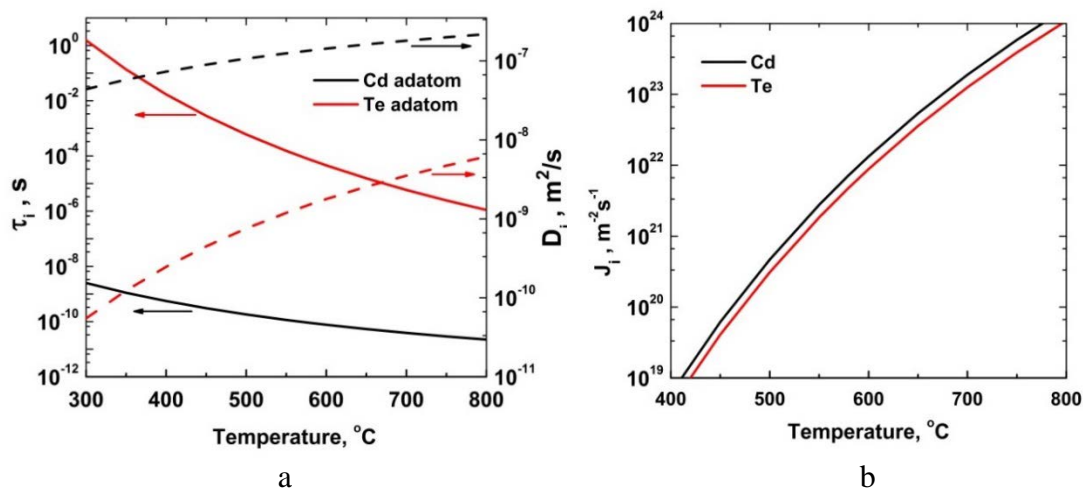


**Fig. 2.** The dependences of the adatom lifetimes, diffusion coefficients and flux densities of Cd and Te atoms on the substrate temperature; (a) the dependences of the adatom lifetimes ( $\tau_{\text{Cd}}$ ,  $\tau_{\text{Te}}$ ) and diffusion coefficients ( $D_{\text{Cd}}$ ,  $D_{\text{Te}}$ ); (b) the dependences of the flux densities of Cd and Te atoms.

The results of the calculation of  $J_{\text{Cd}}$  and  $J_{\text{Te}}$  are shown in Fig. 2b. After the flux densities are calculated, it is easy to estimate the adatom concentrations using the formula  $C_i = n_i/N_0 = J_i\tau_i/N_0$ , where  $n_i$  is the surface density of the  $i$ -th adatom. To determine the value of the effective surface energy of island  $\gamma$ , the results of the work [32] on the surface energy calculation of CdTe are used. Thus, we equal  $\gamma$  to  $0.65 \text{ J} \cdot \text{m}^{-2}$  in the further computations.

The mechanical stress  $\sigma$  produced during the growth of the CdTe film on the SiC/Si substrate is estimated by means of the analysis of the Raman spectrum of the CdTe/SiC/Si structure [13]. The Raman measurements performed at room temperature [13] show that the Raman shift  $\omega$  of the E(TO) phonon peak has the value of about  $141 \text{ cm}^{-1}$ . According to the work [33], the Raman shift  $\omega_0$  of this peak of the CdTe crystal in the unstressed state has the value of about  $140 \text{ cm}^{-1}$ . The value of the mechanical stress  $\sigma$  in the CdTe/SiC/Si structure is estimated by means of the formula derived in the work [34],  $(\omega - \omega_0)/\omega_0 = k\sigma$ , where  $k \approx -(0.36 \pm 0.1) \text{ cm}^{-1}/100 \text{ MPa}$ . Thus, the CdTe film grown on the SiC/Si substrate has the residual compressive stress of about 200-400 MPa. Note that at the growth temperature the value of the mechanical stresses can be higher or lower than the calculated value depending on the presence of misfit dislocations, lattice mismatch and difference of thermal expansion coefficients of CdTe film and substrate during the growth process [35]. However, in this paper, we assume that the mechanical stress in the volume of CdTe film equals approximately  $\sim 300 \text{ MPa}$ . During the heteroepitaxy growth, the island-substrate interface is often semicoherent. Therefore, the effective mechanical stress is lower than that in the volume of CdTe film. Our estimates show that its value is about 120-150 MPa. It is also important to note that in the case of CdTe growth on the Si substrate the residual stress is several times higher,

about 0.6-1.0 GPa [36]. Moreover, the use of the nanopatterned substrates does not lead to the relaxation of CdTe film on the Si substrate [36].

As a result, the model allows the estimation of the values of the parameters of the CdTe film growth on the SiC/Si substrate at the growth conditions [13]. At the substrate temperature  $T_S = 500$  °C, the Cd adatom lifetime equals  $\tau_{Cd} \sim 2 \cdot 10^{-10}$  s. The Te adatom lifetime is much larger,  $\tau_{Te} \sim 6 \cdot 10^{-4}$  s (Fig. 2a). The estimates of the equilibrium concentrations of adatoms,  $C_{Cd}^{eq}$  and  $C_{Te}^{eq}$ , show that their ratio equals  $C_{Cd}^{eq}/C_{Te}^{eq} \sim 10^{-7}$ . Such a large difference in the adatom lifetime and equilibrium concentrations is caused by the difference in the binding energies of Cd and Te adatoms with the substrate. The binding energy of Cd adatom is approximately three times less than that of Te adatoms. As the material source, the CdTe powder heated up to the temperature of  $T_g = 580$  °C was used in the work [13]. The calculated values of the flux densities of Cd and Te atoms coming to the substrate at  $T_g = 580$  °C equal, correspondently,  $J_{Cd} \sim 7 \cdot 10^{21} \text{ m}^{-2}\text{s}^{-1}$  and  $J_{Te} \sim 5 \cdot 10^{21} \text{ m}^{-2}\text{s}^{-1}$ . Note, the values of  $J_{Cd}$  and  $J_{Te}$  are very close to the value of the flux density of CdTe molecules at the same temperature  $T_g$  obtained experimentally in the work [22]. The concentration of Cd and Te adatoms at such fluxes equal  $C_{Cd} \sim 10^{-7}$  and  $C_{Te} \sim 1$ . The values of  $C_{Cd}$  and  $C_{Te}$  correspond to a very large value of the supersaturation  $\xi$ . In the real growth process, such a large excess of adatoms will be consumed rapidly by the growing islands. This will lead to the decrease of the supersaturation down to the regular value of  $\xi \sim 0.1$ . It can be shown that  $D_{Te}C_{Te}^{eq} \ln(\lambda_{Cd}/r_c) \gg D_{Cd}C_{Cd}^{eq} \ln(\lambda_{Te}/r_c)$  (equation (9)) in the considered temperature range. Consequently, the growth of the CdTe film is limited by the diffusion of Cd adatoms on the substrate and the equation (9) can be represented in the following form  $D_{CdTe} \approx D_{Cd}C_{Cd}^{eq} / \ln(\lambda_{Cd}/r_c)$ . The elastic stresses due to the lattice mismatch between the SiC/Si substrate and CdTe film cause the decrease of the driving force of nucleation compared to the case of unstrained structure. The value of this decrease equals  $\sim 15\%$  that corresponds to  $w \sim 0.048$  eV per atom. As a result, the nucleation rate decreases by three orders of magnitude. However, in the case of nucleation on the Si substrate the driving force is several times lower because the value of the mechanical stresses is several times larger. Our calculations show that the nucleation rate of CdTe islands on the Si substrate is several orders of magnitude lower than the nucleation rate on the SiC/Si substrate. Therefore, the formation of the CdTe film is much easier on the SiC/Si substrate than on the Si substrate.

#### 4. Diagram of the nucleation intensity of CdTe nuclei on the SiC/Si surface. Conditions of optimal epitaxial growth of the CdTe films on SiC/Si

Using the formula (10), it is possible to estimate the nucleation rate  $I(T_g, T_s)$  for different temperatures of the evaporator  $T_g$  and the substrate  $T_s$ . Fig. 3 demonstrates a diagram of the relative intensity of the CdTe islands nucleation on SiC/Si substrate in  $T_g$  and  $T_s$  axes. The color corresponds to the value  $I(T_g, T_s)/I(580 \text{ °C}, 500 \text{ °C})$ , i.e. to the ratio of the intensity of the islands nucleation calculated from the formula (10) for the temperatures  $T_g$  and  $T_s$  to the intensity of the islands nucleation under the growth conditions of the paper [13]. Note that the use of such a relative value is convenient in view of the fact that the growth mechanism of the CdTe film under the conditions of the paper [13] has already been determined experimentally and the film growth rate is known to be about 0.3–0.5  $\mu\text{m/s}$ . Comparing the values  $I(T_g, T_s)$  and  $I(580 \text{ °C}, 500 \text{ °C})$ , it is possible to estimate the regimes and rate of CdTe film growth under other conditions as well. Thus, in Fig. 3 one can distinguish 5 characteristic regions with different rates of CdTe nucleation. It is expected that in the region I (see Fig. 3), the mechanism of CdTe film growth will be similar to that observed in the experiment [13]. In the region II corresponding to much lower values of the supersaturation and more equilibrium conditions of

the film growth, one can get epitaxial layers of high quality. However, it should be taken into account that the growth rate in this case will be much lower. In this regard, if the vacuum is not sufficiently high in the system, the concentration of other substances which present in the gas phase in the reactor will be higher in the resulting CdTe film.

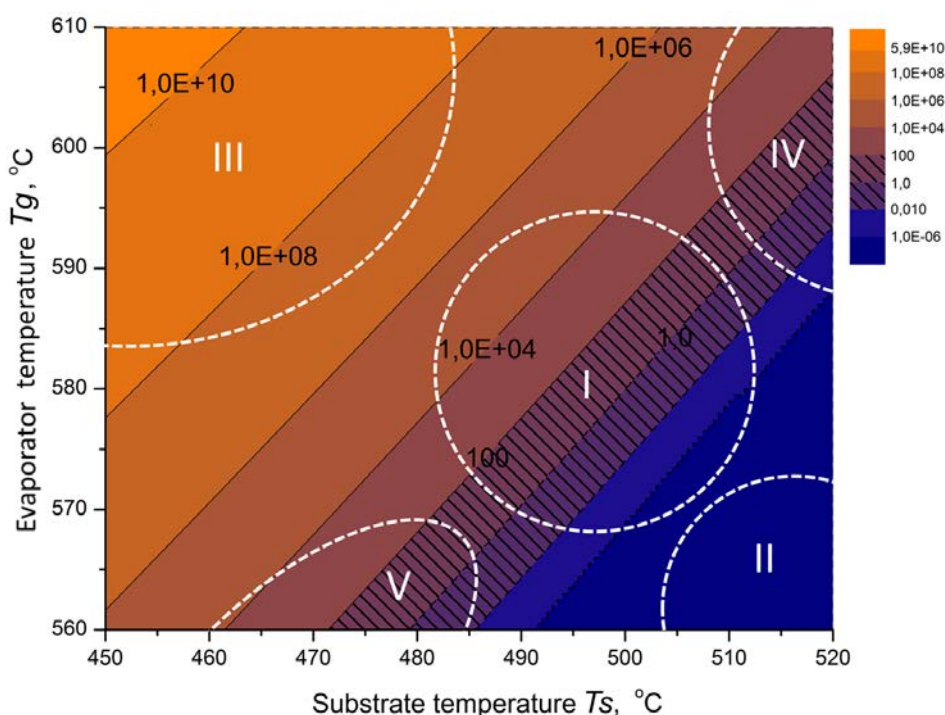


**Fig. 3.** Dependence of the relative intensity of nucleation  $I(T_g, T_s)$  of CdTe islands on evaporator temperature and substrate temperature. The normalization was carried out on the nucleation intensity under the experimental conditions of paper [13].

Moreover, taking into account the small supersaturation and the extremely low nucleation rate, a change of the film growth regime for the two-dimensional growth due to the diffusion of adatoms to the growth steps or to the exit points of screw dislocations is possible. In the region III large supersaturations are observed and the nucleation intensity significantly exceeds the values corresponding to [13]. The growth in such non-equilibrium conditions can lead to the appearance of polycrystals. In addition, significant supersaturation can lead to the development of morphological instability and increase of surface roughness [37, 38]. The region IV corresponds to nucleation rates comparable to [13], but the growth occurs at high substrate temperatures. As a result, the diffusion length of adatoms of cadmium and tellurium becomes smaller, which can also contribute to the development of roughness at scales comparable to the diffusion lengths of adatoms [37]. An advantage of the region IV is higher partial pressures of Cd and  $\text{Te}_2$  in the reactor and, as a consequence, lower concentrations of impurities in the film. In the region V, vice versa, the partial pressures of cadmium and tellurium are small, and a large concentration of impurities can be observed. However, the diffusion lengths of the adatoms in this region are much larger, which can lead to smoothing of the roughness with a short spatial wavelength [37].

## 5. Conclusions

The process of cadmium telluride film growth on SiC/Si substrates by the method of thermal evaporation and condensation in vacuum is considered. The model for the formation and growth of CdTe film is developed on the basis of the classical nucleation theory, which takes into account the influence of mechanical stresses that arise in CdTe due to difference in the

parameters of crystalline lattices of the film and the substrate. It is shown that the presence of elastic stresses reduces effective difference of chemical potentials for Cd and Te by  $\sim 15\%$ , which corresponds to  $\sim 0.048$  eV per atom. Such a decrease in the difference of chemical potentials has a significant effect on the nucleation rate, and as a consequence, on the growth mechanism of thin films. Estimates of the mechanical stresses arising in CdTe films grown on SiC/Si and Si substrates showed that in the case of coherent coupling between the film and the substrate in CdTe/SiC/Si heterostructure elastic stresses are of the order of  $\sim 0.2$ - $0.3$  GPa, whereas in CdTe/Si heterostructure the elastic stresses will be  $\sim 0.6$ - $1$  GPa, which are approximately three to four times higher. Such a difference in the elastic stresses significantly affects the activation barriers for CdTe nucleation on Si substrate with a buffer layer of SiC and on pure Si substrate without a buffer layer. The main constants determining the nucleation rate, namely the lifetimes of Cd and Te adatoms are calculated, as well as the generalized adatom diffusion coefficient, which determines the growth rate of CdTe islands. On the basis of these data, a theoretical diagram of the nucleation rate of CdTe nuclei on SiC/Si surface in the temperature range of the evaporator  $560$ - $610$  °C and of the substrate  $450$ - $520$  °C was calculated. The various growth regimes of the film are discussed. It is shown that change in the temperature of the substrate/evaporator by  $10$  °C can lead to a sharp (up to several orders) change in the rate of nucleation, which significantly affects the mechanism and growth rate of thin film, impurity concentration, degree of crystallinity and, ultimately, quality of the grown CdTe films.

### Acknowledgements

*This work was supported by the Russian Science Foundation (№ 14-12-01102). The experimental results were partially obtained using the unique scientific facility "Physics, chemistry and mechanics of crystals and thin films" (IPME RAS, St. Petersburg).*

### References

- [1] V. Di Carlo, F. Marzo, F. Di Giulio, M. Prete, N. Lovergine, In: *AISEM Annual Conference on Sensors and Microsystems* (Springer, Cham, 2017), p. 279.
- [2] B.A. Korevaar, J.R. Cournoyer, O. Sulima, A. Yakimov, J.N. Johnson // *Progress in Photovoltaics: Research and Applications* **22** (2014) 1040.
- [3] A.P. Belyaev, V.P. Rubets, M.Y. Nuzhdin, I.P. Kalinkin // *Semiconductors* **37** (2003) 617.
- [4] B.M. Başol, B. McCandless // *Journal of Photonics for Energy* **4** (2104) 040996.
- [5] C. Szeles // *Physica Status Solidi (b)* **241** (2004) 783.
- [6] J. Britt, C. Ferekides // *Applied Physics Letters* **62** (1993) 2851.
- [7] A. Bylica, P. Sagan, I. Virt, G. Wisz, M. Bester I. Stefaniuk, M. Kuzma // *Thin Solid Films* **511** (2006) 439.
- [8] T.W. Kim, B.J. Koo, M. Jung, S.B. Kim, H.L. Park, H. Lim, H., K.N. Kang // *Journal of Applied Physics* **71** (1992) 1049.
- [9] R.N. Bicknell, R.W. Yanka, N.C. Giles, J.F. Schetzina, T.J. Magee, C. Leung, H. Kawayoshi // *Applied Physics Letters* **44** (1984) 313.
- [10] S. Rujirawat, L.A. Almeida, Y.P. Chen, S. Sivananthan, D.J. Smith // *Applied Physics Letters* **71** (1997) 1810.
- [11] N.V. Sochinskii, V. Munoz, V. Bellanim L. Vina, E. Dieguez, E. Alves da Silva, J.C. Soares, S. Bernardi // *Applied Physics Letters* **70** (1997) 1314.
- [12] G.M. Lalev, J. Wang, J.W. Lim, S. Abe, K. Masumoto, M. Isshiki // *Applied Surface Science* **242** (2005) 295.
- [13] V.V. Antipov, S.A. Kukushkin, A.V. Osipov // *Physics of the Solid State* **59** (2017) 399.
- [14] S.A. Kukushkin, A.V. Osipov // *Journal of Physics D: Applied Physics* **47** (2014) 313001.
- [15] S.A. Kukushkin, A.V. Osipov // *Journal of Applied Physics* **113** (2103) 024909.

- [16] D.G. Diso, T.S. Bichi, M.A. Y. Hotoro, I.A. Faragai, A.O. Musa // *Bayero Journal of Pure and Applied Sciences* **8** (2015) 58.
- [17] A.D. Compaan A. Gupta, S. Lee, S. Wang, J. Drayton // *Solar Energy* **77** (2004) 815.
- [18] S. Lalitha, S.Z. Karazhanov, P. Ravindran, S. Senthilarasu, R. Sathyamoorthy, J. Janabergenov // *Physica B: Condensed Matter* **387** (2007) 227.
- [19] E.W. Jones, V. Barrioz, S.J.C. Irvine, D. Lamb // *Thin Solid Films* **517** (2009) 2226.
- [20] K.K. Muravyeva, I.P. Kalinkin, V.B. Aleskovsky, I.N. Anikin // *Thin Solid Films* **10** (1972) 355.
- [21] A.P. Belyaev, V.P. Rubets, I.P. Kalinkin // *Physics of the Solid State* **39** (1997) 333.
- [22] I.P. Kalinkin, V.B. Aleskovskii, A.V. Simashkevich, *Epitaxial Films of II–VI Compounds* (Leningrad State University, Leningrad, 1978). (In Russian).
- [23] S.A. Kukushkin, A.V. Osipov, In: *Encyclopedia of Nanoscience and Nanotechnology*, ed. by H.S. Nalwa (USA, 2004), Vol. 8, p. 113.
- [24] Ya.B. Zel'dovich // *Journal of Experimental and Theoretical Physics* **12** (1942) 525.
- [25] S.A. Kukushkin // *Thin Solid Films* **207** (1992) 302.
- [26] A.A. Koryakin, S.A. Kukushkin, N.V. Sibirev // *Semiconductors* **52** (2018). (In print).
- [27] S.A. Kukushkin, V.N. Bessolov, A.V. Osipov, A.V. Luk'yanov // *Physics of the Solid State* **43** (2001) 2229.
- [28] H.R. Moutinho, M.M. Al-Jassim, D.H. Levi, P.C. Dippo, L.L. Kazmerski // *Journal of Vacuum Science and Technology A: Vacuum, Surfaces, and Films* **16** (1998) 1251.
- [29] M.A. Herman, O. Jylhä, M. Pessa // *Crystal Research and Technology* **21** (1986) 841.
- [30] M.A. Herman, O. Jylhä, M. Pessa // *Crystal Research and Technology* **21** (1986) 969.
- [31] R.F. Brebrick, A.J. Strauss // *Journal of Physics and Chemistry of Solids* **25** (1964) 1441.
- [32] B. N. Osherin // *Physics of the Solid State* **34** (1976) 181.
- [33] R.K. Ram, S.S. Kushwaha, J.S. Rajput // *Journal of the Physical Society of Japan* **58** (1989) 4032.
- [34] V.C. Stergiou, N.T. Pelekanos, Y.S. Raptis // *Physical Review B* **67** (2003) 165304.
- [35] R.S. Telyatnik, A.V. Osipov, S.A. Kukushkin // *Physics of the Solid State* **57** (2015) 162.
- [36] R. Bommerna, T. Seldrum, L. Samain, R. Sporcken, S. Sivananthan, S.R.J. Brueck // *Journal of Electronic Materials* **37** (2008) 1255.
- [37] A.V. Redkov, A.V. Osipov, S.A. Kukushkin // *Physics of the Solid State* **57** (2015) 2524.
- [38] S.A. Kukushkin, A.V. Osipov, A.V. Redkov // *Physics of the Solid State* **56** (2014) 2530.

# ON INFLUENCE OF SHEAR TRACTION ON HYDRAULIC FRACTURE PROPAGATION

A. M. Linkov<sup>1,2</sup>

<sup>1</sup>Rzeszow University of Technology, Poland

<sup>2</sup>Peter the Great St. Petersburg Polytechnic University, Russia

\*e-mail: voknilal@hotmail.com

**Abstract.** The paper concerns with the problem important for proper simulation of hydraulic fractures. Its objective is to answer the recently raised question: Can we neglect the impact of the hydraulically induced shear stress when using the elasticity equation, which connects the fracture opening with the net-pressure? The estimations, given in the paper, show that the answer is “Yes”. The impact can be confidently neglected. Its influence is well beyond physical significance, computational abilities of computers and practical applications of HF.

**Keywords:** hydraulic fracture, shear traction, elasticity equation.

## 1. Introduction

It is well known that viscous shear is the main force resisting to fluid flow in a narrow channel of a given small width. Meanwhile, in hydraulic fracture (HF) problems, the width itself depends on the deformation of the channel walls and it is zero at the contour of a propagating fracture. In these problems, the width is defined by the deformation of embedding rock; it is found from the elasticity equation connecting the channel width (opening in this case) with the tractions on the channel (fracture) surfaces.

Starting from the pioneering paper by Spence and Sharp [21], the shear traction, entering the elasticity equation, has been neglected in all papers on HF (e.g. [1-8, 10, 13, 15, 19-21, 23]). However, recently [24] it has been suggested that the shear traction is to be included into the elasticity equation, as well. An example of self-similar solution, given by the authors, shows that the input of the shear term is 10%, at most. Still, the question arises, if it is reasonable always to neglect this input when simulating HF propagation?

The objective of the present paper is to answer the question. We estimate the input of the shear term into the elastic response of embedding rock in HF problems. It is shown that for values of input parameters, typical in HF practice, the influence of the shear term discussed is far-beyond practical significance and computational abilities of modern computers.

## 2. Problem formulation

The problem formulation is conventional (e.g. [1-8, 10, 13, 15, 19-21, 23]) except for the only difference: the shear traction is accounted for in the elasticity equation. Below we use the formulation employing the fundamental speed equation [9, 12] and the particle velocity [13] rather than the flux (see also [14-17, 23]). Consider the plane strain problem for a straight fracture driven by a viscous fluid, studied, for instance, in the papers [1, 13, 21, 23, 24]. The  $x$ -axis is located along the fracture in the propagation direction. The  $y$ -axis is directed to the left of  $x$ . The quite general power law describes the fluid velocity across the opening:

$$\sigma_{xy} = -M(\dot{\gamma}\text{signy})^n\text{signy}, \quad (1)$$

where  $\sigma_{xy}$  is the shear stress;  $n$  and  $M$  are, respectively, the behavior and consistency indices;  $\dot{\gamma} = 2\dot{\epsilon}_{xy}$ ;  $\dot{\epsilon}_{xy} = 1/2 \left( \frac{\partial v_x}{\partial y} + \frac{\partial v_y}{\partial x} \right)$  is the shear strain rate;  $v_x, v_y$  are the components of the fluid velocity. For a Newtonian fluid,  $n = 1$  and  $M = \mu$  is the dynamic viscosity.

For a narrow channel, the flow is assumed to be of the Poiseuille type, predominanatly in-plane and steady. Then the out-of-plane component  $v_y$  is neglected in (1) as compared with  $v_x$ , while the movement equation of the Navier-Stokes type yields

$$\sigma_{xy}(y) = -i_* y, \tag{2}$$

where  $i_* = -\partial p/\partial x$  is the pressure gradient taken with the minus sign ( $i_* > 0$ ). Equation (2) implies linear distribution of the shear stress along the channel width  $w$ :

$$\sigma_{xy} = -\frac{y}{w/2} \tau, \tag{3}$$

where  $\tau$  is the shear traction on the lower shore ( $y = -w/2$ ) of the channel. Using (3) in (2) gives (e. g. [22]):

$$\tau = \frac{1}{2} w i_* \tag{4}$$

On the other hand, using (2) in (1) and integration provide the profile of the velocity  $v_x(y)$ . The latter, being averaged over the cross-section, yields the conventional average particle velocity  $v = \int_{-w/2}^{w/2} v_x(y) dy / w$  (e.g. [15]):

$$v = w \left( \frac{w}{\mu'} i_* \right)^{1/n}, \tag{5}$$

where  $\mu' = 2 \left( 2 \frac{2n+1}{n} \right)^n M$ . For a Newtonian fluid,  $\mu' = 12\mu$ . In view of (4), equation (5) may be re-written in terms of the shear traction as

$$\tau = \frac{\mu'}{2} \left( \frac{v}{w} \right)^n \tag{6}$$

The fracture propagation speed  $v_*$ , by the speed equation is  $v_* = \lim_{r \rightarrow 0} v$ , where  $r$  is the distance from the fluid front. For a continuous particle velocity  $v$ , this infers that in the near-front zone, equation (6) becomes:

$$\tau = \frac{\mu'}{2} \frac{v_*^n}{w^n} \tag{7}$$

Neglect, as usual, the lag (e.g. [1, 13, 21, 23, 24]). Then the propagation speed  $v_*$ , being finite and non-zero, equation (7) implies that near the fracture contour, the shear traction behaves as  $\tau = O\left(\frac{1}{w^n}\right)$ . It is singular, because the opening  $w$  goes to zero at the fracture contour.

To the moment, the elasticity equation, defining the opening, hasnot been employed. When accounting for the shear traction, from the classical solution by Muskhelishvili's [18], it follows (e.g. [11]):

$$p(x) = \frac{E'}{4\pi} \int_{-x_*}^{x_*} \frac{\partial w / \partial \xi - 2k_\tau \tau(\xi) / E'}{x - \xi} d\xi, \tag{8}$$

where  $E' = E/(1 - \nu^2)$  is the plane-strain elasticity modulus,  $E$  is the Young's modulus,  $\nu$  is the Poisson's ratio,  $x_*$  is the fracture half-length,  $k_\tau = \frac{1-2\nu}{1-\nu}$  is the factor depending merely on the Poisson's ratio. For physically significant values of the latter ( $0 \leq \nu \leq 0.5$ ), the factor  $k_\tau$  never exceeds 1; it equals to zero when  $\nu \leq 0.5$  and it reaches its maximal value 1 when  $\nu = 0$ . For commonly used value  $\nu = 0.3$ , it is 0.531.

As mentioned, in all the papers on HF, except for the paper [24], the term  $2k_\tau \tau(\xi) / E'$ , which includes the shear traction, is neglected. Our objective is to compare the input of this term into the net-pressure  $p(x)$  with that of the term  $\partial w / \partial \xi$  conventionally accounted for.

### 3. Comparison of conventional and shear terms

The reltive input of the shear traction into the net-pressure, as compared with that of the conventional term  $\partial w / \partial \xi$ , is given by the ratio

$$R_\tau = -\frac{2k_\tau \tau(x)}{E' \partial w / \partial x} \quad (9)$$

The compared terms are greatest in the near tip zone, where the both of them are singular. In this zone  $\partial w / \partial x = -\partial w / \partial r$ , where  $r$  is the distance from the tip, and equation (7) is applicable. Then the ratio (9) becomes:

$$R_\tau = k_\tau \frac{\mu'}{E'} \frac{v_*^n}{w^n dw/dr} \quad (10)$$

Estimations of  $R_\tau$  for toughness, viscosity and leak-off dominated regimes may employ well-known asymptotics for these regimes (e.g. [4, 7, 8, 10, 15, 21]). Commonly the asymptotics of the opening are of the form

$$w = A_w r^\alpha \quad (11)$$

where explicit formulae for the factor  $A_w$  and the exponent  $\alpha$  are given in the cited papers. Then  $dw/dr = \alpha w/r$ , and (10) becomes

$$R_\tau = k_\tau \frac{\mu'}{E'} \frac{v_*^n}{\alpha A_w^{n+1} r^{\alpha(n+1)-1}} \quad (12)$$

Consider the regimes studied in [24], which are (i) viscosity dominated, and (ii) toughness dominated.

(i) *Viscosity dominated regime.* In this case,  $\alpha = 2/(n+2)$  and

$$A_w = A_\mu (t_n' v_*)^{1-\alpha}, \quad (13)$$

where  $A_\mu = [(1-\alpha)B(\alpha)]^{1/(n+2)}$ ,  $B(\alpha) = \frac{\alpha}{4} \cot[\pi(1-\alpha)]$ ,  $t_n' = (\mu'/E')^{1/n}$ . Then  $\alpha(n+1) - 1 = n/(n+2)$ , and substitution (13) into (10) yields:

$$R_\tau = k_\tau \frac{1}{\alpha A_\mu^{n+1}} \left( \frac{t_n' v_*}{r} \right)^{n/(n+2)} \quad (14)$$

Consider, for certainty, a Newtonian fluid ( $n = 1$ ).

Then  $\alpha = 2/3$ ,  $A_\mu = 2^{1/3} 3^{5/6} = 3.1473$ ,  $t_n' = \mu'/E' = 12\mu/E'$ . Using these values in (13) and substitution into (14) gives:

$$R_\tau = 0.1514 k_\tau \left( \frac{12\mu v_*}{E' r} \right)^{1/3} \quad (15)$$

For the values  $\mu = 10^{-7}$  MPa·s,  $E' = 2.5 \cdot 10^4$  MPa, typical for HF (e.g. [1, 3, 5, 10, 15]), equation (15) becomes  $R_\tau = 0.5503 \cdot 10^{-4} k_\tau \left( \frac{v_*}{r} \right)^{1/3}$ . Take the maximal value  $k_\tau = 1$  and quite a large value of the fracture propagation speed  $v_* = 0.1$  m/s (360 m/hour). Then equation (15) implies that the input of the shear traction  $\tau(x)$  reaches 1% of the input of the conventional term  $-\partial w / \partial x$ , that is  $R$  grows to 0.01, only at the distance  $r$  from the tip less than  $1.67 \cdot 10^{-8}$  m. This shows that the input of the shear traction reaches the level of 1% only at the distance of atomic sizes. Surely, it is beyond physical significance, computational abilities of computers and practical applications of HF.

(ii) *Toughness dominated regime.* In this case,  $\alpha = 2/3$ ,  $A_w = \sqrt{\frac{32 K_{IC}}{\pi E'}}$ , where  $K_{IC}$  is the critical stress intensity factor. Then equation (12) reads:

$$R_\tau = 2k_\tau \frac{\mu'}{E'} \left( \sqrt{\frac{\pi E'}{32 K_{IC}}} \right)^{n+1} v_*^n r^{(1-n)/2} \quad (16)$$

For a Newtonian fluid ( $n = 1$ ), equation (16) becomes:

$$R_\tau = 2k_\tau \frac{\pi \mu'}{32 E'} \left( \frac{E'}{K_{IC}} \right)^2 v_* \quad (17)$$

As known (e.g. [7, 8, 15]), the toughness dominated regime occurs when  $(L_\mu/L_k)^{1/2} \ll 1$ , where  $L_k = \frac{32}{\pi} \left( \frac{K_{IC}}{E'} \right)^2$ ,  $L_\mu = t_n' v_*$ . Thus, for the toughness dominated regime,

$\sqrt{\frac{\pi \mu'}{32 E'} v_* \frac{E'}{K_{IC}}} \ll 1$ . Being squared, the inequality becomes square stronger  $\frac{\pi \mu'}{32 E'} \left( \frac{E'}{K_{IC}} \right)^2 v_* \ll 1$ .

When used in the right hand side of (17), it implies that  $R_\tau \ll 1$ . This means that in the toughness dominated regime, the input of the shear traction into elasticity equation is negligible, as well.

*Comment on self-similar solution with exponentially growing injection rate.* The paper [24] contains an example, which served authors to illustrate the input of the shear traction in the elasticity equation. To employ a self-similar solution, the authors assumed exponential growth of the injection rate. They considered a fracture driven by a Newtonian fluid ( $n = 1$ ). From the numerical results, shown in figures 7 and 8 of this paper, it appears that for regimes with large toughness, the influence of the shear term is indistinguishable. This agrees with the conclusion above for such a regime. However, in the case of the viscosity dominated regime, for which  $K_{IC} = 0$ , the calculated injection pressure is about 10% greater if the shear term is taken into account (Fig. 8a of the paper). This result disagrees with the estimation (15) for the viscosity dominated regime. According to this estimation, such influence of the shear term may occur merely for very high values of the fracture propagation speed  $v_*$ .

Thus, it is reasonable to estimate the physical speed  $v_*$  for the example of the paper [24]. Below we employ the notation of this paper and the definitions of the normalized and self-similar quantities given in its equations (53) and (84)-(87). These definitions imply that the physical injection rate  $q_0(t)$  and the physical speed  $v_*(t)$  of the fracture propagation are:

$$q_0(t) = \frac{1}{t_n} \bar{q}_0 e^{2\alpha t/t_n}, v_*(t) = v(t, l) = \frac{1}{\sqrt{t_n}} \sqrt{\frac{\bar{q}_0}{t_n}} e^{2\alpha t/t_n} \frac{\hat{v}_0}{\sqrt{L_0}}, \quad (18)$$

where  $t_n = 2\pi M/E'$ ,  $M = \mu' = 12\mu$ ,  $E' = E/(1 - \nu^2)$ ,  $L_0 = \sqrt{\hat{v}_0/\alpha}$ ,  $\hat{v}_0 = \hat{v}(1)$  is the self-similar propagation speed; the factor  $\bar{q}_0$  and the exponent  $\alpha$ , characterizing the intensity of the flux, are assigned values. The authors of the paper [24] set  $\alpha = 1/3$ ; the values of  $\hat{v}_0 = \hat{v}(1)$  of the self-similar propagation speed are defined by Fig. 7b of their paper. From this figure it appears that for the viscosity dominated regime, when  $K_{IC} = 0$ , the self-similar propagation speed is approximately  $\hat{v}(1) = 0.625$ . Then  $L_0 = 1.369$  and  $\hat{v}_0/\sqrt{L_0} = 0.5341$ . The parameter  $\bar{q}_0$  characterizes the influx at a specified time instant  $t_0$ . If at an instant  $t_0$  the influx has a value  $q_{0HF}$ , typical for practice of hydraulic fracturing ( $q_0(t_0) = q_{0HF}$ ), then equations (18) become:

$$q_0(t) = q_{0HF} e^{2\alpha(t-t_0)/t_n}, v_*(t) = 0.5341 \sqrt{\frac{q_{0HF}}{t_n}} e^{\alpha(t-t_0)/t_n} \quad (19)$$

For the typical values  $\mu = 10^{-7}$  MPa·s,  $E' = 2.5 \cdot 10^4$  MPa (e.g. [1, 3, 5, 10, 15]), the definitions of  $t_n$  for  $\alpha = 1/3$  yields  $t_n = 3.016 \cdot 10^{-10}$  s,  $\alpha/t_n = 1.10 \cdot 10^9$  1/s. Then for the typical influx  $q_{0HF} = 0.5 \cdot 10^{-4}$  m<sup>2</sup>/s (e.g. [3, 5]), the speed defined by the second of (19) is  $v_*(t) = 688 \cdot \exp[(t - t_0)1.10 \cdot 10^9]$  m/s.

Therefore, the solution of the example, considered in the paper [24], implies that if at some time instant  $t = t_0$  the influx has a typical order of  $10^{-4}$  m<sup>2</sup>/s, then at this instant the propagation speed  $v_*$  is of order km/s. Such a speed is much greater than values typical in practice of HF: normally the propagation speed is four orders less. Even more extraordinary is that during a very short time interval  $t - t_0 = 10^{-8}$  s after  $t_0$ , the propagation speed exceeds the speed of light  $c = 3 \cdot 10^8$  m/s. Therefore, the example corresponds to quite exotic, to say the least, problem. This explains why the authors of the paper [24] obtained non-negligible influence of the shear term in the elasticity equation on the calculated injection pressure (some 10%) for the viscosity dominated regime.

#### 4. Reason of different results

It remains to clarify why the authors of the paper [24] came to the different conclusions on the impact of the shear stress? They inferred these conclusions by considering the ratio  $\tau/|p|$  in the line of Spence and Sharp [21].

For the magnitude of the pressure  $|p|$ , the asymptotic equation is (e.g. [15]):

$$|p| = E' A_w B(\alpha) r^{\alpha-1} \quad (20)$$

where  $\alpha$  and  $B(\alpha)$  are defined as in equation (13). By using (20) and equation (7) for the shear traction, we obtain for the ratio  $\tau/|p|$ :

$$\frac{\tau}{|p|} = \frac{\alpha}{2B(\alpha)} \frac{\mu'}{E'} \frac{v_*^n}{\alpha A_w^{n+1} r^{\alpha(n+1)-1}} \quad (21)$$

Equation (21) is analogous to equation (12) for the ratio  $R_\tau$ . The only difference between (12) and (21) is in the factors  $k_\tau$  and  $\frac{\alpha}{2B(\alpha)}$  on the right hand sides. Consider the case of zero toughness ( $K_{IC} = 0$ ), for which the impact of the shear traction is maximal. Then for a Newtonian fluid, considered in [24],  $\alpha = 2/3$ ,  $B(\alpha) = 1/(6\sqrt{3})$ ,  $\frac{\alpha}{2B(\alpha)} = 2\sqrt{3}$ . Hence, similar to (12), the factor in (21) is of order 1. Consequently, using (21) implies the same conclusions as those above.

Unfortunately, the authors of the paper [24] have not derived equation (7), which provided us with quantitative estimations. Not having this equation, they formally tended  $r$  to zero when considering the ratio  $\tau/|p|$ . Clearly, the ratio goes to infinity, what leads to an illusion that the shear stress should be accounted for in the elasticity equation. This explains the reason of erroneous claims made in the cited paper on the impact of the shear traction and on the viscosity dominated regime.

## 5. Conclusion

The estimations, given for the impact of the shear term in the elasticity equation on the net-pressure, show that it can be confidently neglected when solving practical problems of hydraulic fracturing. Its influence is well beyond physical significance, computational abilities of computers and practical applications of HF.

**Acknowledgements.** This research was financed by Ministry of Education and Science of the Russian Federation within the framework of the Federal Program "Research and development in priority areas for the development of the scientific and technological complex of Russia for 2014-2020", Activity 1.2., Agreement on Grant No. 14.575.21.0146 of 26 September, 2017, unique identifier: RFMEFI57517X0146.

## References

- [1] J. Adachi, E. Detournay // *International Journal for Numerical and Analytical Methods in Geomechanics* **26(6)** (2002) 579.
- [2] J. Adachi, E. Seibrits, A. Peirce, J. Desroches // *International Journal of Rock Mechanics and Mining Sciences* **44** (2007) 739.
- [3] E. Dontsov, A. Peirce // *Engineering Fracture Mechanics* **142** (2015) 116.
- [4] E.V. Dontsov, A.P. Peirce // *Computer Methods in Applied Mechanics and Engineering* **313** (2017) 53.
- [5] D.I. Garagash // *International Journal for Numerical and Analytical Methods in Geomechanics* **30** (2006) 1439.
- [6] D.I. Garagash, E. Detournay // *Journal of Applied Mechanics* **67(1)** (2000) 183.
- [7] D.I. Garagash, E. Detournay, J. Adachi // *Journal of Fluid Mechanics* **669** (2011) 260.
- [8] E. Gordeliy, A. Peirce // *Computer Methods in Applied Mechanics and Engineering* **266** (2013) 125.
- [9] L.F. Kemp // *SPE Production Engineering* **5** (1990) 311.
- [10] B. Lenoach // *Journal of the Mechanics and Physics of Solids* **43** (1995) 1025.
- [11] A.M. Linkov, *Boundary Integral Equations in Elasticity Theory* (Dordrecht-Boston-London: Kluwer Academic Publishers, 2002).

- [12] A.M. Linkov // *Doklady Physics* **56** (2011) 436.
- [13] A.M. Linkov // *International Journal of Engineering Science* **52** (2012) 77.
- [14] A.M. Linkov // *Journal of Mining Science* **49(1)** (2013) 8.
- [15] A.M. Linkov // *Journal of Applied Mathematics and Mechanics* **79(1)** (2015) 54.
- [16] A.M. Linkov, G. Mishuris, In: *Effective and Sustainable Hydraulic Fracturing*, ed. by A. Bungler, R.G. Jeffrey, J. McLennan (Brisbane, 2013) 641.
- [17] G. Mishuris, M. Wrobel, A. Linkov // *International Journal of Engineering Science* **61** (2012) 10.
- [18] N.I. Muskhelishvili // *Some Basic Problems of the Mathematical Theory of Elasticity* (Groningen, Noordhoff, 1958).
- [19] A. Peirce, E. Detournay // *Computer Methods in Applied Mechanics and Engineering* **197** (2008) 2858.
- [20] A. Savitski, E. Detournay // *International Journal of Solids and Structures* **39** (2002) 6311.
- [21] D. Spence, P. Sharp // *Proceedings of the Royal Society A: Mathematical, Physical & Engineering Sciences* **400(1819)** (1985) 289.
- [22] V. Tsai, J. Rice // *Featured in Journal of Geophysical Research: Earth Surface* **115(F3)** (2010) 1.
- [23] M. Wrobel, G. Mishuris // *International Journal of Engineering Science* **94** (2015) 23.
- [24] M. Wrobel, G. Mishuris, A. Piccolroaz // *International Journal of Engineering Science* **111** (2017) 28.

# ELASTOMER COMPOSITES BASED ON FILLER WITH NEGATIVE COEFFICIENT OF THERMAL EXPANSION: EXPERIMENTS AND NUMERICAL SIMULATIONS OF STRESS-STRAIN BEHAVIOUR

S.N. Shubin<sup>1\*</sup>, A.G. Akulichev<sup>2</sup>, A.B. Freidin<sup>1,3,4</sup>

<sup>1</sup>Institute for Problems in Mechanical Engineering of Russian Academy of Science, Saint-Petersburg, Russia

<sup>2</sup>Norwegian University of Science and Technology, Trondheim, Norway

<sup>3</sup>Peter the Great Saint-Petersburg Polytechnic University, Saint-Petersburg, Russia

<sup>4</sup>Saint-Petersburg University, Saint-Petersburg, Russia

\*e-mail: ShubinSN@gmail.com

**Abstract.** We consider composites made of hydrogenated nitrile butadiene rubber (HNBR) and particles of zirconium tungstate ( $ZrW_2O_8$ ). We focus on finite element (FE) modelling of a finite-strain mechanical behaviour of the composite and validation of the numerical simulation against experiments. Based on examination of composite microstructure by scanning electron microscope and optical analysis of particle images, realistic representative volume elements (RVE) of microstructure are generated taking into consideration the particles circularity and size distributions. Then FE simulations are performed to study the influence of the microstructure and matrix-filler interface conditions on the mechanical properties of the composites. It is assumed that the mechanical behaviour of rubber is non-linear, while the tungstate particles are modelled by a linear elastic material. The FE simulations reproduce uniaxial compression tests. Two types of interface condition between matrix and particles are simulated: a perfect adhesion and absence of adhesion. Corresponding stress-strain curves are constructed. Comparison with experiments shows that the real stress-strain curves for pre-loaded samples path within intervals given by the modelling, i.e. pre-loading leads to partial damage of bonding between matrix and particles.

**Keywords:** elastomer composite, representative volume element, effective stress-strain curve, damage, debonding.

## 1. Introduction

In the paper, the mechanical behaviour of composites consisting of hydrogenated nitrile butadiene rubber (HNBR) and particles of zirconium tungstate ( $ZrW_2O_8$ ) that exhibits negative coefficient of thermal expansion (CTE) is studied. The fillers with low thermal expansivity provide an opportunity to reduce the thermal shrinkage of the composite in cooling [1, 2]. It is especially relevant in sealing applications for equipment operated at low temperatures. It is known that CTE of rubber is at least an order of magnitude higher than that of steel (see, for instance, [3]). Due to this fact, an elastomer seal compressed in its groove at room temperature may lose interference with the mating part after cooling and, thus, form a leak path for the contained fluid [1, 4]. In the previous work [1], we investigated analytically based on assumptions of linear elasticity how the volume fraction and the shape of the filler particles affect thermo-elastic properties, and, thus, the sealing performance of the composite. We also analysed the micro-stress at the particle-matrix interface caused by the seal squeeze and showed

that debonding may occur.

It is well known, that damage at the filler-matrix interface might significantly impact the mechanical behaviour of composites. This problem has been studied experimentally, analytically and numerically by many researchers. Particularly, particle-matrix debonding is experimentally investigated for elastomeric specimens containing one (e.g. [5]) or an array of rigid spherical particles (e.g. [6, 7, 8]). Analytical treatments provide a suitable approach to model debonding for idealized relatively simple composite microstructure and have well-known limits related to the non-linear behaviour of elastomer matrix, large deformation, high volume fraction, etc. A review of analytical modelling approaches together with a discussion on the limits of models could be found in [9]. On the other hand, numerical simulation allows to bridge the gap between analytical models and the real behaviour of composites with complicated microstructure (see an interesting discussion of this question in [10], where comparison between two methods is given). In some studies, a plane-strain assumption is used to model composites with circular particles distributed periodically (e.g. [11]) or randomly (e.g. [6, 10, 12, 13, 14, 15, 16]) and a composite with randomly distributed polygons (e.g. [15]). More appropriate three-dimensional models with randomly distributed spherical inclusions are researched in recent studies (e.g. [7, 15, 17, 18, 19, 20, 21]). However, to the authors' knowledge, there are no numerical studies focusing on debonding of ellipsoidal particles in composites with random microstructure.

In the present study, we focus on finite element (FE) modelling the large-strain mechanical behaviour of the HNBR-ZrW<sub>2</sub>O<sub>8</sub> composite and validation of the numerical simulation against experiments. A multi-scale material modelling approach is used. Based on the optical analysis of particles images and microstructure images obtained by scanning electron microscope (SEM), realistic representative volume elements (RVE) of the microstructure are generated by using a novel algorithm developed in [22]. In the generated RVE, the shapes of the inclusions are approximated by prolate ellipsoids distributed randomly inside the RVE. The particle circularity and size distributions are taken into account. Then, the generated RVEs are transferred into ABAQUS [23] for subsequent non-linear finite element simulation to find out the overall mechanical properties of the composites. In the modelling approach, it is assumed that the mechanical behaviour of rubber is non-linear and described by the Marlow model [24]. The stiffness of ZrW<sub>2</sub>O<sub>8</sub> is greater than that of rubber by a factor of 1000, therefore a linear behaviour of the filler material is assumed. The FE simulations are performed to reproduce uniaxial compression tests. Special attention is paid to the influence of the adhesive layer between matrix and particles on the effective mechanical properties.

The paper is structured in the following way. At the beginning, the material details and performed experiments are described. Next section is aimed to detail the RVE generation process for the FE simulation of the composites microstructure. Finally, simulation of uniaxial compression tests is performed for two limiting cases of the matrix-particle interface with perfect bond and no-adhesion. The stress-strain response given by simulations and experiments are then compared.

## 2. Materials and test methods

Composites of HNBR filled with various amount of zirconium tungstate up to 40 vol.% are prepared. The elastomer matrix material is based on HNBR with 96 % saturated polybutadiene with 36 % acrylonitrile content. A zirconium tungstate powder is obtained for the experiments from Alfa Aesar and used as a filler in HNBR [2]. The matrix material composition and manufacturing process of the composites were described in detail earlier in [2]. The microstructure of the composites is examined by scanning electron microscope (SEM) and optical microscopy. In addition, the filler particle size and circularity distributions are measured using a Malvern G3 Particle size analyser based on optical analysis of images of dispersed

particles at objective magnifications of 50, 10 and 2.5 [2].

The mechanical properties of the composite materials are investigated in a uniaxial compression mode using a Netzsch-Gabo Eplexor 150 DMTA machine with a 1.5 kN load cell and parallel plate specimen holders. For the experiments, button-shape specimens with 20 mm diameter and 10 mm height are produced by compression moulding. Smaller specimens of 10 mm diameter and 6 mm height are also employed due to the increased level of stiffness in HNBR with a high volume fraction of  $ZrW_2O_8$ . Silicone grease lubrication was employed to minimise barrelling. The investigated range of nominal compressive strains is 10-20 % which is relevant for rubber seals. The loading is performed stepwise with a nominal-strain step length of 5 % followed by a 3-hours stress relaxation period as in [25]. Prior to the experiments, the specimens were pre-treated with 4 full deformation cycles in order to minimise the Mullins effect [26] and left unloaded for at least 24 hours to restore the original shape.

### 3. Geometrical model of the microstructure

In order to accurately simulate the composite mechanical data, an adequate mathematical description of the actual filler inclusions in the composites is required. In the present work, we approximate the shape of the particles by prolate ellipsoids, see an example in Fig. 1. Despite the particles embedded into the HNBR matrix do not exactly resemble ellipsoids, such shape approximation can be justified by Hill's theorem [27]. The theorem suggests that a slightly uneven form of the particle surface has a minor effect on the overall elastic properties and, thereby, can be ignored (see discussion of this question in [28]).

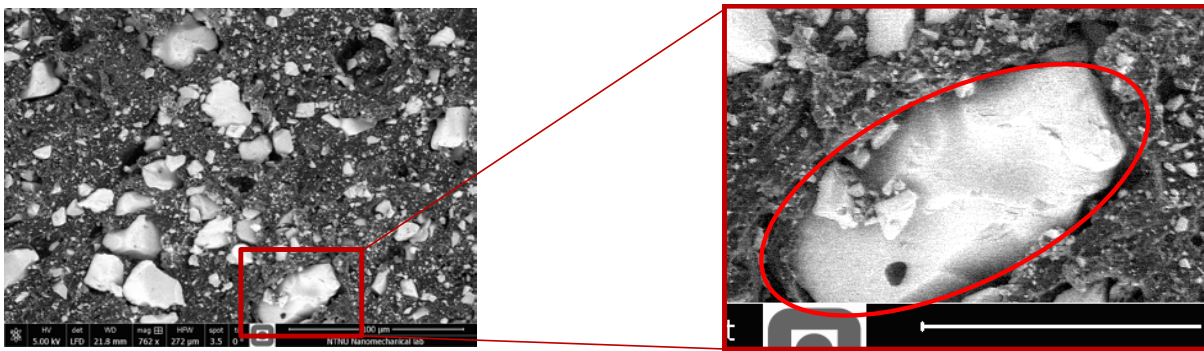


**Fig. 1.** The composite microstructure [2] and ellipsoidal approximation of the particle shape.

The microscopical image analysis of the particles enables to deduce their shape. In the analysis process, 3D particles are captured as a 2D image and two shape parameters are extracted from examination: circle equivalent (CE) diameter and circularity. CE diameter is the diameter of circle with an equivalent area in the 2D image. The particle circularity represents “closeness” of the particle shape to a perfect circle. The circularity is defined as follows:

$$\text{Circularity} = 4\pi A / P^2, \quad (1)$$

where  $A$  is the particle area;  $P$  is the particle perimeter. In case of the ellipsoidal approximation, the particle area is given by

$$A = \pi ab, \quad (2)$$

where  $a$  and  $b$  are the semi axes of ellipse. The ellipse perimeter could be calculated with help of the Ramanujan's approximation [29]

$$P = \pi(3(a+b) - \sqrt{(3a+b)(a+3b)}). \quad (3)$$

By substituting (2) and (3) into (1) and introducing aspect ratio  $\gamma = a/b$ , we obtain the following equation

$$\text{Circularity} = 4\gamma / (3(\gamma+1) - \sqrt{(3\gamma+1)(\gamma+3)})^2. \quad (4)$$

Equation (4) could be solved numerically for each value of circularity.

The particle size distribution obtained by the image analysis is shown in Fig. 2a and marked by a dotted line. The filler particles size takes values between 0.3 (defined by the instrument detection limit) and 12  $\mu\text{m}$ . This interval is divided into 12 sections of equal length in order to create a geometrical model of RVE. The diameter of the particles is assumed to be constant in each of these sections. Thus, the non-linear distribution is approximated by a piece-wise linear function, given as a solid line in Fig. 2a. The same procedure is applied to the aspect ratio distribution, see Fig. 2b.

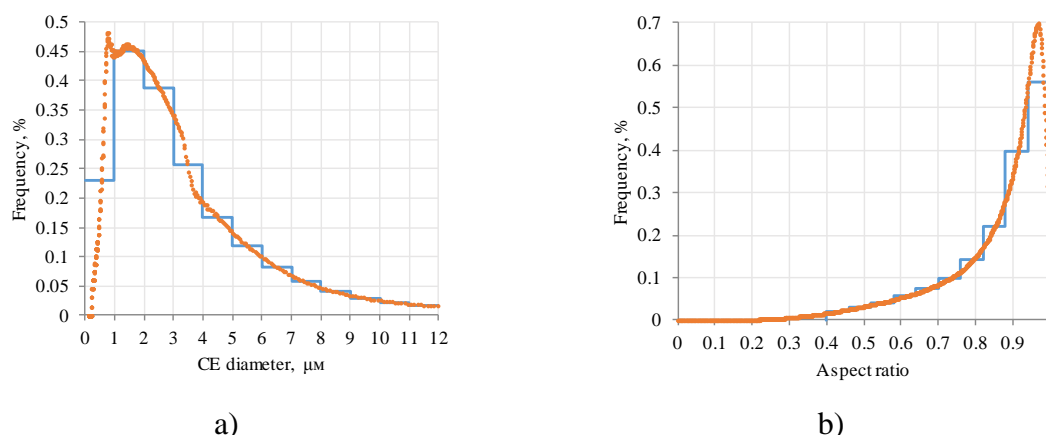


**Fig. 2.** Particle circle equivalent (CE) diameter (a) and aspect ratio (b) distributions. Dotted lines represent the results of the particle image analysis, solid lines show piece-wise linear approximations.

It should be noted, that the particle shape analysis procedure does not allow to get both size and aspect ratio for each particle, i.e. it yields the overall distribution. Therefore, the following stochastic technique is applied to create a geometrical model of RVE. In accordance with the graphs shown in Fig. 2, two element arrays are created. The number of elements in the arrays is equal to the number of particles. The first array is supplied with values of the particle diameter in accordance with the particle size distribution (for instance, if an RVE consists of 100 particles, then 12 particles have a diameter of 0.5  $\mu\text{m}$  and the first 12 elements of the array equal to 0.5  $\mu\text{m}$ ). The same method is used to fill the second array with values of the particle aspect ratio. Then, both arrays are combined randomly (for instance, the 25th element of the first array is combined with the 73rd element of the second array). Thus, the size and the shape of the particles can be considered stochastic. As an example, Fig. 3 illustrates an RVE with 100 particles for 17.3% and 35.8% of volume fraction. In the work, a novel algorithm for generation of (RVE) with randomly-oriented ellipsoidal filler particles of high volume fraction [22] is utilised.

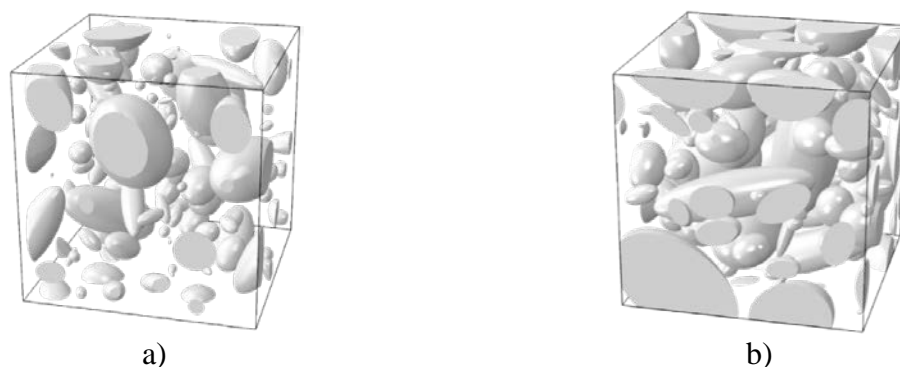


**Fig. 3.** Examples of RVEs containing 100 particles with the size and shape distributions which correspond to the optical analysis of particle images. The volume fractions of filler are 17.3% (a) and 35.8% (b).

#### 4. Effective mechanical properties

In addition to the filler inclusions, an accurate representation of the matrix behaviour is also necessary to obtain the effective properties and match the experimental stress-strain curves. It is assumed that the matrix material is incompressible with a non-linear behaviour described by the Marlow model [24]. The model is independent of the second strain invariant and based on the spline interpolation of the stress-strain data enabling exact representation of the stress-strain curve of rubber-like materials. An experimental stress-strain curve for uniaxial compression of the HNBR with a fitted line given by the Marlow model is shown in Fig. 4. The stiffness of  $ZrW_2O_8$  is much larger than that of rubber (e.g. by a factor of 1000), therefore a linear behaviour of the filler material is assumed with the Young's modulus of 88.3 GPa and the Poisson's ratio of 0.3 [30].

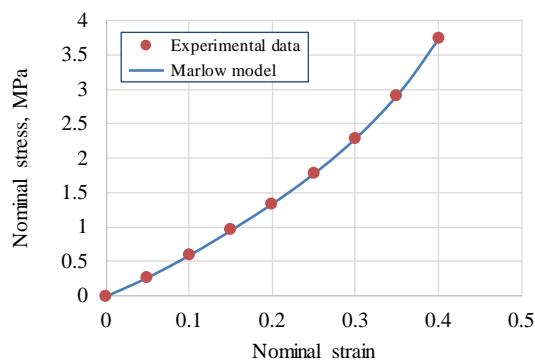


**Fig. 4.** Experimental stress-strain curve of the HNBR at uniaxial compression fitted by the Marlow model.

For finite element modelling, three RVEs for each volume fraction are created. Quadratic tetrahedral elements with hybrid formulation [23] are used for meshing. The averaged element size is equal to 0.05 in relation to the RVE edge. Averaged numbers of nodes and elements are about 300 000 and 200 000, respectively. The examples of FE models are shown in Fig. 5.

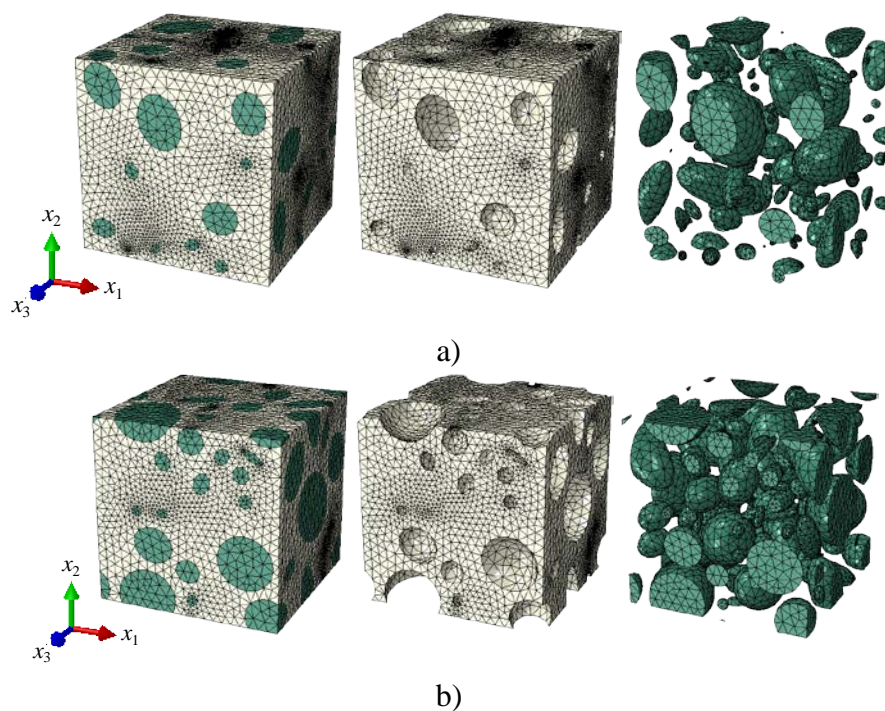


**Fig. 5.** Examples of FE models of RVEs containing 100 particles with the volume fractions of filler 17.3% (a) and 35.8% (b).

The mechanical response of each RVE is not strictly isotropic because the finite number of particles is simulated. Therefore, we perform simulation of compression in three orthogonal directions, and then the results are averaged. For the compression in  $x_1$  direction, the following boundary conditions (5) are applied:

$$\begin{aligned} x_1 = 0: & \quad u_1 = 0, \sigma_{12} = 0, \sigma_{13} = 0; & x_1 = L: & \quad u_1 = -u_1^0, \sigma_{12} = 0, \sigma_{13} = 0; \\ x_2 = 0: & \quad u_2 = 0, \sigma_{12} = 0, \sigma_{23} = 0; & x_2 = L: & \quad u_2 = \tilde{u}_2, \sigma_{12} = 0, \sigma_{23} = 0; \\ x_3 = 0: & \quad u_3 = 0, \sigma_{13} = 0, \sigma_{23} = 0; & x_3 = L: & \quad u_3 = \tilde{u}_3, \sigma_{13} = 0, \sigma_{23} = 0, \end{aligned} \quad (5)$$

where  $u_1^0$  is the applied displacement;  $\tilde{u}_2$  and  $\tilde{u}_3$  are unknown displacements defined during simulation, i.e. periodicity conditions are applied at faces  $x_2 = L$  and  $x_3 = L$ . To obtain full stress-strain curves, the problem is solved with several linearly increasing values of  $u_1^0$ . As a result, we get stress and strain distributions for each value of  $u_1^0$ . The macroscopic stress and strain are then defined as the spatial averages (6):

$$\sigma_{11}^*(u_1^0) = \frac{1}{V} \int_V \sigma_{11} dV, \quad \varepsilon_{11}^*(u_1^0) = \frac{1}{V} \int_V \varepsilon_{11} dV. \quad (6)$$

Thus, the effective stress-strain curve in compression in  $x_1$  direction is defined parametrically. The average stresses and strains in two other orthogonal directions are defined in the same manner.

For each volume fraction, stress-strain curves are obtained for three variants of RVE. The averaged stress-strain curves for both volume fractions are given in Fig. 6 with 95% confidence intervals together with experimental data. Experiments are performed for both filler volume fractions. As it can be seen, FE solutions yield higher values of stiffness in comparison with the experimental data for both volume fractions. This difference could be explained by damage of the interface between matrix and particles due to cycling pre-loading to large deformations. Such debonding, as it will be demonstrated below, in turn results in a considerable decrease in the composite stiffness.

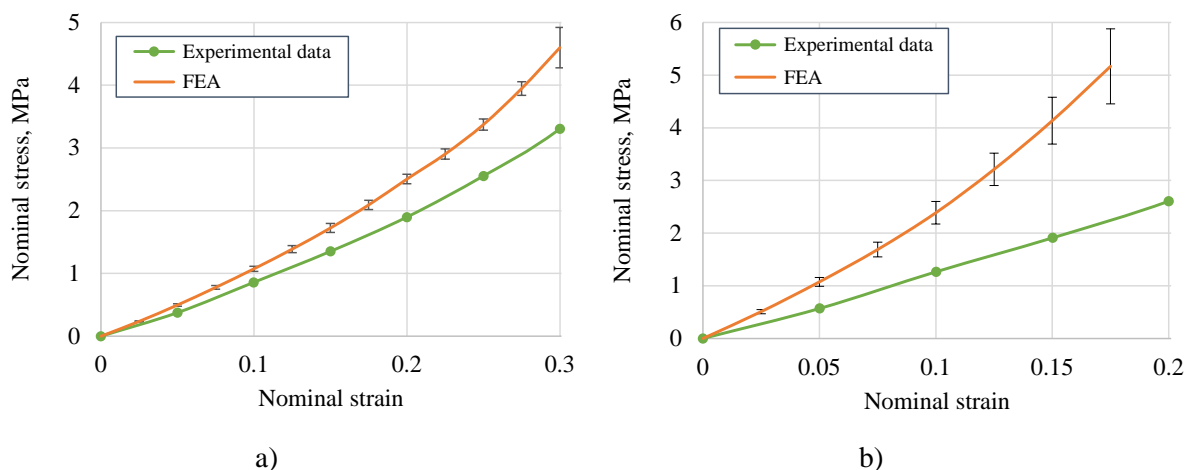


**Fig. 6.** Stress-strain diagrams at uniaxial compression of HNBR-ZrW<sub>2</sub>O<sub>8</sub> composites: FE analysis (FEA) and experimental data. The volume fractions of filler are 17.3% (a) and 35.8% (b).

## 5. Impact of particle-matrix interface on the effective mechanical properties

In the previous section, the matrix and particles are assumed to be perfectly bonded (i.e. the matrix and particles have shared nodes in the FE implementation). It might not be easy to achieve such conditions in real composites, if the interface is damaged at the production stage

or after pre-loading, especially to large deformations. It is well known, that the composite becomes softer when there is no adhesion between the matrix and its reinforcing particles. The interface, thus, plays a crucial role in the robustness of the final product. Therefore, this effect should be taken into account in large-strain applications.

Let us assume that adhesion is lost. To simulate the damaged interface, a contact interaction without friction between matrix and particles is applied. As in the previous section, compression in three orthogonal directions is modelled for various realizations of RVE with 17.3 and 35.8 vol.% of the filler inclusions. The deformed shapes of RVEs at various applied displacements are depicted in Fig. 7 and 8. It is clear, that the particles detach from matrix in the directions orthogonal to the compression direction manifesting voids occurring in the particle-matrix interfaces. The void growth progressively takes place with increasing longitudinal compressive deformation. Fig. 9 illustrates the results of FE simulations averaged over 3 simulation tests. Evidently, the FEA modelling results provide an interval which enclose the experimental data. Thus, it could be concluded, that the interface between particles and the matrix is partially damaged in the studied pre-loaded specimens which is manifested in a significant decrease of stiffness. For instance, the stress response in the composite with 35.8 vol.% of filler with intact interface subjected to the nominal compressive strain of 0.175 is about two times greater than that in the composite with a damaged interface. Comparison of experimental and modelling results shows that the level of interface damage depends on the volume fraction. For 17.3 vol.% of the filler, the experimental stress-strain curve is between the bounds given by FE simulations, while for 35.8 vol.%, experimental data are closer to the modelling results with no-adhesion. The point is that higher filler volume fraction leads to a higher stress level at particle-matrix interfaces, and, therefore, a higher damage level of the interfaces.

It should be noted that the performed FE simulation gives the lower and upper bounds for the effective finite-strain properties of the composite: the upper bound corresponds to a perfect particle-matrix interface is considered, while the damaged interface provides the lower bound. The proposed approach is important for the industrial applications of composites giving a range of the effective properties. Hence, the performance of composites could be analysed taking various levels of debonding into account. Note also, that estimation of the damage level in the composite (at least qualitatively) is possible if compare experimental results with the theoretical bounds of stiffness at finite strains with the ideal and fully damaged interfaces.

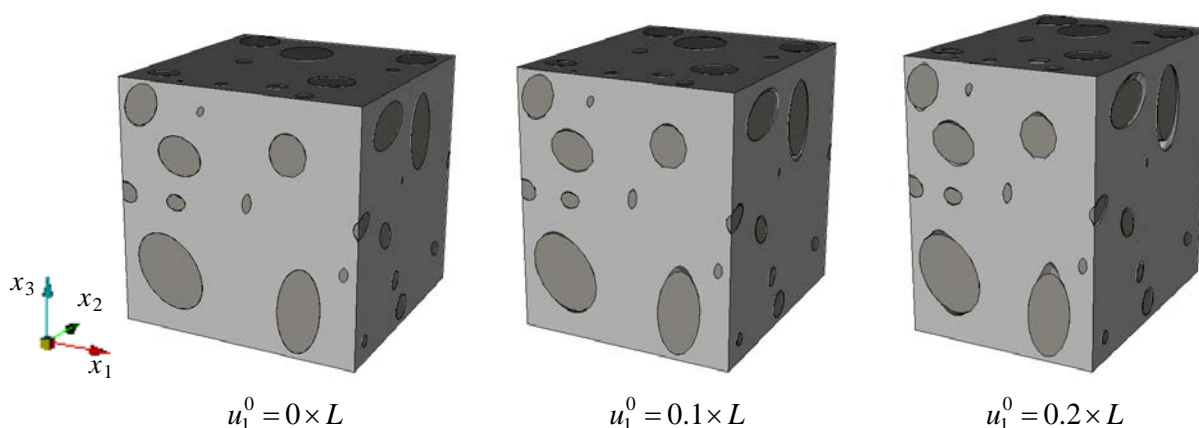


**Fig. 7.** The original and deformed shapes of RVE with 17.3 vol.% of filler due to uniaxial compression in  $x_1$  direction.

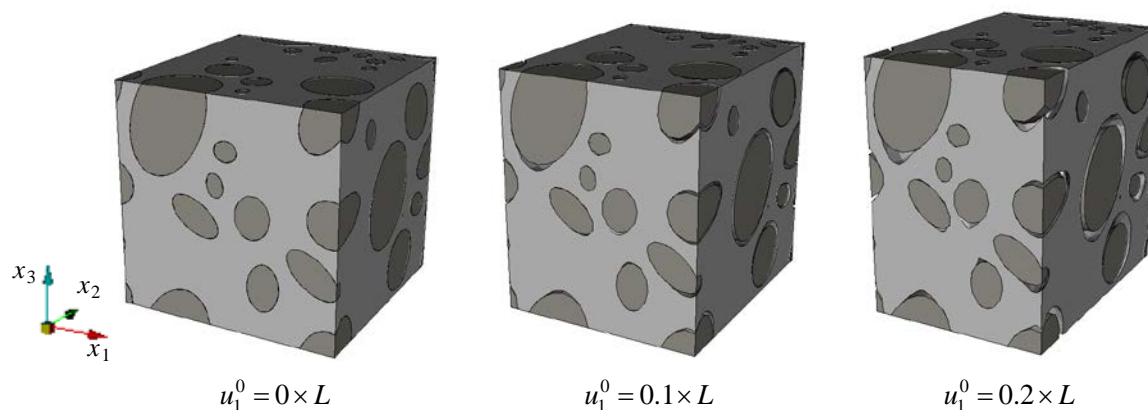


**Fig. 8.** The original and deformed shapes of RVE with 35.8 vol.% of filler due to uniaxial compression in  $x_1$  direction.

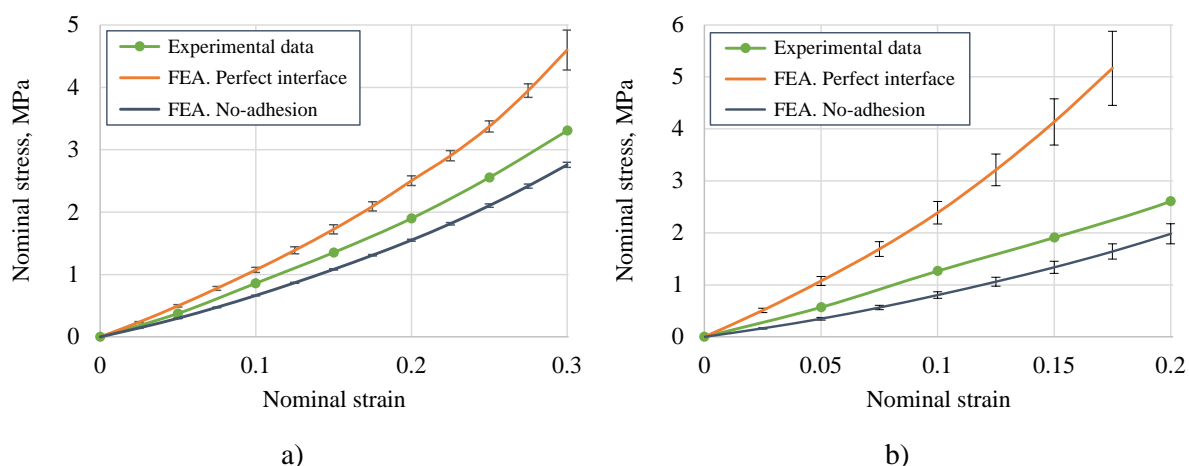


**Fig. 9.** Stress-strain diagrams at uniaxial compression of HNBR- $ZrW_2O_8$  composites: FE analyses (FEA) for two the types of interaction between matrix and particles (Perfect interface and No-adhesion) and experimental data (Test 1, 2). The volume fractions of filler are 17.3% (a) and 35.8% (b).

## 6. Summary and concluding remarks

The paper aims to study the mechanical behaviour of composites made of hydrogenated nitrile butadiene rubber (HNBR) and particles of zirconium tungstate  $ZrW_2O_8$  prepared with various tungstate volume fractions. Microstructure of the composites was studied by scanning electron microscope (SEM), and the particle shape parameter distributions were computed using optical analysis of the images of dispersed tungstate particles. The composites were subjected to cycling pre-loading to remove the Mullins effect prior to the main mechanical experiments.

The behaviour of the composites was studied at uniaxial compression experimentally and simulated by a micro-mechanical approach using finite element method (FEM). In the work, a novel algorithm for generation of representative volume element (RVE) with randomly-oriented ellipsoidal filler particles of high volume fraction was utilised. Based on measured size and aspect ratio distributions, three RVEs containing 100 randomly distributed ellipsoidal particles were generated for both 17.3% and 35.8% of filler volume fractions and further used in FE simulations. The non-linear stress-strain behaviour of HNBR was accurately reproduced by the Marlow model, while rigid particles were assumed linear elastic. Two limiting cases of a contact interaction between matrix and particles were considered: a perfect interface and the absence of the adhesive bonding between filler and matrix.

The investigation of the mechanical behaviour of the composites began with an

assumption that the interfacial layer between particles and matrix is intact. We showed that the FEM predictions of the effective stress-strain curves do not correspond to the experimental data for the composites: the FE simulations yield a stiffer response than the real composite material actually exhibits. We believed that the reason of the material softening is debonding of the filler inclusions from the matrix due to the cycling pre-loading performed before the uniaxial compression tests. As we had showed earlier [1], mechanical loading could lead to a large strain at the interface between particles and matrix, therefore the cycling loading could have damaged the interface. In order to verify this hypothesis, interaction between matrix and particles was changed to the “no-adhesion” condition. For this interaction model, FE simulation demonstrates a decrease of the effective stiffness of the composites. Two limiting cases of the interface modelling provide bounds for real effective properties of the composites at finite strains. It was also shown that the damage level increases with increasing filler volume fraction.

In the modelling approach, it was assumed that all particles are either perfectly interacted with the matrix or debonded from the matrix. For further investigation of the problem, it would be interesting to incorporate the cohesive-zone model [31, 32] to simulate the damage accumulation process in the filler-matrix interface with progressive deformation and also cycling loading. It should also be noted that the  $ZrW_2O_8$  particles used here are not pretreated, whereas surface modification of  $ZrW_2O_8$  has been reported [33, 34] to improve interaction with different polymer matrices. Therefore, it would be interesting to research the effect of a particle pretreatment on the mechanical properties and the degree of debonding at finite strains.

### Acknowledgements

*This work was supported in part by the Research Council of Norway (Project 234115 in the Petromaks2 programme). The first and third authors acknowledge the financial support from the Russian Foundation for Basic Research (Grant No. 16-01-00815). We thank Ben Alcock and Christelle Denonville at SINTEF Materials and Chemistry for the measurement of  $ZrW_2O_8$  particle size and circularity distribution.*

### References

- [1] S.N. Shubin, A.B. Freidin, A.G. Akulichev // *Archive of Applied Mechanics* **86** (2016) 351.
- [2] A.G. Akulichev, B. Alcock, A. Tiwari, A.T. Echtermeyer // *Journal of Materials Science* **51** (2016) 10714.
- [3] R.F. Robbins, Y. Ohori, D.H. Weitzel // *Rubber Chemistry and Technology* **37** (1964) 154.
- [4] A.G. Akulichev, A.T. Echtermeyer, B.N.J. Persson // *International Journal of Pressure Vessels and Piping* (2017). doi: 10.1016/j.ijpvp.2017.11.014
- [5] A.N. Gent, B. Park // *Journal of Materials Science* **19** (1984) 1974
- [6] P.A. Toulemonde, J. Diani, P. Gilormini // *Mechanics of Materials* **93** (2016) 124.
- [7] P. Gilormini, P.-A. Toulemonde, J. Diani // *Mechanics of Materials* **111** (2017) 57.
- [8] P.-A. Toulemonde et al. // *Journal of Materials Science* **52** (2017) 878.
- [9] A.P.S. Selvadurai // *Continuum Mechanics and Thermodynamics* **28** (2016) 617.
- [10] H.M. Inglis et al. // *Mechanics of materials* **39** (2007) 580.
- [11] X.A. Zhong, W.G. Knauss // *Journal of Engineering Materials and Technology* **119** (1997) 198.
- [12] J. Moraleda, J. Segurado, J. Llorca // *International Journal of Solids and Structures* **46** (2009) 4287.
- [13] L. Yang et al. // *Composites Science and Technology* **72** (2012) 1818.
- [14] P. A. Toulemonde et al. // *Matériaux et Techniques* **103** (2015) 306-1-7.
- [15] H. Arora et al. // *Computational Materials Science* **110** (2015) 91.
- [16] L. Riaño, L. Belec, Y. Joliff // *Composite Structures* **154** (2016) 11.
- [17] K. Matous, P.H. Geubelle // *Computer Methods in Applied Mechanics and Engineering*

- 196** (2006) 620.
- [18] K. Matous et al. // *Composites Science and Technology* **67** (2007) 1694.
- [19] D. Sodhani, S. Reese // *Macromolecules* **47** (2014) 3161.
- [20] D.W. Spring, G.H. Paulino // *Computational Materials Science* **109** (2015) 209.
- [21] Y. Cho et al. // *Materials* **10** (2017).
- [22] S.N. Shubin, A.B. Freidin // *PNRPU Mechanics Bulletin* **4** (2016) 317.
- [23] Abaqus, *Dassault Systemes Simulia Corporation* (Providence, RI, USA, 2012).
- [24] R.S. Marlow, In *Constitutive Models for Rubber III* (UK, AA Balkema Publishers, 2003), 157
- [25] A.G. Akulichhev, B. Alcock, A.T. Echtermeyer // *Polymer testing* **63** (2017) 226.
- [26] L. Mullins // *Rubber Chemistry and Technology* **42** (1969) 339.
- [27] R. Hill // *Journal of the Mechanics and Physics of Solids* **11** (1963) 357.
- [28] M. Kachanov, I. Sevostianov // *International Journal of Solids and Structures* **42** (2005) 309.
- [29] G.H. Hardy, A.P.V. Seshu, B.M. Wilson, *Collected papers of Srinivasa Ramanujan* (Cambridge University Press London, Fetter Lane, 1927).
- [30] F.R. Drymiotis et al. // *Physical Review Letters* **93** (2004) 059903.
- [31] K. Park, G.H. Paulino // *Applied Mechanics Review* **64** (2011) 060802-1.
- [32] D.W. Spring, O. Giraldo-Londono, G.H. Paulino // *Mechanics Research Communications* **78** (2016) 100.
- [33] C. Lind et al. // *Physica Status Solidi B* **1** (2011) 123.
- [34] L.M. Sullivan, C.M. Lukehart // *Chemistry of Materials* **17** (2005) 2136.

## FABRICATION OF P-TYPE TRANSPARENT OXIDE FILMS WITH DELAFOSSITE STRUCTURE BY SOL-GEL PROCESSING

E.V. Shirshneva-Vaschenko<sup>1\*</sup>, L.A. Sokura<sup>1,2</sup>, T.G. Liashenko<sup>1</sup>, E. Podlesnov<sup>1</sup>,

V.E. Bougrov<sup>1</sup>, A.E. Romanov<sup>1,2</sup>

<sup>1</sup>ITMO University, Kronverkskiy 49, Saint Petersburg, 197101, Russia

<sup>2</sup>Ioffe Institute, Polytechnicheskaya 26, Saint Petersburg, 194021, Russia

\*e-mail: ev.vaschenko@gmail.com

**Abstract.** CuAlO<sub>2</sub>, CuAl<sub>1-x</sub>Mg<sub>x</sub>O<sub>2</sub>, CuCrO<sub>2</sub>, CuCr<sub>1-x</sub>Mg<sub>x</sub>O<sub>2</sub> and CuAl<sub>0.5</sub>Cr<sub>0.5</sub>O<sub>2</sub> thin films were deposited on quartz substrates by sol-gel processing using spin coating technique. The elemental compositions, synthesis mechanisms, optical transmittance and resistivity of prepared films were studied. CuAl<sub>0.5</sub>Cr<sub>0.5</sub>O<sub>2</sub> films had the best characteristics under lower temperature of synthesis. Optical transmittance of CuAl<sub>0.5</sub>Cr<sub>0.5</sub>O<sub>2</sub> reached 70 % in visible region. The resistivity of CuAl<sub>0.5</sub>Cr<sub>0.5</sub>O<sub>2</sub> was 0,4 kΩ·cm and was stable with time. Thus, CuAl<sub>0.5</sub>Cr<sub>0.5</sub>O<sub>2</sub> films may have potential applications for transparent optoelectronics as p-conductivity transparent oxides.

**Keywords:** p-type transparent oxide films; quartz substrate; delafossite structure; sol-gel processing.

### 1. Introduction

Transparent conductive oxide films of n-type conductivity are widely used as transparent conductive electrodes in optoelectronic devices: LEDs, photodetectors, solar panels, to increase their productivity [1]. Nowadays, the industry of thin-film oxide films is focused on the development and production of thin-film materials of p-type conductivity. The preparation of p-type conductivity transparent films will significantly expand the boundaries of thin-film structures applications and lead to the development of "transparent" thin-film optoelectronics based on a transparent p-n heterojunction. Transparent oxide films of p-type conductivity have only recently attracted an attention of researchers due to the complex technology of such materials preparing. The interest in materials with the delafossite structure appeared after first p-type CuAlO<sub>2</sub> thin film was fabricated in 1997 [2, 3]. However, until now, in terms of their electrical characteristics, these films are inferior to the well-proven n-type thin oxide films, such as aluminum-doped zinc oxide (AZO) and indium-doped tin oxide (ITO) [4, 5]. Currently, the problem is to increase the conductivity of the p-type oxide films with decrease the cost of production technology owing to reducing process temperature. At present, the main methods for fabricating films of the delafossite structure are the pulsed laser deposition method, magnetron sputtering and electron beam sputtering [6, 7]. At the same time, the method of films preparing from solutions, namely the sol-gel method [8-14], could become an alternative competitive approach for the production of such materials.

In this paper, we describe the sol-gel processing of Cu (I) -based delafossite oxides on quartz substrates and comparison their optical and electrical characteristics.

## 2. Experimental and results

Different sol solutions were examined for each structure  $\text{CuAlO}_2$ ,  $\text{CuAl}_{1-x}\text{Mg}_x\text{O}_2$  ( $x=0.01$ ),  $\text{CuCrO}_2$ ,  $\text{CuCr}_{1-x}\text{Mg}_x\text{O}_2$  ( $x=0.05$ ) and  $\text{CuAl}_{0.5}\text{Cr}_{0.5}\text{O}_2$ . The molar ratio of Mg to Cu in each solution was determined by the  $x$  value and then the molar ratio of Al species was equal to the  $(1-x)$  value. To yield a homogeneous solution the prepared sol stirred at room temperature for 5 hours. The fused quartz plates with 15 mm in diameter were used as substrate. The film was deposited layer by layer on substrate at a speed of 4000 rpm for 20 s. Each layer was preheated for at to remove organic residues. Ten layers were deposited for each film. Finally, deposited films were annealed for several hours at 900-1150 °C in air or argon.

For  $\text{CuAlO}_2$  films precursor solution consisted of  $\text{Cu}(\text{CH}_3\text{COO})_2 \cdot \text{H}_2\text{O}$ ,  $\text{Al}(\text{NO}_3)_3 \cdot 9\text{H}_2\text{O}$ , 2-Methoxyetanol. The molar ratio of Cu/Al was 1.2:1. The concentration of solution was 0.4 M. The film was annealed in argon for 4 hours at 1200 °C. At annealing in air the phase  $\text{CuAlO}_2$  was not obtained.

For  $\text{CuAl}_{1-x}\text{Mg}_x\text{O}_2$  ( $x=0.01$ ) films the solution was prepared by dissolving mixtures of  $\text{Cu}(\text{CH}_3\text{COO})_2 \cdot \text{H}_2\text{O}$ ,  $\text{Al}(\text{NO}_3)_3 \cdot 9\text{H}_2\text{O}$ ,  $\text{Mg}(\text{NO}_3)_2 \cdot 6\text{H}_2\text{O}$  and isopropanol. The molar ratio of Cu/Al was 1:1. The concentration of solution was 0.2 M. The film was annealed in air for 4 hours at 1200 °C.

For  $\text{CuCrO}_2$  films the solution was prepared by dissolving mixtures of  $\text{Cu}(\text{CH}_3\text{COO})_2 \cdot \text{H}_2\text{O}$ ,  $\text{Cr}(\text{NO}_3)_3 \cdot 9\text{H}_2\text{O}$ , 2-Methoxyetanol. The molar ratio of Cu/Cr was 1:1. The concentration of solution was 0.2 M. The film was annealed in air for 1 hours at 1000 °C.

For  $\text{CuCr}_{1-x}\text{Mg}_x\text{O}_2$  films the solution was prepared by dissolving mixtures of  $\text{Cu}(\text{CH}_3\text{COO})_2 \cdot \text{H}_2\text{O} + \text{Cr}(\text{NO}_3)_3 \cdot 9\text{H}_2\text{O} + \text{Mg}(\text{NO}_3)_2 \cdot 6\text{H}_2\text{O} + 2$ -Methoxyetanol. The molar ratio of Cu/Cr was 1:1. The concentration of solution was 0.2 M. The film was annealed in air for 1 hours at 1000 °C.

For  $\text{CuAl}_{0.5}\text{Cr}_{0.5}\text{O}_2$  films precursor solution consisted of  $\text{Cu}(\text{CH}_3\text{COO})_2 \cdot \text{H}_2\text{O} + \text{Al}(\text{NO}_3)_3 \cdot 9\text{H}_2\text{O} + \text{Cr}(\text{NO}_3)_3 \cdot 9\text{H}_2\text{O}$ . The molar ratio of Cu/Al/Cr was 1:0.5:0.5. The concentration of solution was 0.2 M. The film was annealed in air for 1 hours at 1000 °C.

The thickness of one deposited layer was 20-40 nm. The total thickness of films was 0,2-0,4  $\mu\text{m}$ .

The electrical resistivity of films was measured by 4-probe method with used source meter Keithley 2450. Optical absorption measurements of films were performed with fiber spectrometer AvaSpec-2048.

Figs. 1-5 illustrate the transmittance of  $\text{CuAlO}_2$  (S1),  $\text{CuAl}_{1-x}\text{Mg}_x\text{O}_2$  ( $x=0.01$ ) (S2),  $\text{CuCrO}_2$  (S3),  $\text{CuCr}_{1-x}\text{Mg}_x\text{O}_2$  ( $x=0.05$ ) (S4) and  $\text{CuAl}_{0.5}\text{Cr}_{0.5}\text{O}_2$  (S5) thin films in the range 300-1200 nm.

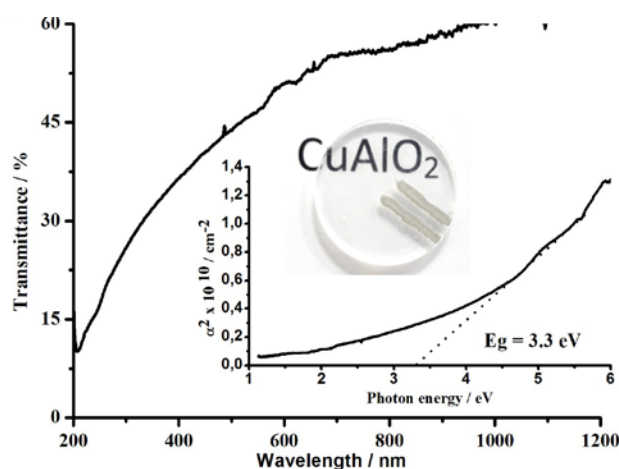


**Fig. 1.** Optical transmittance of  $\text{CuAlO}_2$  (S1). The insets show the  $\text{CuAlO}_2$  optical band gaps calculated by Tauc's relation.

The average transmittance of the samples S1, S2, S3, S4 and S5 at 400-800 nm were 41 %, 50 %, 36 %, 26 %, and 53 %, respectively.

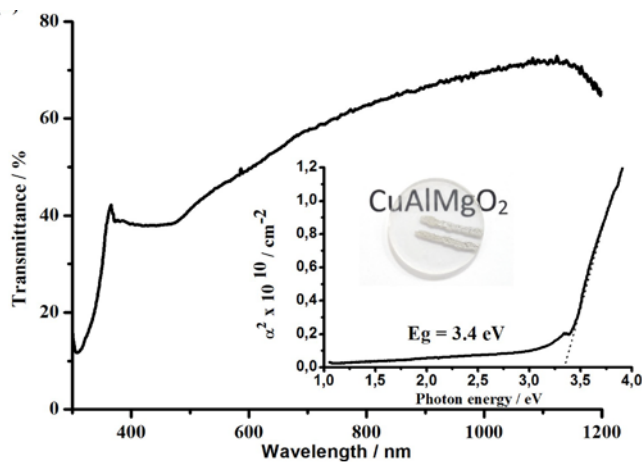


**Fig. 2.** Optical transmittance of CuAl<sub>1-x</sub>Mg<sub>x</sub>O<sub>2</sub> (x=0.01) (S2). The insets show the CuAl<sub>1-x</sub>Mg<sub>x</sub>O<sub>2</sub> (x=0.01) optical band gaps calculated by Tauc's relation.

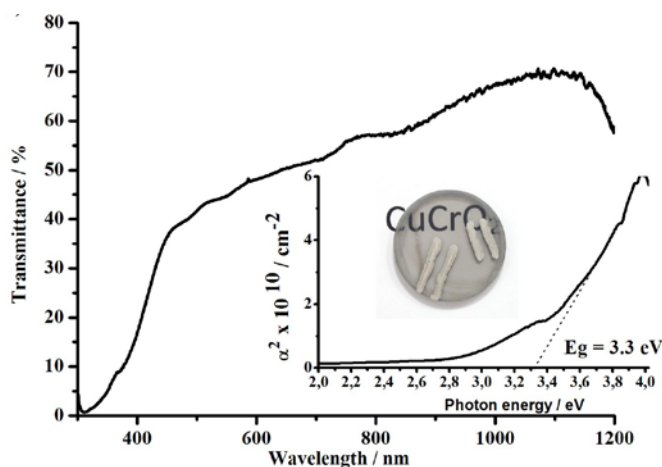


**Fig. 3.** Optical transmittance of CuCrO<sub>2</sub> (S3). The insets show the CuCrO<sub>2</sub> optical band gaps calculated by Tauc's relation.

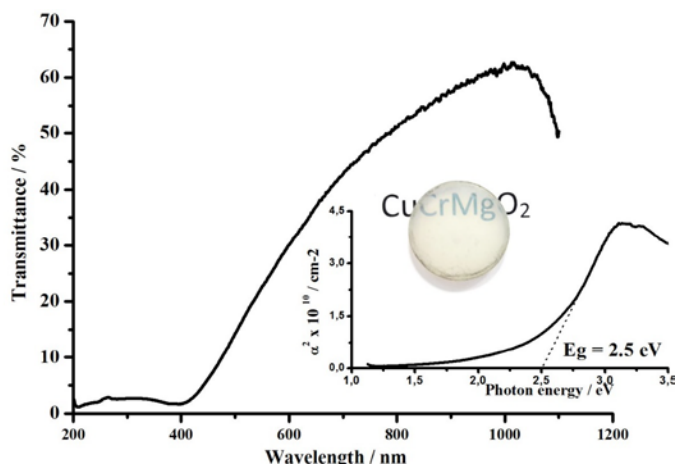


**Fig. 4.** Optical transmittance of CuCr<sub>1-x</sub>Mg<sub>x</sub>O<sub>2</sub> (x=0.05) (S4). The insets show the CuCr<sub>1-x</sub>Mg<sub>x</sub>O<sub>2</sub> optical band gaps calculated by Tauc's relation.

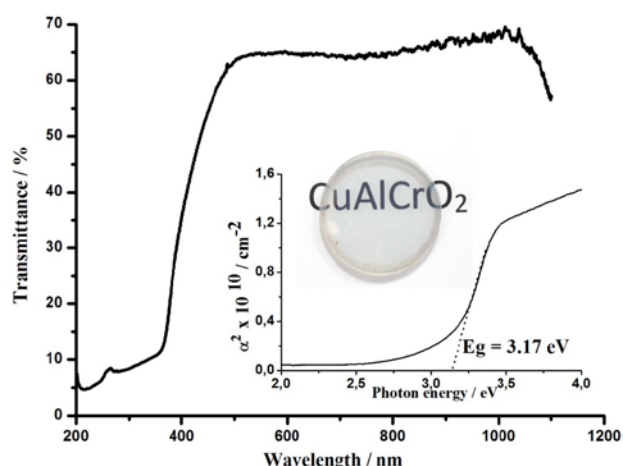


**Fig. 5.** Optical transmittance of  $\text{CuAl}_{0.5}\text{Cr}_{0.5}\text{O}_2$  (S5). The insets show the  $\text{CuAl}_{0.5}\text{Cr}_{0.5}\text{O}_2$  optical band gaps calculated by Tauc's relation.

The optical band gap was estimated by the Tauc's relation [15], expressed as

$$\alpha h\nu^n = A(h\nu - E_g^{\text{opt}}), \quad (1)$$

where  $A$  is a constant,  $E_g^{\text{opt}}$  is the band gap of the films,  $h\nu$  is the photon energy,  $\alpha$  is the absorption coefficient. For a direct allowed transition,  $n$  is 2.

As shown in Fig. 1-5 (insets), for the direct transition, optical band gap of the samples S1, S2, S3, S4 and S5 were 3,3 eV, 3,4 eV, 3,3 eV, 2,5 eV, 3,17 eV, respectively.

The electrical resistivity of the films S1, S2, S3, S4 and S5 were 9  $\text{k}\Omega\cdot\text{cm}$ , 1.8  $\text{k}\Omega\cdot\text{cm}$ , 0.8  $\text{k}\Omega\cdot\text{cm}$ , 0.4  $\text{k}\Omega\cdot\text{cm}$  and 0.4  $\text{k}\Omega\cdot\text{cm}$ , respectively.

### 3. Conclusions

We deposited  $\text{CuAlO}_2$ ,  $\text{CuAl}_{1-x}\text{Mg}_x\text{O}_2$ ,  $\text{CuCrO}_2$ ,  $\text{CuCr}_{1-x}\text{Mg}_x\text{O}_2$  and  $\text{CuAl}_{0.5}\text{Cr}_{0.5}\text{O}_2$  thin films on quartz substrates by sol-gel processing using spin coating technique. Prepared films had high optical transmittance comparable to films prepared by other physics methods. Optical transmittance of  $\text{CuAlO}_2$  and  $\text{CuAl}_{1-x}\text{Mg}_x\text{O}_2$  films reached 60-75 % in visible region. The average transmittance for these films at 400-800 nm was 50 % and 41 %, respectively. The resistivity of  $\text{CuAlO}_2$  and  $\text{CuAl}_{1-x}\text{Mg}_x\text{O}_2$  were 9  $\text{k}\Omega\cdot\text{cm}$  and 1.8  $\text{k}\Omega\cdot\text{cm}$ , respectively. The resistivity of  $\text{CuAlO}_2$ ,  $\text{CuAl}_{1-x}\text{Mg}_x\text{O}_2$  films increased with time. The optical transmittance of  $\text{CuCrO}_2$ ,  $\text{CuCr}_{1-x}\text{Mg}_x\text{O}_2$  films was lower  $\sim$  30-40%, when resistivity was 0,8  $\text{k}\Omega\cdot\text{cm}$  and 0,4  $\text{k}\Omega\cdot\text{cm}$ , respectively. Resistivity measurements showed that doping of pure  $\text{CuAlO}_2$  and  $\text{CuCrO}_2$  was helpful in increasing conductivity of the films.  $\text{CuAl}_{0.5}\text{Cr}_{0.5}\text{O}_2$  films had the best characteristics under lower temperature of synthesis. The resistivity of  $\text{CuAl}_{0.5}\text{Cr}_{0.5}\text{O}_2$  was 0,4  $\text{k}\Omega\cdot\text{cm}$  and optical transmittance reached 70 %. The resistivity of  $\text{CuCrO}_2$ ,  $\text{CuCr}_{1-x}\text{Mg}_x\text{O}_2$ ,  $\text{CuAl}_{0.5}\text{Cr}_{0.5}\text{O}_2$  films was stable with time. Followed on from the results we suggested that  $\text{CuAl}_{0.5}\text{Cr}_{0.5}\text{O}_2$  films could be considered as perspective candidates for p-type transparent conductive oxides with the lowest resistivity 0.4  $\text{k}\Omega\cdot\text{cm}$  and the highest transmittance under lower temperature of synthesis.

**Acknowledgements.** This work was supported by the Ministry of Education and Science of the Russian Federation in the framework of the Federal Target Program "Research and development on priority directions of a scientific-technological complex of Russia for 2014-2020", the code 2017-14-576-0003, agreement № 14.575.21.0127 of September 26, 2017, unique ID RFMEFI57517X0127.

**References**

- [1] T. Kawashima, T. Ezure, K. Okada, H. Matsui, K. Goto, N. Tanabe // *Journal of Photochemistry and Photobiology A: Chemistry* **164** (2004) 199.
- [2] H. Kawazoe, M. Yasukawa, H. Hyodo, M. Kurita, H. Yanagi, H. Hosono // *Nature* **389** (1997) 939.
- [3] H. Yanagi, S.-I. Inoue, K. Ueda, H. Kawazoe, H. Hosono, N. Hamada // *Journal of Applied Physics* **88** (2000) 4159.
- [4] J.J. Valenzuela-Jauregui, R. Quintero-Gonzalez, J. Hernandez-Torres, A. Mendoza-Galvan, R. Ramirez-Bon // *Vacuum* **76** (2004) 177.
- [5] E.P. Zaretskaya, V.F. Gremenok, A.V. Semchenko, V.V. Sidsky, R.L. Juskenas // *Semiconductors* **49** (2015) 1253.
- [6] Y. Kakehi, K. Satoh, T. Yotsuya, S. Nakao, T. Yoshimura, A. Ashida, N. Fujimura // *Journal of Applied Physics* **97** (2005) 083535.
- [7] H. Yanagi, T. Hase, S. Ibuki, K. Ueda, H. Hosono // *Applied Physics Letters* **78** (2001) 1583.
- [8] M.J. Han, Z.H. Duan, J.Z. Zhang, S. Zhang, Y.W. Li, Z. G. Hu, J.H. Chu // *Journal of Applied Physics* **114** (2013) 163526.
- [9] G. Li, X. Zhu, H. Lei, H. Jiang, W. Song, Zh. Yang, J. Dai, Y. Sun, X. Pan, S. Dai // *Journal of Sol-Gel Science and Technology* **53** (2010) 641.
- [10] T. Ehara, T. Nakanishi // *MATEC Web Conference* **67** (2016) 04012.
- [11] K. Tonooka, K. Shimokawa, O. Nishimura // *Thin Solid Films* **411** (2002) 129.
- [12] H.F. Jiang, X.B. Zhu, H.C. Lei, G. Li, Z.R. Yang, W.H. Song, J.M. Dai, Y.P. Sun, Y.K. Fuc // *Journal of Alloys and Compounds* **509** (2011) 1768.
- [13] Y. Wang, Y. Gu, T. Wang, W. Shi // *Journal of Alloys and Compounds* **509** (2011) 5897.
- [14] S. Götzendörfer, R. Bywalez, P. Löbmann // *Journal of Sol-Gel Science and Technology* **52** (2009) 113.
- [15] J. Tauc, A. Menth // *Journal of Non-Crystalline Solids* **8** (1972) 569.

# APPLICATION OF QUANTUM-CHEMICAL MODELING RESULTS IN EXPERIMENTAL INVESTIGATIONS OF SILICONE COMPOSITES

H.H. Valiev<sup>1\*</sup>, V.V. Vorobyev<sup>2</sup>, Yu.N. Karnet<sup>1</sup>, Yu.V. Kornev<sup>1</sup>, O.B. Yumashev<sup>1</sup>

<sup>1</sup> Foundation Russian Academy of Sciences, Institute of Applied Mechanics RAS, Moscow, Russia

<sup>2</sup> Interdisciplinary Center "Analytical Microscopy" KFU, Kazan, Russia

\*e-mail: hhvlv@mail.ru

**Abstract.** The results of direct numerical simulation obtained earlier, within the cluster quantum-chemical approximation, are used in experimental investigations of polydimethylsiloxane composites with shungit. The surface structure of these composites by scanning electron and atomic force microscopy was studied. Correlation of the distribution of micro and nano - dimensional filler in the polymer matrix with the physical mechanical properties of the elastomers was established.

**Keywords:** polydimethylsiloxane composites, nanoshungit filler, scanning electron and atomic force microscopy.

## 1. Introduction

The problems of increasing the strength of polymer materials are important for both fundamental science and applied research. For example, the polydimethylsiloxanes as representative of organosilicon polymers are of the great importance in industry. However, they have low mechanical strength. Increasing the resistance to fracture of these polymers is usually achieved with fillers [1]. Therefore, it is necessary to study new reinforcing substances from disperse fillers of various nature.

Of great interest in this respect is the use of shungit, natural composite, consisting of silica, dispersed in matrices of amorphous carbon [2]. There seems advisable preliminary to perform the molecular computational modeling, which is an effective method of a virtual analysis of the structural, energetic and micromechanical properties of micro and nanocomposites.

As reported in [3], the energetic and structural characteristics of elastomer complexes with shungit have been calculated quantum - chemically under developed NDDO / sp-sp<sup>2</sup> semiempirical original program [4]. Numerical calculations on the supercomputer MBC-5000 in the Interdepartmental Supercomputer Center were performed. The microscopic characteristics of nanomechanical behavior, deformation and fracture characteristics of shungit adsorbates with polyisoprene during uniaxial tension based on this program in the cluster approximation were examined. It was deduced, that one can expect a substantial reinforcement for such composites.

As reported in [5], the quantum - chemical studies of deformation in polydimethylsiloxane oligomer molecules in contact with the particles of silicates predict strong interactions between these components.

The results of these calculations were used by us in the practical synthesis of siloxane composites with shungit. It has also been developed the multistage physical chemical

modification technology for obtaining the active nanostructured schungit filler for rubbers, based on these quantum chemical calculations.

According to the results of [6] there is an increase in the tear resistance and in the specific work of the deformation during fracture, with preservation of the increased strength properties of synthetic thermally stable low-molecular-weight silicone elastomers based on SCTN-A, filled with micro and nanoscale schungit.

To further elucidate the nature of the onset of strengthening effects, knowledge of the distribution of fillers in these elastomeric matrices is necessary. The surface structure of these composites, using electron and atomic force microscopy, in the present paper was studied.

## 2. Experimental procedures and materials

As a filler of elastomers, a natural schungit mineral was used (Zazhoginsky deposit, Carbon-Schungite Trade Ltd, Karelia, Russia). The rock is a natural composite, in the carbon matrix of which are distributed highly dispersed silicate particles and small amounts of other oxides. The chemical composition of schungit used in this work is shown in Table 1.

Table 1. Chemical composition of schungit (%) [2].

| SiO <sub>2</sub> | TiO <sub>2</sub> | Al <sub>2</sub> O <sub>3</sub> | FeO | MgO | CaO | Na <sub>2</sub> O | K <sub>2</sub> O | S   | C    | H <sub>2</sub> O <sub>cryst</sub> |
|------------------|------------------|--------------------------------|-----|-----|-----|-------------------|------------------|-----|------|-----------------------------------|
| 57.0             | 0.2              | 4.0                            | 2.5 | 1.2 | 0.3 | 0.2               | 1.5              | 1.2 | 29.0 | 4.2                               |

As the basis of the composite matrix, silicone low-molecular rubbers SKTN-A were chosen. Filler was both the original schungit and the grounded one in a ball planetary mill PM100 (Retsch, Germany) under different environments. The introduction and dispersion of the filler and the mixing of all the ingredients were carried out in a laboratory mixer [6]. Table 2 shows the compositions of the samples studied.

Table 2. Composition of the synthesized samples.

| Ingredients name    | Code of mixture |      |      |      |      |      |      |      |      |
|---------------------|-----------------|------|------|------|------|------|------|------|------|
|                     | C300            | C301 | C302 | C303 | C304 | C305 | C306 | C307 | C308 |
|                     | %               |      |      |      |      |      |      |      |      |
| SKTN-A rubber       | 100             | 90   | 80   | 70   | 60   | 90   | 80   | 70   | 60   |
| Schungit (original) |                 | 10   | 20   | 30   | 40   |      |      |      |      |
| Schungit (grounded) |                 |      |      |      |      | 10   | 20   | 30   | 40   |
| Total               | 100             | 100  | 100  | 100  | 100  | 100  | 100  | 100  | 100  |

The fillers were added to the SKTN-A rubber according to the compositions given in Table. 2, kneaded by hand, and then passed through rolls. The resulting mixtures were evacuated for 15 minutes, and then a catalyst was introduced with a certain concentration for each composition and again evacuated. The samples were placed in teflon forms and cured.

The Scanning Electron Microscope (SEM) Merlin (Carl Zeiss, Germany) worked with an accelerating voltage of 5 kV and beam current of 300 pA.

The atomic-force microscope (AFM) easyScan (Nanosurf, Switzerland), operating in a contact mode at ambient conditions, using also the force modulation mode, or in the semi-contact mode with the phase contrast mode, were used. In a semi-contact mode, a SuperSharpSilicon probe (Nanosensors, Switzerland) with a tip radius of about 2 nm was used. Image processing was performed using the SPIP™ - advanced software package for processing and analyzing microscopy images at nano- and microscale (Image Metrology, Denmark).

Investigations of the physical mechanical properties of the composites were conducted [6] on universal testing machine UTS-10 (Ulm, Germany).

### 3. Experimental results

Initially shungit samples, after deposition on the surface of highly oriented pyrolytic graphite (HOPG) from a suspension in toluene, were tested by AFM. The AFM topography images of shungit powders on the HOPG surface and phase contrast images established the particle sizes of the original shungit in the range from 1 to 5  $\mu\text{m}$  and the grounded powders in the range from 70 to 250 nm. Examples of AFM scans on the synthesized composites from the table 2 are shown in figure 1 - 2. The AFM surface images of pure SCTN-A rubber are presented in Fig. 1 and AFM surface images of C 308 composite - in Fig. 2. The distribution and sizes of shungit fillers, presented as bright dots in the background of polymeric matrix, clearly are visualized in right images of material contrast Fig. 2.

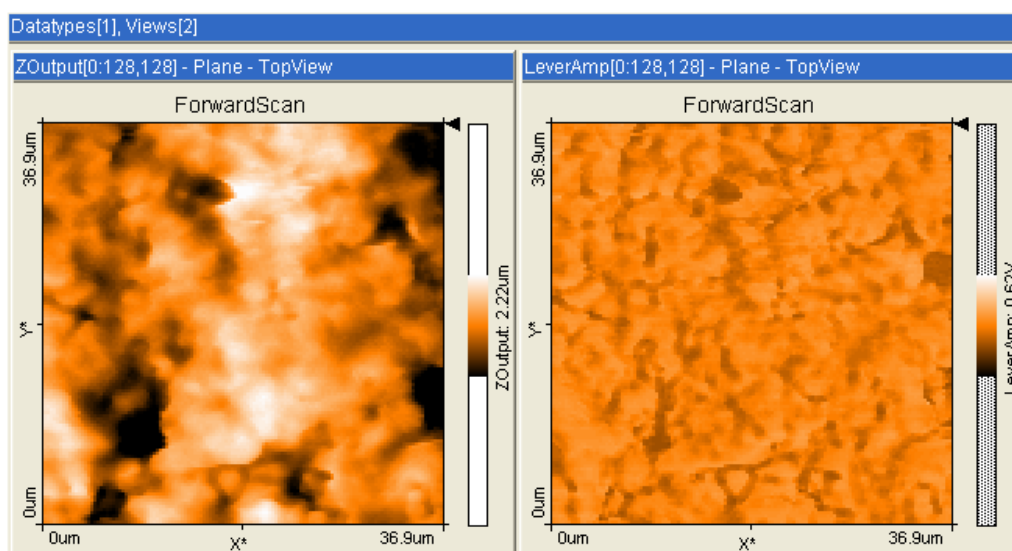


**Fig. 1.** AFM surface images of pure SCTN-A rubber  
Scans  $36.9 \times 36.9 \mu\text{m}^2$ . Left - topography, right – material contrast.

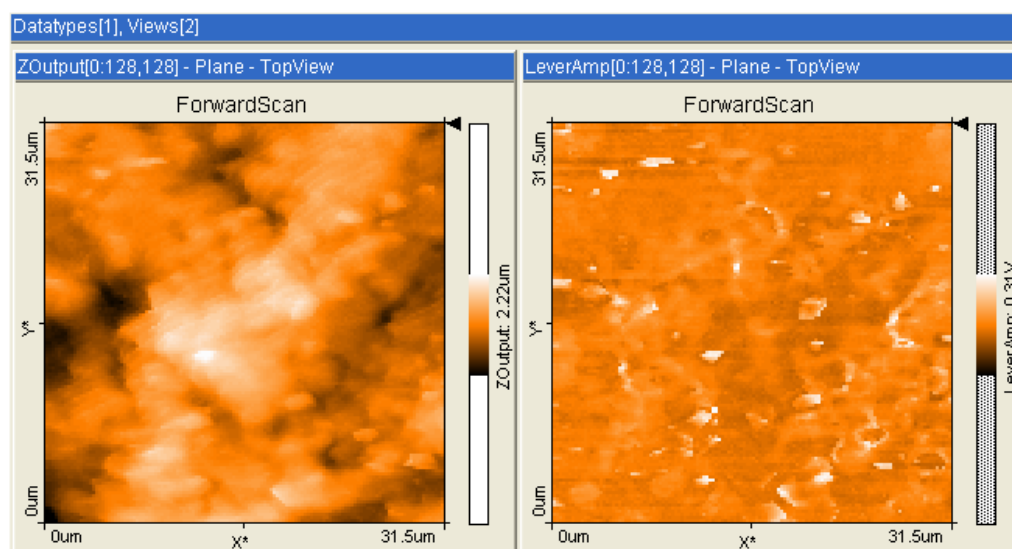


**Fig. 2.** AFM surface images of C 308 composite (b).  
Scans  $31.5 \times 31.5 \mu\text{m}^2$ . Left - topography, right – material contrast.

The AFM images data processing showed that the aggregate sizes of these nanostructured schungit filler in composite C 308 are located in the range 50 nm to 2  $\mu\text{m}$ , and the nearest distances between them on the average in 300 nm.

Electron microscopic photographs of the C 308 composite are shown in Fig. 3a, b. The SEM surface topography C 308 composite, prepared in the form of plate, is presented in Fig. 3a and SEM images of its perpendicular cross – section in Fig. 3b.

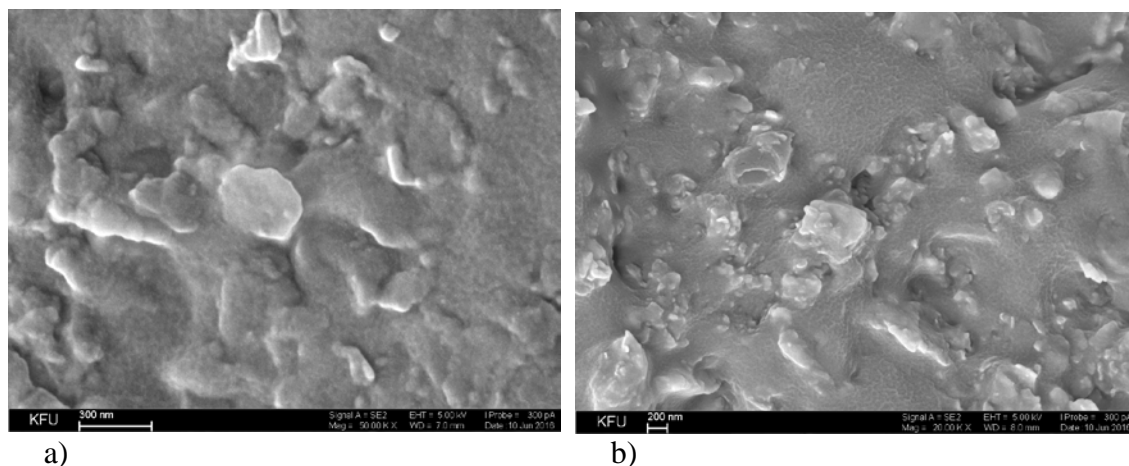


**Fig. 3.** SEM images of the top surface topography plate C 308 composite (a) and of the plate perpendicular cross – section (b).  
Unite scales: 300 and 200 nm respectively.

These SEM images shows the same approximate values of filler aggregate sizes as deduced from AFM measurements, and additionally visualize the space arrangement of fillers in the elastomer matrix. The application of SEM and AFM methods to visualize topography of surfaces and sections of investigated silicone rubber composites with schungit fillers allowed direct observation of changes in the structure of composite elastomers on the micro and nanometer range with increasing concentrations of reinforcing fillers.

#### 4. Discussions

Correlation these results with the physical mechanical properties of these materials, studied in [6], makes it possible to understand the cause of the enhancing ability of nanostructured schungit in organosilicon elastomers, as due to the formation of a spatial filler network in the polymer matrix. These data make it possible to understand the reasons for the shungit filler manifestation of the reinforcing properties in the SKTN-A rubber, as conditioned not only by the chemical affinity of the amorphous carbon and the silica with the polydimethylsiloxane matrix, but also by a fairly uniform spatial distribution of the filler in the composite. The role of polar hydroxyl groups (OH) bound to silica part of the shungit (silanol groups) interacting with siloxane segments (Si - O - Si) of matrix is also important, because the formed complex prevent the macroscopic agglomeration of initial schungit particles during introduction to the polymer. The resulting increase in the interaction surface of the nanostructured filler with the polymer macromolecules leads to an effective reinforcement of the initial polydimethylsiloxane matrix. As reported in [6] the tests of these composites on a machine UTS-10 showed an increase in the tensile strength from about 0.5 MPa in pure SCTN-A rubber to 3.6 MPa in C 308 composite and tear resistance from 1.3 kN / m to 7.0 kN / m, respectively. It was also showed that C 308 composite is comparable in the maximum value of the specific work deformation for destruction with well known silicon composite reinforced by silica. These results, when compared with traditional silicon dioxide filler [1, 6], show good effectiveness of the present nanostructured shungit as reinforcement filler in polydimethylsiloxane. The

experimental verifications about theoretical predictions that nano shungit may be active also in the reinforcement of butadiene - styrene rubbers was shown in [7].

## 5. Conclusions

The application of SEM and AFM methods to visualize topography of surfaces and sections of investigated silicone rubber composites with schungit fillers allowed direct observation of changes in the internal structure of composite elastomers in the micro and nanometer range. The correlation these results with the physical mechanical properties of the composites is important for the development the basic principles of reinforcement material strengths. The preliminary direct numerical calculations within the framework of the cluster quantum-chemical approximation [3 - 5] of the shungit nanostructure and its components, predicting the effectiveness of its use as filler in elastomers proved to be valuable for conducting these experiments. The presented experimental results show both theoretical and practical significance of the quantum - chemical approach proposed in [3 - 5] for computer selection of components in elastomeric composites and ways of modifying their fillers in order to predict the technologies for obtaining materials with improved strength characteristics. This developed computational technique can be applied in similar problems of designing new advanced materials.

## References

- [1] J.E. Mark, D.W. Schaefer, Gui Lin, *The Polysiloxane* (Oxford University Press, USA, 2015).
- [2] M.M. Filippov, A.I. Golubev, P.V. Medvedev, *Organic matter of schungite-bearing rocks of Karelia: genesis, evolution, methods of study* (Petrozavodsk, Karelian Research Center, RAS, 1994).
- [3] Yu.G. Yanovsky, N.N. Myagkov, E.A. Nikitina, Yu.N. Karnet, H.H. Valiev, V.A. Zhogin, Yu.A. Gamlitsky // *Mechanics of composite materials and structures* **12** (2006) 513.
- [4] The software component NDDO / sp-spd of high-precision semi-empirical calculations in SP- and SPD-bases, which includes a set of programs for obtaining structural, electronic, energy, deformation and spectroscopic characteristics of atomic-molecular systems up to 1000 atoms. // *Certificate of state registration of the computer program No. 209614949*. (2009).
- [5] Yu.G. Yanovsky, E.A. Nikitina, A.V. Teplukhin, Yu.A. Basistov, P.A. Filipenkov, Yu.N. Karnet // *Physical mesomechanics* **6** (2003) 129.
- [6] Yu.V. Kornev, S.V. Chirkunova, O.V. Boyko, M.Ya. Simonova, V.O. Shugaeva, Yu.G. Yanovsky // *Kauchuk and Rubber* **6** (2012) 10.
- [7] H.H. Valiev, Yu.N. Karnet, N.L. Kochurov, M.S. Parshina, N.A. Semenov, O.B. Yumashev, Yu.G. Yanovsky // *Materials Physics and Mechanics* **26** (2016) 45.

# EXPERIMENTAL VERIFICATION OF POSTULATE OF ISOTROPY AND MATHEMATICAL MODELING OF ELASTOPLASTIC DEFORMATION PROCESSES FOLLOWING THE COMPLEX ANGLED NONANALYTIC TRAJECTORIES

V.G. Zubchaninov<sup>1</sup>, A.A. Alekseev<sup>1\*</sup>, E.G. Alekseeva<sup>2</sup>, V.I. Gultiaev<sup>1</sup>

<sup>1</sup>Tver State Technical University, nab. Afanasiya Nikitina, 22, Tver, 170026, Russia

<sup>2</sup>Bauman Moscow State Technical University, ul. Baumanskaya 2-ya, 5/1, Moscow, 105005, Russia

\*e-mail: alexeev@bk.ru

**Abstract.** The results of numerical simulation for 45 steel deformation with the use of general and linearized models of the theory of processes along flat smooth trajectories with curvilinear sectors are presented. The results of calculation are compared with the data of thin-walled cylindrical specimen deformation experiment, carried out on SN-EVM testing complex. It is shown that for the realized types of experimental trajectories symmetric with respect to the bisector of a right angle Ilyushin's postulate of isotropy is fulfilled in the proper way.

**Keywords:** elastoplastic deformation; postulate of isotropy; numerical simulation.

## 1. Introduction

Systematic tests on metals and alloys mechanical behavior behind elastic limit at the deflected mode were conducted to verify key provisions and a reasonable creation of elastoplastic deformation mathematical models of materials [1-10]. A. A. Ilyushin's postulate of isotropy [11-12] is one of the most important laws of the theory of elastoplastic processes, it was checked by many researchers for different materials on different trajectories [8-11]. In particular, in [10] trajectories, considered to be smooth on A. A. Ilyushin terminology [11], are symmetric relatively bisectors of the right angle. On the first sites of flat trajectories [10] deformation on the quarter of circle was realized, and then the trajectory without break, but with curvature change, passed into straight section. In the work verification of reliability of A. A. Ilyushin's postulate of isotropy and results of mathematical modeling is considered at complex deformation on the flat nonanalytic trajectories having the curvilinear site and point of break.

## 2. Main equations

In the linear-combined space  $E_6$  of tension and deformations with orthonormalized basis  $\{\hat{i}_k\}$  stress tensors  $\sigma_{ij}$  and deformations  $\varepsilon_{ij}$

$$\sigma_{ij} = \sigma_0 \delta_{ij} + S_{ij}, \quad \sigma_0 = \sigma_{ij} \delta_{ij} / 3, \quad \varepsilon_{ij} = \varepsilon_0 \delta_{ij} + \mathcal{E}_{ij}, \quad \varepsilon_0 = \varepsilon_{ij} \delta_{ij} / 3 \quad (1)$$

vectors are put in compliance

$$\bar{S} = S_0 \hat{i}_0 + \bar{\sigma}, \quad \bar{\sigma} = S_k \hat{i}_k, \quad \bar{\varepsilon} = \mathcal{E}_0 \hat{i}_0 + \bar{\mathcal{E}}, \quad \bar{\mathcal{E}} = \mathcal{E}_k \hat{i}_k, \quad (k = 1, 2, \dots, 5), \quad (2)$$

where coordinates of vectors  $S_k$ ,  $\mathcal{D}_k$  are connected with components of tensors  $\sigma_{ij}$ ,  $\varepsilon_{ij}$  and deviators  $S_{ij}$ ,  $\mathcal{D}_{ij}$  tension, and deformations, by the known biunique transformations [1, 2]. Volumetric strain in  $E_6$  is supposed elastic according to the law of elastic change of the volume  $\sigma_0 = 3K\varepsilon_0$ , where  $K$  is the modulus of volume elasticity.

According to A. A. Ilyushin's postulate of isotropy, vectors of tension  $\bar{\sigma}$  and deformations  $\bar{\mathcal{D}}$  of forming are connected by the defining ratios [1, 2]

$$\frac{d\bar{\sigma}}{ds} = M_1 \frac{d\bar{\mathcal{D}}}{ds} + \left( \frac{d\sigma}{ds} - M_1 \cos \vartheta_1 \right) \frac{\bar{\sigma}}{\sigma}, \quad \frac{d\vartheta_1}{ds} + \kappa_1 = -\frac{M_1}{\sigma} \sin \vartheta_1, \quad (3)$$

where,  $M_1$ ,  $\frac{d\sigma}{ds}$  is the functionalities of the process of deformation depending on parameters of complex loading:  $s$  is lengths of the arc of the trajectory of deformation, its curvature  $\kappa_1$ , and corners of break  $\vartheta_1^0$ . The approach angle  $\vartheta_1$  characterizes the direction of the vector  $\bar{\sigma}$  in relation to the tangent to deformation trajectory in each its point and reflects the influence on the process of deformation of vector material properties.

**General mathematical model of the theory of processes.** For the case of flat trajectories ( $\vartheta_2 = 0$ ,  $\kappa_2 = 0$ ) the defining ratios can be given to the system of the equations of the task of Cauchy in the scalar form [1]:

$$\begin{cases} \frac{dS_k}{ds} = M_1 \frac{d\mathcal{D}_k}{ds} + M \frac{S_k}{\sigma}, & (k=1, 3), \\ \frac{d\vartheta_1}{ds} + \kappa_1 = -\frac{M_1}{\sigma} \sin \vartheta_1, \end{cases} \quad (4)$$

for which solution in work the numerical method of Runge-Kutta of the fourth order of accuracy in the realized application for the system of computer mathematics MATLAB was used.

At the numerical solution of system (4), V. G. Zubchaninov's universal approximations of functionalities were used [1, 2]

$$M_1 = 2G_p + (2G - 2G_p^0) f^q e^{-\gamma_1 \Delta s}, \quad M = \frac{d\sigma}{ds} - M_1 \cos \vartheta_1, \quad (5)$$

$$\sigma = \Phi(s) + Af_0^p \Omega(\Delta s), \quad \frac{d\sigma}{ds} = \frac{d\Phi}{ds} + Af_0^p \frac{d\Omega}{ds},$$

where  $G$ ,  $G_p$  is elastic and plastic modules of shearing;  $G_p^0$  is value of  $G_p$  in trajectory break-point;  $\Delta s = s - s_k^T$  is increment of length of the arc of trajectory after its break in some point  $K$ ;

$$\Omega(\Delta s) = -\left[ \gamma \Delta s e^{-\gamma \Delta s} + b(1 - e^{-\gamma \Delta s}) \right] \quad (6)$$

– function which after break of trajectory describes scalar dive of tension at difficult unloading and the subsequent secondary plastic deformation;

$$f = \frac{1 - \cos \vartheta_1}{2}; \quad f_0 = f(\vartheta_1^0) = \frac{1 - \cos \vartheta_1^0}{2} \quad (7)$$

– the function considering the orientation of vector of tension in the course of deformation and its value in break-point at the value of approach angle for nonanalytic trajectory.

For approximation of Odqvist-Ilyushin's general function of hardening  $\Phi(s)$  at simple loading expressions were used

$$\sigma = \Phi(s) = \begin{cases} \frac{2G}{\alpha} (1 - e^{-\alpha s}), & \text{при } 0 \leq s \leq s_*^T, \\ \sigma^T + 2G_*(s - s_*^T) + \sigma_* \left( 1 - e^{-\beta(s - s_*^T)} \right), & \text{при } s > s_*^T; \end{cases} \quad (8)$$

where  $\sigma^T = \sqrt{2/3}\sigma_T$ ;  $\sigma_T$  is limit of stretching strain;  $s_*^T$  is the border of sites of the chart of deformation dividing elastic part of the chart and site of flowability ( $0 \leq s \leq s_*^T$ ) from the site of self-hardening of material ( $s > s_*^T$ );  $\sigma_*$ ,  $G_*$ ,  $\alpha$ ,  $\beta$ ,  $A$ ,  $b$ ,  $\gamma$ ,  $\gamma_1$ ,  $p$ ,  $q$  are experimentally determined parameters of the structural material.

**Linearized model.** In the simplified linearized option [1, 13-14] of mathematical model for flat trajectories in the assumption of trifle of size  $\vartheta_1$  ( $\sin \vartheta_1 \approx \vartheta_1$ ,  $\cos \vartheta_1 \approx 1$ ) follows the differential equation

$$\frac{d\vartheta_1}{ds} + \kappa_1 = -n\vartheta_1, \quad (9)$$

in which, for active processes at  $0 < \vartheta_1 < 90^\circ$  it is possible to accept

$$n(s) = \frac{M_1}{\sigma} \approx \frac{\alpha_1 2G}{\sigma_k^T} = k, \quad (10)$$

where  $k = \text{const}$ ;  $\alpha_1$  is constant coefficient ( $0 < \alpha < 1$ );  $\sigma_k^T$  is the value of the module  $\bar{\sigma}$  in deformation trajectory break point. The solution of the equation (9) leads to expression

$$\vartheta_1 = \vartheta_1^* + (\vartheta_1^0 - \vartheta_1^*) e^{-k\Delta s}, \quad (11)$$

where  $\vartheta_1^* = -\kappa_1 / k$ . For piecewise and broken trajectories if to accept more difficult approximation

$$n(s) = \frac{1}{s} + k, \quad (12)$$

that from (9) can be received [15]

$$\vartheta_1 = \frac{s_0}{s} e^{-k\Delta s} \left\{ \vartheta_1^0 - \vartheta_1^* \left( 1 - \frac{1}{ks_0} \right) \right\} + \vartheta_1^* \left( 1 - \frac{1}{ks} \right), \quad (13)$$

where  $s_0$  is length of the arc in trajectory break point. In particular, for two-unit broken lines at  $\vartheta_1^* = 0$  from (13) follows

$$\vartheta_1 = \frac{s_0}{s} \vartheta_1^0 e^{-k\Delta s}. \quad (14)$$

### 3. Results of tests and mathematical modeling

As samples for tests on the SN-EVM rated and experimental complex of A. A. Ilyushin thin-walled barrel shells from steel 45 having in working part have been used:  $l = 110$  mm length, the  $h = 1$  mm thickness, and diameter of the median surface of  $d = 31$  mm. The initial isotropy of material of samples with sufficient precision ratio has been confirmed in experiences on simple loading (stretching, compression, and torsion) and when processing these charts, the following values of material parameters for steel 45 have been accepted in approximations (8):  $\sigma^T = 310$  MPa,  $s_*^T = 1,1 \cdot 10^{-2}$ ,  $2G = 1,57 \cdot 10^5$  MPa,  $\beta = 70$ ,  $\alpha = 900$ ,  $\sigma_* = 82$  MPa,  $2G_* = 2700$  MPa.

Two broken nonanalytic trajectories with preliminary elastoplastic deformation on the site of constant curvature which are mirroring of each other rather direct, slanting to coordinate axes  $\mathcal{E}_1$  and  $\mathcal{E}_3$  (fig. 1) are realized to verify A. A. Ilyushin's postulate of isotropy and assessment of reliability of results on the mathematical models described above in space of deformations  $\mathcal{E}_1 - \mathcal{E}_3$ .

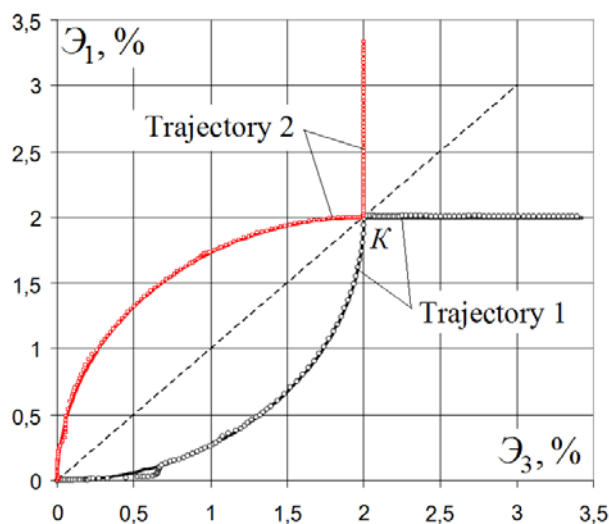


**Fig. 1.** Deformation trajectories.

The first of two trajectories of deformation (trajectory 1, in fig. 1 is designated in black color) on the first site represents a quarter of a circle radius  $\rho = 2\%$  with a center of curvature  $\mathcal{E}_1^0 = 2\%$ ,  $\mathcal{E}_3^0 = 0$ , on which joint stretching with torsion of a sample to a point  $K$ . Then, with a break on the corner  $90^\circ$  the trajectory passes to the second straight section where torsion on coordinate  $\mathcal{E}_3$  was implemented. In specularly reflected trajectory (trajectory 2 in fig. 1) on the first site to the point  $K$  joint stretching and torsion on a quarter of a circle were also carried out at  $\rho = 2\%$ ,  $\mathcal{E}_1^0 = 0$ ,  $\mathcal{E}_3^0 = 2\%$ , and on the second site - only stretching on  $\mathcal{E}_1$ . In the point  $K$  joint of the first and second sites of trajectories in addition to the existence of salient points their curvature changes, means the first and second derivatives of the functions  $\bar{\mathcal{E}} = \bar{\mathcal{E}}(s)$ , describing trajectories in a vector space, undergo a gap.

Results of numerical calculations and experimental data for a trajectory 1 (see fig. 1) are given in fig. 2-7, and results and the experimental data for reflected trajectory 2 are given in fig. 8-13. Experimental data in drawings are noted by points: for a trajectory 1 – circles of black color; for a trajectory 2 – small squares of red color. Curves 1 (blue color) are results of calculations for the general mathematical model of the theory of processes, curves 2 (black color) – of the linearized model. Results of calculations and experiments rated are given in representation of deformations and tension according to A. A. Ilyushin's postulate through coordinates of the corresponding vectors of forming [1-2, 11-12].

In calculations, identical values of material parameters in approximations of functionalities of plasticity for both trajectories were taken. On the first site was taken:  $q = 0.1$ ,  $\gamma_1 = 25$ ; on the second:  $q = 0.3$ ,  $\gamma_1 = \gamma = 50$ ,  $p = 4$ ,  $b = 0.35$ . For the initial value of  $\mathcal{E}_1^0$  on the second site after a salient point of a trajectory was taken  $\mathcal{E}_1^0 = 90^\circ - \mathcal{E}_1^k \approx 72^\circ$ , where  $\mathcal{E}_1^k$  – the value of an approach angle on the first site in a trajectory breaking point  $K$  in the calculation

of the general model ( $\vartheta_1^k \approx 18^\circ$ ). On the linearized model in calculations was taken  $\alpha_1 = 0.7$ ,  $k = 258$ ; on the first site the corner  $\vartheta_1$  was defined on (11) where  $\vartheta_1^0 = 0$ ,  $\vartheta_1^*$  at  $\kappa_1 = 1/\rho = 50$  was taken  $\vartheta_1^* \approx 0,193$  rad. On the second site of a trajectory, the approach angle  $\vartheta_1$  was defined on (14) at  $\vartheta_1^0 = 90^\circ - \vartheta_1^k \approx 79^\circ$ , where  $\vartheta_1^k \approx 11^\circ$  is a calculated value of a corner on the linearized model in a point the end of the first site of a trajectory of deformation.

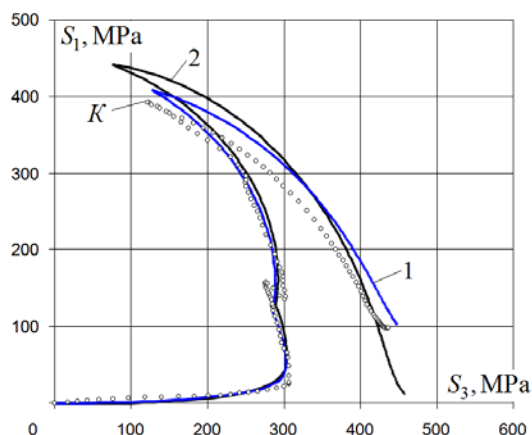


Fig. 2. Trajectory 1. Response  $S_1 - S_3$ .

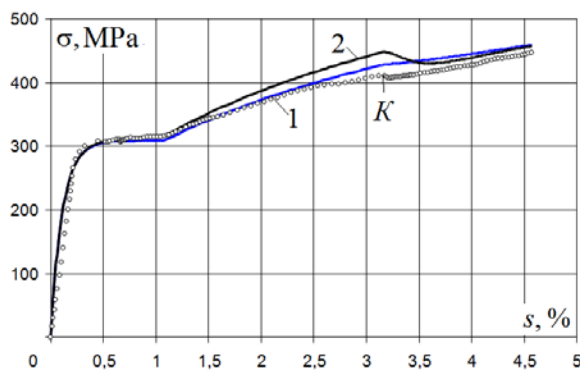


Fig. 3. Trajectory 1. Chart of deformation  $\sigma - s$ .

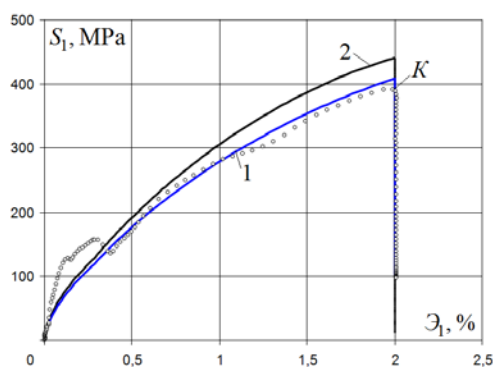


Fig. 4. Trajectory 1. Chart  $S_1 - \vartheta_1$ .

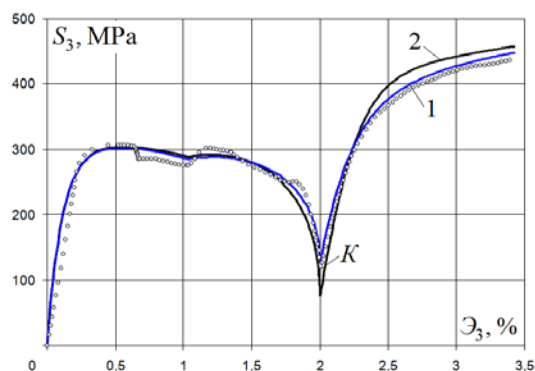


Fig. 5. Trajectory 1. Chart  $S_3 - \vartheta_3$ .

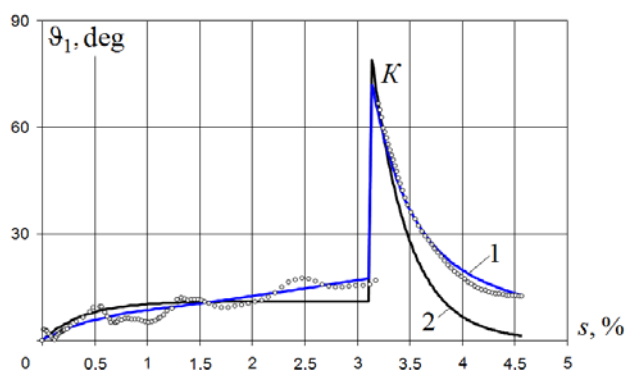


Fig. 6. Trajectory 1. Chart  $\vartheta_1 - s$ .

The results received on the general mathematical model for charts  $\sigma - s$  (curves 1 in fig. 3, 8) and  $\vartheta_1 - s$  (curves 1 in fig. 6, 11), the scalar and vector material properties reflecting

respectively are well coordinated with data of tests. Good compliance of rated results on the general model with the experimental data is also observed on a response in space of tension  $S_1 - S_3$  (fig. 2, 7) and to local charts of deformation at stretching and compression  $S_1 - \mathcal{E}_1$  (fig. 4, 9) and torsion  $S_3 - \mathcal{E}_3$  (fig. 5, 10). On the basis of it is possible to claim that the V. G. Zubchaninov's general mathematical model of yields adequate results at the description of patterns of elastoplastic behavior of material for the considered types of difficult nonanalytic trajectories with a breaking point.

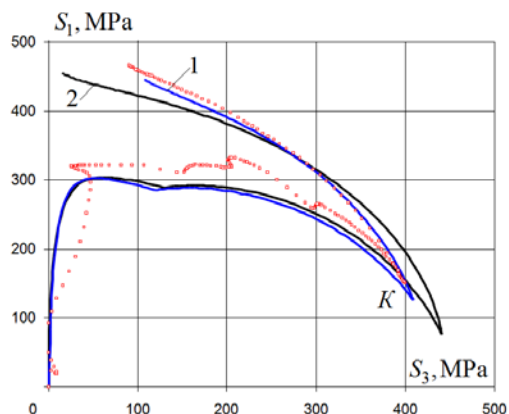


Fig. 7. Trajectory 2. Response  $S_1 - S_3$ .

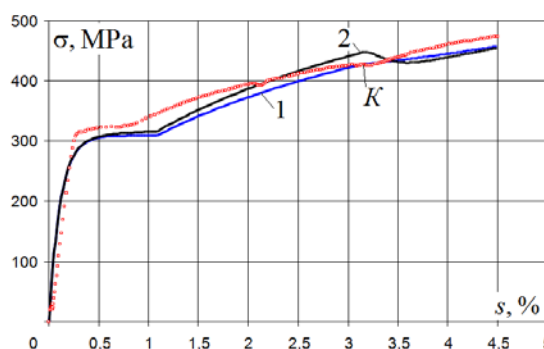


Fig. 8. Trajectory 2. Chart of deformation  $\sigma - s$ .

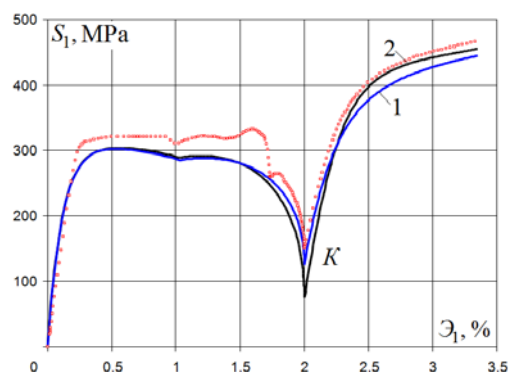


Fig. 9. Trajectory 2. Chart  $S_1 - \mathcal{E}_1$ .

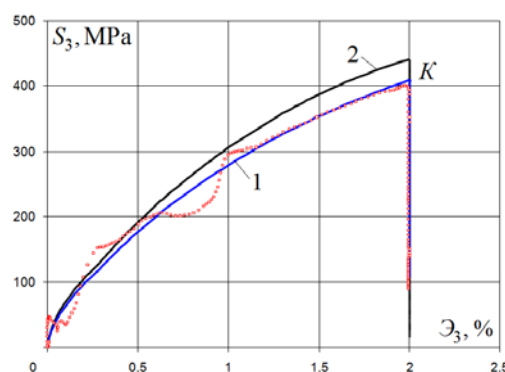


Fig. 10. Trajectory 2. Chart  $S_3 - \mathcal{E}_3$ .

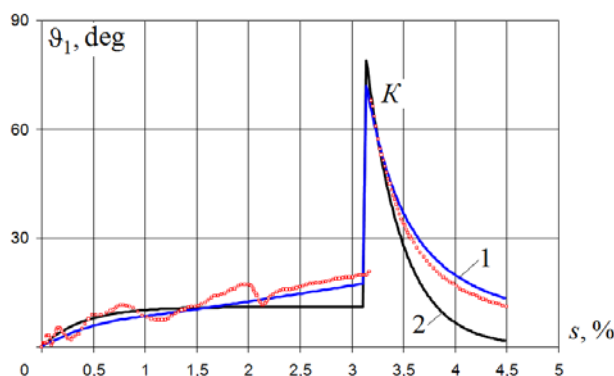
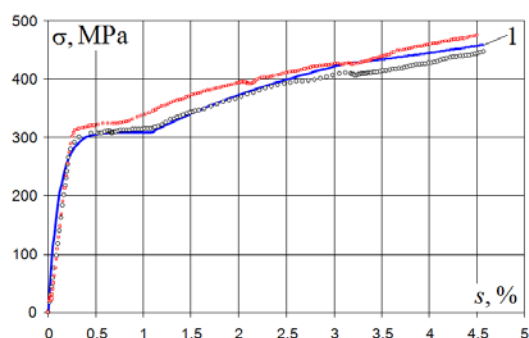


Fig. 11. Trajectory 2. Chart  $\mathcal{E}_1 - s$ .

Results on the linearized model give essential deviations on vector properties (curves 2 in fig. 6, 11). On scalar properties due to the fact that on the considered trajectories active

process of deformation ( $0 < \vartheta_1 < 90^\circ$ ) is carried out, and the parameter of complexity of the process  $\vartheta_1^0 < 90^\circ$ , the linearized model shows acceptable results.

To verify the postulate of isotropy for trajectories 1 and 2 on fig. 12-13 the reflecting scalar and vector material properties, and also results of mathematical modeling with use of the general model (curves 1 in fig. 12-13) are presented combination of experimental results for charts  $\sigma - s$  and  $\vartheta_1 - s$ .



**Fig. 12.** Trajectories 1 and 2. Charts of deformation  $\sigma - s$ .

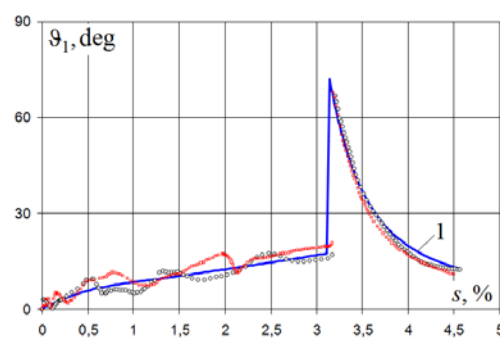


**Fig. 13.** Trajectories 1 and 2. Charts  $\vartheta_1 - s$ .

The comparison shows that experimental charts of specularly reflected trajectories of deformation matched among themselves a sufficient precision ratio. Therefore, it is possible to believe that for these types of difficult trajectories with a break and the preliminary elastoplastic deformation preceding it on the site with constant curvature, the postulate of isotropy is carried out on scalar and vector properties.

## References

- [1] V.G. Zubchaninov, *Mechanics of processes of plastic environments* (Fizmatlit, Moscow, 2010).
- [2] V.G. Zubchaninov, *Stability and plasticity. Vol. 2. Plasticity* (Fizmatlit, Moscow, 2008).
- [3] V.P. Degtyarev, *Plasticity and creep of engineering structures* (Mashinostroenie, Moscow, 1967). (In Russian).
- [4] F.M. Mitenkov, I.A. Volkov, L.A. Igumnov, A.V. Kaplienko, YU.G. Korotkih, V.A. Panov, *Applied theory of plasticity* (Fizmatlit, Moscow, 2015).
- [5] V.V. Moskvitin, *Plasticity at variable loadings* (Izdatelstvo MGU, Moscow, 1965).
- [6] V.S. Lenskij, In: *Questions of the theory of plasticity* (Izdatelstvo AN USSR, 1961), p. 58.
- [7] Yu.N. Shevchenko, N.N. Tormahov // *International Applied Mechanics* **35** (1999) 13.
- [8] V.G. Zubchaninov, A.A. Alekseev, V.I. Gul'tyaev // *PNRPU Mechanics Bulletin* **3** (2014) 71.
- [9] V.G. Zubchaninov // *Mechanics of Solids* **46** (2011) 21.
- [10] V.G. Zubchaninov, A.A. Alekseev, E.G. Alekseeva // *Materials Physics and Mechanics* **29(2)** (2016) 150.
- [11] A.A. Ilyushin, *Plasticity: Fundamentals of the general mathematical theory* (Izdatelstvo AN USSR, Moscow, 1963). (In Russian).
- [12] A.A. Ilyushin, *Proceedings (1946-1966). Vol. 2 Plasticity* (Fizmatlit, Moscow, 2004). (In Russian).
- [13] V.G. Zubchaninov // *Problemy prochnosti i plastichnosti* **67** (2005) 5. (In Russian).
- [14] V.G. Zubchaninov, E.G. Alekseeva // *Vestnik ChGPU im. I. Ia. Iakovleva. Seriya: Mekhanika predel'nogo sostoianiia* **8** (2010) 172. (In Russian).
- [15] Dao Zui Bik // *Vestnik MSU* **2** (1965) 67.

## TESTING OF STEEL 45 UNDER COMPLEX LOADING ALONG THE CYLINDRICAL SCREW TRAJECTORIES OF DEFORMATION

V.G. Zubchaninov, V.I. Gultiaev, A.A. Alekseev\*, V.V. Garanikov, S.L. Subbotin

Tver State Technical University, nab. Afanasiya Nikitina, 22, Tver, 170026, Russia

\*e-mail: alexeev@bk.ru

**Abstract.** The results of the experiment on complex loading of a thin-walled tubular steel specimen with three parameter action of axial force, torsion, and internal pressure are presented. The experiment was carried out on A.A. Ilyushin's testing complex SN-EVM. The program of the experiment in the deformation space is a cylindrical, helical trajectory with a displaced center of a screw curvature. Scalar and vector properties of the material steel 45 were investigated.

**Keywords:** plasticity; complex loading; trajectory of deformation; helical trajectory; scalar and vector properties of material; thin-walled tubular steel.

### 1. Introduction

The experimental investigations conducted for studying of patterns and effects of structural materials deformation the behind elastic limit at compound stress condition and under disproportionate loading are an important component of mechanics of deformable solids and plastic theory. The phenomenological approach is the basis for the development of new mathematical models of deformation of materials behind elastic limit, and also for certification and assessment of limits of applicability of the modern theory of plasticity existing models.

A large number of systematic experimental investigations was carried out under materials deformation along flat multilink piecewise and broken rectilinear and curvilinear trajectories of constant and variable curvature [1-10]. Tests at uniaxial ratcheting and difficult cyclic deformation on the closed trajectories [11-15] represent a special case of the sign variable theory of plasticity. The experiments executed on space trajectories of deformation of constant and variable curvature are practically absent [1, 3, 16, 17]. Series of tests on thin-walled tubular specimens made of 45 steel at rigid loading along the dimensional trajectories in deviatory space of deformations  $\mathcal{E}_{(3)}$  showing an uncommon connection between tension and deformations at the elastoplastic deformation of material has been carried out in TvSTU mechanical laboratories. In the series of the tests at different parameters of internal geometry were implemented:

- cylindrical screw trajectories of constant curvature and torsion with screw center of curvature in datum origin on the plane  $\mathcal{E}_1 - \mathcal{E}_3$ ;
- cylindrical screw trajectories of constant curvature and torsion with the displaced screw center of curvature on the plane  $\mathcal{E}_1 - \mathcal{E}_3$ ;
- the conic screw trajectories of variable curvature and torsion  $\mathcal{E}_1 - \mathcal{E}_3$  presenting folding and unfolding Archimedes's spirals in the planes  $\mathcal{E}_1 - \mathcal{E}_3$ .

The screw axis in all experiences had been oriented in the direction of coordinate  $\mathcal{O}_2$ . Testing was carried out on the Ilyushin's automatic testing complex SN-EVM, realizing the three-parametrical impact on a specimen (axial tension-compression, torsion, and internal pressure) in the automatic mode according to the set deformation program. When carrying out deformation tests were measured by means of the extensometer working together with the SN-EVM complex.

## 2. Technique of experiment and main equations

The technique of experimental studies conducting is based on the A. A. Ilyushin's theory of elastoplastic processes [1, 2, 18, 19], where deviator of tension and deformations with components

$$S_{ij} = \sigma_{ij} - \delta_{ij}\sigma_0, \quad \mathcal{O}_{ij} = \varepsilon_{ij} - \delta_{ij}\varepsilon_0, \quad (i, j = 1, 2, 3) \quad (1)$$

are presented in the form of tensions  $\bar{\sigma}$  and deformations  $\bar{\mathcal{O}}$  vectors of forming in five-measured deviator space

$$\bar{\sigma} = \sigma \hat{\sigma} = S_k \hat{i}_k, \quad \bar{\mathcal{O}} = \mathcal{O} \hat{\mathcal{O}} = \mathcal{O}_k \hat{i}_k \quad (k = 1, 2, 3), \quad (2)$$

where  $\sigma_{ij}$ ,  $\varepsilon_{ij}$  are components of stress and deformations tensors,  $\delta_{ij}$  is the Kronecker's symbol,  $\sigma_0 = \sigma_{ii}/3$ ,  $\varepsilon_0 = \varepsilon_{ii}/3$  are average tension and deformation;  $\hat{\sigma}$ ,  $\hat{\mathcal{O}}$  is unit vectors;

$$\sigma = \sqrt{S_k S_k} = \sqrt{S_1^2 + S_2^2 + S_3^2}, \quad \mathcal{O} = \sqrt{\mathcal{O}_k \mathcal{O}_k} = \sqrt{\mathcal{O}_1^2 + \mathcal{O}_2^2 + \mathcal{O}_3^2} \quad (3)$$

are modules  $\bar{\sigma}$  and  $\bar{\mathcal{O}}$ ;  $\{\hat{i}_k\}$  is orthonormalized motionless basis;  $S_k$ ,  $\mathcal{O}_k$  are coordinates of vectors  $\bar{\sigma}$  and  $\bar{\mathcal{O}}$  in the basis, for which

$$\begin{aligned} S_1 &= \sqrt{\frac{3}{2}} S_{11} = \sqrt{\frac{2}{3}} \left( \sigma_{11} - \frac{1}{2} (\sigma_{22} + \sigma_{33}) \right), \quad S_2 = \sqrt{2} \left( S_{22} + \frac{1}{2} S_{11} \right) = \frac{1}{\sqrt{2}} (\sigma_{22} - \sigma_{33}), \\ S_3 &= \sqrt{2} S_{12} = \sqrt{2} \sigma_{12}; \\ \mathcal{O}_1 &= \sqrt{\frac{3}{2}} \mathcal{O}_{11} = \sqrt{\frac{3}{2}} (\varepsilon_{11} - \varepsilon_0), \quad \mathcal{O}_2 = \sqrt{2} \left( \mathcal{O}_{22} + \frac{1}{2} \mathcal{O}_{11} \right) = \frac{1}{\sqrt{2}} (\varepsilon_{22} - \varepsilon_{33}), \\ \mathcal{O}_3 &= \sqrt{2} \mathcal{O}_{12} = \sqrt{2} \varepsilon_{12}. \end{aligned} \quad (4)$$

In this case, history of stresses and deformations tensors changing is represented geometrically in vector (deviator) spaces of forming in the form of images of the processes containing trajectory, and its points assigned with lengths of arc  $s$  or  $\Sigma$  characteristics of process: vectors  $\bar{\sigma}$  or  $\bar{\mathcal{O}}$  and their increments, and also scalar parameters (temperature, average stress  $\sigma_0$  and deformation  $\varepsilon_0$  etc). At the same time, the connection between tensions and deformations is described by the scalar properties, characterizing connection between invariants of deviator of tensions and deformations, and the vector properties, characterizing misalignment of deviator of tensions, deformations and their increments. The provision of vector of tension  $\bar{\sigma}$  is defined by unit vector for which

$$\hat{\sigma} = \frac{\bar{\sigma}}{\sigma} = \cos \vartheta_1 \hat{p}_1 + \sin \vartheta_1 (\cos \vartheta_2 \hat{p}_2 + \sin \vartheta_2 \hat{p}_3), \quad (5)$$

where unit vectors of the Frenet frame  $\{\hat{p}_k\}$

$$\hat{p}_1 = \frac{d\bar{\mathcal{O}}}{ds}, \quad \hat{p}_2 = \frac{1}{\kappa_1} \frac{d^2\bar{\mathcal{O}}}{ds^2}, \quad \hat{p}_3 = \frac{1}{\kappa_2} \left[ \kappa_1 \frac{d\bar{\mathcal{O}}}{ds} + \frac{d}{ds} \left( \frac{1}{\kappa_1} \frac{d^2\bar{\mathcal{O}}}{ds^2} \right) \right], \quad \dots; \quad (6)$$

$\kappa_1, \kappa_2$  are parameters of curvature and torsion of the internal geometry of trajectory of deformation;  $\vartheta_1$  is vector  $\bar{\sigma}$  approach angle with a tangent vector  $\vec{p}_1$  to deformation trajectory;  $\vartheta_2$  is the deplanation corner characterizing vector  $\bar{\sigma}$  deviation from vector  $\vec{p}_2$  projected to the normal plane  $\vec{p}_1 \vec{p}_3$ . At the creation of experimental dependencies, it is necessary to consider features of the behavior of both scalar, and vector material properties.

Cylinder thin-walled shells from steel 45 in the condition of delivery which had the  $h = 1$  mm wall thickness,  $r = 15,5$  mm radius of the median surface of the cross-section, and  $l = 110$  mm length of working part used as physical models for researching on the SN-EVM testing complex. In walls of specimens at a relation of  $r/h$  homogeneous flat stress condition is implemented. The material of specimens sufficiently was initially isotropic that was confirmed by basic tests at simple loading on trajectories like the "central fan" including tests on stretching, compression, torsion and internal pressure. While processing results of experimental data, dependencies [1, 3] were used to identify components of tensors of deformations  $\varepsilon_{ij}$  ( $i, j = 1, 2, 3$ ) and tension  $\sigma_{ij}$ .

$$\begin{cases} \varepsilon_{11} = \frac{\Delta l}{l}, \quad \varepsilon_{22} = \frac{\Delta r}{r}, \quad \varepsilon_{12} = \frac{r\psi}{2l}, \quad \varepsilon_{13} = \varepsilon_{23} = 0, \\ \varepsilon_{33} = -(\varepsilon_{11} + \varepsilon_{22}) + \frac{\sigma_0}{K}, \quad \varepsilon_0 = \frac{1}{3}(\varepsilon_{11} + \varepsilon_{22} + \varepsilon_{33}), \end{cases} \quad (7)$$

$$\begin{cases} \sigma_{11} = \frac{P}{2\pi r h}, \quad \sigma_{22} = q \frac{r}{h}, \quad \sigma_{12} = \frac{M}{2\pi r^2 h}, \quad \sigma_{33} \approx 0, \quad \sigma_{13} = \sigma_{23} = 0, \\ \sigma_0 = \frac{1}{3}(\sigma_{11} + \sigma_{22} + \sigma_{33}), \quad K = \frac{E}{3(1-2\mu)}, \end{cases} \quad (8)$$

where  $\Delta l$  and  $\Delta r$  – increments of  $l$  and  $r$ ;  $\psi$  – cross-section turning angle;  $P$  – the stretching axial force;  $q$  – intensity of internal pressure;  $M$  – torque;  $E$  – Young's modulus;  $\mu$  – Poisson's ratio;  $K$  – Bulk modulus. When processing experimental data the condition of incompressibility of material ( $\varepsilon_0 = 0$ ), was accepted inasmuch as with the advent of plastic deformations  $\mu_p$  the coefficient of cross deformation quickly approached value  $\mu_p = 0,5$ .

The article is about the program of deformation along cylindrical screw trajectory with the displaced screw center of curvature from the origin on the plane  $\vartheta_1 - \vartheta_3$  (fig. 1-4) realized in tests.

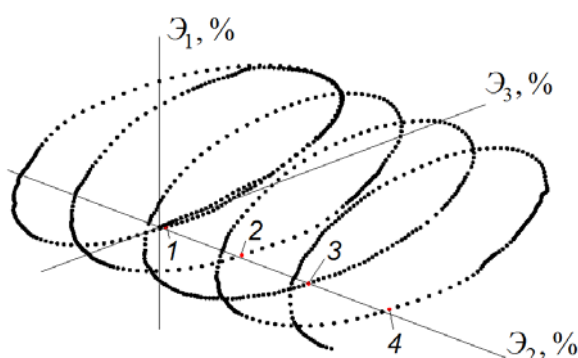


Fig. 1. Space trajectory of deformation.

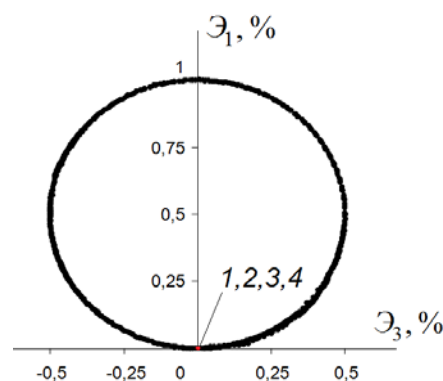
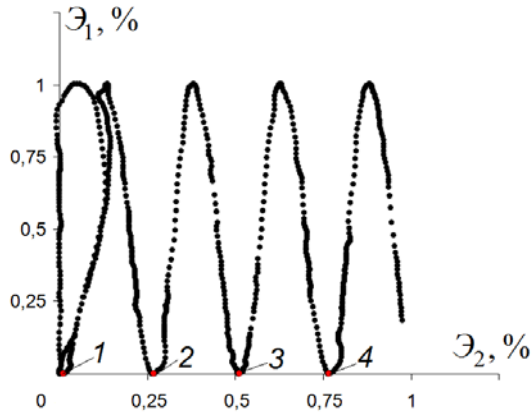
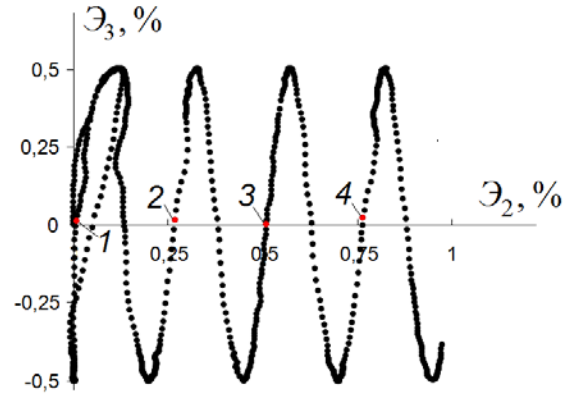


Fig. 2. Deformation trajectory on the plane  $\vartheta_1 - \vartheta_3$ .



**Fig. 3.** Deformation trajectory on the plane  $\mathfrak{A}_1 - \mathfrak{A}_2$ .



**Fig. 4.** Deformation trajectory on the plane  $\mathfrak{A}_2 - \mathfrak{A}_3$ .

The trajectory with constant curvature in the form of radius circle  $R = 0,5 \%$ , whose pole coordinates were  $\mathfrak{A}_1^* = 0,5 \%$ ,  $\mathfrak{A}_3^* = 0$  and curvature was  $\kappa_1 = 1/R = 200$  was implemented at the first site, tension with torsion jointed in the experiment. After whole turnover of the circle by means of internal pressure on the second site deformation along axis  $\mathfrak{A}_2$  along screw trajectory in the number of 4 incomplete rounds with propeller pitch  $H = 0,25 \%$  and parameter of torsion  $\kappa_2 \approx 15,7$  was implemented. The digits 1, 2, 3, 4 in figures 1-4 have designated points of the beginning of the first and the subsequent rounds of the screw. The experience in the mode of continuous specimen deformation with fixed speed  $\dot{\varepsilon} = 10^{-6} \text{ s}^{-1}$ , allowing to choose short-term creep of material at standard temperature continued for more than 9 hours.

For implementation of cylindrical screw trajectory on the second site of the program of experiment the Cartesian coordinates of vectors on the SN-EVM automated complex were set in the form of [1, 3]

$$\mathfrak{A}_1 = \mathfrak{A}_1^0 + R \sin \varphi, \quad \mathfrak{A}_2 = \mathfrak{A}_2^0 + b\varphi, \quad \mathfrak{A}_3 = \mathfrak{A}_3^0 + R \cos \varphi, \quad (9)$$

where  $\mathfrak{A}_1^0$ ,  $\mathfrak{A}_2^0$ ,  $\mathfrak{A}_3^0$  – Cartesian coordinates of curvilinear part of trajectory pole;  $\varphi$  is the polar corner counted from axis  $\mathfrak{A}_1$  against the course of the hour hand;  $b = H/2\pi$ . For presented in fig. 1-4 trajectories  $\mathfrak{A}_1^0 = 0,5 \%$ ,  $\mathfrak{A}_2^0 = \mathfrak{A}_3^0 = 0$ . As propeller pitch is  $H = 0$  we have  $b = 0$ , and from (9) the circle equation realized on the first site follows.

When processing results of experimental studies on strain and stress vectors coordinates forming were defined by components of tensors on formulas (4), and vector modules on formulas (3). For definition of approach angles  $\mathfrak{A}_1$ , deplanation angles  $\mathfrak{A}_2$  and the contact angles  $\psi_1$ , characterizing the influence of vector material properties on deformation process were used expressions

$$\cos \mathfrak{A}_1 = \hat{\sigma} p_1 = \frac{1}{\sigma \dot{s}} \left\{ S_2 b + R \left[ S_1 \cos \varphi - S_3 \sin \varphi \right] \right\}, \quad (10)$$

$$\sin \psi_1 = \hat{\sigma} p_3 = \frac{1}{\sigma \dot{s}} \left\{ S_2 R - b \left[ S_1 \cos \varphi - S_3 \sin \varphi \right] \right\}, \quad \sin \mathfrak{A}_2 = \frac{\hat{\sigma} p_3}{\sin \mathfrak{A}_1} = \frac{\sin \psi_1}{\sin \mathfrak{A}_1},$$

where

$$\dot{s} = \sqrt{R^2 + b^2}, \quad \sin \varphi = (\mathfrak{A}_1 - \mathfrak{A}_1^0) / R, \quad \cos \varphi = (\mathfrak{A}_3 - \mathfrak{A}_3^0) / R. \quad (11)$$

### 3. Experimental results

In fig. 5-11 experimental results of testing of a tubular specimen on the program submitted in fig. 1-4 are presented. In fig. 5-8 the response in space of tension  $S_{(3)}$ , in fig. 9 local charts of deformation on coordinates  $S_k - \mathcal{E}_k$ , in fig. 10 - the general charts of deformation  $\sigma - \mathcal{E}$  and  $\sigma - s$ , the characterizing scalar material properties, where  $s$  is the length of the arc of deformation trajectory are presented. The dependences of corners  $\mathcal{E}_1, \mathcal{E}_2$  and  $\psi_1$  on  $s$  characterizing vector material properties is given in fig. 11.

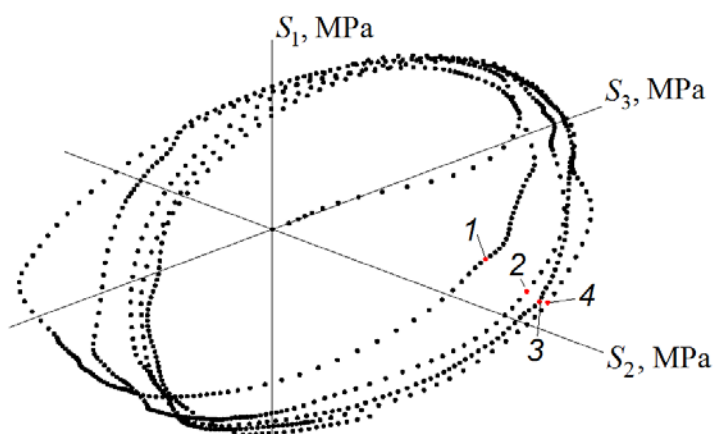


Fig. 5. A response in space of tension  $S_{(3)}$ .

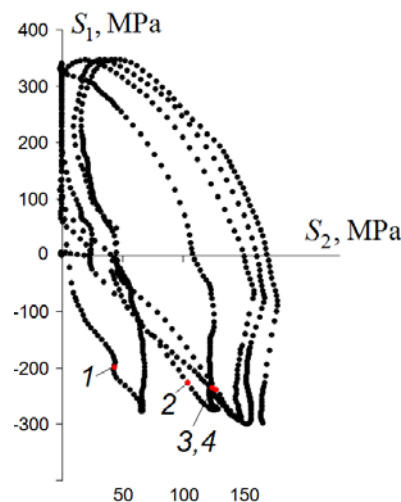


Fig. 6. Response to the plane  $S_1 - S_2$ .

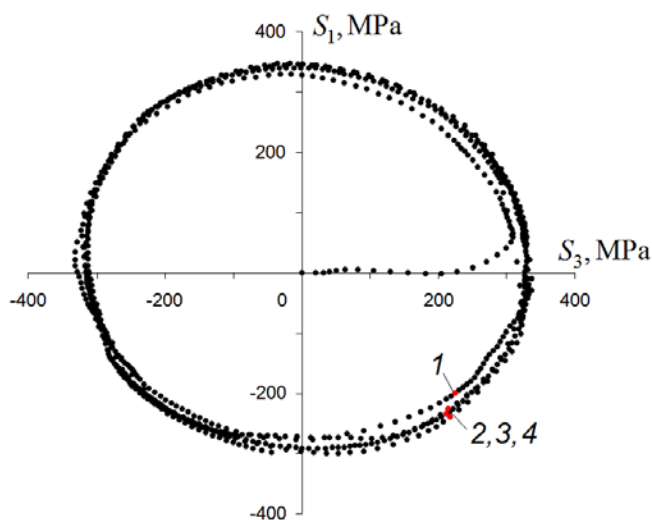


Fig. 7. Response to the plane  $S_1 - S_3$ .

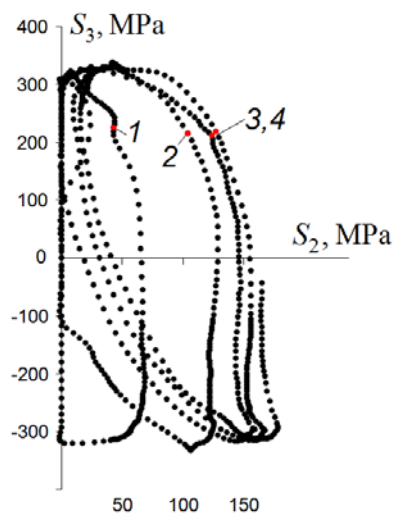


Fig. 8. Response to the plane  $S_3 - S_2$ .

While deformation on the site of circle the  $\mathcal{E}_2$ -effect [1], which is followed by the emergence of deformation anisotropy and growth of component  $\mathcal{E}_2$ , which peak value was 0,13% was observed. At further deformation value of  $\mathcal{E}_2$  decreased, and before screw trajectory was close to zero.

On the chart  $\sigma - s$  (fig. 10) on the site of the circle and four rounds five "direct" dives of tension and on the chart  $\sigma - \mathcal{E}$  are five "return" dives of partial elastic unloading are

traced. This obviously differs from the Odkqist-Ilyushin's law of hardening  $\sigma = \Phi(s)$ . The size of tension dives decreased each time: on the site of circle the size of dive was  $\Delta\sigma \approx 54\text{MPa}$ , on the last spiral turn –  $\Delta\sigma \approx 18\text{MPa}$ . Material in the course of plastic deformation, in general, has received hardening, but it was insignificant and was only 45 MPa that at the value of liquid limit  $\sigma^T \approx 315\text{MPa}$  corresponds to the value of  $\sigma \approx 360\text{MPa}$ .

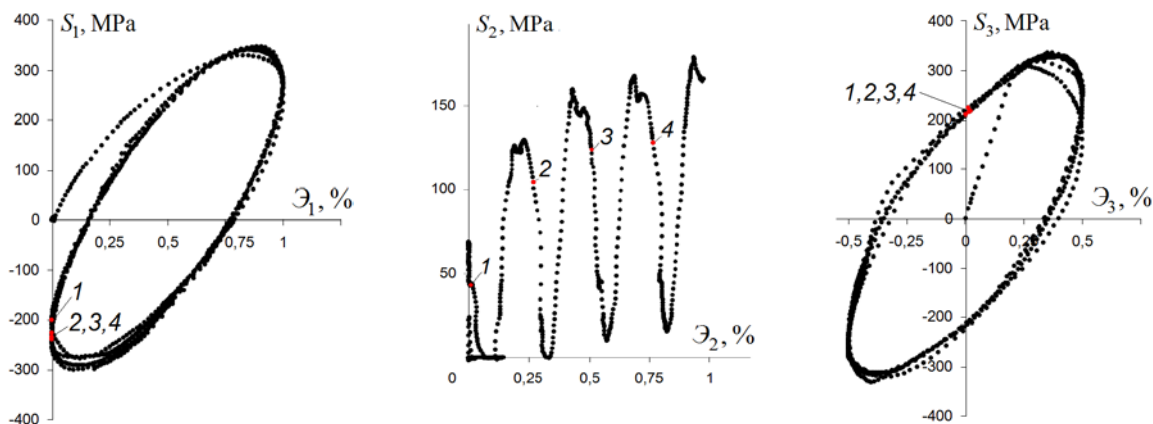


Fig. 9. Local charts of deformation  $S_1 - E_1, S_2 - E_2, S_3 - E_3$ .

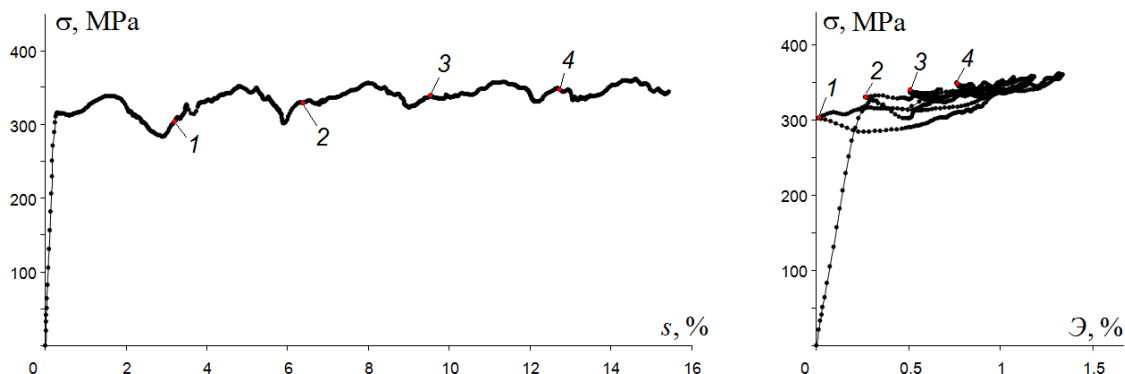


Fig. 10. General charts of deformation  $\sigma - s, \sigma - E$ .

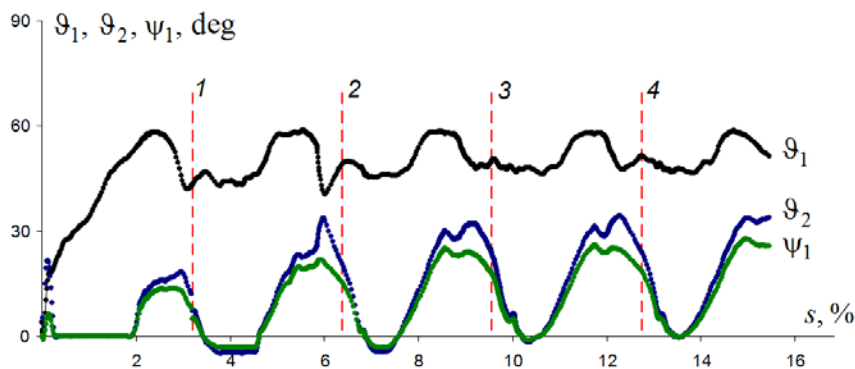


Fig. 11. Charts  $\vartheta_1 - s, \vartheta_2 - s, \psi_1 - s$ .

Change of coordinate size  $S_2$  on screw rounds has practically not impacted on coordinates  $S_1$  and  $S_3$  (see fig. 7). At the same time, explicit frequency of local charts of stretching compression  $S_1 - E_1$  and torsion  $S_3 - E_3$  is observed (see fig. 9). Also, explicit

frequency on rounds of the screw is observed for corners  $\vartheta_1$ ,  $\vartheta_2$ , and  $\psi_1$ . Peak values of  $\vartheta_2$  and  $\psi_1$  corners was  $33^\circ$  and  $25^\circ$  respectively. Values of the approach angle  $\vartheta_1$  averaged  $50^\circ$ , therefore elementary deformation work  $dA = \bar{\sigma}d\bar{\mathcal{E}} = \sigma ds \cos \vartheta_1$  for corners  $\vartheta_1 < 90^\circ$  is  $dA > 0$ . It means that there is an active deformation process at all sections of the given trajectory.

#### 4. Conclusion

The experimental data presented in the article for dimensional elastoplastic processes of deformation are necessary for the solution of an important problem of reliable creation of approximations of functionalities of the plasticity of the general defining ratios of the theory of processes [1, 2], and the adequate description of difficult space processes of loading of continuous environments.

#### References

- [1] V.G. Zubchaninov, *Mechanics of processes of plastic environments* (Fizmatlit, Moscow, 2010). (In Russian).
- [2] V.G. Zubchaninov, *Stability and plasticity. Vol. 2. Plasticity* (Fizmatlit, Moscow, 2008).
- [3] V.G. Zubchaninov, N.L. Okhlopkov, V.V. Garanikov, *Experimental plasticity. The process of complex deformation*. (TvSTU, Tver, 2003). (In Russian).
- [4] V.P. Degtyarev, *Plasticity and creep of engineering structures* (Mashinostroenie, Moscow, 1967). (In Russian).
- [5] A.M. Zhukov, In.: *Questions of the theory of plasticity* (Izd-vo AN USSR, 1961), p. 30. (In Russian).
- [6] A.A. Lebedev, B.I. Koval'chuk, N.M. Kulchitsky, A.F. Khakimov // *Journal Strength of Materials* **3** (1988) 7.
- [7] B.D. Annin, V.M. Zhigalkin, Behavior of materials under complex loading (Izd-vo SO RAN, Novosibirsk, 1999). (In Russian).
- [8] Y. Ohashi, E. Tanaka // *Transactions of the ASME* **4** (1981) 287.
- [9] V.G. Zubchaninov, A.A. Alekseev, V.I. Gulyaev // *Deformation and fracture of materials* **9** (2016) 14.
- [10] Y. Ohashi, M. Tokuda, Y. Kurita, T. Suzuki // *Izv. AN USSR. Mechanics of Solids* **6** (1981) 53. (In Russian).
- [11] H.S. Lamba, O.M. Sidebottom // *Theoretical Foundations of Engineering Calculations* **1** (1978) 108.
- [12] D.L. McDowell // *Theoretical Foundations of Engineering Calculations* **4** (1985) 98.
- [13] A. Benallal, D. Marquis // *Journal of Engineering Materials and Technology* **109** (1987) 326.
- [14] Y. Ohashi, E. Tanaka, M. Ooka // *ASME Journal of Engineering Material Technology* **107** (1985) 286.
- [15] I.A. Volkov, Yu.G. Korotkikh, *The equation of state viscoplasticity environments with damage* (Fizmatlit, Moscow, 2008). (In Russian).
- [16] F.M. Mitenkov, I.A. Volkov, L.A. Igumnov, A.V. Kapliencko, YU.G. Korotkih, V.A. Panov, *Applied theory of plasticity* (Fizmatlit, Moscow, 2015). (In Russian).
- [17] R.A. Vasin, A.S. Vavakin, V.V. Viktorov, *Ekspierimental'noye issledovaniye uprugoplasticheskogo deformirovaniya stali pri slozhnom nagruzhenii po krivolinyeynym prostranstvennyym trayektoriyam* (Dep. in VINITI 16.10.86 № 2798, Moscow, 1986). (In Russian).
- [18] A.A. Ilyushin, *Mechanics of solid* (Izdatelstvo MSU, Moscow, 1990). (In Russian).
- [19] A.A. Ilyushin, *Plasticity: Fundamentals of the general mathematical theory* (Izdatelstvo AN USSR, Moscow, 1963). (In Russian).

# VALIDATION OF THE MATHEMATICAL MODEL OF ISOTROPIC MATERIAL USING PARAMETRIC OPTIMIZATION OF ITS PHYSICAL AND MECHANICAL CHARACTERISTICS

**A.I. Borovkov, O.I. Klyavin, O.I. Rozhdestvenskiy, M.V. Aleshin, A.N. Leontev\*,  
S.P. Nikulina, K.S. Ivanov, A.P. Okunev**

Peter the Great St.Petersburg Polytechnic University, Polytechnicheskaya, 29, St.Petersburg, 195251, Russia

\*e-mail: leontev@compmechlab.ru

**Abstract.** In the article the questions connected with modeling of isotropic material on an example of carbon steel St3ps [1] for subsequent use in analysis of power protective frames of cabins of agricultural machinery in accordance with regulatory requirements are considered [14]. The choice of the Johnson-Cook (JC) material model for performing tasks of this type is substantiated. Full-scale tests of steel specimens were carried out, on the basis of which the mathematical model of material was validated.

**Keywords:** isotropic material; carbon steel; Johnson-Cook material model.

## 1. Introduction

Nowadays in the design of new products there is a growing importance of virtual testing based on the finite element method [5]. In accordance with this, there is an urgent need for more accurate modeling of the static and dynamic behavior of materials used in design models of structures [3, 4, 7]. Generally, the most common materials in engineering industry are isotropic materials with steel as a dominant material.

The most famous model of behavior of steel materials is the JC model [2]. Many works are devoted to the study of the behavior of steel materials on the basis of this model [8-12].

In the study [11] devoted to modeling the behavior of containers in throwing (simulating emergencies) based on the JC model the authors emphasize the need to take into account the temperature component of this material model when performing similar tasks in the nuclear industry. The authors give a comparison of modeling using the JC model and a tabulated model of plasticity.

The paper [9] devoted to the study of the incubation time criterion (in the form of fracture and yielding flow criteria), describing the dynamic effects of the strength behavior in brittle fracture and the yield stress during plastic deformation. The advantage of the approach is in a single macroscopic time parameter, independent of geometry, load mode and phenomenologically related to structural changes in the material at the micro level. The author proposes to interpret the effect of filler, metal fibers on the strength properties of the material in a wide range of external influences (under dynamic loads, the change is most pronounced) on the basis of the concept of incubation time. An important part of the work is devoted to the introduction of the phenomenological model of the deformation curve of elastoplastic materials for various deformation rates on the basis of the concept of incubation time. The author suggests applying the calculated model of the deformation curve to fine-grained and coarse-grained metals and their alloys.

A numerical comparative study of the dynamic properties of metals on the basis of the Kolskiy method and on the basis of the JC model was carried out in paper [10]. The use of the rheological and energy characteristics of impact compression based on the Kolskiy method is proposed to determine the relaxation time of tangential stresses and to find the relationship between the thermal internal energy of a material based on an aluminum alloy.

In work [12] studies on the applicability of the JC model in the modeling of technological stamping processes were carried out. The authors show that it is necessary to take into account the dynamic component of the JC model in simulating such high-speed technological processes by the finite element method, and also to identify the parameters of this model with the Mie-Gruneisen state equation.

Comparative analysis of the JC model with the Cooper-Simonds and Zerilli-Armstrong models was carried out in work [13] using the finite element simulation of the process of volume stamping. The author suggests using the JC model to solve a wide range of plastic deformation problems, as the most simple, satisfactorily describing the curve of plastic yielding flow of a metal in a wide range of changes in basic physical parameters and available in most software packages of numerical analysis.

Thus, the JC material model can be used to simulate the roll-over protective structure (ROPS) of agricultural machinery with the appropriate selection and validation of the material model based on full-scale testing of the specimens. Standard [14] provides for the performance of tests with relatively low (in comparison with the processes of processing metal pressure) speed of impactors and normal temperature conditions.

## 2. Formulation and solving methods

To model the material needed to describe shock phenomena with high strain rates, the LS-Dyna application software [6] often uses the JC material model (\*MAT\_JOHNSON\_COOK). According to this model, the von Mises flow stress  $\sigma$  is calculated by the following formula [2]:

$$\sigma = (a + b\varepsilon^n)(1 + c \ln \dot{\varepsilon}^*)(1 - T^{*m}), \quad (1)$$

where  $\varepsilon$  – equivalent plastic strain;  $\dot{\varepsilon}^* = \dot{\varepsilon}/\dot{\varepsilon}_0$  is the dimensionless plastic strain rate for  $\dot{\varepsilon}_0 = 1.0 \text{ s}^{-1}$ ,  $T^*$  – is the dimensionless temperature, and  $T^* = (T - T_{room})/(T_{melt} - T_{room})$ ,  $T_{melt}$  is the melting temperature of the material,  $T_{room}$  is the room temperature. The five material constants are  $a$  – yield stress,  $b$  – the hardening modulus,  $c$  – the strain rate sensitivity coefficient,  $n$  – the hardening coefficient,  $m$  – the thermal softening coefficient.

Formula (1) is an equation of flow stress, which is defined as the instantaneous value of stress required to continue the plastic flow of material - to keep the metal flowing. The JC model is purely empirical and it's the most widely used of the strain-rate dependent plasticity models. It makes it possible to take into account the effects of isotropic (static) strengthening, kinematic strengthening, temperature variation and the associated variation in yield strength. This model takes into account both kinematic strengthening and adiabatic heating of the material undergoing strains. Moreover, the JC model is easily implemented in computational codes due to its simplicity.

All the parameters are coupled due to the multiplicative nature of the model. However, difficulties exist with determining them. The problem of determining the numerical values of the parameters of the JC material model can be successfully solved using the parametric optimization tool. However, the accuracy of the description of the deformation curve will largely depend on the objective function used in the optimization process. In practice, the most common objective function is the root-mean-square averaged difference between the values of the experimental and calculated curves. At the same time, the accuracy of the deformation curve description using this objective function is quite high, however, due to modern requirements to the accuracy of computational models, there is a need for more accurate material modeling.

### 3. Results and Discussion

**Gathering of testing data.** For full-scale testing, steel grade St3ps is chosen as the most popular material for the manufacture of power-frame of cabins and base elements of agricultural machinery. Specimens of standard sizes are cut from this material (Fig. 1). To evaluate the reliability of the data obtained is needed to test three specimens.

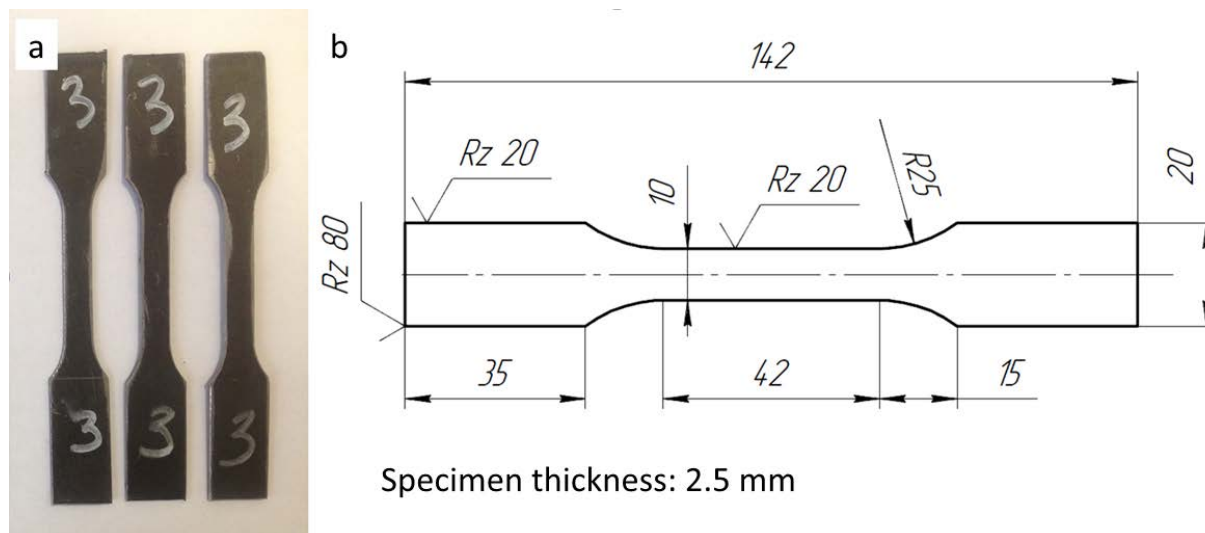


**Fig. 1.** The standard specimen: a – for natural testing, b – drawing.

The chemical composition of the material is described in Table 1.

Table 1. The chemical composition of the material test specimens.

| Grade of steel | Mass content of chemical elements |             |             |
|----------------|-----------------------------------|-------------|-------------|
|                | Carbon                            | Manganese   | Silicon     |
| St3ps          | 0.14...0.22                       | 0.40...0.65 | 0.05...0.15 |

Full-scale testing of sample materials is carried out on a certified tensile testing machine, which in real time, during the test, records the stresses occurring in the material and the corresponding deformation (Fig. 2).

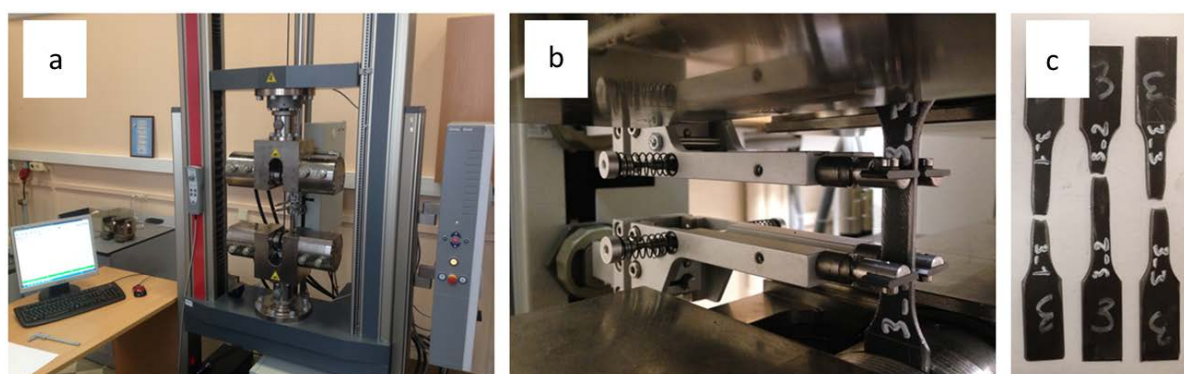


**Fig. 2.** Testing equipment (a, b) and standard experimental specimens after testing (c).

The results of stress measurements, as a function of deformations for three specimens is shown in Fig. 3. This dependence is presented in engineering units.

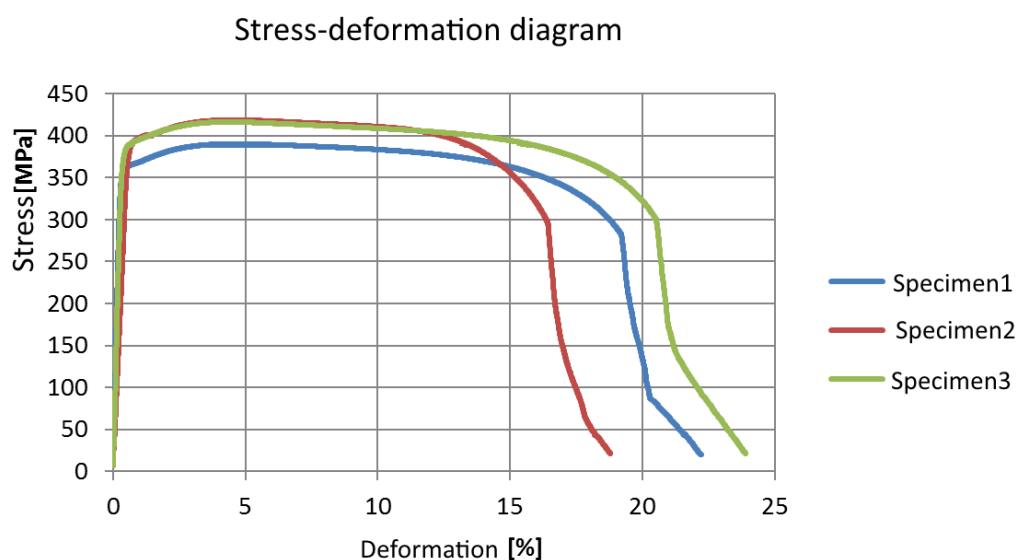


**Fig. 3.** Experimentally measured deformation diagrams in engineering dimensions.

The obtained data are averaged and transferred from engineering ones to true units by the following formulas:

$$\delta = \ln(\varepsilon + 1), \quad (2)$$

$$S = \sigma(\varepsilon + 1), \quad (3)$$

where  $\delta$  – true deformations;  $\varepsilon$  – engineering deformations;  $S$  – true stress;  $\sigma$  – engineering stress.

As a result, the deformation diagram is presented in the form in which it can be used to validate the finite element model (Fig. 4).

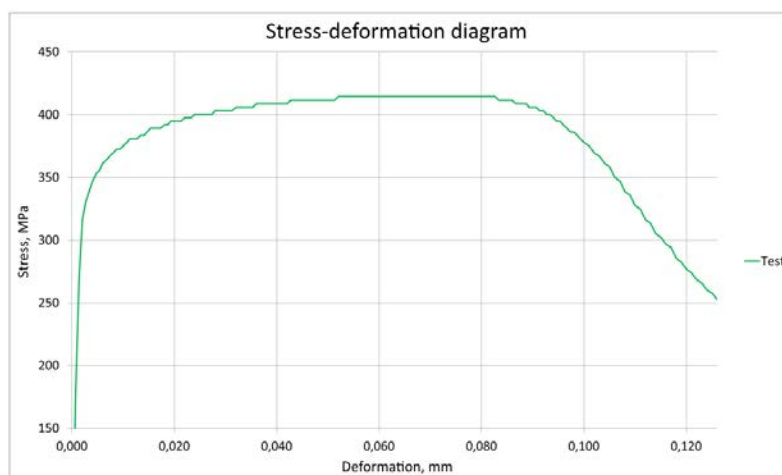


**Fig. 4.** The averaged experimental deformation diagram in true dimensions.

**Specimen modeling, parametrization and optimization of the model.** Finite element model of the specimen is modeled by shell elements in accordance with the drawing, which was used to excise the samples during testing (Fig. 5).



**Fig. 5.** Finite element model of standard specimen.

The thickness of the elements is equal to the thickness of the test specimens. The developed model is stretched along the X axis in both directions to repeat the impact test bench. The model without destruction is considered.

The example of mathematical model card of material (\*MAT\_JOHNSON\_COOK) is shown in Fig. 6.

```

*MAT_JOHNSON_COOK
Law_2
$      RHO_I      .0027
$      E          Nu          .33
$      a          b          n          EPS_max          SIG_max0
$      110        120        .15        0          280
$      c          EPS_0      ICC      Fsmooth          F_cut
$      0          0          0          0          0
$      m          T_melt      rhoC_p          T_r
$      0          0          0          0

```

**Fig. 6.** The card of JC material.

As a result, of the modelling, a deformation diagram was obtained, which has a significant discrepancy with the curve obtained from the tests (Fig. 7).

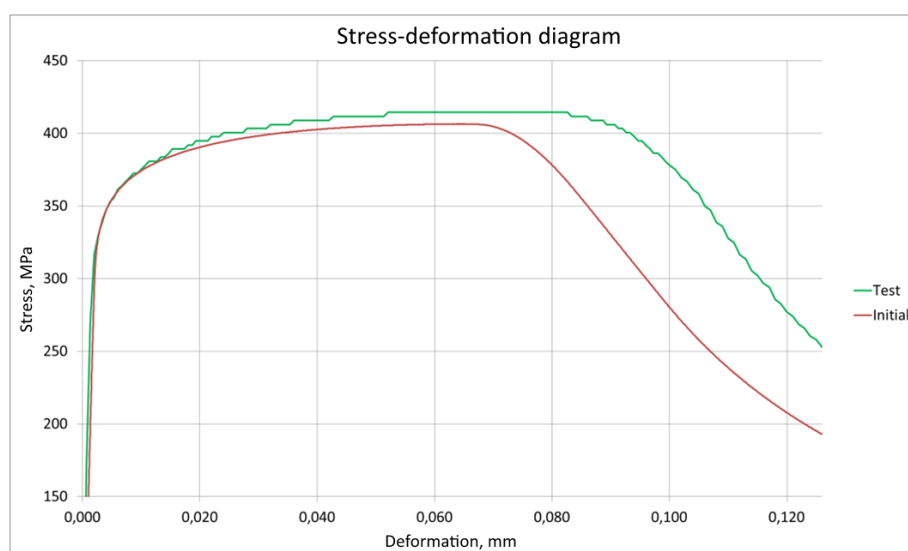


**Fig. 7.** Comparison of experimental and initial stress-deformation diagrams

For accurate reproduction of the test results, it is necessary to optimize the physical and mechanical properties of the material laid down in the JC card. It is necessary to parameterize the model.

Variable parameters include the yield point, hardening module, strengthening index, and the Young's modulus of the material.

Optimization was carried out in the application software HyperStudy developed by Altair. It was proposed to optimize in three ways:

- minimizing the area between curves;
- minimization of the difference between the corresponding values of two graphs averaged by the mean square method;
- adjustment of values in characteristic points of the graph.

Let us consider in detail each of the proposed methods of optimization.

**Minimizing the area between curves.** To set the optimization response, a script was written to calculate the area between the two curves. The text of this script is given below:

```

function area_between_two_curves(v1x,v2x,v1y,v2y)
{
    newx = sync2(v1x, v2x)           [1]
    newy1 = lininterp(v1x, v1y, newx) [2]
    newy2 = lininterp(v2x, v2y, newx) [3]
    suby = newy1-newy2              [4]
    area_value = absarea(newx, suby)  [5]
    return area_value               [6]
}

```

The first line of code performs synchronization of values along the X-axis of two curves. In the second and third lines, the Y-axis values for the new X values are calculated by linear interpolation. The fourth line determines the difference between the corresponding values along the Y axis. The fifth line calculates the area between the two curves. The sixth line displays the result.

The goal of optimization is to minimize the calculated area between the two curves. The optimization history by iteration is shown in Fig. 8.

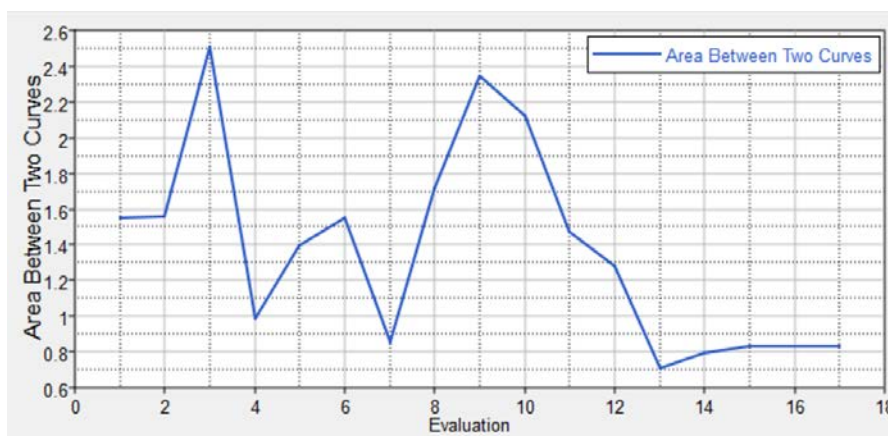


**Fig. 8.** The history of optimization by iterations (minimizing of area).

As a result, the area between the curves was reduced more than twice.

**Minimizing the RMS difference.** To set the optimization response, a script was written for the root-mean-square averaging of the differences between the two curves. The text of this script is given below:

```

function area_between_two_curves(v1x,v2x,v1y,v2y)
{
    newx = sync2(v1x, v2x)           [1]
    newy1 = lininterp(v1x, v1y, newx) [2]
    newy2 = lininterp(v2x, v2y, newx) [3]
    suby = newy1-newy2              [4]
    aver = rms(suby)                 [5]
    return aver                       [6]
}

```

The first line of code performs synchronization of values along the X-axis of two curves. In the second and third lines, the Y-axis values for the new X values are calculated by linear interpolation. The fourth line determines the difference between the corresponding values along the Y axis. The fifth line produces the mean-square averaging of the differences obtained. The sixth line displays the result.

The goal of optimization is to minimize the calculated RMS value. The history of optimization by iteration is shown in Fig. 9.

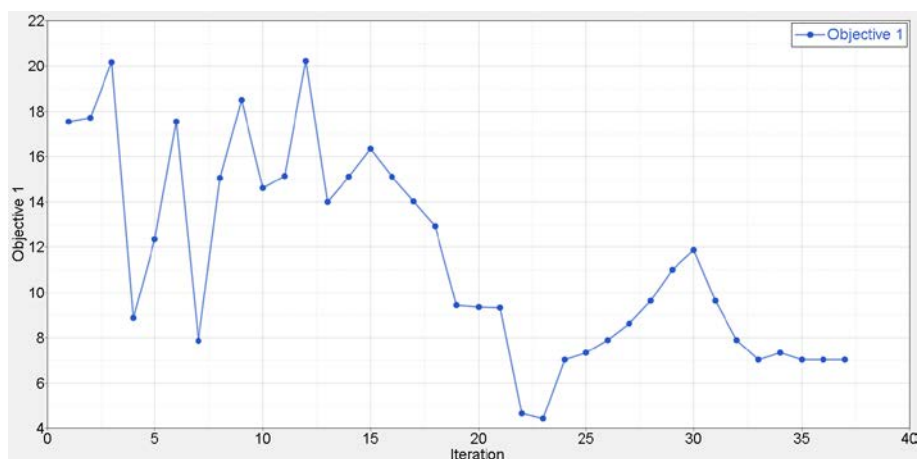


**Fig. 9.** The history of optimization by iterations (root-mean-square difference).

As a result, the root-mean-square difference between the curves was reduced by more than four times.

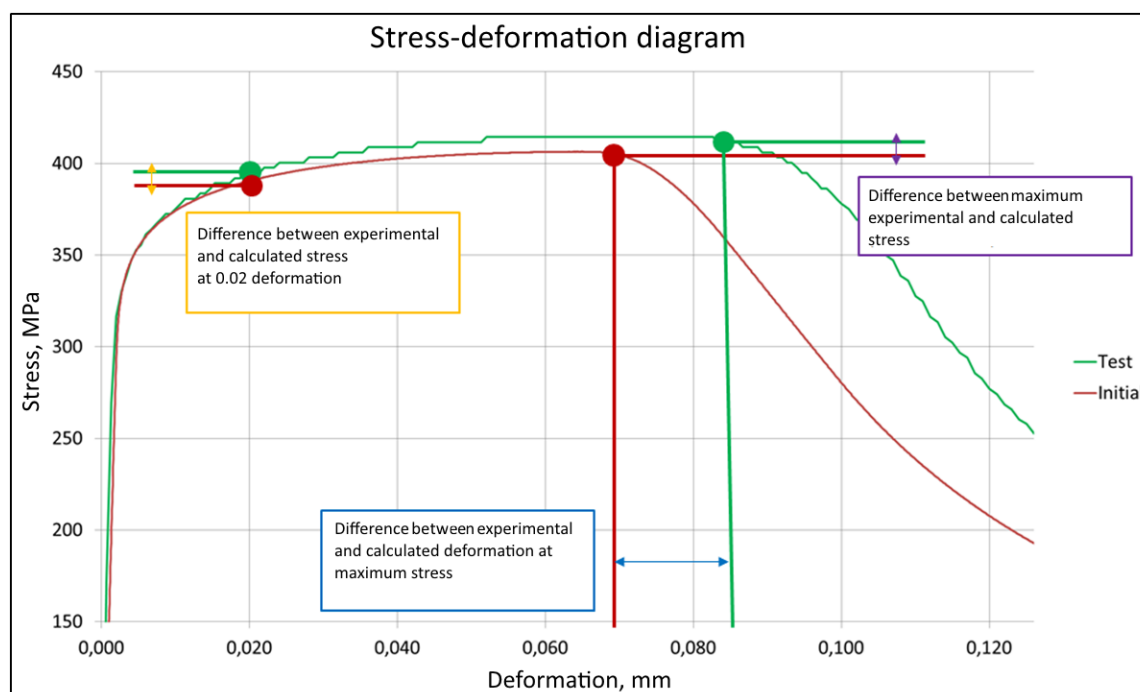


**Fig. 10.** Characteristic points for optimization.

**Determination of values in characteristic points.** Optimization responses are the values of stresses and strains at characteristic points of the curve, with a deformation of 0.02 mm, and also with the maximum stresses achieved (Fig. 10). Targets for these parameters are taken from the experimental curve; the achievement of these parameters is the goal of the optimization.

The history of optimization by iterations is shown in Fig. 11. As a result, of optimization, all indicators reached their target values.

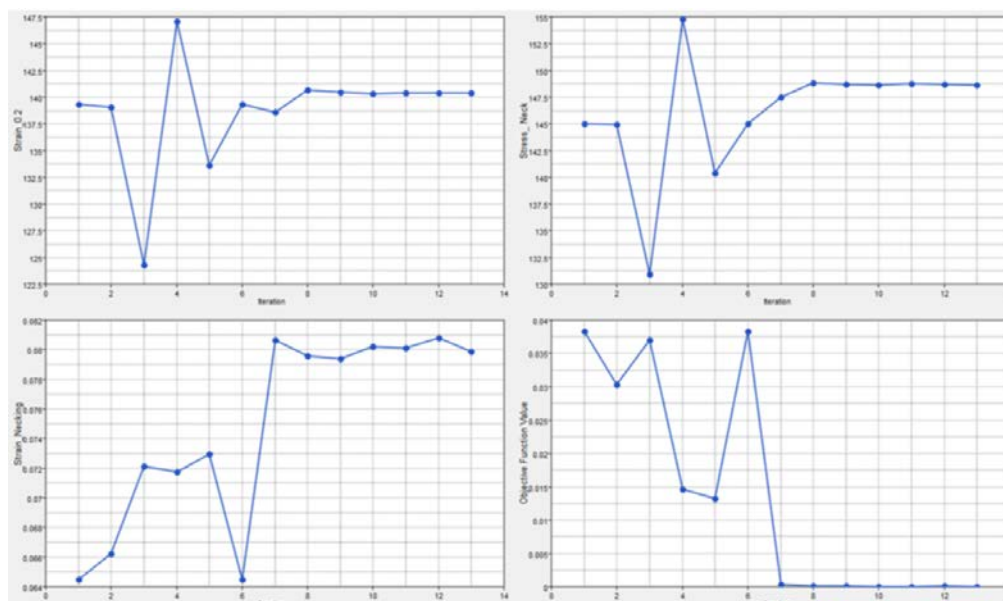


**Fig. 11.** The history of optimization by iterations (characteristic points).

**Comparison of results.** Optimization for each type of objective functions was carried out using the same convergence conditions. The resulting comparative criterion for estimating the coincidence of the calculated curve with the experimental estimate is the root-mean-square averaged difference in their ordinates. Time of optimization is also one of the important parameters for comparison. Table 2 compares the three optimizations using different objective functions.

Table 2. Comparison of results with the use of various objective functions.

| Objective function                          | RMS average | Number of Iterations |
|---|-------------|----------------------|
| Minimization of area                        | 9,19        | 17                   |
| Minimization of root-mean-square difference | 7,51        | 37                   |
| Fitting of values at characteristic points  | 7,24        | 13                   |

Comparative analysis shows that minimizing the root-mean-square difference and adjusting the values at characteristic points gives the same results in terms of deviation from the experimental curve. But in terms of time required for optimization, minimizing the root-mean-square difference takes about three times the fitting of values at characteristic points.

A visual comparison of the stress-deformation diagrams obtained for various optimizations is shown in Fig. 12.

Comparison of the root-mean-square deviation and the visual behavior of the deformation diagram showed that the best objective function for parametric optimization of the physical-mechanical properties of the material is to "adjust values at characteristic points".

#### 4. Conclusions

For the validation of the mathematical model of material used to solve problems on shock phenomena and high-speed deformations, the most effective approach to parametric optimization is the method of characteristic points, which turned out to be more accurate than

the mean-square averaging method. The method of optimization by area has proven to be insufficiently precise, therefore is not recommended for further practical implication.

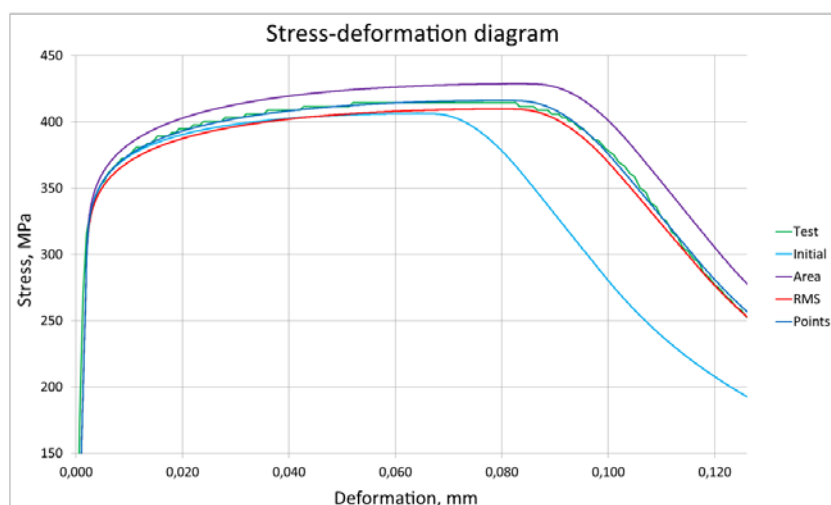


**Fig. 12.** Comparison of stress-deformation diagrams.

### Acknowledgements

The work is carried out with financial support of the Ministry of Education and Science of the Russian Federation within the framework of the Federal Program "Research and Development in Priority Areas for the Development of the Russian Science and Technology Complex for 2014-2020", Activity 1.3., Agreement on the Grant No. 14.578.21.0206 of 03.10.2016, the unique identifier of the program of research and experimental works: RFMEFI57816X0206.

### References

- [1] GOST 380-2005 *Common quality carbon steel. Grades.*
- [2] G.R. Johnson, W.H. Cook, In: *Proceedings of 7-th Symposium on Ballistics* (Hague, Netherlands, 1983), p. 541.
- [3] T. Ozel, Y. Karpat // *Materials and Manufacturing Processes* **22** (2007) 659.
- [4] M.J. Loikkanen, M. Buyuk, C. Kan, N. Meng, In: *Proceedings of 5-th European LS-DYNA Users Conference* (Birmingham, UK, 2005), CD-ROM format, Article 3c, p. 79.
- [5] R.H. Gallagher, *Finite Element Analysis. Fundamentals* (Mir, Moscow, 1984).
- [6] J.O. Hallquist, *LS-DYNA: Theoretical manual* (Livermore Software Technology Corporation, Livermore, 1998).
- [7] J.S. Sun, K.H. Lee, H.P. Lee // *Journal of Material Processing Technology* **105** (2000) 110.
- [8] G.R. Johnson, W.H. Cook // *Engineering Fracture Mechanics* **21(1)** (1985) 31.
- [9] N.S. Selutina, *Destruction and plastic deformation of structural materials under shock wave loads. PhD Thesis* (Saint-Petersburg State University, St. Petersburg, 2016).
- [10] V.M. Kosenkov, V.M. Bychkov // *Applied Mechanics and Technical Physics* **53(6)** (2012) 134.
- [11] A.V. Sobolev, M.V. Radchenko // *Journal of the Russian Universities. Nuclear Energy* **3** (2016) 82.
- [12] V.A. Kuzkin, D.S. Mihaluk // *Computational Mechanics of Continuous Media* **3(1)** (2010) 32.
- [13] A.A. Hodko // *Aerospace Engineering and Technology* **5(112)** (2014) 11.
- [14] GOST R ISO 5700-2008 *Wheeled tractors for agriculture and forestry. Roll-over protective structures. Static test method and acceptance conditions.* (In Russian).

# ON USING QUASI-RANDOM LATTICES FOR SIMULATION OF ISOTROPIC MATERIALS

Vadim A. Tsaplin<sup>2</sup>, Vitaly A. Kuzkin<sup>1,2\*</sup>

<sup>1</sup>Peter the Great Saint Petersburg Polytechnic University, Saint Petersburg 195251, Russia,

<sup>2</sup>Institute for Problems in Mechanical Engineering RAS, Saint Petersburg 199178, Russia,

\*e-mail: kuzkinva@gmail.com

**Abstract.** Elastic properties of three-dimensional lattices are usually anisotropic. This fact limits the range of applicability of lattice models in solid mechanics problems. In the present paper, we propose a simple three-dimensional lattice model with isotropic elastic properties. A quasi-random lattice is generated by randomly displacing particles of the face-centered cubic lattice. Then particles are connected by linear and angular springs such that initially forces in all springs are equal to zero. It is shown numerically that the resulting quasi-random lattice has isotropic elastic properties, provided that amplitudes of random displacements are sufficiently large. Poisson's ratio of the lattice depends on number of angular springs per particle and stiffnesses of these springs. In the present model, values of Poisson's ratio belong to the interval [0;0.41]. The model can be used, in particular, for simulation of deformation and brittle fracture of rocks in hydraulic fracturing.

**Keywords:** particle dynamics; quasi-random lattice; face-centered cubic lattice; effective elastic properties; isotropy; molecular dynamics.

## 1. Introduction

Discrete mechanical models are widely used for simulation of deformation and fracture of materials at different length scales [1,2]. In these models, a material is represented as a set of interacting particles (e.g. material points or rigid bodies). Then mechanical properties of the material are determined by its structure (particle positions) and interparticle interactions.

Specifying initial positions of particles (structure of the material) can be a challenge [1]. The simplest arrangement of particles is a perfect lattice. If crystals are concerned, lattices arise naturally. For other materials, lattices are used as coarse-grained models [3-5]. Advantage of lattice models is that, in many cases, relations between microscopic and macroscopic properties of the material can be derived analytically [4,6-9]. Therefore calibration of model parameters (e.g. parameters of interparticle interactions) is relatively straightforward. At the same time, symmetry of lattices significantly influence their mechanical properties. In particular, elastic properties of three-dimensional lattices are usually anisotropic (see e.g. [1, 9, 10,11]). Influence of lattice symmetry on fracture processes is even more pronounced. Therefore for simulation of isotropic materials, more complicated irregular packings of particles should be used.

A natural way for simulation of isotropic materials is generation of random (amorphous) [5,12-14] or polycrystalline structures [15]. For example, algorithms for generation of random close-packings of spheres are proposed, in papers [13,14]. Creation of polycrystalline materials is discussed in paper [15]. However, implementation of

algorithms [13-15] is relatively time-consuming, especially in three-dimensional case. Therefore, more efficient and simple algorithms are required.

In the present paper, we present a simple discrete model with isotropic elastic properties. Quasi-random lattice is generated. Particles in the lattice are connected by linear and angular springs. It is shown that proper choice of parameters of the model allows to simulate isotropic materials with prescribed elastic moduli.

## 2. Generation of the quasi-random lattice

The quasi-random lattice is generated as follows. Initially, the particles form a perfect face-centered cubic lattice (FCC). Radius vectors of the particles have form

$$\mathbf{R}_{nmk} = a(n \mathbf{e}_1 + m \mathbf{e}_2 + k \mathbf{e}_3), \quad a = \frac{d}{\sqrt{2}}, \quad (1)$$

where  $n, m, k, \frac{n+m+k}{2}$  are integers,  $\mathbf{e}_1, \mathbf{e}_2, \mathbf{e}_3$  are orthogonal unit vectors,  $2a$  is the lattice spacing.

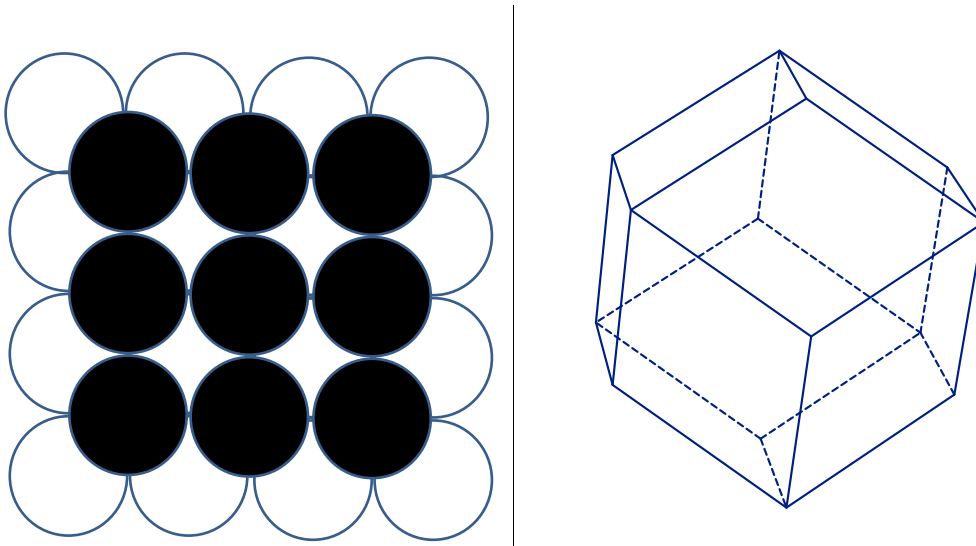


**Fig. 1.** Two layers of particles (left) and a unit cell (right) of the FCC lattice.

Particles are randomly displaced from their positions given by formula (1). Amplitudes of random displacements are chosen according to the following algorithm. The minimum distance,  $d_{min}$ , between the particles is specified. For each particle, the corresponding unit cell is constructed. The particle is connected to 12 nearest neighbors by line segments. Then planes, orthogonal to segments, and passing through their centers are drawn. The unit cell is a body bounded by these planes. In the case of FCC, the unit cell has a shape of rhombic dodecahedron (see figure 1). The unit cell is compressed by the following factor:

$$k_{dev} = 1 - \frac{d_{min}}{d} \quad (2)$$

Random displacements of particles are chosen such that the following three conditions are satisfied. Firstly, the particle belong to the compressed unit cell. Secondly, the particle is outside the sphere, inscribed into the compressed cell. Thirdly, the particle is outside the cube such that midpoints of its edges coincide with middle points of sides of the compressed unit cell. Thus, particle positions belong to the volume given by the difference between the compressed unit cell and union of the inscribed sphere and the cube.

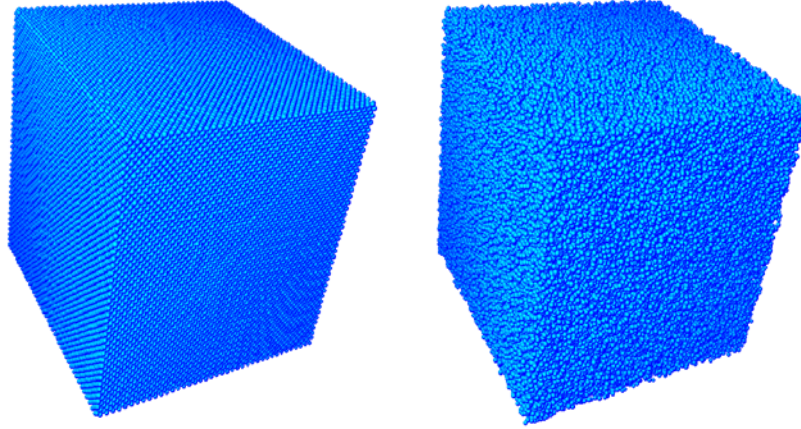


**Fig. 2.** Regular FCC lattice ( $k_{\text{dev}} = 0$ , left) and quasi-random lattice ( $k_{\text{dev}}=0.7$ , right).

Thus, amplitude of particle displacements is determined by parameter  $k_{\text{dev}}$ . For  $k_{\text{dev}} = 0$ , particles form a perfect FCC lattice. For  $0 < k_{\text{dev}} < 1$ , particle positions are random. At the same time, particles remain in their unit cells. Therefore, the lattice is referred to as the quasi-random.

Interparticle interactions are described by linear springs. Two particles are connected by the spring, if the distance between them is less than  $a_{\text{cut}}$ . Equilibrium length of the spring is equal to the initial distance between particles. Therefore initially forces in all springs are equal to zero. Force  $\mathbf{F}_{ij}$  acting between particles  $i, j$  is calculated as

$$\mathbf{F}_{ij} = c_{ij}(R_{ij} - d_{ij})\mathbf{e}_{ij}, \quad (3)$$

where  $\mathbf{e}_{ij} = \frac{\mathbf{R}_{ij}}{R_{ij}}$ ,  $\mathbf{R}_{ij} = \mathbf{R}_j - \mathbf{R}_i$ ,  $c_{ij}$  is the bond stiffness,  $d_{ij}$  is the equilibrium bond length.

The bond stiffness is inversely proportional to bond length, i.e.

$$c_{ij} = c_L \frac{d}{d_{ij}}, \quad (4)$$

where  $c_L$  is characteristic value of the bond stiffness,  $d$  is the characteristic distance between neighboring particles, given by formula (1).

Thus, elastic properties of the quasi-random lattice depend on four parameters:  $c_L$ ,  $d$ ,  $a_{\text{cut}}$ ,  $k_{\text{dev}}$ . In the following sections, we show that fitting these parameters yields isotropic material with prescribed elastic properties.

### 3. Isotropy of the quasi-random lattice

In the present section, we show that a proper choice of random displacements of particles ( $k_{\text{dev}}$ ) allows to create a material with isotropic elastic properties.

Elastic properties of the quasi-random lattice are calculated numerically as follows. By construction, the lattice is orthotropic and it has cubic symmetry. Therefore two test problems are sufficient for calculation of elastic properties. In the first problem, the cubic sample under periodic boundary conditions is subjected to uniform uniaxial strain,  $\varepsilon_{11}$ . Normal stresses in the direction of stretching,  $\sigma_{11}$ , and in the orthogonal direction,  $\sigma_{22}$ , are calculated. Then coefficients of the stiffness tensor  $C_{11}, C_{12}$  are calculated as

$$C_{11} = \frac{\sigma_{11}}{\varepsilon_{11}}, \quad C_{12} = \frac{\sigma_{22}}{\varepsilon_{11}} \quad (5)$$

In the second problem, the cubic sample is subjected to uniform shear deformation,  $\varepsilon_{12}$ . Corresponding shear stresses are calculated. Then the stiffness coefficient is as follows

$$C_{44} = \frac{\sigma_{12}}{2 \varepsilon_{12}} \quad (6)$$

Thus, the test problems yield components  $C_{11}, C_{12}, C_{44}$  of the stiffness tensor.

Anisotropy of the material is characterized by the following parameter [10]:

$$\eta = \frac{2C_{44}}{C_{11}-C_{12}} \quad (7)$$

The anisotropy parameter  $\eta$  is equal to 1 for isotropic materials. Since  $\eta$  is dimensionless, then it depends only on dimensionless parameters of the model  $k_{\text{dev}}$  and  $a_{\text{cut}}/d$ . The value of  $a_{\text{cut}} = 1.9d$  was chosen using trial and error approach in the problem of crack propagation. This value ensures that strength of the lattice is isotropic. Therefore it is sufficient to consider the dependence of  $\eta$  on  $k_{\text{dev}}$ . Parameters of numerical simulations are summarized in table 1.

Table 1. Numerical parameters used for calculation of elastic properties. Here  $\beta_{\text{cr}} = \sqrt{c_L m}$ ,  $m$  is particle's mass. Leapfrog integration scheme is used.

|   |   |
|---|---|
| Interaction radius ( $a_{\text{cut}}$ )   | $1.9 d$   |
| Size of the computational domain  | $28 d$  |
| Initial deformation ( $\varepsilon_{11} = \varepsilon$ , $\varepsilon_{12} = \varepsilon/2$ ) | $\varepsilon = 10^{-4}$   |
| Viscous friction coefficient  | $1.0 \cdot \beta_{\text{cr}}$   |
| Time step   | $0.02 \pi \left(\frac{d_{\text{min}}}{d}\right)^{1/2} \sqrt{\frac{m}{c_L}}$ |

Resulting dependence of the anisotropy parameter,  $\eta$ , on the amplitude of random displacements of particles ( $k_{\text{dev}}$ ) is shown in figure 3. As expected, the anisotropy parameter decreases for sufficiently large  $k_{\text{dev}}$ . Isotropy of elastic properties is reached at  $k_{\text{dev}} \approx 0.67$ .

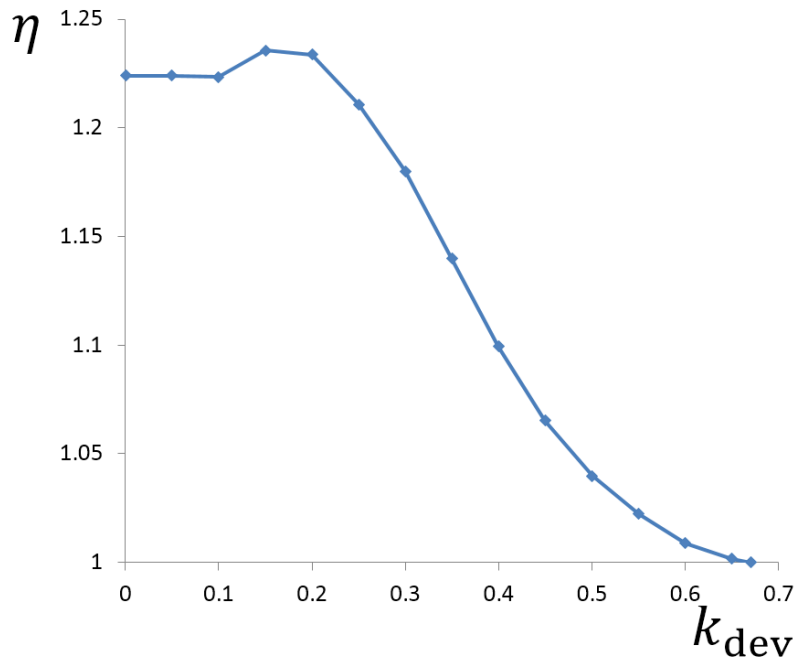


**Fig. 3.** Dependence of the anisotropy parameter on the amplitude of random displacements of particles ( $a_{\text{cut}} = 1.9 d$ ). Points show the results averaged over 10 realizations.

#### 4. Changing Poisson's ratio of the quasi-random lattice

Elastic properties of the isotropic material, described in the previous section, are characterized by Young's modulus and Poisson's ratio. Proper choice of bond stiffnesses,  $c_L$ , allows to fit any value of Young's modulus. At the same time, Poisson's ratio of this material is fixed. Numerical simulations show that it is equal to 0.255. In the present section, we show that adding three-particle interactions (angular springs) allows to change Poisson's ratio in the interval from 0 to 0.414.

Potential energy of the spring connecting pairs of particles  $i, j$  and  $i, k$  reads

$$\Pi = \frac{1}{2} c_\varphi (\varphi - \varphi_0)^2, \quad (8)$$

where  $c_\varphi$  is the stiffness of angular spring,  $\varphi$  is the angle between the bonds,  $\varphi_0$  is the initial value of  $\varphi$ . Forces acting on particles  $i, j, k$ , caused by the spring, are the following

$$\mathbf{F}_j = \frac{c_\varphi}{R_{ij}} \Delta\varphi \times \mathbf{e}_{ij}, \quad \mathbf{F}_k = -\frac{c_\varphi}{R_{ik}} \Delta\varphi \times \mathbf{e}_{ik},$$

$$\Delta\varphi = (\varphi - \varphi_0) \frac{\mathbf{e}_{ij} \times \mathbf{e}_{ik}}{|\mathbf{e}_{ij} \times \mathbf{e}_{ik}|}, \quad \mathbf{F}_i = -\mathbf{F}_j - \mathbf{F}_k, \quad (9)$$

where  $\mathbf{e}_{ij} = \frac{\mathbf{R}_{ij}}{R_{ij}}$ ,  $\mathbf{R}_{ij} = \mathbf{R}_j - \mathbf{R}_i$ ,  $\mathbf{R}_i$  is radius vector of particle  $i$ .

Angular springs are added using the following algorithm. For particle number  $i$ , all neighbors are found such that for each neighbor,  $j$ , the inequalities  $L_{\min} < R_{ij} < a_{\text{cut}}$  are satisfied. Then all different triples  $i, j, k$  are formed such that distances  $R_{ij}$ ,  $R_{ik}$ , and  $R_{jk}$  are all greater than  $L_{\min}$ . For each of these triples, three angular springs (in all three angles) are introduced. Stiffness of the angular spring between pairs  $i, j$  and  $i, k$  depends on lengths  $R_{ij}$ ,  $R_{ik}$  as follows

$$c_\varphi = c_{\varphi_0} \left( \frac{\min(R_{ij}, R_{ik})}{d} \right)^2 \quad (10)$$

For now on, the model has two additional dimensionless parameters  $c_{\varphi_0}/(c_L d^2)$  and  $L_{\min}/d$ . These parameters are used in order to change Poisson's ratio of the quasi-random lattice. Dependence of Poisson's ratio on stiffness of the angular spring for fixed  $L_{\min} = 1.7d$  is shown in figure 4.

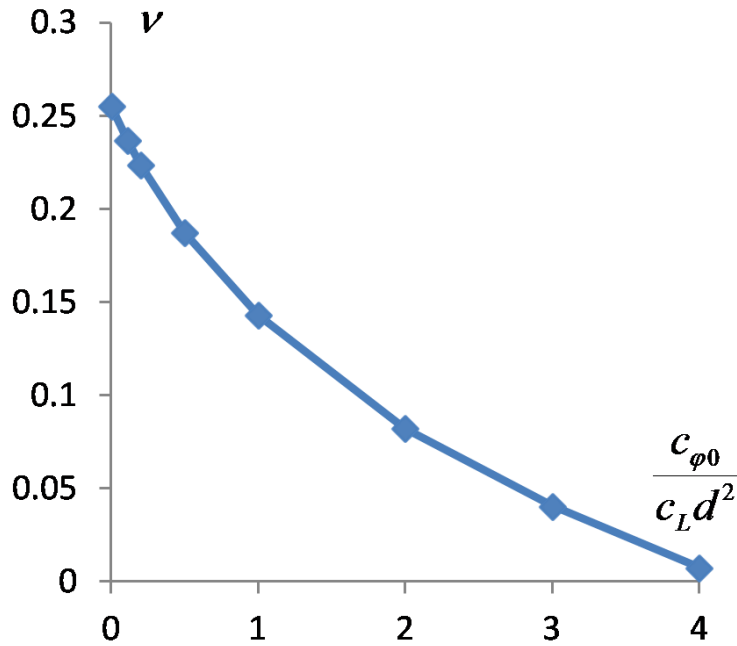


**Fig. 4.** Dependence of Poisson's ratio on angular stiffness  $c_{\varphi_0}/(c_L d^2)$ .

It is seen that increasing the angular stiffness, we change Poisson's ratio in the interval from 0.255 (for  $c_{\varphi_0} = 0$ ) to 0 (for  $c_{\varphi_0} \approx 4c_L d^2$ ).

In order to achieve Poisson's ratios larger than 0.255, angular springs with negative stiffness should be used. Then we fix  $c_{\varphi_0} = -0.11c_L d^2$  and change the ratio  $L_{\min}/d$ . The ratio controls the average number of angular springs per particle. For  $L_{\min} = a_{\text{cut}} = 1.9d$ , angular springs are absent. The dependence of Poisson's ratio on  $L_{\min}/d$  is shown in figure 5.

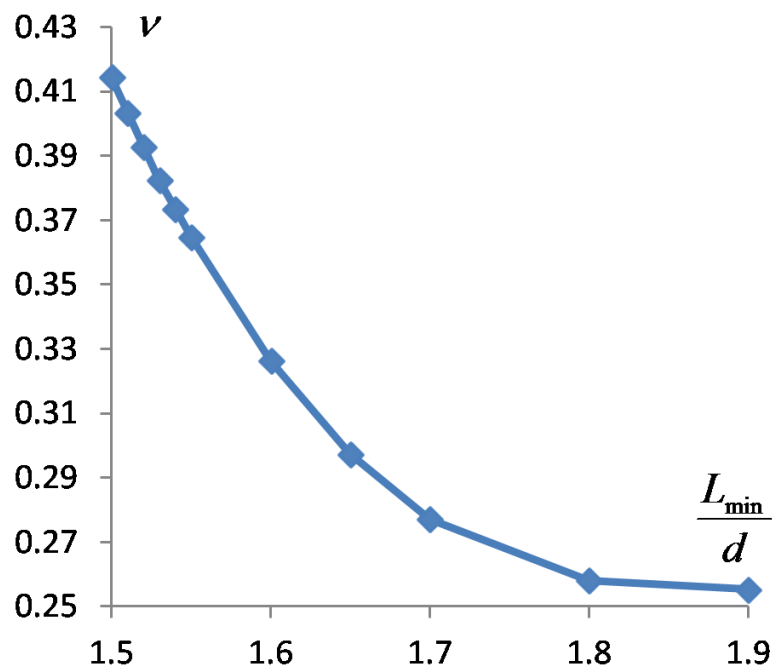


**Fig. 5.** Dependence of the Poisson's ratio on number of angular springs per particle, controlled by parameter  $L_{\min}/d$ .

Thus changing the number of angular springs per particle (parameter  $L_{\min}/d$ ), values of Poisson's ratio up to 0.414 can be reached.

## 5. Conclusions

An algorithm for generation of three-dimensional quasi-random lattices was presented. Particle positions were generated by randomly displacing nodes of the face-centered cubic lattice. It was shown that elastic properties of the quasi-random lattice are isotropic, provided that the amplitude of random displacements is sufficiently large. In order to control both Young's modulus and Poisson's ratio of the material, the particles were connected by linear and angular springs. Choosing stiffness of linear springs, any value of Young's modulus can be fitted. Angular springs allows to change Poisson's ratio in the interval  $[0; 0.414]$ , which is sufficient in many applications. Simulation of incompressible materials ( $\nu = 0.5$ ) remains a challenge.

The presented model can be generalized in order to simulate brittle fracture. A criterion for bond breakage should be added. Then preliminary calculations show that if elastic properties of the quasi-random lattice are isotropic, then its strength is also isotropic. Therefore, the model can be used, for example, for simulation of crack propagation in isotropic materials. In particular, hydraulic fracturing in naturally fractured reservoirs [16] can be simulated. However, detailed discussion of crack propagation is beyond the scope of the present paper.

**Acknowledgements.** This work was supported by Ministry of Education and Science of the Russian Federation within the framework of the Federal Program "Research and development in priority areas for the development of the scientific and technological complex of Russia for 2014-2020" (activity 1.2), grant No. 14.575.21.0146 of September 26, 2017, unique identifier: RFMEF157517X0146. Industrial partner of the project is LLC "Gazpromneft NTC". The authors are deeply grateful to A.M. Krivtsov, G.V. Paderin and E.V. Shel for useful discussions.

**References**

- [1] A.M. Krivtsov, *Deformation and fracture of solids with microstructure* (Fizmatlit, Moscow, 2007). (in Russian).
- [2] R.V. Goldshtein, N.F. Morozov // *Physical Mesomechanics* **10** (2007) 17.
- [3] A.A. Vasiliev, S.V. Dmitriev, Y. Ishibashi, T. Shigenari // *Physical Review B* **65** (2002) 094101.
- [4] Y. Wang, P. Mora // *Journal of the Mechanics and Physics of Solids* **56** (2008) 3459.
- [5] P.D. Beale, D.J. Srolovitz // *Physical Review B* **37** (1988) 5500.
- [6] E.A. Ivanova, A.M. Krivtsov, N.F. Morozov // *Doklady Physics* **47** (2002) 620.
- [7] E.A. Ivanova, A.M. Krivtsov, N.F. Morozov // *Journal of Applied Mathematics and Mechanics* **71** (2007) 543.
- [8] I.E. Berinskii, E.A. Ivanova, A.M. Krivtsov, N.F. Morozov // *Mechanics of Solids* **42** (2007) 663.
- [9] I.E. Berinskii, A.M. Krivtsov // *Mechanics of Solids* **45** (2010) 815.
- [10] A.M. Krivtsov, *Theoretical mechanics. Elastic properties of monoatomic and diatomic crystals* (SPb: Izd. Polytechn. Univ. 2009). (in Russian).
- [11] M. Born, H.Kun, *Dynamical theory of crystal lattices* (Clarendon Press, Oxford, 1954).
- [12] D.O. Potyondy, P.A. Cundall // *International Journal of Rock Mechanics and Mining Science* **41** (2004) 1329.
- [13] A.Z. Zinchenko // *Journal of Computational Physics* **114** (1994) 298.
- [14] D. He, N.N. Ekere, L. Cai // *Physical Review E* **60** (1999) 7098.
- [15] A.M. Krivtsov // *Meccanica* **38** (2003) 61.
- [16] T. Bratton, D.V. Cahn, N.V. Que, N.V. Duc, P. Gillespie, D. Hunt, B. Li, R. Marcinew, S.Ray, B. Montaron, R. Nelson, D. Schoderbek. L. Sonneland // *Oilfield Review* **18** (2006) 4.

# REVIEW OF THE COMPUTATIONAL APPROACHES TO ADVANCED MATERIALS SIMULATION IN ACCORDANCE WITH MODERN ADVANCED MANUFACTURING TRENDS

A.V. Shymchenko\*, V.V. Tereshchenko, Y.A. Ryabov, S.V. Salkutsan, A.I. Borovkov

<sup>1</sup>Peter the Great St. Petersburg Polytechnic University, Polytechnicheskaya, 29, St. Petersburg, 195251, Russian Federation

\*e-mail: shimchenko\_av@spbstu.ru

**Abstract.** In order to be competitive, modern manufacturers have to offer best-in-class products. Superior quality of the product requires introduction of new materials, digital design methods and advanced manufacturing technologies into production process. Special attention is given to numerical simulation as the most time efficient, flexible and cheap method to evaluate the level of optimality and viability of the proposed solution as well as to predict further Product Life-Cycle. Accurate setting of material properties and representation of complex material structure is crucial for product design employing simulation. Commonly, material representation for simulation purpose is based on the analytical relationships that provide approximate data and cannot provide multiscale information about structure. Initiation of Material Genome Initiative (MGI) as well as the study of Big Data and Machine Learning concepts leads to development of new, more accurate and reliable instruments for product design that involve material simulation and optimization of material selection process.

**Keywords.** Factory of Future (FoF), Material Genome Initiative (MGI), Integrated Computational Materials Engineering (ICME), Computer-Aided Engineering, Big-Data, Machine Learning.

## 1. Introduction

Nowadays, there is keen interest in development of advanced manufacturing. This interest has been embodied in emergence of some programs and initiatives such as Industry 4.0, Industry + and Advanced Manufacturing Partnership 2.0. Taking into account these trends, a lot of studies are dedicated to automatization and digitalization of manufacturing processes as the key instruments to build the Factories of Future (FoF). The modern computer design systems such as Computer-Aided Design (CAD), Computer-Aided Engineering (CAE) and Computer-Aided Optimization (CAO), improve quality of products and reduce final costs of produced goods. The modern machine tools and equipment have computer numerical control (CNC) that in combination with Computer-Aided Manufacturing (CAM) allows to reduce the time of manufacturing of highly-customized products. Simultaneously the utilization of Internet of Things (IoT) leads to optimization of the whole production process and enables control over the product data and characteristics at all stages of manufacturing.

One more way to improve manufacturing process is to introduce advanced materials. Although, the advanced materials aren't directly related to advanced manufacturing or FoF concepts, the application of this group of resources is often vital to create the designed best-in-class products and implement advanced manufacturing technologies. The importance of materials to key industry sectors and technologies is widely recognized all over the world. For

this reason, there are advanced materials-related strategies in countries that seek to increase the competitiveness of their industry. For example, the US Advanced Manufacturing Strategy that identifies advanced materials as a critical ‘cross-cutting technology’ R&D priority underpinning advanced manufacturing competitiveness. [1] In fact, most of the advanced manufacturing roadmaps and strategies highlight the important role of advanced materials for novel production technologies such as additive manufacturing (AM) or technologies related to robotics and autonomous systems. [1] For example, successful application of Additive technologies as well as the quality of printed products directly depends on the applied materials. Not only have the advanced materials a significant impact on manufacturing stage but also on such crucial stage as product design where the design characteristics of the product that constitute its global competitiveness are defined and ensured.

The usage of computer-aided techniques at the design stage allows to substantially decrease the cost and production time of the whole manufacturing process. In this case, the first step (Simulation-Based Design) becomes the most expensive part of manufacturing process. However, this expenditure allows to reduce or completely eliminate the subsequent cycles of physical product testing and production changeovers (Fig. 1). Thus, the accurate and reliable simulation models is required. Nowadays, there are a lot of various instruments and methods for calculation of complex structures. However, the key input data for each of them consists of the material properties and the representation of material structure. Taking into account the rapid development of material science, the modern numerical algorithms and approaches for simulation of material characteristics during Simulation-based design stage are of particular interest. The implementation of these methods as an integral part of FoF concept can significantly increase the quality of manufactured goods and provide the manufacturing of “best-in-class” products.

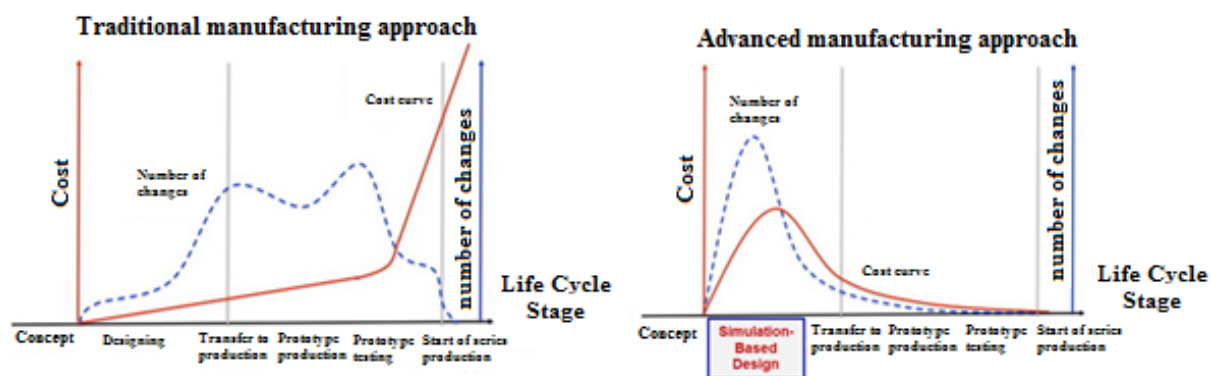


**Fig. 1.** The impact of computer simulation and design approach on the manufacturing cost[2].

This work provides a review of the most efficient solutions for material simulation and modeling for product design purposes. Fiber-reinforced composite material as the most common and representative advanced material type is discussed in this work. The work is organized as follows. The Section 2 presents a general description of traditional computational simulation of advanced materials using an example of a fiber-reinforced composite materials. The Section 3 provides information about modern approaches based on the combination of experimental and computational instruments, an open data bases as well as several frameworks for integration of various software tools. The Section 4 includes a comparison between traditional and modern approaches and provides general information about usage of Big Data concept for product design purposes.

## 2. Modelling of material properties in numerical simulation-based design

Substantial development of computing systems as well as the emergence of high-performance computer machines made the computational analysis of composite materials more effective and attractive compared to analytical methods based on solid mechanics. Computational analysis of composite structure and behavior in case of load application is based on the use of numerical integration of the state equations by transforming the system of partial differential equations to a system of linear and linearized algebraic equations with the subsequent solution by means of the mathematical apparatus of the calculus of variations. [3] Nowadays, the finite-element method (FEM) is a commonly used numerical algorithm realized in analytical software applicable for this purpose. The application of FEM as the computational tool is associated with calculation of a significant number of equations and requires high-performance computing resources. However, this method is able to perform calculation of samples with complex geometry and structure. The advantages associated with calculation of complex geometry by usage of linear and linearized equations systems are achievable only through realization of function of the sample partition to the nodes and finite-elements. In case of computing software this partition is realized as meshing step. [3]

The automation sample meshing is realized on the base of mathematical approaches such as Delaunay triangulation and Advancing Front (AF) approaches. [4] Both approaches are widely used to create tetrahedral (tet) mesh. However, there are differences between these methods. AF is based on adding mesh elements starting at the boundaries by inserting one new point or merging different existing points. In this case, the main criteria of adequate triangulation is the intersection absence. The disadvantage of AF method is a very complex analysis of the partition region and surroundings of mesh elements. In that case the Delaunay triangulation is more flexible. For performing this method, the other triangulation methods may be used as the base segmentation. The subsequent algorithm implies checking compliance of base triangulation with Delaunay requirements and further improvement when necessary. In general, the triangulation satisfies Delaunay condition, if none of the given triangulation points fall within the area inside of the circle escribed around any of the built triangles. However, in case of conformity check, the algorithms are based on the theorem that can be formulated as *“Among all possible triangulations, in case of Delaunay triangulation there is the maximum sum of the smallest angles of all built triangles”* The requirement complemented by the theorem provides four analytical instruments for conforming check:

1. Use of the circumscribed circle equation.

The equation of circle circumscribed the triangles built on points  $(x_1, y_1), (x_2, y_2), (x_3, y_3)$  can be expressed as: [4]

$$(x^2 + y^2) \cdot a - x \cdot b + y \cdot c - d = 0, \quad (1)$$

where

$$a = \begin{vmatrix} x_1 & y_1 & 1 \\ x_2 & y_2 & 1 \\ x_3 & y_3 & 1 \end{vmatrix}, b = \begin{vmatrix} x_1^2 + y_1^2 & y_1 & 1 \\ x_2^2 + y_2^2 & y_2 & 1 \\ x_3^2 + y_3^2 & y_3 & 1 \end{vmatrix}, c = \begin{vmatrix} x_1^2 + y_1^2 & x_1 & 1 \\ x_2^2 + y_2^2 & x_2 & 1 \\ x_3^2 + y_3^2 & x_3 & 1 \end{vmatrix}, d = \begin{vmatrix} x_1^2 + y_1^2 & x_1 & y_1 \\ x_2^2 + y_2^2 & x_2 & y_2 \\ x_3^2 + y_3^2 & x_3 & y_3 \end{vmatrix}$$

The Delaunay condition is feasible if for any point  $(x_0, y_0)$  does not fall into the circle region. This condition can be expressed as:

$$((x_0^2 + y_0^2) \cdot a - x_0 \cdot b + y_0 \cdot c - d) \cdot \operatorname{sgn} a \geq 0 \quad (2)$$

2. Checking with the previously calculated circumscribed circle.

Use of the circle equation mentioned above, requires a significant number of arithmetic calculations that leads to an increase in computation time. The usage of previously calculated circumscribed circle method allows to overcome this shortcoming. This method is based on the calculation of center  $(x_c, y_c)$  and radius  $r$  of circumscribed circles for each triangle. [4]

$$x_c = \frac{b}{2a}, \tag{3}$$

$$y_c = \frac{-c}{2a}, \tag{4}$$

$$r^2 = \frac{(b^2+c^2-4ad)}{4a^2}, \tag{5}$$

The Delaunay condition is feasible if the distance from any point  $(x_0, y_0)$  to the centre of circle is bigger than radius. [4]

$$(x_0 - x_c)^2 + (y_0 - y_c)^2 \geq r^2 \tag{6}$$

The advantage of this method is the absence of necessity to calculate the parameters of circles for each triangle. The check of Delaunay condition is always performed for pair of triangles, which leads to necessity to calculate the circle just for one of them. That method allows to reduce the amount of calculated circles by 25 - 45% and to reduce the number of arithmetic computations by third.

### 3. Checking of the sum of the opposite angles.

The primary sources of this method are earlier works [5,6]. According to the authors, the Delaunay condition is feasible if for any point  $(x_0, y_0)$  used for area triangulation there is  $\alpha + \beta \leq \pi$ . (Fig. 2)

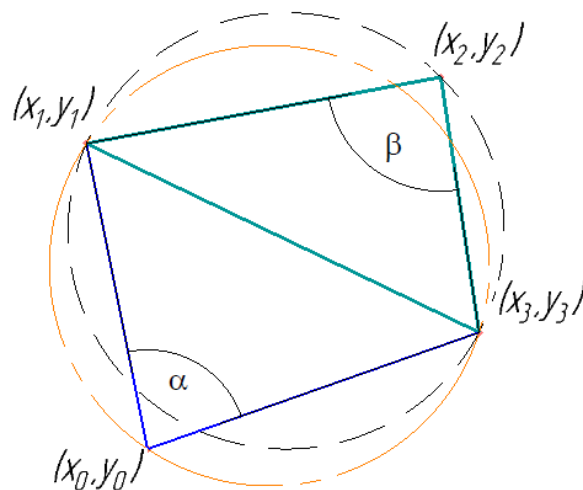


**Fig. 2.** A check the sum of the opposite angles.

This condition can be expressed as [7]:

$$\sin \alpha \cdot \cos \beta + \cos \alpha \cdot \sin \beta \geq 0, \tag{7}$$

where

$$\cos \alpha = \frac{(x_0-x_1)(x_0-x_3) + (y_0-y_1)(y_0-y_3)}{\sqrt{(x_0-x_1)^2 + (y_0-y_1)^2} \sqrt{(x_0-x_3)^2 + (y_0-y_3)^2}} \tag{8}$$

$$\cos \beta = \frac{(x_2-x_1)(x_2-x_3) + (y_2-y_1)(y_2-y_3)}{\sqrt{(x_2-x_1)^2 + (y_2-y_1)^2} \sqrt{(x_2-x_3)^2 + (y_2-y_3)^2}} \tag{9}$$

$$\sin \alpha = \frac{(x_0-x_1)(y_0-y_3) - (x_0-x_3)(y_0-y_1)}{\sqrt{(x_0-x_1)^2 + (y_0-y_1)^2} \sqrt{(x_0-x_3)^2 + (y_0-y_3)^2}} \tag{10}$$

$$\sin \beta = \frac{(x_2-x_1)(y_2-y_3) - (x_2-x_3)(y_2-y_1)}{\sqrt{(x_2-x_1)^2 + (y_2-y_1)^2} \sqrt{(x_2-x_3)^2 + (y_2-y_3)^2}} \tag{11}$$

#### 4. Modified check of the sum of the opposite angles.

This method is similar to ‘checking of the sum of the opposite angles’ method. However, in order to reduce amount of calculation there is a pre-stage that implies partial calculation of equation (7). For this method, the parameters  $s_\alpha$  and  $s_\beta$  must be calculated. [4]

$$s_\alpha = (x_0 - x_1)(x_0 - x_3) + (y_0 - y_1)(y_0 - y_3) \quad (12)$$

$$s_\beta = (x_2 - x_1)(x_2 - x_3) + (y_2 - y_1)(y_2 - y_3) \quad (13)$$

According to [7] if parameters  $s_\alpha$  and  $s_\beta$  are either positive or equal to 0 then the Delaunay condition will be fulfilled. If the  $s_\alpha$  and  $s_\beta$  are both negative then the Delaunay condition will not be fulfilled and triangulation must be improved. The other combinations of these parameter values lead to subsequent calculation by the equation (7). On average, this modified method allows to reduce the number of arithmetic computations by 20 - 40%.

Proposed analytical tools allow to check the correctness of the existing mesh in case of Delaunay triangulation, while the meshing based on Delaunay triangulation is performed by various algorithms such as iterative algorithms, merging algorithms, algorithms for direct construction and two-pass algorithms. Each algorithm is applied for some specific case and is discussed in detail in works [7].

The meshing step is a preparatory stage for subsequent calculations. In general, the existing Computer-aided engineering (CAE) software has solver modules which allows to deal with mechanics, thermomechanics and fluid tasks. In general CAE software is able to provide the following analysis types.

1. Static strength analysis that can provide information about displacement, strain and stress taking place in the sample under mechanical load. The basic equation for this analysis can be expressed as: [7].

$$[K]\{u\} = \{F\}, \quad (14)$$

where  $[K]$  is the stiffness matrix;  $\{u\}$ - displacement vector;  $\{F\}$ - force vector, that can be represented by concentrated forces, temperature loads, pressure and inertia forces.

This type of analysis can be suitable in case of the negligible impact on the structure behavior from action of inertia forces or energy dissipation processes.

2. Dynamic strength analysis can be used for construction study in case of time-dependent load application. The examples of these loads are sudden loads (shocks), cyclic loads (rotation), etc. Analysis of this type of loads is based on equation: [7].

$$[M]\{u''\} + [C]\{u'\} + [K]\{u\} = \{F(t)\}, \quad (15)$$

where  $[M]$  - the mass matrix;  $[C]$ - the damping matrix;  $[K]$ - the stiffness matrix;  $\{u''\}$ - the nodal acceleration vector;  $\{u'\}$  - the nodal speed vector;  $\{u\}$ - the vector of nodal displacement;  $\{F\}$ - the loads vector and  $t$  is the computation time.

The values of variables  $\{u\}$ , that at any instant of time satisfy the equilibrium conditions of the system, are the solution of equation (15).

3. Analysis of the construction stability that allows to define the load level that leads to decrease of stability as well as reverse task - the state of construction under applied load can be performed by linear and nonlinear methods. The analytical equation of linear method is [7].

$$([K] - \lambda[S])\{u\} = 0, \quad (16)$$

where  $[K]$ - the stiffness matrix;  $[S]$ - the matrix of effective stiffness;  $\lambda$ - scale factor;  $\{u\}$ - buckling vector.

Nonlinear method is more complex and accurate method:

$$[K]_{i-1}(\{u\}_i - \{u\}_{i-1}) = \{F\} - \{F^{el}\}_{i-1}, \quad (17)$$

where  $[K]_{i-1}$  is the stiffness matrix at the previous iteration;  $\{u\}_i$ ,  $\{u\}_{i-1}$ - the displacement stiffness at the current and previous iteration respectively;  $\{F\}$  - the vector of applied loads;

$\{F^{el}\}_{i-1}$  - the vector of the elastic forces correspondent to displacements at the previous iteration ( $i-1$ ).

4. Thermal analysis allows to obtain temperature stress and strain, phase transformations, unsteady temperature conditions, etc. The basic equation for this type of analysis can expressed as: [7].

$$[C]\{T'\} + [K]\{T\} = \{Q\}, \tag{18}$$

where  $[C]$  - the matrix of specific heat capacity;  $\{T'\}$  - derivative of temperature;  $[K]$  - the effective thermal conductivity matrix;  $\{T\}$ - vector of nodal temperature;  $\{Q\}$ - the vector of effective heat flux in nodes.

Basic equations of the described analysis contain elements that strongly depend on the properties of construction materials. These parameters are the matrixes of specific heat capacity and effective thermal conductivity for thermal analysis as well as the stiffness matrix for other types of mechanical analysis. For example, stiffness matrix strongly depends on the effective Young's moduli and effective Poisson's ratio. [8]

Traditional bottom-up product design approach involves two simultaneous processes such as design of geometric parameters of product as well as selection of appropriate materials. The information about product functions and conditions of use provides engineers with the information about loading type, concentration and value of stresses that can be used to make an assumption about the required set of material properties. The task of engineers is to choose the material that best meets these requirements. [9]

However, in real application there can be a few materials that allow to fulfill the final product requirements. In this case, the material selection is associated with solution of multi-criteria optimization task. Commonly, material selection charts (Ashby charts) are used to find the most optimal solution. In general, Ashby charts demonstrate material properties plotted against each other on logarithmic scales. Obtained property-space is occupied by each material class and sub-class represented by bubbles that allow to visually compare the combination of properties between various materials. There is a lot of variants of Ashby charts plotted by using combination of about 30 mechanical and thermal properties such as density, Young's moduli, ultimate strength, etc. The example of Young's moduli - density Ashby chart is shown in Fig. 3.

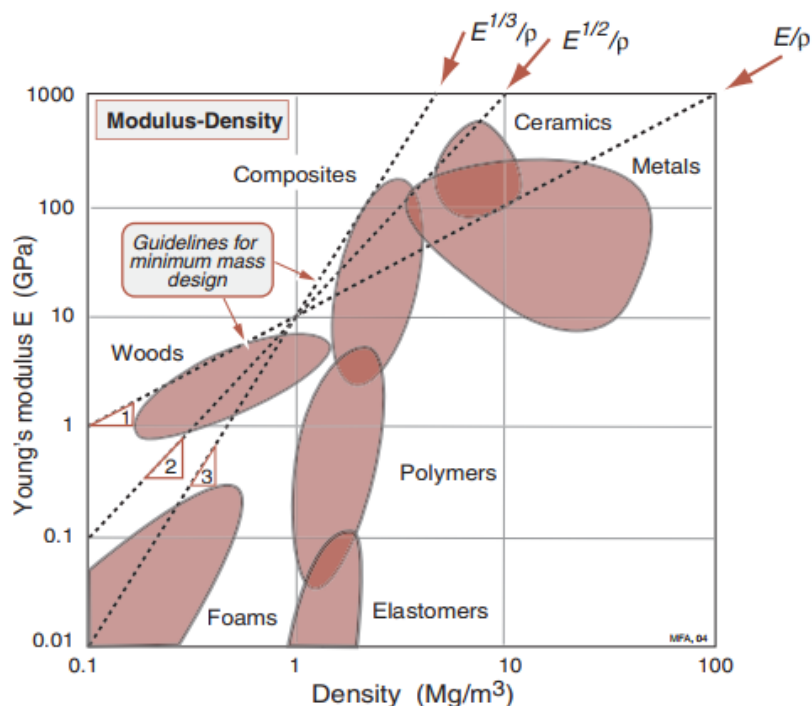


**Fig. 3.** A schematic Young's moduli - density Ashby chart [10].

In general, the Ashby's method of multi-criteria material selection process involves plotting and usage of material indexes that can be obtained analytically. Basically, the product performance criteria ( $P$ ) are the function of loading requirements ( $F$ ), geometry requirements ( $G$ ) and material properties requirements ( $M$ ). [10]

$$P = f(F, G, M) \quad (19)$$

Needless to say, that material selection is based only on material properties requirements. Thus, there is need to separate variables related with material properties from the others. For example, the performance criteria related with design of light and stiff beam (Fig.4) can be represented by system: [10]

$$\begin{cases} m = A \cdot L \cdot \rho \\ \delta_{max} \geq \frac{C_1 E I F}{L^3}, \end{cases} \quad (20)$$

where  $L$  – the length of beam;  $A$  – the beam cross-section;  $\rho$  – the material density;  $E$  – Young's moduli;  $F$  – force applied to beam;  $C_1$  – constant that depends on the load distribution;  $I$  – the second moment of the area of the section, that can be defined as:

$$I = \frac{A^2}{12} \quad (21)$$

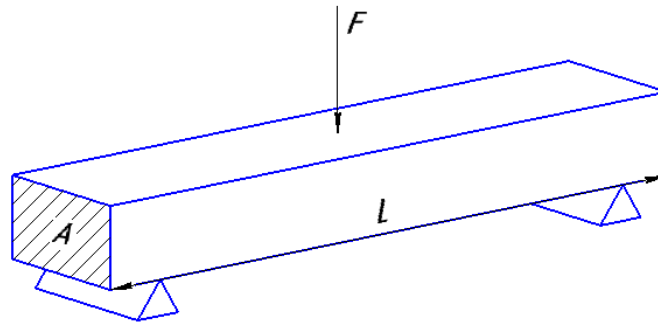


Fig. 4. A beam of square section, loaded in bending [10].

The  $\delta_{max}$  is the permissible value of bending that must not be exceeded. Taking into account equations 20, 21, the optimization of beam mass can be written as:

$$m \geq \sqrt{\frac{12F}{LC_1 \delta_{max}}} \cdot L^3 \cdot \left(\frac{\rho}{E^2}\right) \quad (22)$$

According to equation 22, material properties requirements can be represented as:

$$f(M) = \left(\frac{\rho}{E^2}\right) \quad (23)$$

Therefore, the best materials for a light and stiff beam are those with the smallest values of  $f(M)$ . However, usually engineers invert  $f(M)$  in order to obtain material index. For the considered case, the material index is  $\sqrt{E}/\rho$ . On the Ashby chart, the material index are plotted as a family of straight parallel lines of slope 2 and can be used to find the material with optimal relation of  $\sqrt{E}/\rho$  (Fig. 3). The bubbles crossed by the same straight line present materials with the same value of material index. The material that located under or above the material index line have lower or higher value of  $\sqrt{E}/\rho$  relation, respectively. According to the Fig. 3, some types of composites, wood and ceramics have the greater value of  $\sqrt{E}/\rho$  material index comparing with the metals, polymers and foams. Therefore, in case of presence of composite and metal beams with the same stiffness, the composite beam will be less heavy comparing with the metal one. In works [10], there is description of other material indexes and their applications for engineering tasks.

In order to minimize the search region, the additional limits can be used. Potential materials obtained by the Ashby's method than studied by using supported information in order

to find the best solution. Further, the effective properties of chosen material are used for CAE computation and design confirmation.

The effective properties can be characterized as the averaged material properties of investigated part or whole structure. It is true even in case of analysis of homogeneous materials. The reason is the presence of grains, particles with various dimension and orientation. There is the interaction between these elements that can have influence on the material behavior. However, this interaction can be referred to micro-mechanical investigation. For homogeneous materials the mechanical analysis commonly deals with macro scale that represent level of components and structural parts. The absence of differences in properties on macro scale level allows to avoid the segmentation of calculated structure. On the other hand, the analysis of heterogeneous materials such as composite materials is more complex and requires an investigation on the meso scale (level of composite phases) and micro scale. [11] There are several methods that can be used for property description of composite materials to perform computational analysis.

The most common type of composite materials are plastic materials reinforced by continuous fibers. In fact, this type of composite materials has two types of heterogeneity. The first one is characterized by the presence of two phases such as matrix and reinforcement fibers. The second one represents the heterogeneity provided by layered structure consisting of layers with the certain direction of the fibers ( $0^\circ, 90^\circ, \pm 45^\circ$ ). Commonly for the calculation of the structure behavior and mechanical analysis, only the second type of heterogeneity is taken into account. In these case, the composite material is represented as a number of layers with known properties. [12]

The same approach is commonly used for calculation of lamination composite materials. On the other hand, the structures with fillers represented by spheres, plates, tubes, etc. are commonly exposed to the homogenization process that represents the composite structure as a homogeneous material with effective properties calculated on basis of volume fractions. The study of these composites on the micro scale level is more complex and can be performed when the interaction between matrix and fillers phases must be investigated. [13]

According to [14,15] the minimum set of properties required for computational calculation includes effective Young's modulus along and across of the fibers ( $E_1, E_2$ , respectively) (Fig.5); effective shear modulus  $G_{12}$ ;  $\sigma_{1B}^+, \sigma_{1B}^-$  - ultimate strength under uniaxial tension and compression across the fibers;  $\sigma_{12}^+$  - shear strength;  $\mu_{12}$  - effective Poisson ratio (where the first index shows the direction of load action, while the second - the direction of the relevant transverse deformation), while the  $\mu_{21}$  can be expressed as [15]:

$$\mu_{21} = \mu_{12} \frac{E_2}{E_1} \tag{24}$$

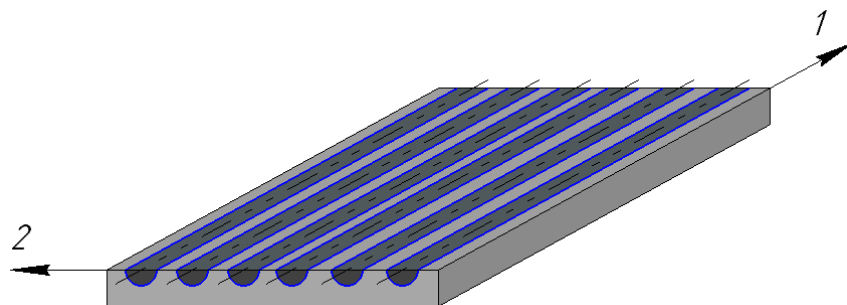


**Fig. 5.** Cross-section of unidirectional monolayer.

In case of multilayer composite materials reinforced by continuous fibers the set of effective properties must be provided for each layer that is accepted as the homogeneous structure. This process is known as homogenization and is based on the 'Rules of Mixture' prediction model (ROM). There are several models of ROM. For example, the ROM model

based on the assumption that all components of structure undergo the same deformation in the same direction is known as Voigt-type ROM. [16] Commonly, this model is used for calculation of Young's modulus along fibers ( $E_l$ ) in case of the load application in direction of fibers.

$$E_1 = \xi_M E_{1M} + \xi_F E_{1F}, \quad (25)$$

where  $\xi_M$ ,  $\xi_F$ - the volume fractions of matrix and fiber components, respectively;  $E_{1M}$ ,  $E_{1F}$ - Young's modulus of matrix and fiber components, respectively.

At the same time, the effective shear modulus  $G_{12}$  can be calculated by means of Reuss-type ROM based on the equal load distribution among the whole structure.

$$\frac{1}{G_{12}} = \xi_M \frac{1}{G_M} + \xi_F \frac{1}{G_F}, \quad (26)$$

where  $G_M$ ,  $G_F$ - shear modulus of matrix and fiber components, respectively.

Although, this model is accurate for laminate composite materials, in case of matrix based composites Reuss-type ROM cannot provide adequate results. More accurate version of models above is the Reuss–Voigt bounds that provides the upper (Voigt) and lower (Reuss) values of the effective elastic properties.

$$(\xi_M E_{1M}^{-1} + \xi_F E_{1F}^{-1})^{-1} \leq E_1 \leq \xi_M E_{1M} + \xi_F E_{1F}. \quad (27)$$

In works [16,15,17,18,19], authors demonstrate the usage of Hashin-Shtrikman bounds and Mori-Tanaka methods to calculate the effective elastic properties of two and three phase composites. Moreover, these methods are in line with the test results and can be used for composites with randomly oriented fibers or inclusions of irregular shapes.

In general, other parameters such as mass density, ultimate strength and thermal conductivity of composite materials can be calculated by ROM method.

$$\left(\frac{\xi_F}{\rho_F} + \frac{\xi_M}{\rho_M}\right)^{-1} \leq \rho_{eff} \leq \xi_F \rho_F + \xi_M \rho_M, \quad (28)$$

$$\left(\frac{\xi_F}{\sigma_F} + \frac{\xi_M}{\sigma_M}\right)^{-1} \leq \sigma_{1B}^+ \leq \xi_F \sigma_F + \xi_M \sigma_M, \quad (29)$$

where  $\rho_F$ ,  $\rho_M$  – density of fiber and matrix, respectively;  $\sigma_F$ ,  $\sigma_M$  – ultimate tensile strength of fiber and matrix, respectively.

The analytical calculation of composite properties provides the range in which the values of effective properties are. For this reason, in case of FEM analysis of composite structure there is a necessity to use the properties obtained from experimental tests in order to increase accuracy of final results.

The obtained effective parameters can be used to describe the elasticity characteristics of the studied construction. The Hooke's law expressed in stiffness form can be used for this purpose. [15]

$$[\sigma] = [K][\varepsilon], \quad (30)$$

where  $[\sigma]$  is the matrix of stress arising in the studied structure;  $[\varepsilon]$  - the strain matrix of structure;  $[K]$ - the stiffness matrix.

In case of multilayer composites reinforced with continuous fibers, the stiffness matrix depends on the effective properties of materials as well as geometry of construction. The matrix can be expressed as:

$$[K] = \frac{1}{H} \sum_{i=1}^n [k]_i h_i, \quad (31)$$

where  $H$ - the thickness of construction;  $h_i$  - thickness of  $i$ -th layer;  $[k]_i$  - the stiffness matrix of  $i$ -th layer.

$$[k]_i = [T]_i [\bar{k}]_i [T]_i^T, \quad (32)$$

where  $T$  is the transformation matrix that can be expressed as:

$$[T]_i = \begin{bmatrix} \cos^2 \theta_i & \sin^2 \theta_i & -2 \cos \theta_i \cdot \sin \theta_i \\ \sin^2 \theta_i & \cos^2 \theta_i & 2 \cos \theta_i \cdot \sin \theta_i \\ \cos \theta_i \cdot \sin \theta_i & -\cos \theta_i \cdot \sin \theta_i & \cos^2 \theta_i - \sin^2 \theta_i \end{bmatrix} \quad (33)$$

where  $\theta_i$ - the fiber orientation of i-th layer;  $[\bar{k}]_i$  is the stiffness matrix in local coordinates of i-th layer. [15]

$$[\bar{k}]_i = \begin{bmatrix} \frac{E_{1,i}}{1-\mu_{12,i}\mu_{21,i}} & \frac{\mu_{12,i}E_{2,i}}{1-\mu_{12,i}\mu_{21,i}} & 0 \\ \frac{\mu_{21,i}E_{1,i}}{1-\mu_{12,i}\mu_{21,i}} & \frac{E_{2,i}}{1-\mu_{12,i}\mu_{21,i}} & 0 \\ 0 & 0 & G_{12,i} \end{bmatrix}, \quad (34)$$

The obtained stiffness matrix can be used as input data for CAE analysis (eq. 14 -17).

Besides the elastic properties, the solver algorithms must be equipped with the failure criteria that strongly depends on the composite material strength. There are various methods for failure criteria setting. However, the most common method is Tsai-Wu criterion. [15] The simple form of this criterion is equation 35.

$$F_1\sigma_{11} + F_2\sigma_{22} + F_{11}\sigma_{11}^2 + F_{22}\sigma_{22}^2 + F_{33}\sigma_{12}^2 + 2F_{12}\sigma_{11}\sigma_{22} = 1, \quad (35)$$

where

$$F_1 = \frac{1}{\sigma_{1B}^+} + \frac{1}{\sigma_{1B}^-}; \quad F_2 = \frac{1}{\sigma_{2B}^+} + \frac{1}{\sigma_{2B}^-} \quad (36)$$

$$F_{11} = -\frac{1}{\sigma_{1B}^+\sigma_{1B}^-} \quad F_{22} = -\frac{1}{\sigma_{2B}^+\sigma_{2B}^-} \quad F_{33} = -\frac{1}{\sigma_{12B}^2} \quad (37)$$

$F_{12}$  is the coefficient that characterizes the interinfluence of  $\sigma_{11}$  and  $\sigma_{22}$ . This coefficient can only be determined by experimental measurements. (Fig. 6)

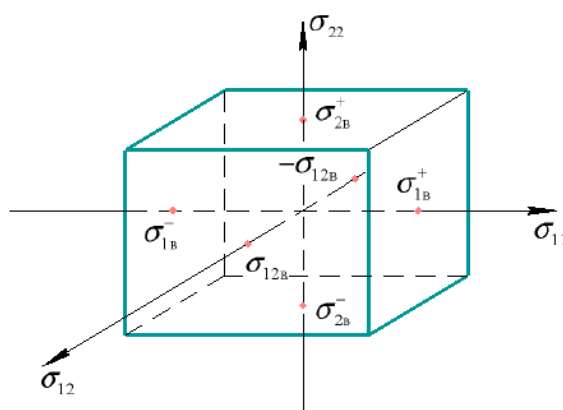


**Fig. 6.** Surface of maximum stresses.

In these simple forms the Tsai-Wu criterion takes into account only three parameters ( $\sigma_{11}, \sigma_{22}, \sigma_{12}$ ). However, the real numerical calculation deals with stresses in each direction (nine parameters) and coefficients of mutual influence between stresses in plane xy, yz, xz. [15]

$$A + B < 1, \quad (38)$$

where

$$A = -\frac{\sigma_{xx}^2}{\sigma_{xt}^f \sigma_{xc}^f} - \frac{\sigma_{yy}^2}{\sigma_{yt}^f \sigma_{yc}^f} - \frac{\sigma_{zz}^2}{\sigma_{zt}^f \sigma_{zc}^f} + \frac{\sigma_{xy}^2}{(\sigma_{xy}^f)^2} + \frac{\sigma_{yz}^2}{(\sigma_{yz}^f)^2} + \frac{\sigma_{xz}^2}{(\sigma_{xz}^f)^2} + \frac{C_{xy}\sigma_{xx}\sigma_{yy}}{\sqrt{\sigma_{xt}^f \sigma_{xc}^f \sigma_{yt}^f \sigma_{yc}^f}} + \quad (39)$$

$$+ \frac{C_{yz}\sigma_{yy}\sigma_{zz}}{\sqrt{\sigma_{yt}^f \sigma_{yc}^f \sigma_{zt}^f \sigma_{zc}^f}} + \frac{C_{xz}\sigma_{xx}\sigma_{zz}}{\sqrt{\sigma_{xt}^f \sigma_{xc}^f \sigma_{zt}^f \sigma_{zc}^f}},$$

$$B = \left(\frac{1}{\sigma_{xt}^f} + \frac{1}{\sigma_{xc}^f}\right)\sigma_{xx} + \left(\frac{1}{\sigma_{yt}^f} + \frac{1}{\sigma_{yc}^f}\right)\sigma_{yy} + \left(\frac{1}{\sigma_{zt}^f} + \frac{1}{\sigma_{zc}^f}\right)\sigma_{zz}, \quad (40)$$

where  $\sigma_{xx}, \sigma_{yy}, \sigma_{zz}, \sigma_{xy}, \sigma_{yz}, \sigma_{xz}$  - stress components in the material coordinate system;  $\sigma_{xt}^f, \sigma_{yt}^f, \sigma_{zt}^f$  - failure tensile stress along x, y and z axes in the material coordinate system;  $\sigma_{xc}^f, \sigma_{yc}^f, \sigma_{zc}^f$  - failure compressive stress along x, y and z axes in the material coordinate system;  $\sigma_{xy}^f, \sigma_{yz}^f, \sigma_{xz}^f$  - failure shear stress in plane xy, yz and xz in the material coordinate system;  $C_{xy}, C_{yz}, C_{xz}$  - mutual influence coefficient in plane xy, yz and xz in the material coordinate system.

The inequality fulfillment demonstrates that the construction is able to withstand the applied load. In fact, the value inverse to right part of equation 38 characterizes the safety factor of the tested construction. In addition to the parameters and criteria above, the prediction of the remaining life must be performed by use of the algorithms and models that are able to take into account the material aging during exploitation. [14]

The modern systems for numerical analysis allow to significantly increase the accuracy and quality of the constructions made from composites materials. However, the application of this types of analyses strongly depends on the information about material properties. The mentioned analytical relations and methods used to describe composite properties as well as their structure are not precise enough. They include certain approximation and assumptions. For this reason, the usage of experimental measurements is strongly recommended. However, experimental tools are not always applicable due to the limitations of the composite material theory. Taking into account the duration of the research and development of the new desired material (an average 10 - 20 years), the engineers must look for compromises in the existing materials that deprives the Simulated-based design of one more optimization parameter such as material structure.

### 3. Genome-Oriented Strategy

Nowadays cost-cutting and time-to-market reduction are relevant ways to gain the competitive advantage in the global market. In order to produce faster and at low cost, it is insufficient to optimize the construction parameters. The deployment of the most suitable materials in the different parts of the construction is a key advantage. For this reason, the Material Genome Initiative (MGI) was initiated in the United States. According to the MGI, 'the discovery and deployment of advanced material systems is crucial to achieving global competitiveness in the 21st century'. [20] This program or initiative is focused on involvement of computational capabilities and data management in material science and engineering.

The MGI aims to accelerate the advanced materials research and design by creation wide networks and open source platforms involved in advanced material development. The first step to create this type of advanced materials infrastructure is an adoption of rapidly developing computational technologies as well as the development of more efficient algorithms for prediction and modelling of materials' properties. The involvement of such technologies is crucial for reduction of the time spent on experiments and supplementation of physical experiment data. In addition to the development advanced materials and obtaining information about the structure and related properties, the generated data must be recorded and translated to an open source database. Existence of such open source database allows industry offer new product designs improved by not only an optimization of components by deployment of more suitable materials. [20] An ability to monitor the development of new materials and presence of connection between open source platforms and computer-aided instruments leads to an acceleration of design and improvement of designed constructions.

Thus, the main aim of MGI is an achievement of superiority in advanced material design and implementation by development of new instruments such as digital data platforms and new research and development (R&D) tools. [20]

**3.1. R&D computation instruments.** Traditionally, material developing is completed by testing. The experimental tools for testing and study of obtained results are expensive and their implementation is time-consuming in comparison with computational instruments. However, in spite of this comparison, the experimental/empirical methods of material study are still used for research and development of advanced materials. The results of computational analysis strongly depend on the quality of calculated models that must include accurate and extensive data about material behavior and properties. For new materials, the physical experimentation is the only possible option to obtaining such accurate set of data. Moreover, the experimental tools are the only possible way to validate calculated results of computer modelling of developed materials. For this reason, the experimental tools cannot be neglected during creation of modern advanced materials infrastructure. The simultaneous use of computational and experimental tools allows to overcome the problems that cannot be solved by using theoretical frameworks. While the experimental tools are able to improve calculation model by incorporating new data, the computational tools can use this improved model to perform analysis of structure, properties and optimization by studying a large set of possible configurations. [20]

The development of novel software that allows to connect the experimental and computational tools is an important step for improvement of Design Stage as the key part of Factory of Future. For this reason, the various research groups and companies are involved in development of this kind of software technologies. One of the example of such software is the Simpleware toolkit. In works [21,22] the usage of this software for characterization of heterogeneous material properties and structures is presented. The methodology is represented by step sequence that involves experimental and computational tools. The first step is usage of scan techniques such as Computed tomography (CT), X-ray Microtomography (micro-CT) [22], and serial sectioning (SEM) for generation of image stack that can be converted from 2D pixels into 3D pixels (voxels) by image processing software. The conversion process is accompanied by segmentation of heterogeneous structure into separate regions (different phases, reinforced particles, defects or porous networks etc.). Typically, the data obtained by scan techniques is presented by regular Cartesian grid of greyscale data that demonstrate the amount of radiation passed through the tested samples. The variation in the shades informs about the changes in material throughput that can be related with difference in materials, phases and structures of the tested sample. [4] Regions segmentation process is based on the presence of this data set and implies determination of various phases in sample structure. Some factors such as noise, poor contrast, and other defects related to the quality of scan techniques can influence on the accuracy of segmentation. [4] The need of accurate results requires the use of thresholding and cropping software techniques. For example, a noise reduction required to eliminate variations of brightness and color information can be performed by using a median filter. The tools such as 'island removal' can be used for reassignment of unconnected small areas to the relevant phase, while the 'smoothing' algorithms make a deal with the volume and topology of obtained phases. [21]

The segmented 3D image data can be rapidly processed and converted into multi-part meshes by algorithm such as +FE Grid that is the part of Simpleware software or the other finite-element based methods and techniques such as 'Enhanced Volumetric Marching Cubes' (EVoMaC). The usage of image-based meshing approach allows to obtain more accurate and complete meshes comparing with CAD-based approaches. The main reason of this is the usage of model segmentation for generation of mesh with different dimension or configuration depending on the size and complexity of local phases. Mostly, this meshing is possible due to the EVoMaC algorithm, that generates hexahedral elements from voxels lying in mask interiors, while the tetrahedral meshing applies to voxels lying close to mask interfaces. [21,4] In case of CAD-based approach, the mesh creation is often accompanied by loss of volume or topology that leads to decrease in model accuracy. Obtained meshed model can be used for calculation

of behavior and properties of tested samples by using existing computational tools mentioned earlier. Typically, the calculation of heterogeneous materials is performed by numerical homogenization. In case of Simpleware, homogenization is carried out by software modules such as +SOLID, +LAPLACE and +FLOW. The work of these modules is based on use of a built-in finite element solvers that allows to calculate and analyze the behavior of a material cuboidal sample in case of boundary conditions. The operability of proposed methodology is demonstrated with studying of advanced materials such as Berea sandstone [23] and Aluminum Matrix Composite with PMMC particles [22].

Without a doubt there are other methods used for converting the 2D scan data to the 3D model. For example, Yiu et al. use the CT image data to generate 3D microstructural model of asphalt mixture. [24,25,26] The study of asphalt mixture structure and properties (shear modulus) by usage of X-ray CT and FEM tools is presented in work [27]. In work [28, 29,30], the X-ray CT is used as the instrument for reconstruction of more detailed “real” model of 3D woven and other types of textile composite materials. In general, the approach proposed to study textile composite material structure is similar to Simplicware methodology, however to classify the material phases there is the database of “training set” that allows to train the program classifier module on the examples. In works [31, 32, 33] the authors perform numerical and experimental studies of delamination process and their prediction for carbon fiber reinforced polymers (CFRP). For this purpose, the Spectral Element Method (SEM) is applied to support numerical analysis as well as Scanning Laser Doppler Vibrometry (SLDV) is related with experimental research.

In fact, the experimental tools can be used not only for initial data obtaining but also to confirm the correctness of the calculated model and the predicted behavior of structure. For example, nanoindentation techniques can be used to measure mechanical properties in a pattern at nanoscale. [34] In work [35], the technique for collection of Acoustic Emission data is applied to validate the numerical prediction of L-flange behavior under quasi-static load conditions. However, the application of this technique provides a small amount of data for numerical model validation. In fact, AE is the audio records that include sequence of sound spikes with regard to time. These spikes cannot be used to identify the area of fracture or the magnitude of deformation. However, the obtained data can be compared to numerical results in terms of moments of deformation and fracture occurrence. In fact, strength testing allows to provide more information that can be used for validation. [36]

Nowadays, there is a large number of instruments and methods of empirical investigation that can be used for improvement of numerical algorithms. This approach allows to obtain highly-accurate data that further can be used to design the high-quality constructions as well as to create platform for material R&D. However, the undeniable advantage of systems such as Simpleware software compared to using various separate tools is a quick data transferring and usage of data format transparent for all software modules. The involvement of existing methods and improvement of performance in digital research and design trends is possible due to development of data representation standards as well as various frameworks provided interaction between different experimental and numerical instruments.

The development of such frameworks is mentioned in work [35]. In order to numerically predict L-flange behavior under quasi-static load conditions the authors involve a variety of tools such as COMPRO software, Abaqus Simulation and Autodesk Heliux PFA softwares. In this work, the model of composite structure is performed by means of COMPRO software that are able to provide additional information about the structure behavior during processing as well as to predict the deformation and to calculate residual stresses. Partly on the base of this model, the model of L-flange mechanical properties such as the ply-level strength is calculated by means of Abaqus Simulation software. The data obtained from these tools and design steps is transferred into the final step carried out by means of Autodesk Heliux PFA software. It is

the powerful instrument of progressive FE analysis that allows to perform more advanced multiple failure analysis of composite structures. Each of these software instruments can be applied separately for providing high-quality results with subsequent analytical calculation or replaced by other numerical tools. However, the main aim of the proposed calculation method is the combination of their advantage in order to obtain fast and accurate results and construction behavior prediction. Such integration and data communication is provided by usage of commercially available ModelCenter software package. The advantage of this software is an ability to interface with other standalone applications and to automate the data transfer process by integration of applications outputs into a system model. In fact, the proposed in the work [35] framework covers the stages from composite material preparation to testing of construction made from this material. The complex calculation of these stages involves material study on various scale levels such as micro, meso and macro scales. Although this approach requires considerable computing power, but the obtained results allow to understand the links between material creation process, material structure, material properties and behaviors as well as properties of final construction. This approach is known as Integrated Computational Materials Engineering (ICME). [35, 37]

**3.2. Integrated Computational Materials Engineering (ICME) approach as an efficient design instrument for FoF concept.** In general, the ICME approach aim is to provide all stakeholders with a relevant tool for designing materials for targeted performance requirements. [37] Moreover, this approach is a disruptive technology. In order to satisfy the product requirements, the design of micro- and mesostructure of materials can be performed instead of the traditional material selection. This replacement allows to provide the Simulated-based design with one more optimization parameter such as material structure that allows to design best-in-class products with the reduction of time to market parameter.

The improvement of design process by use of ICME approach instead of traditional methods, some basic aspects of which is described in Section 2, can be explained by level of input data. Both approaches are based on the top-down design process in which the function and requirements of final product are target functions used for creation and optimization of product construction. For traditional approach the target functions define the necessary geometry and properties of construction that leads to use of materials with strictly required mechanical, thermal or electrical properties. In case of traditional approach, the designer's work with material is limited by selection of more appropriate materials among the existing options. This selection is based on compromises, which means sacrificing some characteristics for the sake of taking more important ones. In this case, the ideal design solution can be rarely obtained due to the time-consuming nature of the process as well as lack of suitable materials.

The ICME approach ignores material selection step. In fact, required material properties obtained on the macroscope investigation level are used as the input data for meso-, macro- and sometimes nanoscope level design. Requirements of mechanical, thermal and electrical properties are used as the basis for calculation and design of material structure as well as the processing of this materials. For example, such sequence of processing-structure-properties investigations is mentioned in work [38] as the integration of Moldflow and Moldex3D software for characterization of structure and fiber orientation obtained during processing and NX Nastran or Ansys Workbench software to analysis of the properties and behavior of obtained material structure. The involvement of micro- and mesoscale investigation into design process makes the ICME similar to another approach that is commonly associated with properties and behavior prediction. This prediction approach is the bottom-up process that deals with atomic structure. The key process is combinatory search of more optimal atomic configuration that provides the required properties. The examples of such approach is CALculation PHAse Diagram (CALPHAD) method [39,40,41] and Universal Structure Predictor: Evolutionary Xtallography [42, 43] as well as several other methods [44,45].

However, such combinatorial methods deal only with atomic structure while ignoring the morphology of multiple phases and interphase strength. This concentration on atomic structure and properties such as atomic bonding cannot guarantee the multiscale investigation to meet the final product requirements. For this reason, this prediction approach is commonly used for study of new materials in material science, chemistry and physics researches, while the ICME can be integrated into the design process for competitive products. [37]

In fact, the ICME approach combines the top-down and bottom-up methods in order to provide the multiscale product design. The data about product functions and characteristics as well as the information about material genome that includes relationship between microstructure and desirable properties is important information for investigation by this approach. According to [37] the realization of such multiscale approach faces a number of problems such as:

- creation of relations between polyphase microstructures and the properties of construction behavior by considering their behavior at all scales;
- description and determination of responses in higher scales behavior to variations and changes in structure or mechanisms in lower scales;
- description of relations between microstructure and applied processing technology as well as the environment and impurities;
- involvement of the physics and chemistry knowledge into design process and combine them with engineering methods.

The last but not least problem is description of microstructure by means of mathematical and digital methods. In work [46], the microstructure is presented as the key factor that links the different scales during investigations. The authors describe three important types of microstructure representation. The more approximate type is statistical representation that involves statistical tools and instruments. However, the data obtained using these tools cannot provide the highly resolved information for accurate multiscale design valuation. Commonly this type of microstructure representation deals with average value of microstructure parameters such as grain size, aspect ratio, etc. This information as the statistical model of material microstructure is entered into materials equations on the process scale in order to estimate material properties for other scales calculations. On the other hand, there are two more complex types such as Spatial and Numerical representations. In general, any spatial descriptions are based on the use of scalars, vectors and tensors. In order to use numerical algorithms for their calculation and characterization, they must be represented by data arrays with dimension corresponding to the amount of objects/features in the microstructure. Besides the description of objects/features positions, the scalars, vectors and tensors represent concentration fields for individual chemical elements, stress-strain fields and others parameters that allow to describe and take into account various changes in the structure. The Spatial representation method may be based on experimental approach using data from empiric studies (CT, SEM, etc.) or on simulation approach that involves phase-field and crystal plasticity FEM computation algorithms. In addition, the Spatial representation method may use the synthetic approach that use neither experimental nor simulation tools. In fact, this approach involves algorithms that create artificially microstructure design on basis of statistical representation. The third representation method (Numerical) is based on use of voxel type numerical representation and calculation of microstructure. Commonly this method is more suitable for subsequent FEM approaches. More comprehensive description of representation methods is presented in works [47,48, 49].

The described above principles of ICME approach are illustrated in various works. For example, in work [50] the multiscale design is applied to create the car door assembly from fiber reinforced composite material. The main aim is to achieve the best mass-strength ratio. For this purpose, the optimization of composite geometries is performed. The design of door

assembly as well as behavior simulation in case of load applications is performed in ABAQUS software. The assembly components are designed by the use of failure criterion Tsai-Wu and stiffness based deflection criteria. In this case, the preliminary calculation is performed by the use of isotropic material in order to obtain the stress contours and stiffness requirements that can be used for composite structure optimization. For this purpose, a repetitive unit cell model (RUC) is generated by the open source TexGen software. The obtained RUC microstructural models have various structure architectures such as plain, woven and 3D textile weaves. These models are virtually tested with regard to required stiffness parameters generated on the macroscale level until the optimal parameters such as matrix and fiber materials, fibers orientation are obtained. The automatization of ICME approach and data transfer between divided instruments and simulation modules are achieved by a framework based on TCS PREMAP software platform. [50]

In work [38], authors propose a novel framework for FRP parts design that besides traditional CAD/CAE modules includes Computer-Aided Conceptual Design (CACD) tools. According to the authors, the main application of CACD is searching for optimal structure, fiber orientation and distribution in polymer matrix taking into account the minimum fiber consumption requirement. The main object for data representation and transfer between various steps is the heterogeneous feature model (HFM) proposed by the authors. HFM fully describes the fiber-reinforced composite details during design and optimization process and is thoroughly described in work [38]. In general, the HFM is based on structure and material optimization results and is further supplemented by detailed design from CAD modules and processing simulation data from Injection molding CAE tools. The obtained model can be sent to part-scale simulation powered by CAE software. Depended on the obtained results the structure and material optimization can be repeated and the process continues until the optimal solution is obtained.

**3.3. Digital Data.** Nowadays, it is crucial not just to develop the new materials but also to provide the results of study to all concerned participants of advanced material innovation process. This set of data may significantly help the product designer in choosing the material with certain parameters and properties. [20] For this reason the MGI and ICME are based on creation of open databases that contain significant amount of existing material knowledge. The modern material scientists and engineers have access to the information about advanced materials, materials' structures and properties as well as the information about development of new materials more suitable for their purpose. The existing material databases are represented by Total Materia, Material Data Facility [51], the Material Commons [52], the Material Project [53], the Harvard Clean Energy Project [54], Inorganic Crystal Structure Database [55], the Open Quantum Materials Database [56] and the Cambridge Structural Databases [57].

The main goal of such instruments development is serving the needs of the growing advanced materials research community and providing it with the powerful tools for its work. In fact, the presented databases differ from the usual understanding of this term. Modern material data bases are not resources with the lists of existing materials and their properties, but cloud platforms for communication and data exchange between participants of the material research and development process.

For example, the Material Commons is a cloud platform and information repository with computation and experimental results, research publications, storing experience and analytic of the current material science state. Moreover, the Material Commons includes abstracts and description of a data models for material processing-structure-property relationships that can be used for ICME design.

Material Data Facility, like the previous platform, is focused on providing wide range of information. This platform makes raw and derived data available in order to provide a more detailed information about methodology of studies and obtained results. The platform creators

believe that the data accompanying research such as models codes, protocols and experimental conditions are of particular interest to use in similar studies or real applications. Thus, Material Data Facility platform provides simplified access to this type of data.

The platforms such as the Materials Projects and the Harvard Clean Energy Project are open-source analytical tools. Such platforms allow performing numerical calculation to define the properties of compounds, to validate the obtained results and make them available to wide auditory. On the other hand, the databases, such as Total Materia, are a source of significant amount of material properties and characteristics that can be exported into numerical software to perform accurate simulation and analysis of designed products. Moreover, such platforms provide information about materials' structures and can determine the material utilizing the chemical composition obtained with the help of spectrometry, which can be useful for re-engineering purposes.

Modern platforms for generation of material data and sharing of research data contribute to the material science growth and advanced material development. The wide range of existing databases provides information that can be useful for various branches of materials study. Moreover, existing data platforms can be integrated into the work processes that use numerical software, which allows to increase quality of obtained results in product design. The combination of ICME approach and open source material databases allows designing and manufacturing highly competitive products with lower costs. These principles are similar to the idea of Factories of Future. For this reason, the implementation of ICME approach supported by open material data bases in the real production process is an important step towards realization of FoF concept.

#### 4. New strategy

As mentioned before the traditional process of product design involves the selection of more appropriate material on the macroscopic level. [12] The described process may be schematically represented as in the Fig. 7.

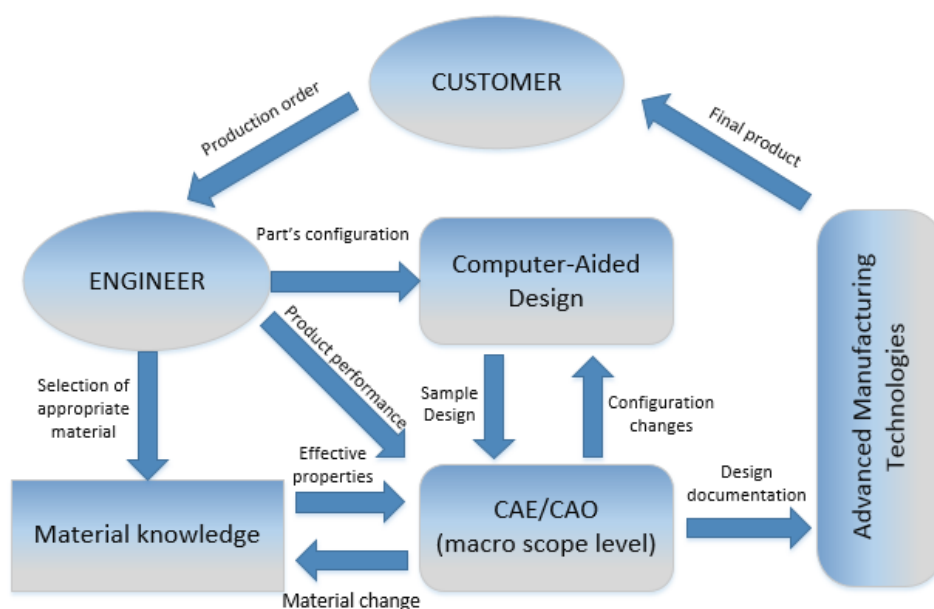


**Fig. 7.** The traditional process of product design.

An engineer obtains the information about the final product characteristics. Based on this information, engineers create the 3D concept of constructions, prepare calculation models for numerical simulation and optimization as well as set material properties. In this case, the material properties are the effective properties analytically evaluated with no regard to the

microstructure as well as the processing of the materials. This approximate data can be used for product simulation-based design. However, there is less optimization parameters that prevent the creation of the most optimal design. In addition, the lack of information about the microstructure and quality of material processing leads to reduction in accuracy of the product life-cycle prediction.

The ICME approach allows for expanding the boundaries of material selection step. The proposed approach of production design involves study and selection of material parameters on each scope level (macro, meso, micro, nano) in order to maximize product optimization and to take into account all structure and processing features that may influence on the product performance. In the ICME approach the cornerstone is the processing - structure - property - performance (PSPP) relationship. The movement from right to the left (top-down design approach) allows finding many possible variants of material structures that match to the one set of product requirements (performance). The top-down approach is concerned with a study of one-to-many relationships that provide the array of available variants. The bottom-up design is undertaken to take the available variant and due to calculation and simulation to find the most optimal solution. The ICME design approach is a resource intensive method that requires a lot of material science data and involves various numerical and experimental instruments. In order to provide collaboration and data transfer between various tools, the framework connected to open material data bases is used. Nowadays, there is no universal framework for ICME product design. However, according to Section 3 the ICME approach may be illustrated by the scheme presented on the Figure 8.

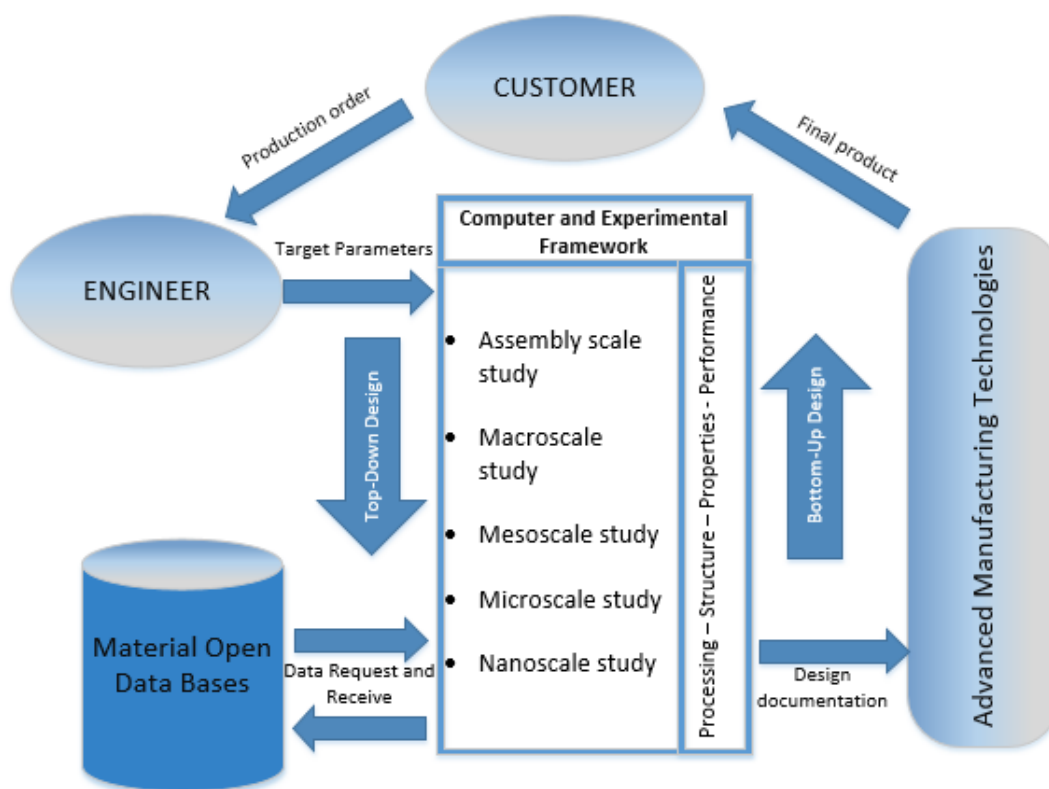


**Fig. 8.** A schematic representation of ICME approach.

However, the combination of experimental and numerical instruments proposed by ICME approach also has some limitations. Both of these instruments are based on theoretical knowledge that is represented in algorithms and analytical relations. Although, the MGI leads to the accelerated development of material science, it is quite difficult to represent PSPP

relationships by computational models and algorithms. It is particularly true for advanced materials, PSPP relationships for which can even be unknown. For this reason, the intelligent and high-performance analyzing algorithm for accurate prediction of material performance is required. Considering the existence of open data bases with colossal amount of material information, the Big Data concept can be mentioned as one of the possible ways to improve design approach. In general, the big volume of valid information from various sources that is being updated with high velocity can be characterized as Big Data. The various algorithms and methods such as Machine Learning, Deep learning, etc. can be used for processing of such open resources and creation of prediction models involved into product design.

In general, the Machine learning as the method for automation creation of prediction model use algorithm that iteratively compares the feature relations from available data in order to find hidden insights non-obvious in terms of the existing theory. According to [58] the basic idea of using machine learning methods for design process is to automate the analyzing and mapping of the nonlinear relationships between the processing-structure-properties-performance features by extracting knowledge from existing empirical data. The result of this method utilization is the model that can be applied for current product design as well as for dealing with the similar design orders in the future.

According to work [59], obtaining of prediction model requires the setting of “goal”, “sample” and “algorithm”. The term “sample” implies the presence of significant volume of available information such as experimental data, protocols, computation results, etc. provided by open source material data bases. In fact, the sample preparation is the first basic step for machine learning method. (Fig. 9) The preparation involves data cleaning from noise and incomplete elements as well as reduction of the amount of inadequate information. In addition, the sample preparation involves feature engineering step that provide some simple physical basis for extraction of main structural and chemical trends to provide fast and accurate material performance prediction. [59]



**Fig. 9.** Basic steps of Machine Learning approach.

The well-prepared sample is the input information for the second basic step - “model building”. The core of this method is the algorithm used for data learning and prediction model generation. For these purpose, the “algorithm” is set of operations with input information that performed under control of “goal” parameters, that may be illustrated by scheme presented in Fig. 10. The “goal” is the target characteristics that must be achieved and used for study of the provided “sample”. The most commonly used algorithms for machine learning is Naive Bayes [60], Logistic regression [61] as well as Linear regression [62], Support vector machine [63], Logistic model tree [64] and Artificial neural networks [65]. The selection of appropriate algorithm is based on the task of prediction and target parameters. In case numerical target parameter such as fatigue strength, etc., the algorithms based on the regression methods is more effective. The target parameters represented by categorical information involves usage of classification techniques and relevant algorithms. In general, the commonly used algorithms are Artificial neural networks (ANN) and Support vector machine (SVM) as the algorithms capable to use both regression and classification techniques.

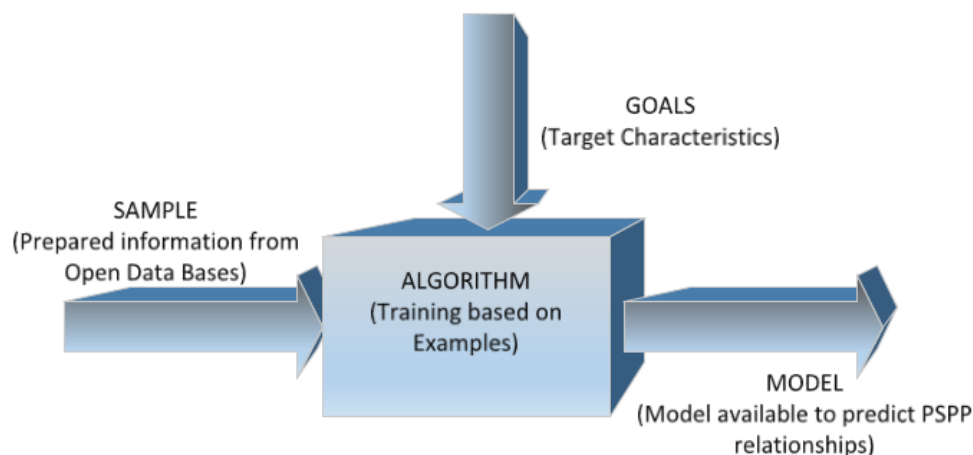


**Fig. 10.** Principle of Model building step.

The process of model building is similar to training by using existing examples. However, the obtained model with mapping function and set of various approximation coefficients, might be able to deal only with the data that was used during the training and be unsuitable for work with previously unseen data. In this case, the model cannot be considered as valid and cannot be used for purposes of product design. The obtained model must be evaluated. Commonly for this purpose the information obtained from data bases is divided into training set used for sample preparation and testing data set. Testing data sets are proposed to the obtained prediction models obtained in order to validate the model suitability. There are various methods of test sets preparation. In general, the initial amount of data is partitioned in proportion of 2/3 to training data and 1/3 to test data (Hold-out method). In case of cross-validation method, the initial data can be divided into  $k$  mutually exclusive subsets of the same size and the  $(k-1)$  sets is the training data set.

Results obtained during evaluation tests allow for evaluating the quality and accuracy of the created prediction model that is vital for their implementation into product design process. According to [60, 59], the model error is represented by the mean absolute percent error (MAPE), the root mean square error (RMSE) and the correlation coefficient ( $R^2$ ).

$$MAPE = \frac{1}{n} \sum_{i=1}^n \frac{|y'_i - y_i|}{y_i}, \tag{41}$$

$$RMSE = \sqrt{\frac{1}{n} \sum_{i=1}^n (y'_i - y_i)^2}, \tag{42}$$

$$R^2 = \frac{[\sum_{i=1}^n (y_i - \bar{y})(y'_i - \bar{y}')]^2}{\sum_{i=1}^n (y_i - \bar{y})^2 \cdot \sum_{i=1}^n (y'_i - \bar{y}')^2}, \tag{43}$$

where  $y_i$  and  $y'_i$  are the original values from SAMPLE and the predicted value by using of obtained model, respectively;  $\bar{y}$  and  $\bar{y}'$  are the averages of the original and predicted values, respectively. [59]

The example of use of Machine Learning and Big Data concepts can be found in work [66]. The authors propose the framework for determining material genome of granular minerals. The proposed framework uses the mineral databases as the source of granular material genome information. The genome of granular materials represents the “parent rocks”, weathering process as well as the mineral composition and structure. The available instruments for genome

study are experimental tools such as scanning electron microscopy (SEM), transmission electron microscopy (TEM), Energy-dispersive X-ray (EDX), etc. According to work [66], these techniques make it possible to link mineral composition with the shape, texture and other morphological characteristics of particles. However, performing these experimental investigations is time consuming. More reasonable approach is to use open data base that can be filled by researches related to this area of material science. The information about minerals presented in data base must involve reference number, mineral, chemical composition, crystal structure information, typical grain size, etc. In addition, the mechanical properties obtained from laboratory experiments and transferred to multiple scales by means of computer simulation approach must be sent to this data base. Significant volume of information accumulated in mineral data base can be considered as a Big Data. The authors, proposed to use algorithms for Big Data processing in order to define relationships between genome and mechanical properties of granular materials. The obtained prediction model can allow for developing materials with required properties as well as reducing the timeline from discovery to implementation of granular materials.

These works among the others [67, 68, 69, 70] show the significance of the role of Big Data and Machine Learning methods for development of new materials. On the other hand, there is a limited number of works that connect the Big Data concept with product design. However, according to [58], Machine Learning is capable of providing model that can be used for both the direct (bottom-up) and for the reverse (top-down) prediction of materials PSPP relationships. This feature is similar to the ICME multiscale design concept that allows making assumption that Big Data and Machine Learning concepts can be used for product design based on ICME approach. The schematic representation of this idea may be represented by Fig. 11.

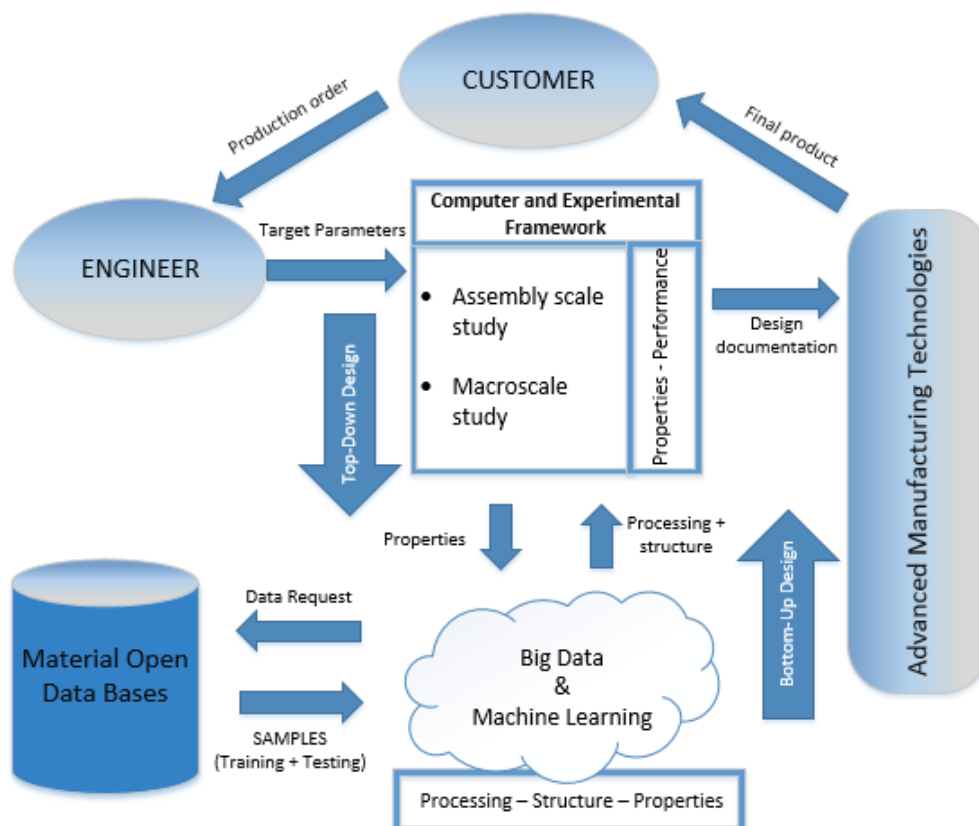


**Fig. 11.** Product design based on ICME and Machine Learning approaches.

Theoretically, the usage of Machine Learning can automate the design process on the nano-, micro- and mesoscale levels by providing prediction models taking the input information

about material properties giving the best structural and processing solutions without involving the additional tools into this optimization process. The simulation of product performance based on the material properties and working conditions is still performed by CAE/CAO macroscale systems under engineers' control. Study of properties-performance relationships by traditional algorithms provides the optimization criteria for prediction model building by the means of Machine Learning. Although, Machine Learning is able to accelerate the process of choosing the optimal material processing and structure solutions, their usage is associated with some limitations. For example, preparation of significant amount of unstructured data and their further analysis require for utilization of high-performance computation resources that might be unavailable. Moreover, the creation of prediction models for specific product design purpose takes time and can be more complex comparing with the existing computer or experimental measurement instruments. However, when developed, such models can be used for design of similar products in future. Thus, the communication environment and open libraries or data bases that publish prepared prediction models are critical for such product design approach. (Fig. 11)

In addition, the implementation of Big Data analysis into the product design process allows for development of digital product models with more information comprehensively characterizing the designed objects. In case of the computer and experimental investigation the obtained information is limited by existing theoretical knowledge while the Big Data analysis can provide links that can be unknown for material science but have significant influence on final product quality. Thus, the implementation of Big Data analysis and Machine Learning approach can be significant push for improvement of Product Life-Cycle management as well as for creation of best-in-class products that is the goal of FoF concept.

## 5. Conclusions

In this work, the review of advanced material representation approaches for product design purpose is presented. The basic information about traditional approaches in simulation of fiber-reinforced composites structure as well as calculation algorithms for analyzing of details made from composite materials are described to illustrate the influence of the accuracy of material data on the quality of prediction of final product performance. In general, the effective properties of composite materials are used for product simulation. Considering the results obtained by the use of the analytical methods as average values for components properties, the effective parameters of composite materials for numerical simulation can be used as an approximate evaluation of the designed products. Thus, the development of more complex frameworks and related computing tools is required for improving Product Life-Cycle management and creation of best-in-class products. Some solutions developed within the Material Genome Initiative (MGI) are represented in this work. Key solutions are related to combination of experimental and computer aided R&D methods as well as the creation of communication environment for cooperation and sharing of generated material science data. The creation of such open material data bases contributes to accumulation of huge amount of experimental and simulation data that can provide comprehensive information about processing-structure-properties-performance relationships for advanced materials. That information lays the foundation for effective product design and simulation. The implementation of Big Data analysis utilizing Machine Learning algorithms in ICME approach allows to automate of material structure optimization and provides engineers with powerful tools for the most efficient optimization of designed product available.

**Acknowledgements.** *This research was financed by Ministry of Education and Science of the Russian Federation within the framework of the Federal Program "Research and development in priority areas for the development of the scientific and technological complex of Russia for*

2014-2020”, Activity 1.1, Agreement on Grant No. 14.572.21.0008 of 23 October, 2017, unique identifier: RFMEFI57217X0006.

## References

- [1] C. Featherston, E. O’Sullivan, *A review of international public sector strategies and roadmaps: A case study in Advanced Materials. A report for Government Office of Science & the Department for Business, Innovation & Skills* (Center for Science Technology and Innovation, Institute for Manufacturing, University of Cambridge, Cambridge, 2014).
- [2] <https://www.cimdata.com/de/resources/complimentary-reports-research/commentaries/item/3345-design-with-confidence-commentary/3345-design-with-confidence-commentary>
- [3] A.G. Kotov, *CAD of products from composite materials. Modeling of the processes of deformation and destruction by the ANSYS software* (Publishing house of Perm. state. tech. university, Permian, 2008). (in Russian).
- [4] P. G. Young, T. B. H. Beresford-West, S. R. L. Coward, B. Notarberardino, B. Walker, A. Abdul-Aziz // *Philosophical Transactions of the Royal Society A* **366** (2008) 3155.
- [5] L. Guibas, J. Stolfi // *ACM Transactions on Graphics* **4(2)** (1985) 74.
- [6] C. Lawson, *Software for C<sup>1</sup> Surface Interpolation*. In: *Mathematical Software III* (Academic Press, NY, 1977) 161.
- [7] A.V. Skvortsov, *Delaunay triangulation and its application* (Tomsk University Publishing House, Tomsk, 2002). (in Russian).
- [8] S. A. Berggren, D. Lukkassen, A. Meidell, L. Simula // *Applications of Mathematics* **48(2)** (2003) 87.
- [9] D. R. H. Jones, M. Ashby, *Engineering Materials 1. An Introduction to Properties, Applications and Design*. 3<sup>rd</sup> Edition (Butterworth-Heinemann, Oxford, 2005).
- [10] M. Ashby, *Material Selection in Mechanical Design*. 3<sup>rd</sup> Edition (Butterworth-Heinemann, Oxford, 2005).
- [11] H. Pettermann, *Continuum Mechanics Modeling of Composite Materials* (Technischen Universitat Wien, Vein, 2003).
- [12] Z. Hashin // *Journal of Applied Mechanics* **50(3)** (1983) 481.
- [13] Xiaowei Ouyang, Guang Ye, Klaas van Breugel // *Construction and Building Materials* **135** (2017) 538.
- [14] C.P. Sturrock, E.F. Begley, *Computerization and Networking of Materials Databases: Fourth Volume* (ASTM International, 1995).
- [15] Yu.V. Skvortsov, S.V. Glushkov, A.I. Khromov, *Modeling of composite structural elements and analysis of their destruction in CAE-systems MSC. Patran-Nastran and ANSYS* (Samara, 2012). (in Russian).
- [16] H. E. Pettermann, H. J. Bohm, J. Alcalá // *Metallurgical and Materials Transactions A* **33(10)** (2002) 3187.
- [17] Carmen Calvo-Jurado, William J. Parnell // *Journal of Computational and Applied Mathematics* **318** (2017) 354.
- [18] Inch-Long Ngo, S. V. Prabhakar Vattikuti, Chan Byon // *International Journal of Heat and Mass Transfer* **114** (2017) 727.
- [19] Yasser Zare // *Polymer Testing* **51** (2016) 69.
- [20] John P. Holdren *Materials Genome Initiative for Global Competitiveness* (Executive office of the president national science and technology council, Washington D.C., 2011).
- [21] Yach Agarwal, Wojciech Smigaj, Philippe G. Young, Ross Cotton, Patrick Tompsett // *Materials Today: Processings* **4** (2017) 1860.
- [22] I. G. Watson, P. D. Lee, R. J. Dashwood, P. Young // *Metallurgical and Materials Transactions A* **37(3)** 551.

- [23] R. Cotton, P. Tompsett, W. Smigaj, K. Genc, P. G. Young, In: *NAFEMS World Congress* (21 – 24 June, San Diego, CA, 2015).
- [24] T. You, R. Abu Al-Rub, E. Masad, D. Little // *Transportation Research Record: Journal of the Transportation Research Board* **2373** (2013) 63.
- [25] T. You, R. K. Abu Al-Rub, M. K. Darabi, E. A. Masad, D. N. Little // *Construction and Building Materials* **28(1)** (2012) 531.
- [26] T. You, R. K. Abu Al-Rub, E. A. Masad, E. Kassem, D. N. Little // *Journal of Materials in Civil Engineering* **26(4)** (2014) 607.
- [27] E. Coleri, J. T. Harvey, K. Yang, J. M. Boone // *Construction and Building Materials* **30** (2012) 783.
- [28] Yang Liu, Ilya Straumit, Dmytro Vasiukov, Stepan V. Lomov, Stephane Panier // *Composite Structure* **179** (2017) 568.
- [29] N. Naouar, E. Vidal-Sallé, J. Schneider, E. Marie, P. Boisse // *Composite Structure* **116** (2014) 156.
- [30] Ilya Straumit, Stepan V. Lomov, Martine Wevers // *Composites Part A: Applied Science and Manufacturing* **69** (2015) 150.
- [31] T. Wandowski, P. Kudela, P. Malinowski, W. Ostachowicz // *Health Monitoring of Structure and Biological Systems* **9805** (2016).
- [32] C. Willberg, S. Koch, G. Mook, J. Pohl, U. Gabbert // *Smart Materials and Structures* **21(7)** (2012).
- [33] P. Kudela, T. Wandowski, P. Malinowski, W. Ostachowicz // *Optics and Lasers in Engineering* **99** (2017) 46.
- [34] O. L. Warren, T. J. Wyrobek // *Measurement Science and Technology* **16(1)** (2004) 100.
- [35] Joshua S. Dustin, Richard Dalgarno, Matt Hockemeyer, *Lessons Learned from the Development of a Structural Finite Element Progressive Failure Simulation for Integration into the ICM2 Framework* (AIAA SciTech, San Diego, 2016).
- [36] Karthik RM, Bhaskar Patham, Swaroop Kavi, Virupakshappa Lakkonavar, Jayaraj Radhakrishnan // *Materials & Design* **89** (2016) 727.
- [37] Jitesh H. Panchal, Surya R. Kalidindi, David L. McDowell // *Computer-Aided Design* **45(1)** (2013) 4.
- [38] Jikai Liu, Yongsheng Ma, Junyu Fu, Kajsa Duke // *Advances in Engineering Software* **87** (2015) 13.
- [39] Yong-Jie Hu, Yi Wang, Samad A. Firdosy, Kurt E. Star, Jean-Pierre Fleurial, Vilupanur A. Ravi, Zi-Kui Liu // *Calphad* **59** (2017) 207.
- [40] Zi-Kui Liu // *Journal of Phase Equilibria and Diffusion* **30** (2009) 517.
- [41] Mehdi Hosseinfar, Dmitri V Malakhov // *Journal of Alloys and Compounds* **505(2)** (2010) 459.
- [42] Andriy O. Lyakhov, Artem R. Oganov, Harold T. Stokes, Qiang Zhu // *Computer Physics Communications* **184(4)** (2013) 1172.
- [43] Maribel Núñez-Valdez, Zahed Allahyari, Tao Fan, Artem R. Oganov // *Computer Physics Communications* **222** (2018) 152.
- [44] Geoffroy Hautier, Chris Fischer, Virginie Ehrlacher, Anubhav Jain, Gerbrand Ceder // *Inorganic Chemistry* **50(2)** (2011) 656.
- [45] S. V. Dudiy, A. Zunger // *Physical Review Letters* **97(4)** (2006).
- [46] G. J. Schmitz, H. Farivar, U. Prahl // *Integrating Materials and Manufacturing Innovation* **6(1)** (2017) 127.
- [47] Georg J. Schmitz, Ulrich Prahl, *Handbook of Software Solutions for ICME* (Wiley-VCH Verlag GmbH & Co. KGaA, Weinheim, 2016).
- [48] A. Reid, S. Langer and S. Keshavarz, *OOF: Flexible finite element modeling for materials science* (2nd International Workshop on Software Solutions for ICME, Barcelona, 2016).

- [49] A. S. Bhadauria, C. Agelet de Saracibar, M. Chiumenti, M. Cervera, *A new approach to interoperability using HDF5* (2nd International Workshop on Software Solutions for ICME, Barcelona, 2016).
- [50] Azeez Shaik, Yagnik Kalariya, Rizwan Pathan, Amit Salvi, *ICME Based Hierarchical Design Using Composite Materials for Automotive Structures*. In: Proceedings of the 4<sup>th</sup> World Congress on Integrated Computational Materials Engineering (ICME 2017) (2017) 33.
- [51] B. Blaiszik, K. Chard, J. Pruyne, R. Ananthkrishnan, S. Tuecke, I. Foster // *JOM* **68(8)** (2016) 2045.
- [52] Brian Puchala, Glenn Tarcea, Emmanuelle A. Marquis, Margaret Hedstrom, H. V. Jagadish, John E. Allison // *JOM* **68(8)** 2035.
- [53] A. Jain, S. P. Ong, G. Hautier, W. Chen, W. D. Richards, S. Dacek // *Apl. Materials* **1(1)** (2013) 011002.
- [54] J. Hachmann, R. Olivaresamaya, S. Atahnevrenk, C. Amadorbedolla, R. S. Sanchezcarrera, A. Goldparker // *The Journal of Physical Chemistry Letters* **2(17)** (2011) 2241.
- [55] A. Belsky, M. Hellenbrandt, V. L. Karen, P. Luksch // *Acta Crystallogr B* **58** (2002) 364.
- [56] S. Kirklin, J. E. Saal, B. Meredig, A. Thompson, J. W. Doak, M. Aykol // *npj Computational Materials* **1** (2015) 15010.
- [57] F. H. Allen // *Acta Crystallogr B* **58** (2002) 380.
- [58] Ankit Agrawal, Alok Choudhary // *APL Materials* **4** (2016) 053208.
- [59] Yue Liu, Tianlu Zhao, Wangwei Ju, Siqi Shi // *Jiurnal of Materiomics* **3(3)** (2017) 159.
- [60] George H. John, Pat Langley, In: *Proceedings of the Eleventh Conference on Uncertainty in Artificial Intelligence* (1995) 338.
- [61] D. Hosmer, S. Lemeshow, *Applied Logistic Regression* (John Wiley and Sons, Inc., 1989).
- [62] Allen L. Edwards, *An Introduction to Linear Regression and Correlation (Series of Books in Psychology)* (W. H. Freeman and Comp., San Francisco, 1976).
- [63] V. N. Vapnik, *The Nature of Statistical Learning Theory* (Springer, 1995).
- [64] Niels Landwehr, Mark Hall, Eibe Frank // *Machine Learning* **59(1-2)** (2005) 161.
- [65] C. Bishop, *Neural Networks for Pattern Recognition* (Oxford University Press, 1995).
- [66] Wenjuan Sun, Wenjing Xue, Yinning Zhang, Linbing Wang // *International Journal of Pavement Research and Technology* (2017). (in Print).
- [67] Vinicius Veloso de Melo, Wolfgang Banzhaf // *Neurocomputing* **246** (2017) 25.
- [68] Zhen Liu, Yifan Li, Diwei Shi, Yaolin Guo, Mian Li, Xiaobing Zhou, Qing Huang, Shiyu Du // *Scripta Materialia* **143** (2018) 129.
- [69] Ashley A. White // *MRS Bulletin* **38(8)** (2013) 594.
- [70] Sergei V. Kalinin, Bobby G. Sumpter, Richard K. Archibald // *Nature Materials* **14** (2015) 973.



The following section contains selected papers from  
45 International Summer School – Conference  
“Advanced Problems in Mechanics – 2017”  
which do not fully correspond to the primary journal topics but in the  
opinion of editorial board are of interest from the point of view of  
relevant scientific areas development.



В следующем разделе представлены отдельные статьи  
45 Международной школы – конференции  
«Актуальные проблемы механики – 2017»,  
которые не полностью соответствуют основным темам журнала,  
но, по мнению редакции, представляют интерес с точки зрения  
развития соответствующих областей науки.

## ON ONE CLASS OF APPLIED GRADIENT MODELS WITH SIMPLIFIED BOUNDARY PROBLEMS

S.A. Lurie<sup>1,2\*</sup>, P. A. Belov<sup>1</sup>, Y.O. Solyaev<sup>1</sup>, E.C. Aifantis<sup>3,4,5,6,7</sup>

<sup>1</sup>Institute of Applied Mechanics of Russian Academy of Science, Moscow, Russia

<sup>2</sup>Lomonosov Moscow State University Moscow, Russia

<sup>3</sup>Aristotle University of Thessaloniki, Thessaloniki 54124, Greece,

<sup>4</sup>Michigan Technological University, Houghton, MI 49931, United States,

<sup>5</sup>BUCEA, Beijing 100044, China,

<sup>6</sup>ITMO University, St. Petersburg 197101, Russia,

<sup>7</sup>Togliatti State University, Togliatti 445020, Russia

\*e-mail: salurie@mail.ru

**Abstract.** We consider the generic gradient elasticity theory of Mindlin-Tupin and try to establish a class of applied models of gradient elasticity, for which the boundary value problems of the gradient theory with static boundary conditions are divided into a sequence of two subtasks, one of which is classical. Such applied models are very effective in applications, because their solutions reduce exactly to a consistent solution of boundary value problems of the second and not of the fourth order. We consider gradient theories with a general structure of tensors of gradient modules that satisfy potentiality conditions and additional symmetry conditions, which is considered as a criterion of correctness.

It is shown that their gradient tensors of the elastic modules are represented in the form of an expansion with respect to the tensor basis of five sixth-rank tensors, three of which satisfy a special property. Each of these basis tensors is represented as a convolution of fourth-rank tensors, and the corresponding quadratic form is a convolution of vectors.

It is shown that for the traditional gradient Mindlin-Tupin theory, the “classical” static conditions on the body surface are not satisfied locally. However, if the gradient modules are represented as a convolution of the “classical” tensors of elastic moduli, then the set of the boundary value problems of such gradient theory admits a full fractionation of the initial boundary value problem into two: the “classical” boundary value problem and the “cohesive” boundary value problem.

It is established the structure of the applied gradient models with such property of separating boundary value problems. They are particular cases of gradient elasticity theories with gradient modulus tensors, representable in the form of an expansion in three basis tensors of the sixth rank, satisfying the properties of the representation in the form of convolution via fourth-rank tensors.

We formulated “vector” gradient Mindlin-Tupin model that preserves the classical form of static boundary conditions. Such a model leads to a specific variant of the gradient theory with a single non-classical modulus, or one-parametrical model. It is shown that the obtained gradient model can be considered as some generalization of the well-known applied theory GradEla providing for it the separation of boundary value problems.

**Keywords:** gradient theories, scale parameters, separation of boundary value problems, “classical” displacement field, “cohesive” displacement field.

## 1. Introduction

In the gradient theory of elasticity the density of potential energy depends not only on first derivatives of the displacement vector, but also on the second derivatives of the displacement vector (first derivatives of deformation tensor in the framework of the Mindlin's Form II models [1]). So, the statement of the gradient theory includes not only classical moduli of elasticity but also physical constants which dimension are different from the classical ones by the square of length. The gradient theory of elasticity was first formulated in [1, 2]. It was shown that in the general case for an isotropic medium, the model contains seven material constants – two classical Lamé parameters and five additional modules.

The development of continuum media models accounting for various micro/nanostructures parameters beyond the theory of classical elasticity appears to be crucial for the description of short-range interactions, cohesion forces, and also for the modeling of other size-dependent effects in the framework of generalized elasticity and plasticity theories. Applied gradient model was developed initially by Aifantis [3]. Robust gradient models were developed for gradient elasticity by Aifantis and co-workers [4-6]. Later it was shown that, within the framework of the gradient theory of elasticity, it is possible to eliminate of the singularities of crack tips [6-8] and dislocations [9-11], correctly describe wave dispersion [12-13] and scale effects for the composite materials [14-22] and others. In this case, usually there are used simplified versions of the gradient theory of elasticity, which contain fewer additional parameters. The determination of additional physical constants requires the involvement of specific experimental approaches [23, 24] or methods of the molecular-dynamics modeling [21, 25-27]. Usually, there are used the applied models that, instead of five modulus [1, 2], contain three additional parameters [23,28] or two parameters [29] or a single additional scale parameter [4-6, 30]. A detailed classification of simplified models of the gradient theory of elasticity was considered in a recent paper [31, 32].

At the present time, gradient theories are actively developed and are increasingly used in various applied problems. However, fundamental questions of the construction of these theories are also discussed. In particular, there are discussed the physical meaning of additional high-order stresses [31,32], the problem of the correct formulation of models of gradient bars and plates [33-36], the problem of the correct formulation of the equilibrium equations and boundary conditions [32, 36-38], the problem of constructing models with allowance for the requirement of symmetry conditions [29] .

In this paper we discuss the problem of constructing a gradient theory of elasticity, in which static boundary conditions and equilibrium equations are written in terms of the same tensor of generalized stresses. In this paper, such stresses are suggested to call as “classical” stresses but not the “total” stresses introduced using terminology of E. Aifantis because the equilibrium equations are a divergence of these stresses, and the boundary conditions represent their convolution with the unit vector of normal to the surface of the body. The class of gradient models considered in the paper is the most attractive from a practical point of view, since for such models the solution of boundary value problems can often be simplified, sequentially solving the classical problem of elasticity theory and then solving the problem for an equation of Helmholtz type in which the right-hand side is the classical solution. Note that the known one-parameter gradient theories (so-called GradEla, SSGET etc. [29, 36, 37]) do not satisfy these requirements and their variational formulation leads to the appearance of natural boundary conditions in the complicated form [29,32,36]. In this paper we show the possibility of constructing a theory of GradEla type that satisfies these requirements, but with an asymmetric tensor of stresses.

## 2. «Vector» gradient model

Let us consider the Lagrangian  $L$  of the Mindlin-Tupin model:

$$L = A - \frac{1}{2} \iiint (C_{ijmn} R_{i,j} R_{m,n} + C_{ijkml} R_{i,jk} R_{m,nl}) dV. \quad (1)$$

Here  $C_{ijmn} = \lambda \delta_{ij} \delta_{mn} + \mu (\delta_{im} \delta_{jn} + \delta_{in} \delta_{jm})$  is the tensor of classical modulus,  $C_{ijkml}$  is the tensor of gradient modulus,  $\delta_{ij}$  is the Kronecker delta,  $A$  - is the work of the external given forces in the volume and on the surface of the body,  $R_i$  is the displacement vector.

We write down the conditions that determine the properties of the tensor of gradient elastic modules:

1. Existence of the density of potential energy:

$$C_{ijkml} = (C_{ijkml} + C_{mnljk}) / 2. \quad (2)$$

2. The symmetry condition, determined by the requirement of continuity of displacements:

$$C_{ijkml} = (C_{ijkml} + C_{ikjml} + C_{ijkmnl} + C_{ikjmln}) / 4. \quad (3)$$

As a result, taking into account conditions (2) and (3), we establish the general structure of the tensor  $C_{ijkml}$ :

$$\begin{aligned} C_{ijkml} = & \\ = C_1 & (\delta_{ij} \delta_{kl} \delta_{mn} + \delta_{ik} \delta_{jn} \delta_{ml} + \delta_{ij} \delta_{kn} \delta_{ml} + \delta_{mn} \delta_{lj} \delta_{ik}) + \\ + C_2 & (\delta_{ij} \delta_{km} \delta_{nl} + \delta_{mn} \delta_{li} \delta_{jk} + \delta_{ik} \delta_{jm} \delta_{nl} + \delta_{ml} \delta_{ni} \delta_{jk}) + \\ + C_3 & (\delta_{in} \delta_{jl} \delta_{km} + \delta_{mj} \delta_{nk} \delta_{li} + \delta_{in} \delta_{mj} \delta_{kl} + \delta_{il} \delta_{jn} \delta_{mk}) + \\ + C_4 & \delta_{im} (\delta_{jn} \delta_{kl} + \delta_{jl} \delta_{nk}) + \\ + C_5 & (\delta_{im} \delta_{jk} \delta_{nl}). \end{aligned} \quad (4)$$

Consequently, in the general form, the gradient elastic modules of the Mindlin-Tupin model depend on five parameters.

We note that sometimes the symmetry requirement for the first two indices is imposed. Then three additional relations are introduced for the parameters of the gradient tensor of the elasticity modulus (4):

$$\begin{aligned} C_{ijkml} \mathcal{E}_{ijr} = & \\ = (C_1 - C_2) & (\delta_{ml} \mathcal{E}_{knr} + \delta_{mn} \mathcal{E}_{klr}) + \\ + (C_2 - C_5) & \delta_{nl} \mathcal{E}_{kmr} + \\ + (C_3 - C_4) & (\delta_{kl} \mathcal{E}_{nmr} + \delta_{nk} \mathcal{E}_{lmr}) = 0, \end{aligned}$$

where  $\mathcal{E}_{ijr}$  is the permutation symbol.

In this case, the gradient part of the energy density of the general model is two-parametrical. Let's call such a gradient model a completely symmetric gradient model.

We propose to introduce the definitions of basis tensors of sixth rank:

$$\begin{aligned}
C_{ijkml} &= C_1 \delta_{ijkml}^1 + C_2 \delta_{ijkml}^2 + C_3 \delta_{ijkml}^3 + C_4 \delta_{ijkml}^4 + C_5 \delta_{ijkml}^5 \\
\left\{ \begin{aligned}
\delta_{ijkml}^1 &= (\delta_{ij} \delta_{kn} \delta_{ml} + \delta_{mn} \delta_{lj} \delta_{ik} + \delta_{ij} \delta_{kl} \delta_{mn} + \delta_{ik} \delta_{jn} \delta_{ml}) \\
\delta_{ijkml}^2 &= (\delta_{ij} \delta_{km} \delta_{nl} + \delta_{mn} \delta_{li} \delta_{jk} + \delta_{ik} \delta_{jm} \delta_{nl} + \delta_{ml} \delta_{ni} \delta_{jk}) \\
\delta_{ijkml}^3 &= (\delta_{in} \delta_{jl} \delta_{km} + \delta_{mj} \delta_{nk} \delta_{li} + \delta_{in} \delta_{mj} \delta_{kl} + \delta_{il} \delta_{jn} \delta_{mk}) \\
\delta_{ijkml}^4 &= \delta_{im} (\delta_{jn} \delta_{kl} + \delta_{jl} \delta_{nk}) \\
\delta_{ijkml}^5 &= (\delta_{im} \delta_{jk} \delta_{nl})
\end{aligned} \right. \quad (5)
\end{aligned}$$

Basis tensors  $\delta_{ijkml}^1$ ,  $\delta_{ijkml}^2$  and  $\delta_{ijkml}^5$  in (5) have the same structure: each term in them is the product of three Kronecker tensors, one of which has both indices belonging to the first triple of the indices of the sixth-rank tensor  $C_{ijkml}$ , the second one has indices belonging to different triples of indices of the sixth-rank tensor  $C_{ijkml}$ , and the third one has indices belonging to the second triple of indices of the sixth-rank tensor  $C_{ijkml}$ . The basis tensors  $\delta_{ijkml}^3$  and  $\delta_{ijkml}^4$  also have the same structure, but it differs from the previous one: all three Kronecker tensors in them have indices belonging to different triples of indices of the sixth-rank tensor  $C_{ijkml}$  (one index is from the first triple, another is from the second triple of the indices of the tensor  $C_{ijkml}$ ). The density of the gradient potential energy, as a result, is divided into the sum of two fundamentally different terms. The first term is determined by the first group of basis tensors  $\delta_{ijkml}^1$ ,  $\delta_{ijkml}^2$  and  $\delta_{ijkml}^5$ , contains, respectively, the modules  $C_1, C_2, C_5$  and determines the quadratic form, composed of the components of two vectors  $\Delta R_i, R_{k,ki}$ . The second term is determined by the second group of basis tensors  $\delta_{ijkml}^3, \delta_{ijkml}^4$ , and contains, respectively, the modules  $C_3, C_4$  and determines a quadratic form composed of the components of the tensor of the third, but not of the first rank.

It can be shown, for example, that the completely symmetric theory of gradient deformation, and the theory of Aero-Kuvshinsky, which is considered the theory of gradient rotations, contain two types of basis tensors: one of the first type, constructed as a linear combination of basis tensors  $\delta_{ijkml}^1, \delta_{ijkml}^2$  and  $\delta_{ijkml}^5$ , second of the second type, constructed as a linear combination of basis tensors  $\delta_{ijkml}^3$  and  $\delta_{ijkml}^4$ .

Further, we will concentrate on the particular cases of gradient models, which contain only basic tensors of the first type. Preference is given to this particular case, because all three basis tensors  $\delta_{ijkml}^1, \delta_{ijkml}^2$  and  $\delta_{ijkml}^5$  can be represented as convolutions with respect to one index of two tensors of the fourth rank.

*Theorem:* "All three basis tensors  $\delta_{ijkml}^1, \delta_{ijkml}^2$  and  $\delta_{ijkml}^5$ , can be represented as convolutions with respect to one index of two tensors of the fourth rank"

*Proof.* In each term of the basis tensor  $\delta_{ijkml}^1, \delta_{ijkml}^2$  and  $\delta_{ijkml}^5$  there is a factor containing indices from different triples of the sixth-rank tensor. We represent it as a convolution of two tensors of Kronecker, for example:  $\delta_{im} = \delta_{ia} \delta_{ma}$ . In a similar way, we will deal with each Kronecker tensor containing indices from different triples:

$$\begin{aligned}
 \delta_{ijkml}^1 &= (\delta_{ij}\delta_{kl}\delta_{ml} + \delta_{mn}\delta_{lj}\delta_{ik} + \delta_{ij}\delta_{kl}\delta_{mn} + \delta_{ik}\delta_{jn}\delta_{ml}) = \\
 &= \delta_{ij}(\delta_{kn})\delta_{ml} + \delta_{mn}(\delta_{lj})\delta_{ik} + \delta_{ij}(\delta_{kl})\delta_{mn} + \delta_{ik}(\delta_{jn})\delta_{ml} = \\
 &= \delta_{ij}(\delta_{ka}\delta_{na})\delta_{ml} + \delta_{mn}(\delta_{la}\delta_{ja})\delta_{ik} + \delta_{ij}(\delta_{ka}\delta_{la})\delta_{mn} + \delta_{ik}(\delta_{ja}\delta_{na})\delta_{ml} = \\
 &= (\delta_{ij}\delta_{ka})(\delta_{ml}\delta_{na}) + (\delta_{ik}\delta_{ja})(\delta_{mn}\delta_{la}) + (\delta_{ij}\delta_{ka})(\delta_{mn}\delta_{la}) + (\delta_{ik}\delta_{ja})(\delta_{ml}\delta_{na}) = \\
 &= (\delta_{ij}\delta_{ka})(\delta_{ml}\delta_{na} + \delta_{mn}\delta_{la}) + (\delta_{ik}\delta_{ja})(\delta_{mn}\delta_{la} + \delta_{ml}\delta_{na}) = \\
 &= (\delta_{ij}\delta_{ka} + \delta_{ik}\delta_{ja})(\delta_{mn}\delta_{la} + \delta_{ml}\delta_{na}) \\
 \delta_{ijkml}^2 &= (\delta_{ij}\delta_{km}\delta_{nl} + \delta_{mn}\delta_{li}\delta_{jk} + \delta_{ik}\delta_{jm}\delta_{nl} + \delta_{ml}\delta_{ni}\delta_{jk}) = \\
 &= \delta_{ij}(\delta_{km})\delta_{nl} + \delta_{mn}(\delta_{li})\delta_{jk} + \delta_{ik}(\delta_{jm})\delta_{nl} + \delta_{ml}(\delta_{ni})\delta_{jk} = \\
 &= \delta_{ij}(\delta_{ka}\delta_{ma})\delta_{nl} + \delta_{mn}(\delta_{la}\delta_{ia})\delta_{jk} + \delta_{ik}(\delta_{ja}\delta_{ma})\delta_{nl} + \delta_{ml}(\delta_{na}\delta_{ia})\delta_{jk} = \\
 &= (\delta_{ij}\delta_{ka})(\delta_{nl}\delta_{ma}) + (\delta_{jk}\delta_{ia})(\delta_{mn}\delta_{la}) + (\delta_{ik}\delta_{ja})(\delta_{nl}\delta_{ma}) + (\delta_{jk}\delta_{ia})(\delta_{ml}\delta_{na}) = \\
 &= (\delta_{ij}\delta_{ka} + \delta_{ik}\delta_{ja})(\delta_{nl}\delta_{ma}) + (\delta_{jk}\delta_{ia})(\delta_{mn}\delta_{la} + \delta_{ml}\delta_{na}) \\
 \delta_{ijkml}^5 &= (\delta_{im}\delta_{jk}\delta_{nl}) = \\
 &= (\delta_{jk}\delta_{ia})(\delta_{nl}\delta_{ma})
 \end{aligned} \tag{6}$$

As a result, the gradient model, built on basic tensors (6), takes the following form:

$$\begin{aligned}
 C_{ijkml} &= \\
 &= C_1 (\delta_{ij}\delta_{ka} + \delta_{ik}\delta_{ja})(\delta_{mn}\delta_{la} + \delta_{ml}\delta_{na}) + \\
 &+ C_2 [(\delta_{ij}\delta_{ka} + \delta_{ik}\delta_{ja})(\delta_{nl}\delta_{ma}) + (\delta_{mn}\delta_{la} + \delta_{ml}\delta_{na})(\delta_{jk}\delta_{ia})] + \\
 &+ C_5 (\delta_{jk}\delta_{ia})(\delta_{nl}\delta_{ma}).
 \end{aligned} \tag{7}$$

In the basis (6), the doubled density of the potential energy of curvature of displacement has the form:

$$C_{ijkml} R_{i,jk} R_{m,nl} = 4C_1 R_{i,ia} R_{m,ma} + 4C_2 R_{i,ia} \Delta R_a + C_5 \Delta R_a \Delta R_a. \tag{8}$$

The quadratic form (8) can be established using equations (7). This form is canonical, and positive definite.

We note that in the expression for the gradient part of the potential energy density there are convolutions of the components of two vectors  $R_{i,ia}$  and  $\Delta R_a$ . Therefore, in what follows, we shall call this particular three-parameter model the "vector" gradient theory of elasticity.

For such a theory, it is easy to establish conditions for positive definiteness. Indeed, in accordance with the Sylvester criterion, for (8), we obtain the following system of inequalities:

$$\begin{cases} C_1 > 0 \\ C_1 C_5 - C_2 C_2 > 0 \end{cases} \tag{9}$$

It follows from (9) that  $C_5^T > 0$  too. Indeed, let us introduce instead of the modulus  $C_5$ , another modulus by the relation:

$$C_1 C_5 - C_2 C_2 = C^2. \tag{10}$$

As a consequence of (10), the second of the conditions (9) is identically satisfied. It also follows from (10):

$$C_1 C_5 = C^2 + C_2 C_2 > 0.$$

From the first condition of (9) and (10) we obtain:

$$C_5 = \frac{C^2 + C_2 C_2}{C_1} > 0.$$

### 3. On classical boundary conditions for the “vector” gradient model

Let us now consider in more detail the gradient theory, which is determined by the potential energy (1), (8) and which can be called the variant of the “vector” gradient theory. Using the relation (8), the density of the potential curvature energy in the “vector” theory (6) can be represented as a canonical positive definite quadratic form.

$$\begin{aligned}
 C_{ijkml} R_{i,jk} R_{m,nl} &= 4C_1 R_{i,ia} R_{m,ma} + 4C_2 R_{i,ia} \Delta R_a + C_5 \Delta R_a \Delta R_a = \\
 &= 4 \frac{C^2 + C_2 C_2}{C_5^T} R_{i,ia} R_{m,ma} + 4C_2 R_{i,ia} \Delta R_a + C_5 \Delta R_a \Delta R_a = \\
 &= 4 \frac{C^2}{C_5} R_{i,ia} R_{m,ma} + C_5 \left( \Delta R_a + \frac{2C_2}{C_5} R_{i,ia} \right) \left( \Delta R_a + \frac{2C_2}{C_5} R_{i,ia} \right).
 \end{aligned} \tag{11}$$

We can state that the “vector” theory in the general case contains three nonclassical moduli, under certain restrictions (9) due to positive definiteness of the canonical quadratic form of the density of the potential curvature energy (11).

We write the variational equation of the “vector” gradient model. From the requirement of stationarity of the Lagrangian (1) it follows that:

$$\begin{aligned}
 \delta L &= \delta A - \iiint [C_{ijmn} R_{m,n} \delta R_{i,j} + C_{ijkml} R_{m,nl} \delta R_{i,jk}] dV = \\
 &= \delta A - \iiint [C_{ijmn} R_{m,n} \delta R_{i,j} + (4C_1 R_{m,ma} + 4C_2 \Delta R_a) \delta R_{i,ia} + (4C_2 R_{i,ia} + C_5 \Delta R_a) \delta \Delta R_a] dV = \\
 &= \delta A - \iiint [C_{ijmn} R_{m,n} \delta R_{i,j} + \\
 &+ [4(C_1 + C_2) R_{m,ma} + (4C_2 + C_5) \Delta R_a] \delta R_{i,ia} + \\
 &+ (4C_2 R_{i,ia} + C_5 \Delta R_a) \delta (\Delta R_a - R_{j,ja})] dV.
 \end{aligned}$$

Using the relation:

$$(R_{a,jj} - R_{j,ja}) = (R_{m,jn} \delta_{ma} \delta_{nj} - R_{m,jn} \delta_{mj} \delta_{na}) = R_{m,jn} (\delta_{ma} \delta_{nj} - \delta_{mj} \delta_{na}) = R_{m,jn} \mathcal{E}_{mnk} \mathcal{E}_{ajk},$$

we can found that the procedure of integrating by parts for the gradient part of the potential energy density will not require further transformations of the surface integral:

$$\begin{aligned}
 \delta L &= \delta A - \iiint [C_{ijmn} R_{m,n} \delta R_{i,j} - (4C_1 + 8C_2 + C_5) \Delta R_{a,a} \delta R_{i,i} - C_5 \Delta R_{a,j} \delta R_{m,n} \mathcal{E}_{mnk} \mathcal{E}_{ajk}] dV - \\
 &- \oint \{ [4(C_1 + C_2) R_{m,ma} + (4C_2 + C_5) \Delta R_a] n_a \delta R_{i,i} + \\
 &+ 2(4C_2 R_{i,ia} + C_5 \Delta R_a) \delta (-R_{m,n} \mathcal{E}_{mnk} / 2) n_j \mathcal{E}_{kja} \} dF.
 \end{aligned}$$

Indeed, let’s introduce the classical definitions for the volume changing deformations  $\theta = R_{i,i}$  and deformations of spins  $\omega_k = -R_{m,n} \mathcal{E}_{mnk} / 2$ . These parameters determine on the surface independent variations of linear combinations of normal and tangential derivatives of displacements, which do not require further integrating by parts. As a result, the variational equation of the “vector” model takes the form:

$$\begin{aligned}
 \delta L &= \iiint [(C_{ijmn} R_{m,n} - (4C_1 + 8C_2 + C_5) \Delta R_{a,a} \delta_{ij} - C_5 \Delta R_{a,c} \mathcal{E}_{ijk} \mathcal{E}_{ack})_{,j} + P_i^V] \delta R_i dV + \\
 &+ \oint \{ [P_i^F - (C_{ijmn} R_{m,n} - (4C_1 + 8C_2 + C_5) \Delta R_{a,a} \delta_{ij} - C_5 \Delta R_{a,c} \mathcal{E}_{ijk} \mathcal{E}_{ack}) n_j] \delta R_i - \\
 &- [4(C_1 + C_2) R_{m,ma} + (4C_2 + C_5) \Delta R_a] n_a \delta \theta - 2(4C_2 R_{i,ia} + C_5 \Delta R_a) \delta (\omega_k n_j \mathcal{E}_{kja}) \} dF = 0.
 \end{aligned} \tag{12}$$

Equilibrium equations can be obtained from (12) as the Euler equations:

$$(C_{ijmn} R_{m,n} - (4C_1 + 8C_2 + C_5) \Delta R_{a,a} \delta_{ij} - C_5 \Delta R_{a,c} \mathcal{E}_{ijk} \mathcal{E}_{ack})_{,j} + P_i^V = 0. \tag{13}$$

We call attention to the fact that the second-rank tensor, which divergence is equal to the external volume force in the equilibrium equations (13), can conditionally be called the “classical” stress tensor:

$$\tau_{ij} = C_{ijmn}R_{m,n} - (4C_1 + 8C_2 + C_5)\Delta\theta\delta_{ij} + 2C_5\Delta\omega_k\mathcal{E}_{ijk}. \quad (14)$$

Since this tensor (14) satisfies three classical equilibrium equations of elasticity theory:

$$\tau_{ij,j} + P_i^V = 0. \quad (15)$$

However, the “classical” stresses (14) differ from the “classical” ones, in the first place, in that this tensor is non-symmetric tensor, since the last term is antisymmetric when free indices are permuted. This term you can remove only if  $C_5 = 0$ . Therefore, the vector model can't operate with the concept of true “classical” stresses.

On the other hand, the stress  $\tau_{ij}$  satisfies not only the three classical equilibrium equations, but also the three classical static boundary conditions:

$$\oint\oint (P_i^F - \tau_{ij}n_j)\delta R_i dF = 0. \quad (16)$$

Indeed, boundary conditions for the considered variant of the “vector” theory break up into three pairs of alternative boundary conditions. The static boundary conditions (16) during variations of displacements completely coincide with the classical ones. Three pairs of alternative nonclassical boundary conditions break up into a pair of scalar alternative boundary conditions:

$$\oint\oint [4(C_1 + C_2)R_{m,ma} + (4C_2 + C_5)\Delta R_a]n_a\delta\theta dF = 0. \quad (17)$$

One of them is connected with variation of spherical tensor of deformation (see (17)). Two other pairs of alternative boundary conditions determine the possible work of some force vector  $f_a = (4C_2R_{i,ia} + C_5\Delta R_a)$  on the variations of another (plane) vector  $v_a = \omega_k n_j \mathcal{E}_{kja}$ :

$$\oint\oint (4C_2R_{i,ia} + C_5\Delta R_a)\delta(\omega_k n_j \mathcal{E}_{kja})dF = 0. \quad (18)$$

It is not difficult to verify that the vector  $v_a = \omega_k n_j \mathcal{E}_{kja}$  in (18) does not have a projection onto the normal to the surface, that is, lies in a tangent plane to the surface of the body  $v_a n_a = (\omega_k n_j \mathcal{E}_{kja})n_a = \omega_k (n_j n_a \mathcal{E}_{jak}) \equiv 0$ .

Let us return to the equilibrium equations and investigate the possibility of separating the equilibrium operator into a product of the classical equilibrium operator and an additional, nonclassical one. In other words, we will find out whether it is possible to represent the operator of equations (13) in the form:

$$[\mu\Delta(\dots)\delta_{ij} + (\mu + \lambda)(\dots)_{,ij}]\{(\dots)\delta_{jk} - l_\omega^2\Delta(\dots)\delta_{jk} - (l_\theta^2 - l_\omega^2)(\dots)_{,jk}\}R_k + P_i^V = 0. \quad (19)$$

By successively applying to the displacement vector  $R_k$ , first the operator in curly brackets (19), and then the operator in square brackets, we get:

$$\mu(\Delta R_i - R_{j,ji}) + (2\mu + \lambda)R_{j,ij} - \mu l_\omega^2\Delta(\Delta R_i - R_{j,ji}) - (2\mu + \lambda)l_\theta^2\Delta R_{j,ji} + P_i^V = 0 \quad (20)$$

Comparing (20) and (13), we find that the equations coincide if the parameters  $l_\theta^2, l_\omega^2$  are related to nonclassical modules by the following relations:

$$\begin{cases} C_5 = \mu l_\omega^2 \\ 4C_1 + 8C_2 = (2\mu + \lambda)l_\theta^2 - \mu l_\omega^2 \end{cases} \quad (21)$$

Applying the operator in curly brackets of equation (19) to the vector  $R_k$  (19), we obtain the definition of “classical” displacements  $U_i$ :

$$\begin{aligned} U_j &= \{(\dots)\delta_{jk} - l_\omega^2\Delta(\dots)\delta_{jk} - (l_\theta^2 - l_\omega^2)(\dots)_{,jk}\}R_k = \\ &= R_j - l_\omega^2(\Delta R_j - R_{k,kj}) - l_\theta^2 R_{k,kj}. \end{aligned} \quad (22)$$

Taking into account the definition (22), the equilibrium equations (19) take the form of the Lamé equations of the classical theory of elasticity in displacements:

$$[\mu\Delta(\dots)\delta_{ij} + (\mu + \lambda)(\dots)_{,ij}]U_j + P_i^V = 0. \quad (23)$$

Since the linear differential operators in (19) are commutative, the equilibrium equations can be rewritten in the following equivalent form:

$$\frac{\mu}{l^2} \{(\dots)\delta_{ij} - l_\omega^2 \Delta(\dots)\delta_{ij} - (l_\theta^2 - l_\omega^2)(\dots)_{,ij}\} l^2 [\Delta(\dots)\delta_{jk} + \frac{(\mu + \lambda)}{\mu} (\dots)_{,jk}] R_k + P_i^V = 0. \quad (24)$$

The first of the operators in (24) is a generalized Helmholtz operator. Therefore, we can introduce a vector of "cohesive" displacements [14-16, 19, 20, 21],  $u_j$ :

$$\begin{aligned} u_j &= -l^2 [\Delta(\dots)\delta_{jk} + \frac{(\mu + \lambda)}{\mu} (\dots)_{,jk}] R_k = \\ &= -l^2 [(\Delta R_j - R_{k,kj}) + \frac{(2\mu + \lambda)}{\mu} R_{k,kj}]. \end{aligned} \quad (25)$$

Taking into account the definition of  $u_j$ , (25) the equilibrium equations give the equilibrium equations of the "cohesive" field:

$$l_\omega^2 (\Delta u_i - u_{j,ji}) + l_\theta^2 u_{j,ji} - u_i + l^2 \frac{P_i^V}{\mu} = 0. \quad (26)$$

Let us consider the definitions (22) and (25) as a linear algebraic system with respect to the vortex field  $(\Delta R_j - R_{k,kj})$  and the potential field  $R_{k,kj}$ :

$$\begin{cases} l_\omega^2 (\Delta R_j - R_{k,kj}) + l_\theta^2 R_{k,kj} = R_j - U_j \\ l^2 (\Delta R_j - R_{k,kj}) + \frac{(2\mu + \lambda)}{\mu} l^2 R_{k,kj} = -u_j \end{cases} \quad (27)$$

It is easy to see that the equation system (27) can be rewritten in the following form:

$$\begin{cases} (\Delta R_j - R_{k,kj}) = \frac{-\frac{(2\mu + \lambda)}{\mu} \frac{1}{l_\omega^2} (R_j - U_j) - \frac{l_\theta^2}{l_\omega^2} \frac{1}{l^2} u_j}{[\frac{l_\theta^2}{l_\omega^2} - \frac{(2\mu + \lambda)}{\mu}]} \\ R_{k,kj} = \frac{\frac{1}{l_\omega^2} (R_j - U_j) + \frac{1}{l^2} u_j}{[\frac{l_\theta^2}{l_\omega^2} - \frac{(2\mu + \lambda)}{\mu}]} \end{cases} \quad (28)$$

The first of equations (28) determines the vortex field  $(\Delta R_j - R_{k,kj})$ . Its divergence is, by definition, equal to zero. Therefore, taking into account (22), (28) we can write:

$$R_{k,k} = U_{k,k} - \frac{\mu}{(2\mu + \lambda)} \frac{l_\theta^2}{l^2} u_{k,k}. \quad (29)$$

The second of the equations (28) determines the potential field  $R_{k,kj}$ . Its rotor is zero, by definition:

$$R_{m,n} \mathcal{E}_{mnr} = U_{m,n} \mathcal{E}_{mnr} - \frac{l_\omega^2}{l^2} u_{m,n} \mathcal{E}_{mnr}. \quad (30)$$

Accordingly, we can write the following equation for the rotor of the rotor:

$$(\Delta R_k - R_{m,mk}) = (\Delta U_k - U_{m,mk}) - \frac{l_\omega^2}{l^2} (\Delta u_k - u_{m,mk}). \quad (31)$$

Substituting (30) and (31) into (23), we obtain the general solution of the “vector” gradient theory  $R_i$  through two fundamental vectors, one of which is a vector of “classical” displacements  $U_i$ , and the second one is a vector of “cohesive” displacements  $u_i$ :

$$R_i = U_i + l_\omega^2(\Delta U_i - U_{k,ki}) + l_\theta^2 U_{k,ki} - \frac{l_\omega^2 l_\theta^2}{l^2}(\Delta u_i - u_{k,ki}) - \frac{\mu}{(2\mu + \lambda)} \frac{l_\theta^2 l_\omega^2}{l^2} u_{k,ki}. \quad (32)$$

Let us write down the tensor of stresses in displacements. Substituting vector of displacements  $R_i$ , with the help of equation (32), into (14) and taking into account the definitions (22), we can get:

$$\begin{aligned} \tau_{ij} = & C_{ijmn} U_{m,n} + \\ & + 2\mu l_\theta^2 \left[ \frac{\mu}{(2\mu + \lambda)} \frac{1}{l^2} u_{k,k} \right] \delta_{ij} + \mu (\delta_{im} \delta_{jn} + \delta_{in} \delta_{jm}) [l_\omega^2 (\Delta U_{m,n} - U_{k,kmn}) + \\ & + l_\theta^2 U_{k,kmn} - \frac{l_\omega^2 l_\theta^2}{l^2} (\Delta u_{m,n} - u_{k,kmn}) - \frac{\mu l_\theta^2 l_\omega^2}{(2\mu + \lambda) l^2} u_{k,kmn}] + 2\mu l_\omega^2 \Delta \omega_k \mathcal{E}_{ijk}. \end{aligned} \quad (33)$$

Let’s make the following remark. In expressions (25), (26), we introduce a scale normalizing parameter when it’s determined the “cohesive” field vector  $u_i$ . We can assume without loss of generality that  $l = l_\omega^2$ . In the general case, both the system of equilibrium equations (24), the general solution of these equations and the expression for the stresses (33), are written in terms of “classical” displacements and “cohesive” displacements are determined only through two scale parameters  $l_\omega^2$  и  $l_\theta^2$ . The spherical tensor of deformations  $R_{k,k}$  and pseudo-vector of rotations  $R_{m,n} \mathcal{E}_{mnr}$  (see equations (29) and (30)) are also written explicitly through “classical” displacements and “cohesive” displacements, and, therefore, depend only on  $l_\omega^2$  and  $l_\theta^2$ . Therefore, if kinematic boundary conditions hold (see (12)), then the problem, as a whole, is two-parametric. In the general case of static boundary conditions, only the static factor with  $f_a = (4C_2 R_{i,ia} + C_5 \Delta R_a)$  depends on the third parameter  $C_2$ . Consequently, the boundary value problem, as a whole, becomes three-parametric only in the case of static nonclassical boundary conditions (12).

Further, if we assume that  $\frac{l_\theta^2}{l_\omega^2} = \frac{(2\mu + \lambda)}{\mu}$ ,  $l^2 = l_\omega^2$ , then we come to a one-parameter model for which the expansion [14-16, 20,22] takes place:  $R_i = U_i - u_i$ .

Finally, we note that the fulfillment of the hypothesis of "classicality", in which the static boundary conditions on the tensor of “classical” stresses have the standard classical form (16), generally leads to the possibility of constructing approximate solutions of a wide class of applied problems with the decrease of order of boundary value problems.

Suppose that there are boundary value problems containing the static boundary condition (16) as one of the boundary conditions on the body surface. We will assume at the first step of constructing an approximate solution, that for the tensor of stresses  $\tau_{ij}$  the defining relation can be approximately written in the form  $\tau_{ij} = C_{ijmn} U_{m,n}$ . Then the displacement vector  $U_i$  can be found from the solution of the first classical boundary-value problem (a problem with static boundary conditions). At the final step, the solution of the boundary value problem for equation (22) is constructed

$$\{(\dots)\delta_{jk} - l_\omega^2 \Delta(\dots)\delta_{jk} - (l_\theta^2 - l_\omega^2)(\dots)_{,jk}\} R_k = U_j,$$

with boundary conditions defined by the variational equality

$$\oint\!\!\!\oint \{ [4(C_1 + C_2)R_{m,ma} + (4C_2 + C_5)\Delta R_a]n_a \delta\theta - 2(4C_2R_{i,ia} + C_5\Delta R_a)\delta(\omega_k n_j \mathcal{E}_{kja}) \} dF = 0$$

Then the field of “cohesive” displacements from equality (25) can be explicitly determined. After that, we can redefine the stresses in formula (33), assuming that the field of “cohesive” displacements is known, and repeat the procedure for constructing the solution, which reduces to a sequence of solving two boundary value problems of second and not fourth order. It is not difficult to see that the algorithm proposed above corresponds to the procedure for constructing a solution using the asymptotic expansion of the solution for a small parameter  $l^2 = l_\omega^2$  and resembles the procedure for the method of elastic solutions. In this case, the equilibrium equations (15) and static boundary conditions (16) are satisfied exactly at each step, and the defining relations are considered as approximate, which is completely permissible.

#### 4. Applied “vector” gradient models

For applied problems, the simplest gradient models that contain two or even one additional parameter are of interest, comparing with the classical theory of elasticity. Let's consider some variants of such correct “vector” gradient models.

Suppose that in (10)  $C = 0$ . In the future, we will use the same transformations for model analysis as we used in the section 3. The variational equation of the applied gradient two-parameter model in this case has the form:

$$\begin{aligned} \delta L = & \iiint \{ C_{ijmn} R_{m,nj} - C_5 \Delta \Delta R_i - 4C_2 (1 + \frac{C_2}{C_5}) \Delta R_{j,ji} + P_i^V \} \delta R_i dV + \\ & + \oint\!\!\!\oint \{ P_i^F - [C_{ijmn} R_{m,n} - C_5 \Delta R_{i,j} - C_2 \Delta R_{j,i} - C_2 (1 + 2\frac{C_2}{C_5}) \Delta R_{k,k} \delta_{ij} - \\ & - 2C_2 (1 + \frac{C_2}{C_5}) R_{m,mij}] n_j \} \delta R_i dF + \\ & + \oint\!\!\!\oint \{ -C_5 (\Delta R_a + 2\frac{C_2}{C_5} R_{m,ma}) \delta [R_{a,j} n_j + \frac{C_2}{C_5} (n_a R_{j,j} + n_k R_{k,a})] \} dF = 0. \end{aligned} \quad (34)$$

For the model (34), the “classical” equilibrium equations and the “classical” static boundary conditions (with variation of displacements  $\delta R_i$  in (34)) have a clearly classical form:

$$\tau_{ij,j} + P_i^V = 0, \quad \oint\!\!\!\oint (P_i^F - \tau_{ij} n_j) \delta R_i dF = 0,$$

where  $\tau_{ij}$  is the tensor of “classical” stresses:

$$\tau_{ij} = C_{ijmn} R_{m,n} - C_5 \Delta R_{i,j} - C_2 \Delta R_{j,i} - C_2 (1 + 2\frac{C_2}{C_5}) \Delta R_{k,k} \delta_{ij} - 2C_2 (1 + \frac{C_2}{C_5}) R_{m,mij}. \quad (35)$$

The stresses (35), in contrast to (14), can be made paired, requiring in addition:  $C_2 = C_5$ .

The nonclassical boundary conditions in (34) decompose into three pairs of alternative nonclassical boundary conditions:

$$\oint\!\!\!\oint \{ -C_5 (\Delta R_a + 2\frac{C_2}{C_5} R_{m,ma}) \delta [R_{a,j} n_j + \frac{C_2}{C_5} (n_a R_{j,j} + n_k R_{k,a})] \} dF = 0. \quad (36)$$

The “vector” (three-parameter) theory (12), (17) differs from the theory of the “cohesive” field (two-parametric) model (34), (36) in that the boundary conditions contain all three nonclassical parameters.

For the model under consideration, the operator of the equilibrium equation is represented as the product of a classical equilibrium operator and an additional, nonclassical Helmholtz

operator if the scale parameters  $l_\theta^2, l_\omega^2$  in (24) are related to nonclassical modules by the following relations:

$$\begin{cases} C_5 = \mu l_\omega^2 \\ 2C_2 = \sqrt{\mu(2\mu + \lambda)} l_\omega l_\theta - \mu l_\omega^2 \end{cases} \quad (38)$$

The “classical” displacement field, the field of “cohesive” displacements in this model, is also determined by equations (22) and (25), and the general solution is represented by the relation (32).

Let us give one more particular “vector” gradient model, which is a further simplification of the general vector model and is already a one-parameter gradient model. We assume in (11), (14) that  $C = 0$ ,  $C_5 = \mu l^2$ ,  $2C_2 = (\mu + \lambda)l^2$ . Then the density of the gradient part of the potential energy can be represented in a simpler and more compact form:

$$C_{ijkml} R_{i,jk} R_{m,nl} = \mu l^2 [(\Delta R_a - R_{i,ia}) + \frac{(2\mu + \lambda)}{\mu} R_{i,ia}] [(\Delta R_a - R_{i,ia}) + \frac{(2\mu + \lambda)}{\mu} R_{j,ja}]. \quad (37)$$

Here it is taken into account that

$$C_{ijkml} = \mu l^2 [(\delta_{jk} \delta_{ia}) + \frac{(\mu + \lambda)}{2\mu} (\delta_{ij} \delta_{ka} + \delta_{ik} \delta_{ja})] [(\delta_{nl} \delta_{ma}) + \frac{(\mu + \lambda)}{2\mu} (\delta_{mn} \delta_{la} + \delta_{ml} \delta_{na})].$$

For this particular model (37), the variational equation defining the mathematical model (solving the equation and the boundary conditions) has the form:

$$\begin{aligned} \delta L = & \iiint \{ \tau_{ij,j} + P_i^V \} \delta R_i dV + \iint \{ P_i^F - (P_i^F - \tau_{ij} n_j) \} \delta R_i dF + \\ & - \iint l^2 [ \mu \Delta R_a + (\mu + \lambda) R_{m,ma} ] \delta [ R_{a,k} + \frac{(\mu + \lambda)}{2\mu} (R_{j,j} \delta_{ak} + R_{k,a}) ] n_k dF = 0, \end{aligned} \quad (38)$$

where  $\tau_{ij}$  are the “classical” stresses:

$$\begin{aligned} \tau_{ij} = & C_{ijmn} R_{m,n} - l^2 [ \mu \Delta R_{i,j} + \frac{(\mu + \lambda)}{2} \Delta R_{j,i} + \\ & + (\mu + \lambda) \frac{(3\mu + \lambda)}{2\mu} R_{m,mij} + \frac{(\mu + \lambda)}{2\mu} (2\mu + \lambda) \Delta R_{k,k} \delta_{ij} ]. \end{aligned}$$

If we assume  $l_\theta^2 = (2\mu + \lambda)l^2 / \mu$ ,  $l^2 = l_\omega^2$  then for the one-parameter model (38) under consideration, the operator of the equilibrium equation is represented as the product of the Lamé operator and the generalized Helmholtz operator constructed on the base of the Lamé operator (see also [20]):

$$[L_{ij}(\dots)] \{ (\dots) \delta_{jk} - (l^2 / \mu) L_{ij}(\dots)_{,jk} \} R_k + P_i^V = 0, \quad (39)$$

where  $L_{ij}(\dots)$  is the Lamé operator,  $L_{ij}(\dots) = [\Delta(\dots) \delta_{ij} + (\mu + \lambda)(\dots)_{,ij}]$ .

The “classical” displacement field and the field of “cohesive” displacements are determined, respectively, by the equalities:

$$U_j = R_j - [ \mu \Delta R_j + (\mu + \lambda) R_{k,kj} ] l^2 / \mu, \quad u_j = - (l^2 / \mu) L_{jk} R_k \quad (40)$$

and are the solutions of equations:

$$[ \mu \Delta(\dots) \delta_{ij} + (\mu + \lambda)(\dots)_{,ij} ] U_j + P_i^V = 0 \quad (41)$$

$$L_{ij} u_j - (\mu / l^2) u_i + P_i^V = 0$$

The general solution is represented as a decomposition:  $R_i = U_i - u_i$ .

Note that the one-parameter gradient model for which the equalities (39) - (41) are satisfied was widely used in [19, 20, 22] to solve applied problems in the mechanics of

composites with micro/nano-dimension inclusions and was called the applied model of the interphase layer.

### 5. On one generalization of the Aifantis's GradEla model

Finally, we consider an even more particular gradient model, which belongs to the class of vector models.

We suppose that  $C_1 = 0, C_2 = 0, C_5 = \mu l^2$ . Then the relation (11), (14) gives the following representation for the tensor of gradient modules  $C_{ijkml} = \mu l^2 (\delta_{jk} \delta_{ia})(\delta_{nl} \delta_{ma})$ , and the gradient part of the potential energy has the form:

$$C_{ijkml} R_{i,jk} R_{m,nl} = \mu l^2 \Delta R_a \Delta R_a. \quad (42)$$

The variational equation of the vector gradient model under consideration looks like:

$$\begin{aligned} \delta L = \delta A - \iiint [C_{ijmn} R_{m,n} \delta R_{i,j} + C_{ijkml} R_{m,nl} \delta R_{i,jk}] dV = \\ = \oint \{ [P_i^F - (C_{ijmn} R_{m,n} - \mu l^2 \Delta R_{i,j}) n_j] \delta R_i - \mu l^2 \Delta R_a \delta (R_{a,k} n_k) \} dF = 0 \end{aligned} \quad (43)$$

It follows from the variational equality (43) that in the boundary-value problem the "classical" static condition for the "classical" stress  $\tau_{ij}$  is precisely distinguished, and three pairs of alternative nonclassical boundary conditions are given by the variational equality:

$$\oint \mu l^2 \Delta R_a \delta (R_{a,k} n_k) dF = 0.$$

In this case, the "classical" stress has the form

$$\tau_{ij} = C_{ijmn} R_{m,n} - \mu l^2 \Delta R_{i,j}, \quad (44)$$

and, in its structure, almost exactly coincides with the expression for the total stresses of the GradEla model of Aifantis.

It is easy to verify that the equilibrium equation for a given vector model exactly coincides with the equilibrium equation of the GradEla model, and the operator of the equilibrium equation is represented as the product of the Lamé operator and the Helmholtz operator

$$\{ (\dots) - l^2 \Delta (\dots) \} [ \mu \Delta (\dots) \delta_{ik} + (\mu + \lambda) (\dots)_{,ik} ] R_k + P_i^V = 0. \quad (45)$$

The "classical" displacement field  $U_j$  and the "cohesive" displacement field  $u_j$  are determined by the equations:

$$U_j = R_j - l^2 \Delta R_j, \quad [ \mu \Delta (\dots) \delta_{ij} + (\mu + \lambda) (\dots)_{,ij} ] U_j + P_i^V = 0 \quad (46)$$

$$u_i = - [ \Delta (\dots) \delta_{ik} + (\dots)_{,ik} (\mu + \lambda) / \mu ] R_k, \quad \mu l^2 \Delta u_i - \mu u_i + P_i^V = 0, \quad (47)$$

which also coincide exactly with the corresponding equations of the Aifantis GradEla model [36].

Note that although the gradient model determined by the relations (42) - (47) resembles the gradient model of Aifantis (GRADELA) in many ways, does not coincide with it. The model presented above is non-symmetric – the "classical" stresses are non-symmetric. In the Aifantis model, the gradient part of the potential energy is written in the form  $\mu l^2 \varepsilon_{ij,k} \varepsilon_{ij,k}$  and differs from the expression (42), the gradient component of the defining relation for symmetric total stresses is written through Laplacian of the deformation  $\Delta \varepsilon_{i,j}$ , in contrast to expression (44).

The model considered in the article belongs to the class of vector gradient correct models. For it, the static boundary condition, written only for "classical" stresses, is precisely distinguished. In general, this leads to simplifying the construction of solutions of applied problems. The GradEla model of Aifantis does not possess this quality. It does not belong to the class of vector gradient correct models.

The model defined by (42) - (47) we will call the generalized Aifantis model. This generalization allows us to transfer the Aifantis model to a class of correct vector models for which the classical boundary.

### 6. On decomposition of boundary value problems

Let us return to the vector gradient models and briefly examine the possibility of substantially simplifying the solutions of boundary value problems for them using **decomposition** of the general boundary value problem of the fourth order into a sequence of independently solvable boundary value problems of the second order. We assume that the conditions that lead to static boundary conditions of the classical form are satisfied:

$$C_{ijkml} = \mu l_{akij} l_{almn}. \tag{48}$$

Then the following statement holds: The gradient part of the potential energy density for the model in which the gradient modules obey conditions (48) is representable as the potential energy density of vector field. Really, taking into account (48) we obtain:

$$C_{ijkml} R_{i,jk} R_{m,nl} = \mu l_{akij} l_{almn} R_{i,jk} R_{m,nl} = \mu (l_{akij} R_{i,jk}) (l_{almn} R_{m,nl}). \tag{49}$$

The expression (49) is determined by the convolution of the following vectors  $\varepsilon_i = l_{akij} R_{i,jk}$ . Consequently, for the gradient models under consideration, the variational equation, taking into account (48), (49) takes the form:

$$\begin{aligned} \delta L = & \iiint [(C_{ijmn} R_{m,n} + \mu \varepsilon_{a,k} l_{akij})_{,j} + P_i^V] \delta R_i dV + \\ & + \oint \{ [P_i^F - (C_{ijmn} R_{m,n} + \mu \varepsilon_{a,k} l_{akij}) n_j] \delta R_i - \mu \varepsilon_a \delta (l_{akij} n_k R_{i,j}) \} dF = 0. \end{aligned} \tag{50}$$

We can define the second rank tensor in (50) as the tensor of conditional “classical” stresses:

$$\sigma_{ij} = (C_{ijmn} R_{m,n} + \mu \varepsilon_{a,k} l_{akij}). \tag{51}$$

It is easy to see that the stresses  $\sigma_{ij}$  (51) satisfy both the equilibrium equations and the classical static conditions:

$$\begin{aligned} \delta L = & \iiint (\sigma_{ij,j} + P_i^V) \delta R_i dV + \\ & + \oint [(P_i^F - \sigma_{ij} n_j) \delta R_i - \mu \varepsilon_a \delta (l_{akij} n_k R_{i,j})] dF = 0. \end{aligned} \tag{52}$$

The variational equation (52) indicates that nonclassical conditions are determined by three pairs of alternative boundary conditions which do not change the classical boundary conditions  $P_i^F - \sigma_{ij} n_j = 0$ .

Using the classical modulus of elasticity  $C_{ijmn} = \lambda \delta_{ij} \delta_{mn} + \mu (\delta_{im} \delta_{jn} + \delta_{in} \delta_{jm})$ , let’s postulate the following relations:

$$l_{ijmn} = \frac{l}{\mu} C_{ijmn} = l (\delta_{im} \delta_{jn} + \delta_{in} \delta_{jm} + \frac{\lambda}{\mu} \delta_{ij} \delta_{mn}), \quad l_{ijmn} = l_{mni} \tag{53}$$

Therefore, taking into account (49) we find that the following equality must hold:

$$C_{ijkml} = \frac{l^2}{\mu} C_{akij} C_{almn}, \quad C_{almn} = \lambda \delta_{al} \delta_{mn} + \mu (\delta_{am} \delta_{ln} + \delta_{an} \delta_{lm}).$$

In this case, the relation (51) takes the form:

$$\sigma_{ij} = (C_{ijmn} R_{m,n} + \mu \varepsilon_{a,k} l_{akij}) = C_{ijmn} (R_m + l \varepsilon_m)_{,n}. \tag{54}$$

We note, however, that the introduction of hypothesis (53) leads to a loss of symmetry for the “classical” stresses (54).

At last, “classical” displacements  $U_i$  can be found (see eq. (53)):

$$\begin{aligned}
U_i &= R_i + l\varepsilon_i = R_i + l \cdot l_{ilmn} R_{m,nl} = R_i + l^2 (\delta_{im} \delta_{ln} + \delta_{in} \delta_{lm} + \frac{\lambda}{\mu} \delta_{il} \delta_{mn}) R_{m,nl} = \\
&= R_i + [\mu \Delta R_i + (\mu + \lambda) R_{k,ki}] l^2 / \mu.
\end{aligned} \tag{55}$$

“Cohesive” displacements  $u_i$  are defined through the difference between “classical” and total displacements [20, 22]:

$$u_i = \frac{l^2}{\mu} [\mu \Delta R_i + (\mu + \lambda) R_{k,ki}]. \tag{56}$$

Then general solution for the considered variant of the “vector” gradient model has the form:

$$R_i = U_i - u_i \tag{57}$$

Note, that the gradient model defined by equations (50)-(57) is unique one parametrical model which allow to simplify set of boundary value problems using the decompositions of the initial problems of fourth order to the sequence of two problems of second order.

As a result, for the “vector” gradient model, the first fundamental problem splits into two, the classical boundary value problem:

$$\begin{cases} C_{ijmn} U_{m,nj} + P_i^V = 0 \\ \oint (P_i^V - C_{ijmn} n_j U_{m,n}) \delta(U_i - u_i) dF = 0 \end{cases} \tag{58}$$

and the auxiliary boundary value problem:

$$\begin{cases} (l^2 / \mu) C_{ijmn} R_{m,nj} - R_i = -U_i \\ \oint (R_i - U_i) \delta(C_{ijmn} n_j R_{m,n}) dF = 0 \end{cases}$$

The decomposition of the general solution into a superposition of “classical” one and “cohesive” one leads to the fact that the boundary value problems of gradient theories, in some cases, can be represented as a sequence of solutions of two boundary value problems: classical, with respect to the vector of “classical” displacements  $U_i$  and the boundary value problem with respect to the vector of complete displacements  $R_i$ . The non-classical auxiliary to (58) the boundary value problem can be reformulated, in accordance with (57) with respect to “cohesive” displacements  $u_i$ :

$$\begin{cases} C_{ijmn} u_{m,nj} - (\mu / l^2) u_i + P_i^V = 0 \\ \oint u_i \delta C_{ijmn} n_j (U_{m,n} - u_{m,n}) dF = 0. \end{cases} \tag{59}$$

Consequently, for the first fundamental problem, the boundary value problems always disintegrate into “classical” and “cohesive” displacements for the “vector” gradient model under consideration.

## 7. Analysis and decompositions of the boundary value problems

Formally, the boundary value problems of the “vector” gradient model, in the general case, are coupled problems (58), (59):

$$\begin{cases} C_{ijmn} U_{m,nj} + P_i^V = 0 \\ \oint (P_i^V - C_{ijmn} n_j U_{m,n}) \delta(U_i - u_i) dF = 0 \end{cases} \quad \begin{cases} C_{ijmn} u_{m,nj} - (\mu / l^2) u_i + P_i^V = 0 \\ \oint u_i \delta(C_{ijmn} n_j (U_{m,n} - u_{m,n})) dF = 0 \end{cases} \tag{60}$$

For definiteness, we will assume that in the surface integral the multiplier associated with variation determines as the “static factors” in the boundary conditions, and the expression under the variation determines as “kinematic factors”. Let us consider four basic formulations of boundary value problems for statements (60).

1. For “classical” and “cohesive” displacements, it is required to perform static boundary conditions:

$$\begin{aligned} (P_i^V - C_{ijmn} n_j U_{m,n}) &= 0, \\ u_i &= 0. \end{aligned} \quad (61)$$

In this case, we can see that the boundary value problems (60), (61) with respect to vectors of “classical”  $U_i$  and “cohesive”  $u_i$  displacements are separated by their construction.

2. For “classical” displacements, the static boundary conditions are satisfied, and for “cohesive” displacements, are performed the kinematic boundary conditions:

$$\begin{aligned} (P_i^V - C_{ijmn} n_j U_{m,n}) &= 0, \\ \delta(C_{ijmn} n_j U_{m,n} - C_{ijmn} n_j u_{m,n}) &= 0. \end{aligned} \quad (62)$$

Varying  $(P_i^V - C_{ijmn} n_j U_{m,n}) = 0$  and adding up with  $\delta(C_{ijmn} n_j U_{m,n} - C_{ijmn} n_j u_{m,n}) = 0$ , we obtain using (62):

$$\begin{aligned} (P_i^V - C_{ijmn} n_j U_{m,n}) &= 0, \\ \delta(P_i^V - C_{ijmn} n_j u_{m,n}) &= 0. \end{aligned} \quad (63)$$

As a result we again receive the full decomposition of the boundary value problems (60),(63) for the vectors of “classical”  $U_i$  and “cohesive”  $u_i$  displacements.

3. For “classical” displacements, kinematic boundary conditions are performed, and for “cohesive” displacements, the “static” boundary conditions are satisfied:

$$\begin{aligned} \delta(U_i - u_i) &= 0, \\ u_i &= 0. \end{aligned} \quad (64)$$

Varying  $u_i = 0$  and adding up with  $\delta(U_i - u_i) = 0$ , we obtain from (64) the following boundary conditions:

$$\begin{aligned} \delta U_i &= 0, \\ u_i &= 0. \end{aligned} \quad (65)$$

Conditions (65) lead to fully decomposition of the boundary value problems for the vectors of “classical”  $U_i$  and “cohesive”  $u_i$  displacements.

4. The kinematic boundary conditions are satisfied for the “classical” displacements and for “cohesive” displacements:

$$\begin{aligned} \delta(U_i - u_i) &= 0, \\ \delta(C_{ijmn} n_j (U_{m,n} - u_{m,n})) &= 0. \end{aligned} \quad (66)$$

The boundary conditions (66) do not allow to divide boundary volume problems respect to vectors of “classical”  $U_i$  and “cohesive”  $u_i$  displacements. Indeed, since  $C_{ijmn} = C_{ijmp} \delta_{pn}^* + (C_{ijmp} n_p) n_n$  and  $C_{ijmp} \delta_{pn}^* \delta(U_i - u_i)_{,n} = 0$ , from the second condition (66) follows that  $\delta(U_{i,j} n_j - u_{i,j} n_j) = 0$ . Thus, the boundary-value problem for the vectors of “classical”  $U_i$  and “cohesive”  $u_i$  displacements takes the form:

$$\begin{aligned} \delta(U_i - u_i) &= 0, \\ \delta(U_{i,j} n_j - u_{i,j} n_j) &= 0. \end{aligned} \quad (67)$$

Conditions (66) (and (67)) define the coupled boundary value problem respect to vectors of “classical”  $U_i$  and “cohesive”  $u_i$  displacements.

## 8. Conclusions

It is shown that the traditional formulation of gradient theories of elasticity leads to the fact that classical static conditions on the surface of the body are not satisfied locally. A “vector” theory is formulated, it is correct and provides a classical view of static boundary conditions.

Particular cases of vector gradient models are considered and it is shown that there exists a particular vector gradient model whose equilibrium equations coincide with the equations of the well-known applied GradEla model of Aifantis. Such a vector gradient model can be considered as a generalization of the Aifantis model. For it there is an exact decomposition of static boundary conditions to “classical” stresses (full stresses if we use Aifantis definition). Finally, it is shown that if we neglect the symmetry requirement for the gradient-module tensor with respect to the last indices in triples, then it is possible to indicate a unique gradient theory that admits the decomposition of boundary value problems of the fourth order into a sequence of two second-order boundary value problems when we solve a number of boundary value problems.

*Acknowledgements.* This work was carried out with support from MegaGrant Project No. 14.Z50.31.0039 in Togliatti State University

## References

- [1] R. D. Mindlin // *Archive for Rational Mechanics and Analysis* **16** (1964) 51.
- [2] R. D. Mindlin, N. N. Eshel // *International Journal of Solids and Structures* **4** (1968) 109.
- [3] E.C. Aifantis // *Int. J. Engng. Sci.* **30** (1992) 1279.
- [4] B. Altan, E. C. Aifantis // *Scr.Metall.Mater.* **26** (1992) 319.
- [5] C. Ru, E. Aifantis // *Acta Mechanica.* **101(1)** (1993) 59.
- [6] B. S. Altan, E. C. Aifantis // *Journal of the Mechanical Behavior of Materials* **8** (1997) 231.
- [7] S. Lurie, P. Belov // *Engineering Fracture Mechanics* **130** (2014) 3.
- [8] S.A. Lurie, P.A. Belov // *Int. J. Fract.* **50** (2008) 181.
- [9] M. Y. Gutkin, E. C. Aifantis // *Scripta Materialia* **35**(1996) 1353.
- [10] M. Y. Gutkin, E. C. Aifantis // *Scripta Materialia* **36** (1997) 129.
- [11] M. Lazar, D. Polyzos // *International Journal of Solids and Structures* **62**(2015) 1.
- [12] H. Askes, A. V. Metrikine // *European Journal of Mechanics-A/Solids* **21**(2002) 573.
- [13] H. Askes, E. C. Aifantis // *Physical Review B* **80** (2009) 195412.
- [14] S.A. Lurie, P.A. Belov, N. P. Tuchkova // *Int. J. Comp. Mater. Sci.* **36** (2005) 145.
- [15] S.A. Lurie, P.A. Belov, D.B. Volkov-Bogorodsky, N.P. Tuchkova // *J. Mat. Sci.* **41** (2006) 6693.
- [16] S.A. Lurie, D.B. Volkov-Bogorodsky, V.I. Zubov, N.P. Tuchkova // *Int. J. Comp. Mater. Sci.* **45** (2009) 709.
- [17] G.A. Maugin, A.V. Metrikine. In: *One hundred years after the Cosserats*, 1st ed. (Glasgow, Scotland, UK, 2010) Vol. 21, p. 223.
- [18] H. M. Ma, X.-L. Gao // *Acta Mechanica* **225** (2014) 1075.
- [19] D. B. Volkov-Bogorodskii, S. A. Lurie // *Mechanics of Solids* **51** (2016) 161
- [20] S. Lurie, D. B. Volkov-Bogorodsky, A. Leontiev, E. Aifantis // *International Journal of Engineering Science* **49** (2011) 1517.
- [21] A. A. Gusev, S. A. Lurie // *Advanced Engineering Materials* **12** (2010) 529.
- [22] S. Lurie, D. Volkov-Bogorodskii, N. Tuchkova // *Acta Mechanica* **227** (2016) 127.
- [23] D. C. C. Lam, F. Yang, A. C. M. Chong, J. Wang, P. Tong // *Journal of the Mechanics and Physics of Solids* **51** (2003) 1477.
- [24] C. Liebold, W. H. Müller // *Computational Materials Science* **116** (2016) 52.
- [25] R. Maranganti, P. Sharma // *Journal of the Mechanics and Physics of Solids* **55** (2007) 1823.

- [26] R. Barretta, M. Brčić, M. Čanađija, R. Luciano, F. Marotti de Sciarra // *European Journal of Mechanics, A/Solids* **65** (2017) 1.
- [27] H. M. Shodja, A. Zaheri, A. Tehranchi // *Mechanics of Materials* **61** (2013) 73.
- [28] J.W. Hutchinson, T.Y. Wu, In: *Advances in Applied Mechanics* (Academic Press, New York, 1997), Vol.33, pp.295.
- [29] A. A. Gusev, S. A. Lurie // *Mathematics and Mechanics of Solids* **22** (2015) 1.
- [30] H. Askes, E. C. Aifantis // *International Journal of Solids and Structures* **48** (2011) 1990.
- [31] C. A Polizzotto // *European Journal of Mechanics / A Solids* **7** (2016) 261.
- [32] P. A. Belov, S. A. Lurie. *Mathematical theory of defectness media. Gradient theories, Formulations, hierarchy. Analysis. Applications* (Palmarium Academic Publishing, 2014), pp. 337.
- [33] A. Jafari, S. Shirvani Shah-Enayati, A. A. Atai // *European Journal of Mechanics, A/Solids* **59** (2016) 124.
- [34] S. A. Lurie, E. L. Kuznetsova, L. N. Rabinskii, E. I. Popova // *Mechanics of Solids* **50** (2015) 135.
- [35] S. A. Lurie, D. B. Volkov-Bogorodsky, P. A. Belov, E. D. Lykosova // *Nanomechanics Science and Technology: An International Journal* **7** (2016) 261.
- [36] X. L. Gao, S. K. Park // *International Journal of Solids and Structures* **44** (2007) 7486
- [37] M. Lazar, D. Polyzos // *International Journal of Solids and Structures* **62**(2015) 1.
- [38] Elias C. Aifantis // *Theoretical and Applied Mechanics Letters* **4** (2014) 1.

# COMPARISON OF ADAPTIVE ALGORITHMS FOR SOLVING PLANE PROBLEMS OF CLASSICAL AND COSSERAT ELASTICITY

M.A. Churilova<sup>1</sup>, M.E. Frolov<sup>1\*</sup>

<sup>1</sup> Peter the Great St.Petersburg Polytechnic University, Polytechnicheskaya st. 29, Saint-Petersburg, Russia

\*e-mail: frolov\_me@spbstu.ru

**Abstract.** Paper continues developments and numerical testing of functional approach [1-3] to a posteriori error control for 2D problems of classical [2] and Cosserat elasticity [4,5]. The approach yields reliable error bounds (majorants) that are valid for all conforming solutions of problems regardless of methods used for a numerical implementation of a solution process. Efficiency of the above technique is shown on a set of numerical examples including consequent mesh adaptations with MATLAB tools as it was done [6].

**Keywords:** computational mechanics; a posteriori error estimates; finite element method.

## 1. Introduction

Various boundary-value problems of classical elasticity theory have been intensively used for developments, numerical testing and comparison of different approaches to a posteriori error control. Such methods are aimed to explicitly compute some quantitative measure of errors, which appear during numerical simulations, and indicate subdomains with large errors for further refinements. All general frameworks for error estimation and adaptive mesh refinement have been applied to linear elasticity. The first theoretical result appeared in [7] (much earlier than others, like [8-10]). W. Prager and J.L. Synge considered a “geometrical” method of error estimation based on originally intuitive constructions. But this idea gave a rise to another approach of P. Ladevèze and colleagues (see [11-14] for reviews). It is based on the concept of *errors in constitutive relations* or CRE. However, [13] shows that computational efforts to get sharp error estimates with this method can be significant.

Another approach that is widely used nowadays is the so-called *gradient averaging*. It is based on pioneering works of O.C. Zienkiewicz and J.Z. Zhu [9,15]. The last paper includes a comprehensive study of various computational aspects with different examples of implementation of averaging procedures to problems of solid mechanics with different types of finite elements. The main advantage of this method is simplicity, but it isn't able to provide reliable error control and often underestimates true errors. Another series of famous publications of O.C. Zienkiewicz and J.Z. Zhu appeared in 1992 [16-18] with a new approach called *superconvergent patch recovery* or SPR, which is quite popular nowadays – see [19-23].

Group of *residual-based* methods for linear elasticity started to develop from paper by C. Johnson and P. Hansbo [10], which also includes numerical results for plane strain statement. For further research on explicit and implicit residual methods, we refer to [24-33]. Recent results on residual-type indicators and other methods in application to plane problems of linear elasticity theory one can find, for example, in [27,34,35].

Paper [22] contains a comprehensive study and comparison of various modifications of the SPR-method with the same conclusion about possible underestimation of the true error that

yields unreliability of the method. For extended review of the literature, we mention [19] and [36]. In [37] one can find comparison of 6 indicators of different types. Authors of [38] compared CRE and SPR methods (see also [39]). In 1994 paper of I. Babuška and colleagues [40] provided a special methodology for comparison of indicators of different types and presented a review of early results on error estimation theory. Investigation has been continued in [41-43], and in [44] – with adaptations.

It is necessary to note that collection [45] edited by P. Ladevèze and J.T. Oden, and the review by R. Verfürth [46] are also very useful for analysis of various groups of classical methods of a posteriori error control for problems of solid mechanics. Nowadays, the theory of a posteriori error control forms one of the important directions of modern computational mathematics. The amount of the corresponding literature is increasing continuously from the end of 1970-s (see, for instance, [3,47,48] for a review). However, summarizing these results, one can conclude that computationally inexpensive approaches are unreliable, especially in error control of solutions of black-box software for Computer-Aided Engineering (CAE). Some modifications, which increase reliability, may lead to extra computational efforts and rather technical implementations. All standard approaches are based on the fact that controlled numerical solution is an exact solution of a discrete problem generated by Finite Element Methods (FEM). Often, this is not the case for commercial software.

Theoretical background of the functional approach to a posteriori error control, including estimates for various problems of continuum mechanics, has been developed starting from pioneering work of S. Repin and L.S. Xanthis [49]. The early results were mostly theoretical – some references can be found in [2,3,50]. For the last decade, investigations of the functional approach by S. Repin and his colleagues become more practice-oriented. Functional-type a posteriori error majorants for classical linear elastic problems have been obtained in [51] and [2] using two different methodologies.

Cosserat continuum [52] is one of interesting and sufficiently straightforward generalizations of the classical theory (see, for example, [53] and [54] for mathematical statements). Numerical methods for solving problems related to Cosserat continuum began to develop more intensively from the XXI century (see, for example, [55-59]). Nevertheless, first results concerning functional-type error estimates have appeared during the last few years. Totally, there are only few papers addressed to a posteriori error control for computed approximations – [60,61,4,5], and this work requires further developments in construction and comparison of adaptive algorithms.

## 2. Statement

Majorants for both mathematical models under consideration have some important features in common. Estimates for classical and Cosserat elasticity have the form

$$\|e\| \leq M := D(\tilde{u}, s^*) + R(s^*) + \text{penalty terms}, \quad e := u - \tilde{u}, \quad (1)$$

where  $:=$  means “equality by definition”,  $u$  contains all components of the exact solution, which is generally unknown,  $\tilde{u}$  represents approximations of these components, which are explicitly provided from computations,  $e$  is the corresponding error vector formed by components of deviations from exact values,  $s^*$  is a set of auxiliary variables, and  $\|\dots\|$  denotes the global (energy) norm of the error. All components of functional-type error majorants have clear physical meaning and interpretation. Term  $D$  represents errors in constitutive relations. Term  $R$  is a residual term with mesh-independent constants (some proper balance of equilibrium equations). The estimate (1) may contain optional penalty terms that violate the symmetry condition for auxiliary tensors in a weak form. Therefore, the right-hand side of (1), denoted as  $M$ , depends only on known data – approximate solutions, constants, positive parameters, additional variables, and it can be calculated explicitly. This estimate is exact in the sense that the equality can be achieved with a proper setting of parameters and variables. For instance,

estimates for plane problems of the considered types have the form (1) – see [2,4,61] for details. All auxiliary fields can be constructed on a common basis of finite elements suitable for space  $H(\text{div})$  – the Hilbert space of square summable vector-functions with square summable divergence.

A reasonable choice of approximations for free variables in functional-type error estimates allows obtaining accurate guaranteed upper bounds of errors. The functional approach does not impose significant additional restrictions (for example, the assumption about exact satisfaction of equilibrium equations) on free variables. A functional-type error estimate is applicable to any arbitrary approximate solution from the corresponding energy space. It remains valid regardless of the approach used for calculating this solution, thus it allows taking into account various error sources, what is extremely important for additional verification of commercial software for CAE. Additionally to the global error estimation procedure, the functional  $M^2$  can be split and used as an indicator of the local error distribution, considering the contributions to the global error on each finite element. Therefore, it can provide a basis for construction of adaptive algorithms.

Adaptive algorithms for FEM generally consist of four main steps: solve, estimate, mark and refine (see, for example, [62,63]). Concerning the estimate (1) the procedure admits the following interpretation:

1. *step(solve)*: compute  $\tilde{u}$  on some (initial or consequent) finite element mesh;
2. *step(estimate)*: compute the functional  $M$  from all individual contributions to it on every element;
3. *step(mark)*: mark mesh elements with comparatively large local errors by some marking strategy (using some error threshold or percent of the total amount of elements);
4. *step(refine)*: divide marked elements and do local mesh refinements.

Besides of local refinements, for more sophisticated and efficient algorithms one can consider some procedures for local mesh coarsening.

### 3. Numerical results

Adaptive algorithms for plane elasticity problems, mentioned in this paper, are implemented in MATLAB. In the continuation of previous research the mixed-FEM approximations [64,65] are used for computation of upper error bounds and indicators. Extending results of [66], below we consider two examples as an illustration.

For both examples, all material properties are taken from [56].

**Example 1 (square domain with a hole).** We consider the square domain with side 16.2 mm, which contains a circular hole with radius 0.216 mm in the center. The left edge is fully clamped and the tensile loading of 1 MPa is applied to the right edge. Initial mesh is shown in Fig. 1 (a).

Two types of problems are solved – with classical and Cosserat elasticity models. The resulting adaptive meshes are compared. Results for classical elasticity are collected in Table 1, and for Cosserat model – in Table 3. The lowest-order Raviart-Thomas approximation [64] is used for the implementation of the majorant  $M$  from (1).

For this example results were partially presented in [66] with minor modifications of computational algorithms. For instance, final mesh for the majorant for the classical elasticity now consists of 2960 nodes instead of 2955 in [66].

The first block of results in each table corresponds to the uniform mesh refinement with no adaptation. The initial mesh (first column) is provided by a standard MATLAB tool and remains the same for all refinement algorithms. In any uniform refinement step, each element from previous mesh is divided into four new elements. The nodes, elements and relative errors are collected in corresponding table rows. Relative errors are computed with the so-called *reference solution* – an approximate solution obtained on a fine mesh. It is very time-

consuming to calculate the reference solution; therefore, it is provided only for numerical experiments on validation and comparison of different approaches. For engineering practice, it is never used. But the following results show that functional type error majorants can be considered as a reasonable alternative choice.

Table 1. Example 1. Classical elasticity: results for uniform and adaptive mesh refinements.

| <i>Uniform refinement</i>       |      |      |      |       |        |
|---------------------------------|------|------|------|-------|--------|
| MESH                            | 1    | 2    | 3    | 4     | 5      |
| NODES                           | 295  | 1147 | 4522 | 17956 | 71560  |
| ELEMENTS                        | 557  | 2228 | 8912 | 35648 | 142592 |
| RELATIVE ERROR, %               | 10.1 | 6.6  | 4.2  | 2.6   | 1.6    |
| <i>Reference indicator</i>      |      |      |      |       |        |
| NODES                           | 295  | 353  | 423  | 765   | 2050   |
| ELEMENTS                        | 557  | 664  | 793  | 1428  | 3906   |
| RELATIVE ERROR, %               | 10.1 | 6.9  | 4.9  | 2.6   | 1.6    |
| <i>Majorant-based indicator</i> |      |      |      |       |        |
| NODES                           | 295  | 323  | 536  | 876   | 2960   |
| ELEMENTS                        | 557  | 606  | 1002 | 1648  | 5701   |
| RELATIVE ERROR, %               | 10.1 | 7.1  | 3.7  | 2.7   | 1.4    |
| $I_{eff} = M/   e   $           | 1.2  | 1.2  | 1.3  | 1.3   | 1.2    |

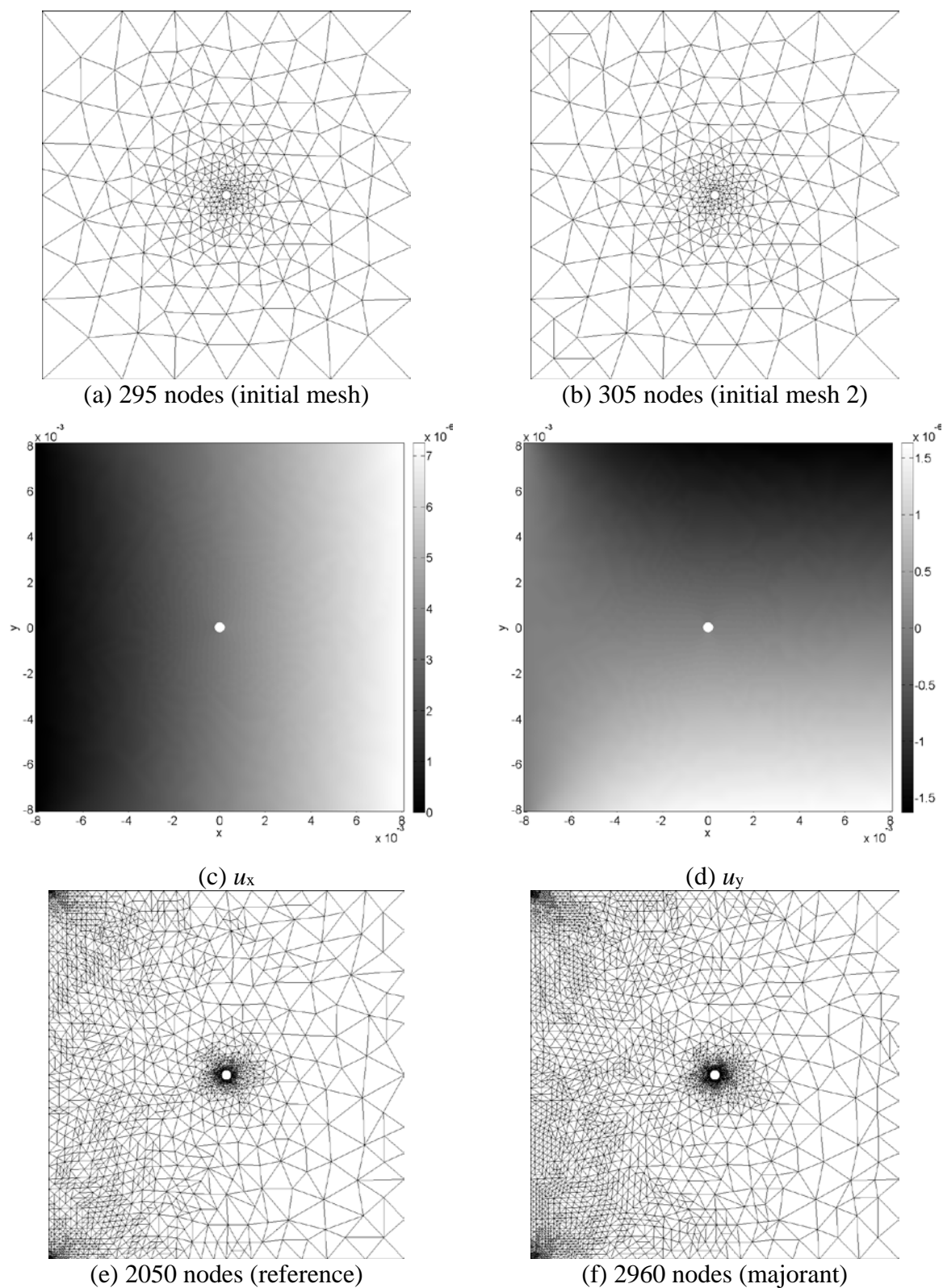
Table 2. Example 1. Classical elasticity: results for another uniform refinement.

| <i>Uniform refinement (another initial mesh)</i> |     |      |      |       |        |
|--|-----|------|------|-------|--------|
| MESH   | 1   | 2    | 3    | 4     | 5      |
| NODES  | 305 | 1183 | 4658 | 18484 | 73640  |
| ELEMENTS   | 573 | 2292 | 9168 | 36672 | 146688 |
| RELATIVE ERROR, %                                | 7.5 | 4.6  | 2.8  | 1.7   | 1.0    |

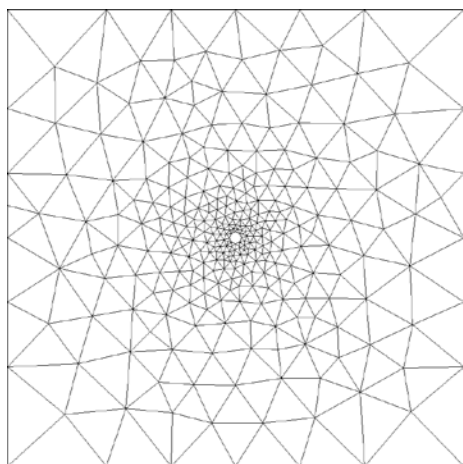
In addition, the uniform refinement procedure is repeated from another slightly different initial mesh (Fig. 1 (b)). Results are collected in Table 2. If the desired relative error level is less or equal to 2%, then for the first uniform sequence the resulting mesh contains 71560 nodes, and for the second one a solution process yields the mesh with 18484 nodes only. Thus, choice of the initial mesh may dramatically affect the uniform refinement results and may increase computational costs caused by necessity to provide accurate results.

Table 3. Example 1. Cosserat elasticity: results for uniform and adaptive mesh refinements.

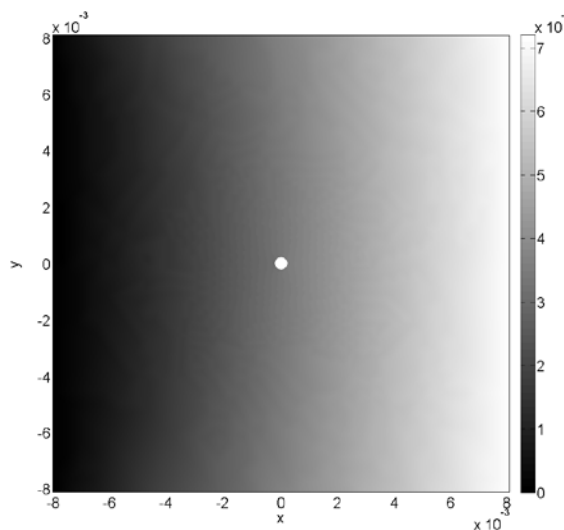
| <i>Uniform refinement</i>       |      |      |      |       |        |
|---------------------------------|------|------|------|-------|--------|
| MESH                            | 1    | 2    | 3    | 4     | 5      |
| NODES                           | 295  | 1147 | 4522 | 17956 | 71560  |
| ELEMENTS                        | 557  | 2228 | 8912 | 35648 | 142592 |
| RELATIVE ERROR, %               | 12.0 | 9.2  | 6.6  | 4.4   | 2.7    |
| <i>Reference indicator</i>      |      |      |      |       |        |
| NODES                           | 295  | 348  | 469  | 899   | 2582   |
| ELEMENTS                        | 557  | 652  | 870  | 1668  | 4899   |
| RELATIVE ERROR, %               | 12.0 | 9.8  | 6.8  | 4.5   | 2.8    |
| <i>Majorant-based indicator</i> |      |      |      |       |        |
| NODES                           | 295  | 317  | 527  | 1039  | 4111   |
| ELEMENTS                        | 557  | 592  | 956  | 1894  | 7674   |
| RELATIVE ERROR, %               | 12.0 | 9.6  | 7.0  | 4.7   | 2.6    |



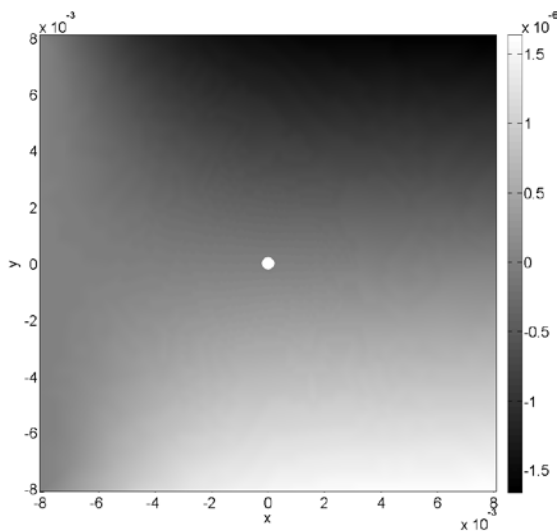
**Fig. 1.** Example 1. Classical elasticity: initial meshes (a,b), components of the solution  $u$  (c,d) (displacements), the result of adaptation by the reference indicator (e), the result of adaptation by majorant-based indicator (f).



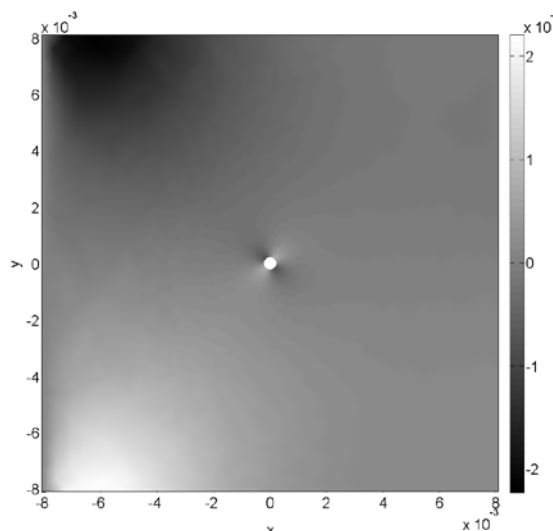
(a) 295 nodes (initial mesh)



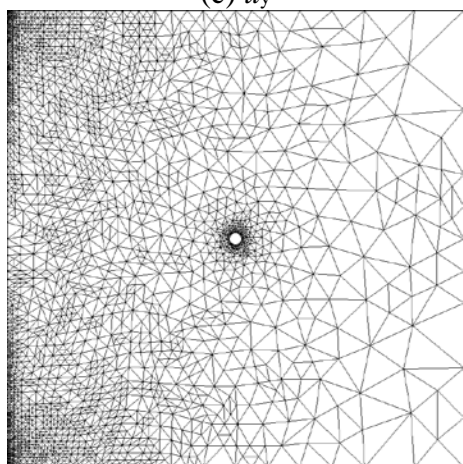
(b)  $u_x$



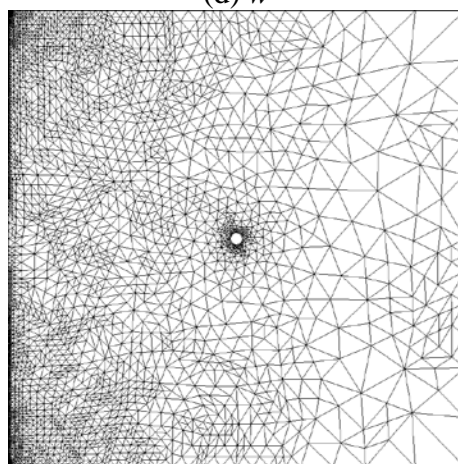
(c)  $u_y$



(d)  $w$



(e) 2582 nodes (reference)



(f) 4111 nodes (majorant)

**Fig. 2.** Example 1. Cosserat elasticity: initial mesh (a), components of the solution  $u$  and  $w$  (b-d) (displacements and rotation), the result of adaptation by the reference indicator (e), the result of adaptation by majorant-based indicator (f).

For the same problem conditions of Cosserat elasticity with the same uniform meshing, the relative error is greater than for the classical one – this effect occurs due to solving equations that are more complex from mathematical point of view.

For analyzing adaptation results, reference (target) meshes are constructed. The adaptation process takes a large amount of steps, refining only several elements on each. Elements to be refined are chosen with reference error indicators, which are based on the energy norm of the difference between solutions on coarse and fine meshes. Results for corresponding reference meshes are collected in the second block of the Table 1 and Table 3, respectively.

In the third blocks of the above-mentioned tables, the results for majorant-based adaptation process are collected. In Table 1 the functional-type error majorant from [2] is used for reliable upper error estimation. The ratio between the error majorant  $M$  and the error  $|||e|||$  is used as a standard quality measure for error control. This parameter is usually called *the efficiency index* – it is denoted by  $I_{eff}$ .

The results for classical elasticity are presented in Fig. 1 with the following subplots: initial mesh, corresponding to Table 1 (a); initial mesh, corresponding to Table 2 (b); classical solution components (c-d); the final mesh for the reference indicator (e) and the final mesh for the majorant-based indicator (f). For Cosserat elasticity, the results are presented in Fig. 2 with the following subplots: initial mesh, corresponding to Table 3 (a); solution components (b-d); the final mesh for the reference indicator (e) and the final mesh for the majorant-based indicator (f). The difference between solutions of classical and Cosserat elasticity problems is moderate.

The results show that for considered parameters, geometry and loading in both cases (classical and Cosserat model) majorant-based error indicators lead to final adaptive meshes, which are similar to reference ones. The adaptation process was stopped after reaching the same error level as on uniform mesh with 71560 nodes. For classical model the number of nodes in the final adaptive mesh is 2960 and for Cosserat model – it is 4111, which is more than 10 times less. These results show that adaptive refinements save a lot of computational resources to get an approximate solution of a good quality.

It is also worth noting that adaptive meshes for different elasticity models have different structure. In first case, the node concentration regions are around the corners of clamped edge and around the hole. In the second case (Cosserat model), the node concentration region is more along the whole clamped edge.

In addition, Table 4 illustrates the behavior of error estimation for several steps with uniform mesh refinements for the simplest Arnold-Boffi-Falk approximation [65]. From these results for Cosserat elasticity we conclude that the efficiency index of estimates remains stable and overestimation of the true error is moderate and acceptable.

Table 4. Example 1. Results for the lowest order Arnold-Boffi-Falk approximation for nested meshes [5].

| MESH              | 1    | 2    | 3    | 4    |
|-------------------|------|------|------|------|
| NODES             | 168  | 624  | 2400 | 9408 |
| RELATIVE ERROR, % | 15.8 | 11.1 | 7.3  | 4.0  |
| $I_{eff}$         | 1.2  | 1.2  | 1.2  | 1.3  |

**Example 2 ( $\Gamma$ -shaped domain).** In this example the  $\Gamma$ -shaped domain is considered. Length of the left and upper edge is 2 m, the other edges are of length 1 m. The left edge is fully clamped and on the upper edge a loading is applied.

As for the Example 1, the results for classical elasticity model are grouped in Table 5, and for Cosserat model – in Table 6.

For this example the difference between the solutions of classical and Cosserat elasticity problems is more significant. In addition, the relative error for the solution of Cosserat elasticity problem is almost two times larger than for classical one. Nevertheless, for both elasticity models the difference in the number of nodes for final adaptive and uniform meshes with the same level of relative error is still significant.

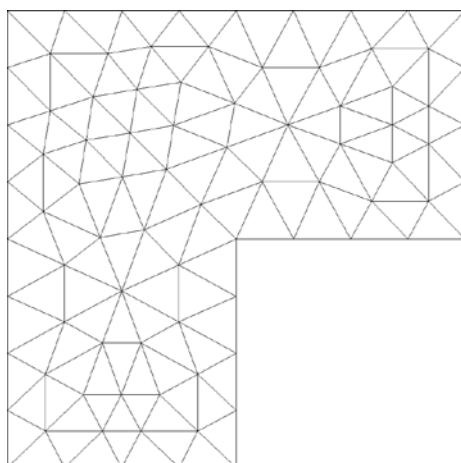
Table 5. Example 2. Classical elasticity: results for uniform and adaptive mesh refinements.

| <i>Uniform refinement</i>       |      |       |      |      |       |        |
|---------------------------------|------|-------|------|------|-------|--------|
| MESH                            | 1    | 2     | 3    | 4    | 5     | 6      |
| NODES                           | 85   | 305   | 1153 | 4481 | 17665 | 70145  |
| ELEMENTS                        | 136  | 544   | 2176 | 8704 | 34816 | 139264 |
| RELATIVE ERROR, %               | 26.2 | 17.9  | 12.0 | 8.1  | 5.4   | 3.7    |
| <i>Reference indicator</i>      |      |       |      |      |       |        |
| NODES                           | 85   | 217   | 357  | 694  | 1591  | 3409   |
| ELEMENTS                        | 136  | 379   | 639  | 1278 | 3004  | 6557   |
| RELATIVE ERROR, %               | 26.2 | 15.3  | 11.4 | 8.1  | 5.4   | 3.7    |
| <i>Majorant-based indicator</i> |      |       |      |      |       |        |
| NODES                           | 85   | 177   | 532  | 1041 | 1898  | 3582   |
| ELEMENTS                        | 136  | 304   | 983  | 1969 | 3643  | 6942   |
| RELATIVE ERROR, %               | 26.2 | 16.52 | 9.8  | 7.3  | 5.4   | 3.9    |
| $I_{eff} = M/\ e\ $             | 1.2  | 1.2   | 1.2  | 1.2  | 1.2   | 1.2    |

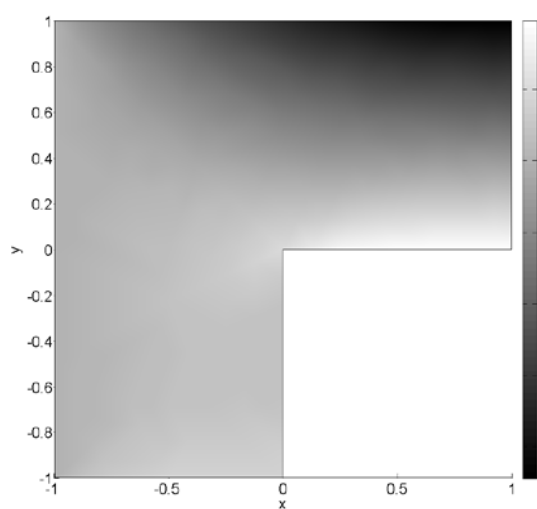
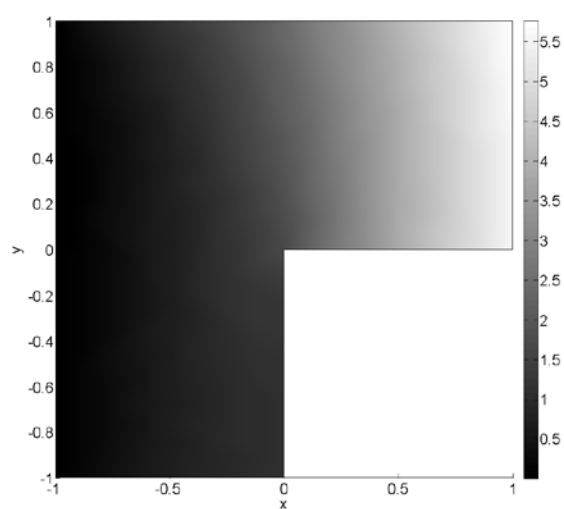
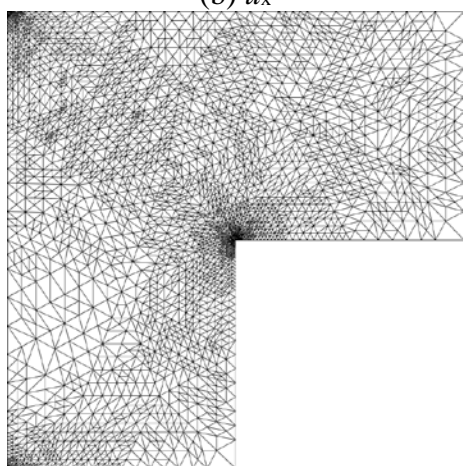
Table 6. Example 2. Cosserat elasticity: results for uniform and adaptive mesh refinements.

| <i>Uniform refinement</i>       |      |      |      |      |       |        |
|---------------------------------|------|------|------|------|-------|--------|
| MESH                            | 1    | 2    | 3    | 4    | 5     | 6      |
| NODES                           | 85   | 305  | 1153 | 4481 | 17665 | 70145  |
| ELEMENTS                        | 136  | 544  | 2176 | 8704 | 34816 | 139264 |
| RELATIVE ERROR, %               | 53.0 | 39.4 | 27.6 | 18.9 | 12.8  | 8.7    |
| <i>Reference indicator</i>      |      |      |      |      |       |        |
| NODES                           | 85   | 227  | 674  | 1640 | 4229  | 10036  |
| ELEMENTS                        | 136  | 398  | 1241 | 3073 | 8049  | 19276  |
| RELATIVE ERROR, %               | 53.0 | 37.6 | 26.4 | 18.9 | 12.7  | 8.7    |
| <i>Majorant-based indicator</i> |      |      |      |      |       |        |
| NODES                           | 85   | 267  | 943  | 1904 | 5582  | 15941  |
| ELEMENTS                        | 136  | 449  | 1680 | 3440 | 10268 | 29642  |
| RELATIVE ERROR, %               | 53.0 | 37.7 | 26.1 | 20.1 | 12.6  | 7.9    |

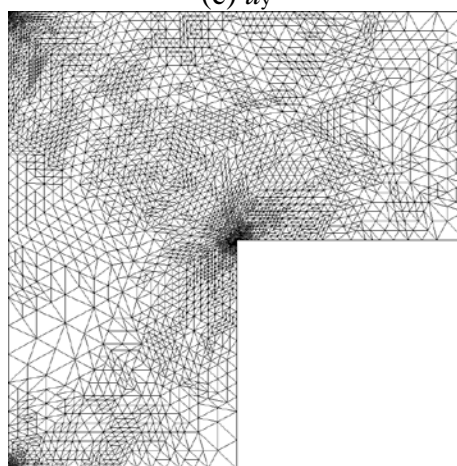
The adaptive meshes corresponding to the last columns of Table 5 and Table 6 are presented in Fig. 3 and Fig. 4. As in Example 1, the adaptive mesh structure is different for classical and Cosserat elasticity models. For the classical elasticity problem node concentration regions are around the corners of clamped edge and around the domain reentrant corner. For the Cosserat elasticity problem the node concentration region is more along the clamped edge and the domain reentrant corner.



(a) 85 nodes (initial mesh)

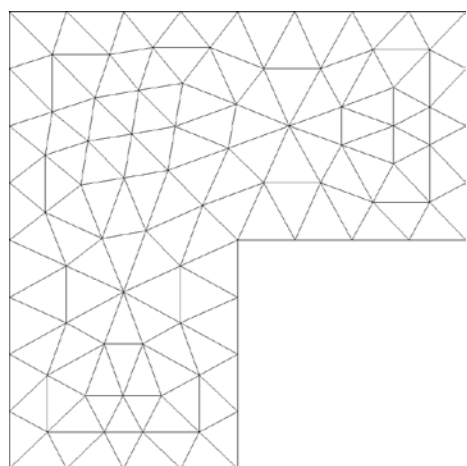
(b)  $u_x$ (c)  $u_y$ 

(d) 3409 nodes (reference)

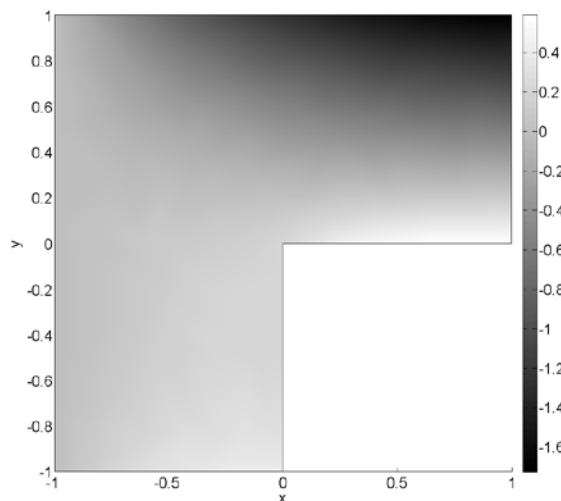


(e) 3582 nodes (majorant)

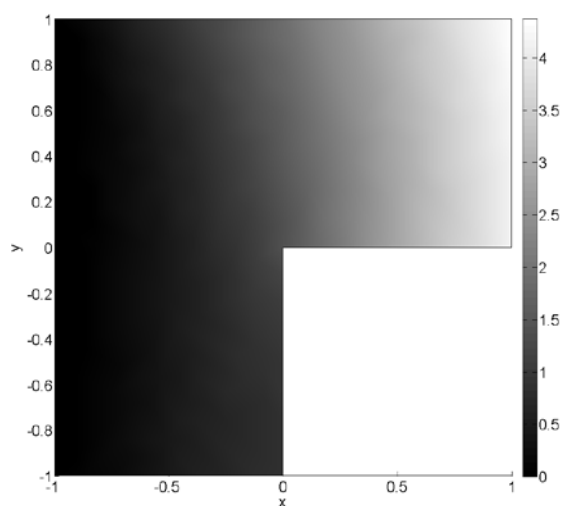
**Fig. 3.** Example 2. Classical elasticity: initial mesh (a), components of the solution  $u$  (b,c) (displacements), the result of adaptation by the reference indicator (d), the result of adaptation by majorant-based indicator (e).



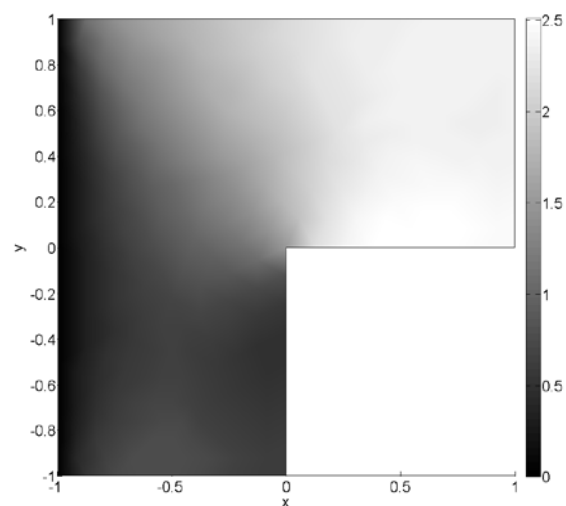
(a) 85 nodes (initial mesh)



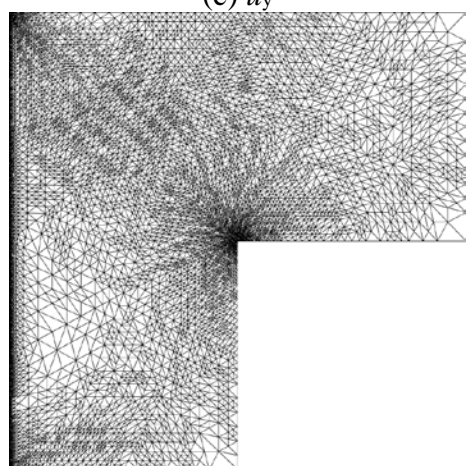
(b)  $u_x$



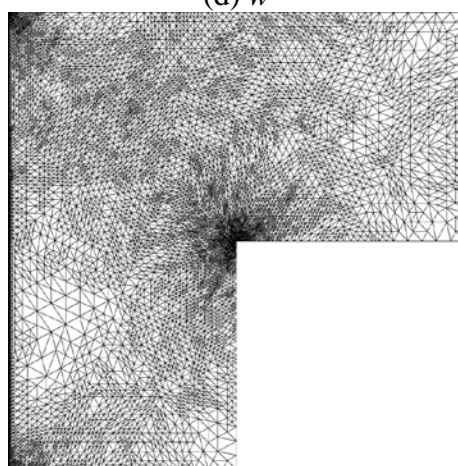
(c)  $u_y$



(d)  $w$



(e) 10036 nodes (reference)



(f) 15941 nodes (majorant)

**Fig. 4.** Example 2. Cosserat elasticity: initial mesh (a), components of the solution  $u$  and  $w$  (b-d) (displacements and rotation), the result of adaptation by the reference indicator (e), the result of adaptation by majorant-based indicator (f).

#### 4. Conclusions

The functional approach is always reliable due to the fact that estimates are guaranteed upper bounds of errors. This property is known from the corresponding mathematical theory and it is numerically approved in the process of implementation of adaptive algorithms. As local error indicators, respective majorants provide useful information about distributions of computational errors that leads to efficient mesh adaptations and significantly saves computational resources for getting accurate approximate solutions (tens of times). For the considered classes of problems, H(div) conforming approximations as Raviart-Thomas or Arnold-Boffi-Falk yield suitable results from the viewpoint of a stability of the efficiency index and a moderate overestimation of the true error.

**Acknowledgement.** Authors are supported by the Grant of the President of the Russian Federation MD-1071.2017.1.

#### References

- [1] S. Repin // *Math. Comp.* **69** (2000) 481.
- [2] S. Repin, *A posteriori estimates for partial differential equations* (de Gruyter, Berlin, 2008).
- [3] O. Mali, P. Neittaanmäki, S. Repin, *Accuracy Verification Methods. Theory and algorithms* (Springer, 2014), Vol. 32.
- [4] M. Frolov // *Journal of Applied Mathematics and Mechanics* **78(4)** (2014) 425.
- [5] M. Frolov, In: *Numerical Mathematics and Advanced Applications - ENUMATH 2013*, Lecture Notes in Computational Science and Engineering (Switzerland, Springer, 2015), Vol. 103, p. 225-232.
- [6] M. Churilova // *St. Petersburg State Polytechnical University Journal. Physics and mathematics* **4(230)** (2015) 139.
- [7] W. Prager, J.L. Synge // *Q. Appl. Math.* **5** (1947) 241.
- [8] P. Ladevèze, D. Leguillon // *SIAM J. Numer. Anal.* **20** (1983) 485.
- [9] O.C. Zienkiewicz, J.Z. Zhu // *Int. J. Numer. Methods Eng.* **24** (1987) 337.
- [10] C. Johnson, P. Hansbo // *Comput. Methods Appl. Mech. Eng.* **101** (1992) 143.
- [11] P. Ladevèze, J.-P. Pelle, *Mastering calculations in linear and nonlinear mechanics* (Springer, New York, 2005).
- [12] F. Pled, L. Chamoin, P. Ladevèze // *Computational Mechanics* **49(3)** (2012) 357.
- [13] F. Pled, L. Chamoin, P. Ladevèze // *International Journal for Numerical Methods in Engineering* **88(5)** (2011) 409.
- [14] L. Gallimard // *International Journal for Numerical Methods in Engineering* **78(4)** (2009) 460.
- [15] J.Z. Zhu, O.C. Zienkiewicz // *Communications in Applied Numerical Methods* **4(2)** (1988) 197.
- [16] O.C. Zienkiewicz, J.Z. Zhu // *International Journal for Numerical Methods in Engineering* **33(7)** (1992) 1331.
- [17] O.C. Zienkiewicz, J.Z. Zhu // *International Journal for Numerical Methods in Engineering* **33(7)** (1992) 1365.
- [18] O.C. Zienkiewicz, J.Z. Zhu // *Computer Methods in Applied Mechanics and Engineering* **101(1-3)** (1992) 207.
- [19] P. Díez, J.J. Ródenas, O.C. Zienkiewicz // *International Journal for Numerical Methods in Engineering* **69(10)** (2007) 2075.
- [20] J.J. Ródenas, M. Tur, F.J. Fuenmayor, A. Vercher // *International Journal for Numerical Methods in Engineering* **70(6)** (2007) 705.
- [21] N.-E. Wiberg, F. Abdulwahab // *International Journal for Numerical Methods in Engineering* **36(16)** (1993) 2703.

- [22] T. Kvamsdal, K.M. Okstad // *International Journal for Numerical Methods in Engineering* **42(3)** (1998) 443.
- [23] O.C. Zienkiewicz, R.L. Taylor, *Finite element method*, Vol. 1: The basis (Butterworth-Heinemann, Oxford, 2000).
- [24] R. Verfürth, *A review of a posteriori error estimation and adaptive mesh-refinement techniques* (John Wiley & Sons, Chichester, B.G. Teubner, Stuttgart, 1996).
- [25] D. Braess, O. Klaas, R. Niekamp, E. Stein, F. Wobschal // *Computer Methods in Applied Mechanics and Engineering* **127(1-4)** (1995) 345.
- [26] W. Bangerth, R. Rannacher, *Adaptive finite element methods for differential equations* (Birkhäuser, Basel, 2003).
- [27] M. Lonsing, R. Verfürth // *Numerische Mathematik* **97(4)** (2004) 757.
- [28] G. Yu, X. Xie, C. Carstensen // *Computer Methods in Applied Mechanics and Engineering* **200(29-32)** (2011) 2421.
- [29] T.P. Barrios, E.M. Behrens, M. González // *Computer Methods in Applied Mechanics and Engineering* **200(1-4)** (2011) 101.
- [30] T.P. Barrios, E.M. Behrens, M. González // *Applied Numerical Mathematics* **84** (2014) 46.
- [31] D. Braess, C. Carstensen, B.D. Reddy // *Numerische Mathematik* **96(3)** (2004) 461.
- [32] P. Hansbo, M.G. Larson // *Computer Methods in Applied Mechanics and Engineering* **200(45-46)** (2011) 3026.
- [33] K.-Y. Kim // *SIAM Journal on Numerical Analysis* **49(6)** (2011) 2364.
- [34] M. Ainsworth, R. Rankin // *International Journal for Numerical Methods in Engineering* **82(9)** (2010) 1114.
- [35] C. Carstensen, J. Thiele // *International Journal for Numerical Methods in Engineering* **73(1)** (2008) 71.
- [36] J.P. Moitinho de Almeida, E.A.W. Maunder // *International Journal for Numerical Methods in Engineering* **79(12)** (2009) 1493.
- [37] P. Beckers, H.-G. Zhong, E. Maunder // *Revue Européenne des Éléments Finis* **2(2)** (1993) 155.
- [38] P. Beckers // *Computational Mechanics* **41(3)** (2008) 421.
- [39] M. Kempeneers, J.-F. Debongnie, P. Beckers // *International Journal for Numerical Methods in Engineering* **81(4)** (2010) 513.
- [40] I. Babuška, T. Strouboulis, C.S. Upadhyay, S.K. Gangaraj, K. Copps // *International Journal for Numerical Methods in Engineering* **37(7)** (1994) 1073.
- [41] I. Babuška, T. Strouboulis, C.S. Upadhyay, S.K. Gangaraj // *Computers and Structures* **57(6)** (1995) 1009.
- [42] U. Brink, E. Stein // *Computer Methods in Applied Mechanics and Engineering* **161(1-2)** (1998) 77.
- [43] A. Benedetti, S. de Miranda, F. Ubertini // *International Journal for Numerical Methods in Engineering* **67(1)** (2006) 108-131.
- [44] G. Castellazzi, S. de Miranda, F. Ubertini // *Finite Elements in Analysis and Design* **46(5)** (2010) 379.
- [45] P. Ladevèze, J.T. Oden (edt.), *Advances in adaptive computational methods in mechanics* (Elsevier, Amsterdam, 1998).
- [46] R. Verfürth // *Computer Methods in Applied Mechanics and Engineering* **176(1-4)** (1999) 419.
- [47] R. Verfürth, *A posteriori error estimation techniques for finite element methods* (Oxford University Press, Oxford, 2013).
- [48] B. Szabó, I. Babuška, *Introduction to finite element analysis. Formulation, verification and validation* (John Wiley & Sons, Hoboken, 2011).
- [49] S. Repin, L.S. Xanthis // *Comput. Methods Appl. Mech. Engrg* **138(1-4)** (1996) 317.

- [50] P. Neittaanmäki, S. Repin, *Reliable methods for computer simulation. Error control and a posteriori estimates* (Elsevier, Amsterdam, 2004).
- [51] A. Muzalevsky, S. Repin // *Russian Journal of Numerical Analysis and Mathematical Modelling* **18(1)** (2003) 65.
- [52] E. Cosserat, F. Cosserat, *Théorie des corps d'éformables* (Hermann, Paris, 1909).
- [53] W. Nowacki, *Theory of elasticity* [Russian transl.] (Mir, Moscow, 1975).
- [54] N.F. Morozov, *Mathematical problems of crack theory* (Nauka, Moscow, 1984). (in Russian).
- [55] E. Providas, M.A. Kattis // *Computers and Structures* **80(27-30)** (2002) 2059.
- [56] H.W. Zhang, H. Wang, P. Wriggers, B.A. Schrefler // *Computational Mechanics* **36(6)** (2005) 444.
- [57] M.A. Wheel // *International Journal for Numerical Methods in Engineering*. **75(8)** (2008) 992.
- [58] A. Hadjesfandiari, G. Dargush // *International Journal for Numerical Methods in Engineering* **89(5)** (2012) 618.
- [59] O. Sadovskaya, V. Sadovskii, In: *Advanced Structured Materials* (Springer, Berlin, 2012), Vol. 21.
- [60] D. Perić, J. Yu, D.R.J. Owen // *International Journal for Numerical Methods in Engineering* **37(8)** (1994) 1351.
- [61] S. Repin, M. Frolov // *Journal of Mathematical Sciences* **181(2)** (2012) 281.
- [62] W. Dörfler // *SIAM Journal on Numerical Analysis* **33(3)** (1996) 1106.
- [63] K. Mekchay, R.H. Nochetto // *SIAM Journal on Numerical Analysis* **43(5)** (2005) 1803.
- [64] P.A. Raviart, J.M. Thomas // *Lecture Notes in Mathematics* **606** (1977) 292.
- [65] D.N. Arnold, D. Boffi, R.S. Falk // *SIAM Journal on Numerical Analysis* **42(6)** (2005) 2429.
- [66] M.A. Churilova, M.E. Frolov, S.I. Repin. In: *Proceedings of the XLV Summer School - Conference "Advanced Problems in Mechanics"* (APM-2017) pp.115-122.

# FINITE ELEMENT MODELLING OF THE MITRAL VALVE REPAIR USING AN IMPLANTABLE LEAFLET PLICATION CLIP

M. D. Stepanov<sup>1\*</sup>, O.S. Loboda<sup>1,4</sup>, Y. V. Novozhilov<sup>2</sup>, N. V. Vasilyev<sup>3</sup>

<sup>1</sup>Peter the Great Saint-Petersburg Polytechnic University, 29 Polytechnicheskaya, St. Petersburg 195251, Russia

<sup>2</sup>«CADFEM-CIS», 15 Kondratyevsky Prospekt, St. Petersburg 195197, Russia

<sup>3</sup>Boston Children's Hospital, Harvard Medical School, 300 Longwood Avenue, Boston, Massachusetts, 02115,  
USA

<sup>4</sup>Institute of Problems in Mechanical Engineering, Bolshoy pr., 61, V.O., Saint-Petersburg, Russia, 199178

\*e-mail: matvey.stepanovD@yandex.ru

**Abstract.** We report the results of numerical simulation of the mitral valve in human heart. The beam-shell geometry model was created based on anatomical atlases and taking into account the heterogeneity of distribution of the mitral valve's leaflets thickness. The full cycle of the mitral valve opening and closure was simulated using the finite element analysis software ANSYS Mechanical. The method of data processing from a computer tomography in a solid CAD model was implemented and tested.

**Keywords:** mitral valve, finite element simulation, computed tomography.

## 1. Introduction

Thorough understanding of the mitral valve (MV) mechanics is needed for surgical decision making such as choosing the type of surgical valve repair applicable for particular patient [1]. Several mathematical models [2, 3 and 4] of the MV have been developed that allowed simulating the valve opening and closure under different conditions. In this study, in addition to modeling normal MV function, we analyzed the leaflet motion in the presence of mitral valve prolapse (MVP) and its repair using novel plication device [5].

## 2. Mitral valve anatomy

The MV consists of the annulus, posterior and anterior leaflets, chordae tendineae that are connected to papillary muscles. Chordae tendineae are tendinous connective fibers that bond the leaflets of the MV with the papillary muscles located on the inner surface of the left ventricle. The main function of the MV is to control the blood flow from the left atrium to the left ventricle. During normal left ventricular diastole, the MV is open and blood flows from the left atrium into the left ventricle. Then, during left ventricular systole the MV closes, and blood is ejected into the aorta. During contraction of left ventricle, papillary muscles contract and tether the chordae preventing prolapse of the MV leaflets.

**2.1 Mitral valve prolapse.** MVP is a disease in which there is the displacement of MV leaflet into the left atrium during left ventricular systole. It is accompanied by the appearance of the blood backflow into the left atrium. Significant amount of the blood in the backflow leads to heart failure over time, which requires surgical correction of MVP.

MVP can be repaired on a beating heart using an implantable device, the Leaflet Plication Clip that has been developed at Boston Children's Hospital [5]. The Clip is attached to the

diseased leaflet and thereby prevents displacement of the leaflet toward the left atrium and reduces mitral regurgitation.

Prior to surgical operation, patient specific MV anatomy needs to be analyzed using high-resolution computed tomography or three-dimensional echocardiography. Then, the imaging data is processed into a 3D model of the MV. Finally, a physician analyzes the model with the purpose of choosing the optimal method of MV surgical repair.

**2.2 Geometry model.** In this study, a geometrical model of the MV (Fig. 1) was created using program ANSYS SpaceClaim. Reliable dimensions of the MV were taken from the previously published articles [6, 7] focused on studying the anatomy of the heart valves.

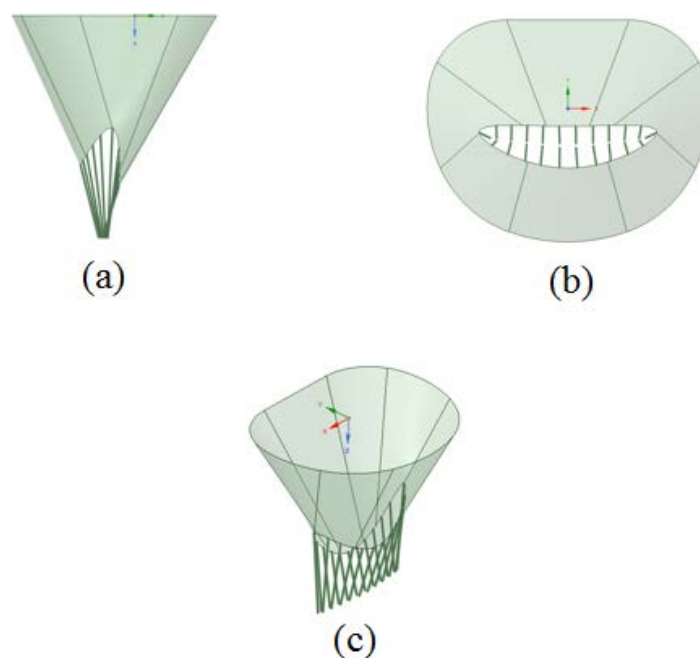


**Fig. 1.** Geometry model of the mitral valve.

A non-uniform thickness distribution (Fig. 2) was implemented with the “External Data” option that allowed importing data in text format from external sources into ANSYS applications. The import procedure allows users to set up the value of the leaflet thickness at the specified points, and then this value is interpolated on the nodes located in the specified range.

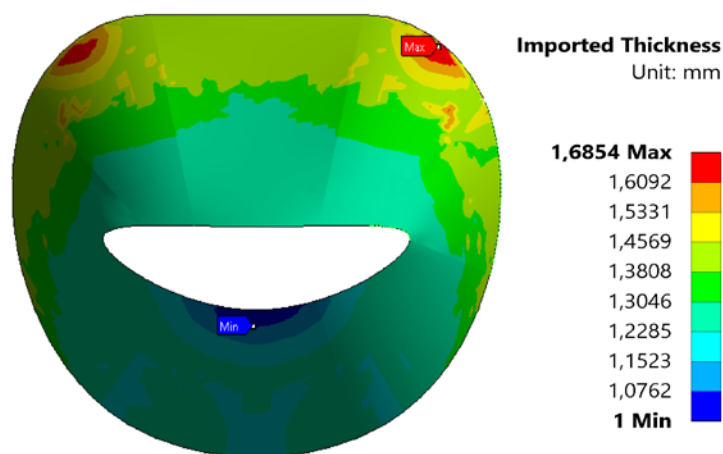


**Fig. 2.** Thickness distribution on the surface of the mitral valve.

**2.3 Finite element model.** According to the geometry model of the MV described above, finite element model (Fig. 3) was created with the following features: element size – 0.5 mm, number of nodes – 5 402, number of elements - 4 794, type of elements: quadrilateral and triangular for modeling of the leaflets(SHELL181) and beam elements for the chordae tendineae (BEAM188).

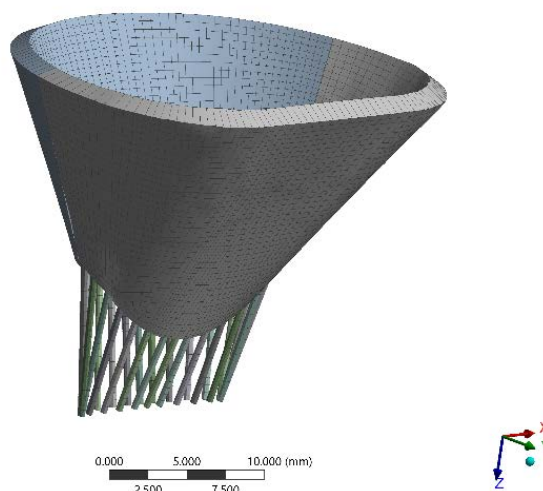


**Fig. 3.** Finite-element model.

**2.4 Natural and essential boundary conditions.** Initial and boundary conditions were simulated taken into account the actual conditions of MV function. At the initial moment of calculation, the valve is in the unstressed state. This corresponds to the transition from the filling phase to the phase of left atrial systole. Based on the pressure curves from the left atrium and the left ventricle [7], the resulting pressure curve was obtained (Fig. 4).

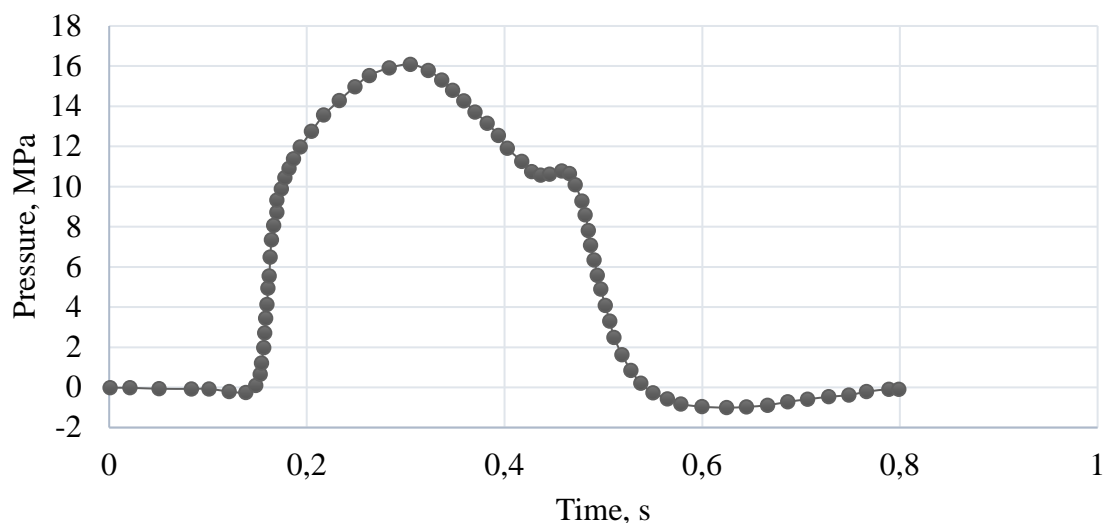


**Fig. 4.** Resulting pressure curve.

Boundary conditions are shown in figure 5. The mitral annulus is fixed in three translational degrees of freedom (A). In addition, points (B) of the lower part of chords are fixed at the place of attachment to the papillary muscle in the left ventricle. Pressure is applied to the surface (C) from the left ventricle and provides closure of the leaflets.

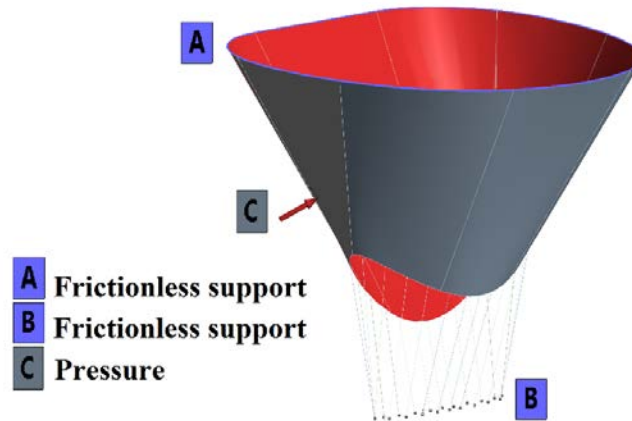


**Fig. 5.** Natural and essential boundary conditions.

**2.5 Constitutive model of the mitral valve tissue.** MV leaflets consist of collagen, elastin and glycosaminoglycan. The relationship between collagen and elastin determine the mechanical behavior of the tissue. Angle measured between the collagen fibers describes that the fiber orientation depends on the considered region and symmetrical to the central radial axis of each MV leaflet.

Most of the biological materials are anisotropic, i.e. their deformation depends on the direction of displacement. Such fiber-reinforced composite material with a single preferred direction is called transversely isotropic material. A network of crimped collagen fibers represents tissue of the MV, particularly in the central region. The angle of these fibers is relatively uniform within the considered experimental region. Therefore, it is assumed that the tissue of the MV can be modeled as a transversely isotropic material.

We assumed local tissue homogeneity, although there is some heterogeneity due to the complicated structure of the valve leaflets. Tissue of the MV consist mainly of water and has got a reduced perfusion (blood supply). Based on these structural and mechanical observations, it can be assumed that the tissue of the MV can be modeled as a hyperplastic incompressible material that is initially and locally transversely isotropic relative to the axis of the collagen fibers.

The strain energy function is a short description of the material of this type. Several types of strain energy functions were proposed in order to account for the transversal isotropy of the soft tissues. Following the method Humphrey [8], it is possible to make an assumption about the subclass of transversely isotropic materials in which the strain energy function  $W$  presumably depends only on the two coordinate invariant measures of finite deformation (i.e., the first invariant of strain and elongation along the fiber direction  $\alpha$ ):

$$W = W(I_1, \alpha), \quad (1)$$

where  $I_1 = \text{tr} \mathbf{C} = \text{tr} \mathbf{B}$  and  $\alpha = \mathbf{N} \cdot \mathbf{C} \cdot \mathbf{N}$ .

$\mathbf{C} = \mathbf{F}^T \cdot \mathbf{F}$ ,  $\mathbf{B} = \mathbf{F} \cdot \mathbf{F}^T$  are the right and left Cauchy-green deformation tensor, respectively, and  $\mathbf{N}$  is a unit vector that defines the presumed direction of the fibers of the material in the undeformed configuration.  $\mathbf{F}$  is the deformation gradient tensor,  $\det(\mathbf{F}) = 1$ , due to incompressibility of the material. The expression of Cauchy stress tensor for a material of this type can be expressed as:

$$\mathbf{T} = -p\mathbf{I} + 2W_1\mathbf{B} + (W_\alpha/\alpha)\mathbf{F} \cdot \mathbf{N} \otimes \mathbf{N} \cdot \mathbf{F}^T, \quad (2)$$

where  $p$  is the multiplier that provides incompressibility,  $\mathbf{I}$  – identity tensor,  $W_1 = \partial W / \partial I_1$ ,  $W_\alpha = \partial W / \partial \alpha$ ,  $\otimes$  denotes tensor product.

Partial derivatives  $W_1$  and  $W_\alpha$  can be calculated directly from the measured stress and strain taking into account the angle  $\varphi$  of the collagen fibers. This formulation means that in the special case when one of the strain invariants is alternately held constant while the other is

varied, i.e., a set of experiments with constant invariant can be used to determine the functional form of  $W$ .

However, to use this type of material we would need the series of experiments to determine mechanical properties of the leaflets. In this study, a linear isotropic model of the MV leaflet material was used. Values for the stiffness matrix (in the isotropic case is the young's modulus and Poisson's ratio) were taken from the article M. A. Hisham [9] devoted to computer modeling of the leaflets of the MV under the action of the systolic pressure.

–material of leaflets:  $E_{\parallel} = 2 \text{ MPa}$ ;  $E_{\perp} = 1 \text{ MPa}$ ;  $\nu = 0.49$

–material of chords:  $E = 250 \text{ MPa}$ ;  $\nu = 0.488$

### 3. Results

**3.1 Initial configuration.** The distribution of values of the principal stresses on the leaflets of the MV at different time points are shown in figure 6. The highest stresses are observed during the transition from tension phase to the expulsion phase in 0.302 sec calculation. At this moment the resulting pressure of 16 kPa acts on the leaflets, this moment is called a full closure of the valve. At the time of full closing of the leaflets oscillation occurs, which is caused by sharply decrease of the blood flow speed not allowing to overcome the closed valve.

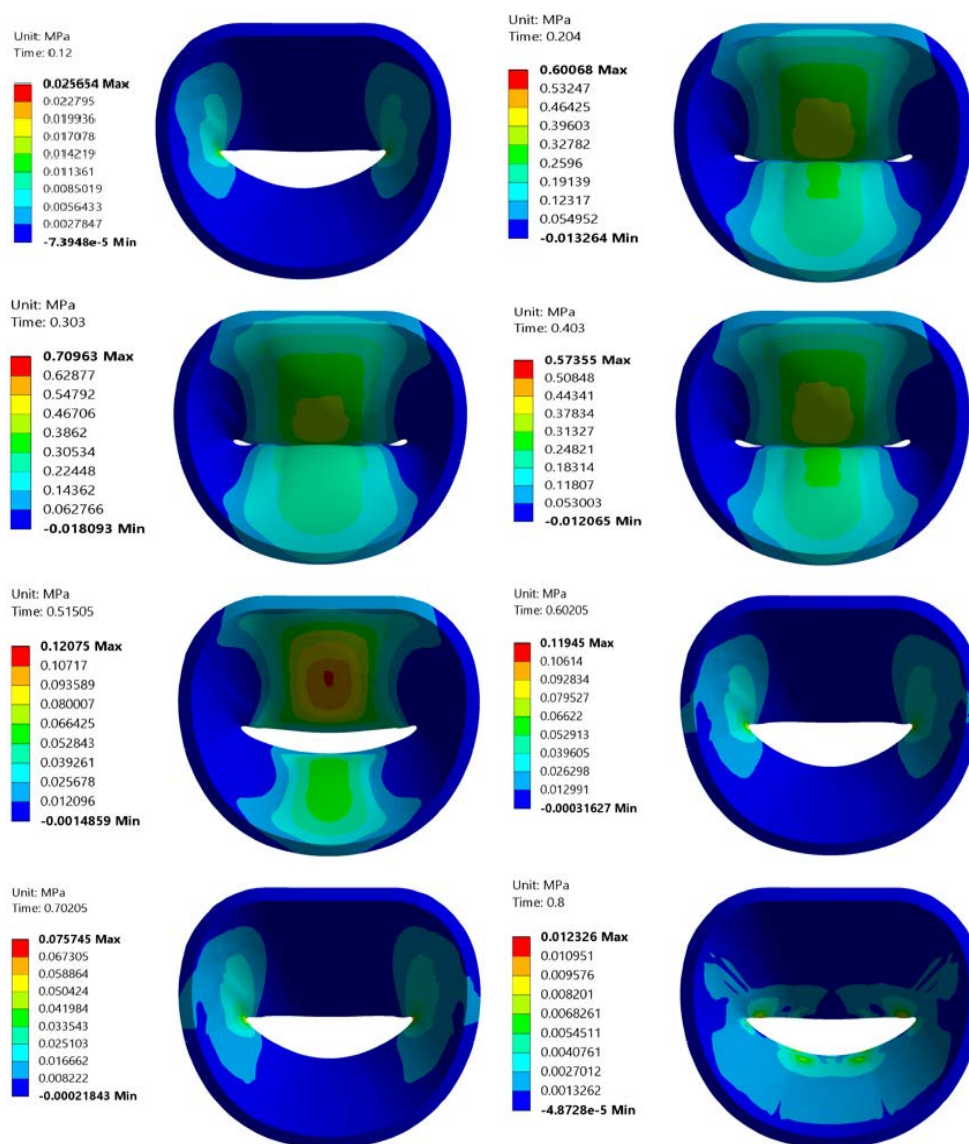
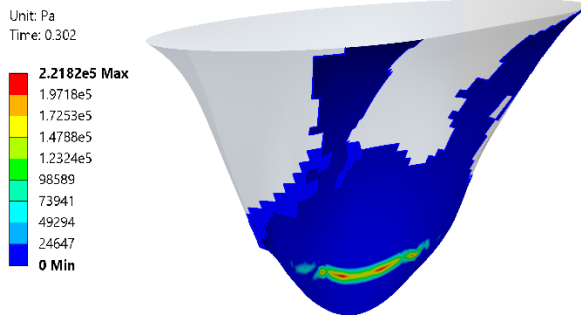


Fig. 6. The values of principal stresses at different time points.

Closure of the MV is confirmed by checking the status of contact elements at the moment of peak stress (Fig.7). The tight closing of the MV can be judged by the image of the middle cross-section (Fig.8).

Tension on the anterior leaflet is greater than the pressure arising at the posterior. In general, stress values vary in the range of 13 kPa during the filling period of the ventricle to 637 kPa during the period of complete closure of the valve. This result is aligned with the data obtained in the articles [2, 3 and 4] devoted to studies of the MV.



**Fig. 7.** The middle cross-section of the valve at the moment of full closure of the valve.

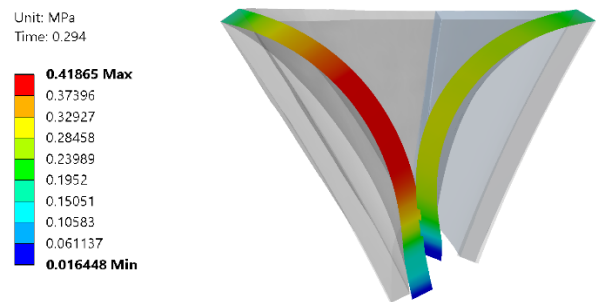


**Fig. 8.** The contact pressure at the moment of maximum closure of the valve.

**3.2 Modified configuration of the mitral valve with the “Clip” on the posterior leaflet.** The analysis of influence of the Leaflet Plication Clip device on the MV during normal operation was executed additionally in this study. “Clip” was modeled as a point mass. The device was installed on the posterior leaflet in the center (Fig.9).

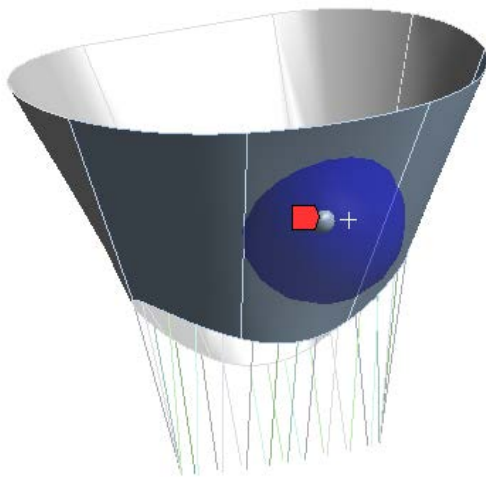


**Fig. 9.** The location of the mass point on the surface of the posterior leaflet.

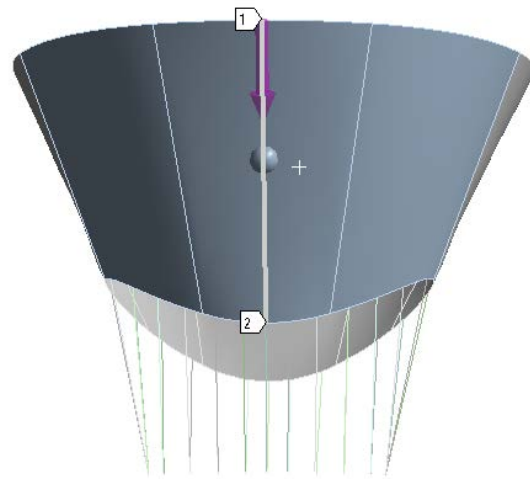


**Fig. 10.** Line along the surface of the leaflet.

The weight of the device was calculated by the formula:

$$m = 4l_c\rho\pi r^2, \quad (3)$$

where  $l_c$  – the maximum distance from the mitral annulus to the free edge of the leaflet,  $\rho = 6.4 \text{ g/cm}^3$  is the density of the material of the device,  $r$  is the radius of the clip.

Thus, the weight of the clip can vary from 0.1 to 0.4 grams. This Study considers three cases: a) the mass of the “Clip” - 0.1 g., which corresponds to a wire radius of 0.5 mm; b) mass of the “Clip” - 0.23 g., the radius is 0.75 mm; c) mass of the “Clip” - 0.4 g., the radius is 1 mm.

The calculation was executed for those three types of the “Clip” and obtained results were compared with the case without the “Clip”.

Analysis of displacements along the line indicated in the figure showed that the maximum divergence of the results is 0.18% for the case without the “Clip” and the case c)  $M_c = 0.4$  g. This suggests that the installation of clip does not significantly affects the movement of MV leaflets during normal operation.

Chart 11 shows the values of the stresses on the installing line of the “Clip” (Fig. 10) for three cases in comparison with the solution without “Clip” on the leaflet.

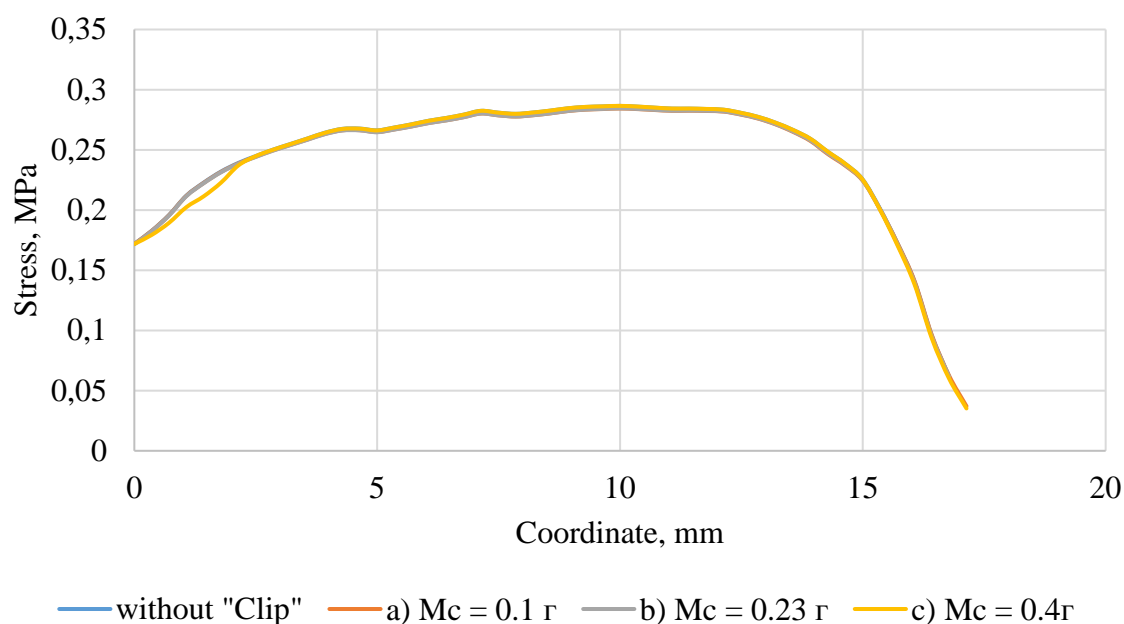


**Fig. 11.** The tension dependence of the coordinates on the line for three types of “Clip” and case without it.

For cases a) and b) large discrepancies were not observed. However, there is divergence of results in the upper region of the valve with the mass increase. The maximum value of the divergence of results is 5.11% detected in case c) when the mass of a “Clip” is equal to 0.4 g. In article [10], the value of the dynamic ultimate tensile strength is 0.9 MPa for the material of the leaflets of the mitral valve. Thus, we can conclude that “Clip” does not entail the appearance of additional tensile stresses that can lead to the destruction of the material of the leaflets.

#### 4. Processing data from a computer tomography

One of the objectives of this study was the creation of 3D model using data obtained from computer tomography. We did not have access to high resolution valve images. The workflow was tested on images of the spinal cord. This process can be divided into two stages: a) Converting data from DICOM format to STL format; b) Creation of solid model using STL model.

**4.2 Converting data from DICOM format to STL format.** Pictures from the computer tomography (figure 12) are the visualization of DICOM data obtained during the survey. Using the software package 3D Slicer, by processing the DICOM files was created STL model of the human spine (figure 13).



**Fig. 12.** Computer tomography image.

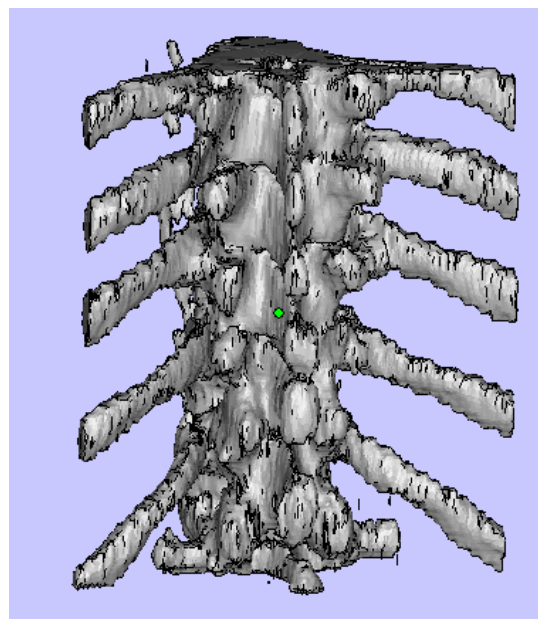
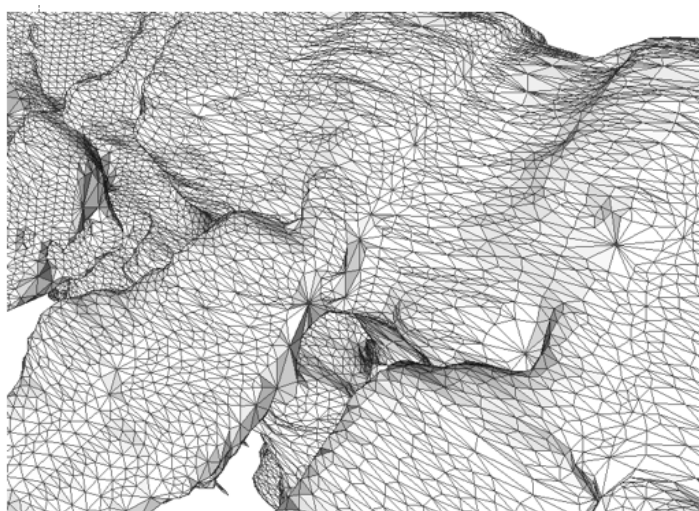
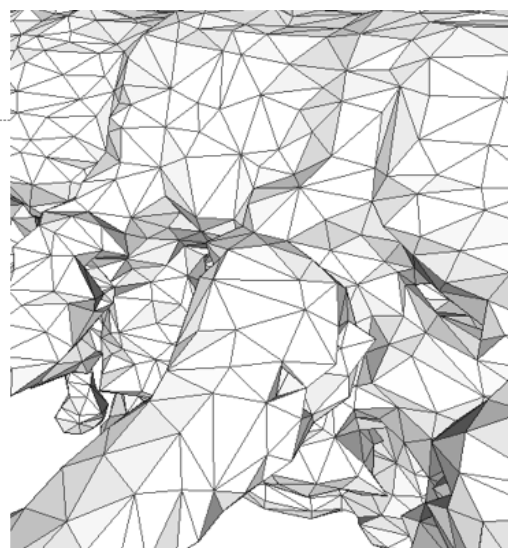


**Fig. 13.** Spine STL model.

The created model has a lot of extra surfaces and irregularities caused by the noise effects during survey. Using the program MeshLab model was filtered out (figure 14).



$N_{faces}=168988$



$N_{faces}=10814$

**Fig. 14.** Comparison of number of surfaces before and after filtration.

**4.2 Converting the STL into a solid model.** STL format is widely used for storing three-dimensional models of objects for use it in technologies of rapid prototyping. Information about the object is stored as a list of triangular facets that describe the surface and their normal lines. However, for use in the calculations in the engineering software packages required to create solid geometry CAD model. Thus, with the help of the program ANSYS SpaceClaim above STL model was converted to a CAD model. This operation allows us to use this geometry model in the calculations of biological structures using finite element method.

## 5. Limitations of the Study

In carrying out the described analysis we made several assumptions. At first, the material model of chordae tendineae and the leaflets should possess the properties of anisotropic hyperelastic material. In the case of chords, the definition of BEAM188 elements does not allow simulation of hyperelasticity. In general, creating a high quality anisotropic hyperelastic material model requires a series of experiments to determine the constants included in the expression for the description of such a model. In this work, the material of the leaflets and chordae tendineae was modeled as a linear hyperelastic at the first order approximation.

At second, detailed studying the behavior of the MV and determining the position of “Clip” on the leaflet requires an anatomically accurate model of the valve obtained from the high resolution computer tomography. Since such equipment was not available to us, geometry model of the MV was constructed according to anatomical atlases with the dimensions confirmed with that data published in articles focused at studying the anatomy of the MV.

## 6. Conclusions

In this study, the numerical simulation of the MV in the human heart was conducted. Based on anatomical atlases beam-shell geometry model was created taking into account the heterogeneity of distribution of the MV leaflets thickness. The full cycle of the MV opening and closure was simulated using the finite element analysis software ANSYS Mechanical. For the numerical solution of this problem transient structural (non-stationary structural) analysis type allowing to determine time-varying displacements, strains, stresses and internal forces in the body under the influence of unsteady loads was selected. For modeling, the material of the MV leaflets was chosen as linearly elastic isotropic model.

Despite the limitations and assumptions chosen for material model, the obtained results for stresses on the leaflets coincide with the data obtained from the articles [2, 3, and 4] devoted to modeling of the MV. In addition, in the framework of numerical simulation it was proven that the valve closes tightly during the transition from phase of tension to the phase of expulsion in 0.302 sec calculation, which coincides with the data for cycle of the mitral valve operation [7].

In addition to modeling the normal functioning of the MV, the simulation of the the MV function with the device “Clip” implanted on the leaflet was executed. Analysis of the obtained results permits to state that “Clip” does not entail the additional tensile stresses that can lead to the destruction of the material of the MV leaflets.

Moreover, in this study we implemented and tested a method of processing data with a computer tomography in a solid model on the example of the spine that can be later used for calculations in software systems of finite element analysis. This method will allow in the future creating of an anatomically accurate model of the MV.

In the future, we plan to use an incompressible, hyperelastic transversely isotropic material and construct the geometrical model of the MV derived from computed tomography images for more precise studies of the valves behavior.

## References

- [1] N.A. Tenenholtz, P.E. Hammer, R.J. Schneider, N.V. Vasilyev, R.D. Howe, *On the Design of an Interactive, Patient-Specific Surgical Simulator for Mitral Valve Repair*. In: IEEE/RSJ International Conference on intelligent Robots and Systems (IROS) (2011) 1327.
- [2] W. Qian, S. Wei // *Annals of Biomedical Engineering* **41(1)** (2013) 142.
- [3] M.S. Sacks, He Z., L. Baijens, S. Wanant, P. Shah, H. Sugimoto, A.P. Yoganathan // *Annals of Biomedical Engineering* **30** (2002) 1281.
- [4] M.Stevanella, F. Maffessanti, C. A. Conti, E. Votta, A. Arnoldi, M. Lombardi, O. Parodi, E. G. Caiani, A. Redaelli // *Cardiovascular Engineering and Technology* **2(2)** (2011) 66.

- [5] E.N. Feins, H. Yamauchi, G.R. Marx, F.P. Freudenthal, H. Liu, P.J. del Nido, N.V. Vasilev // *The Journal of Thoracic and Cardiovascular Surgery* **147(2)** (2014) 783.
- [6] D.S. Kotovich, I.N. Stakan // *Voennaya medicina [Military medicine]* **2** (2010) 58. (In Russian).
- [7] K.V. Sudakov, In: *Physiology. Fundamentals and functional systems* (Medicine, Moscow, 2000) p. 327. (In Russian).
- [8] J.D. Humphrey, R.K. Strumpf, F.C.P. Yin // *ASME Journal of biomechanical engineering* **112** (1990) 333.
- [9] M. A. Hisham, M. Adib, K. Osman, N. Hazreen, M. Hasni, O. Maskon, F. Naim, Z. Ahmad, I. Sahat and A. N. Mu'tasim. In: *International Conference on Environment and BioScience* (IACSIT Press, Singapore, 2012), Vol.21, p. 6.
- [10] Anwarul Hasan // *Journal of Biomechanics* **47(9)** (2014) 1949.

### **Submission of papers:**

Manuscript should be submitted (**both MS Word and PDF**) by e-mail to: [mpmjournal@spbstu.ru](mailto:mpmjournal@spbstu.ru)

After a confirmation of the paper acceptance, the authors should send the signed hard copy of the "Transfer of Copyright Agreement" form (available at <http://www.mpm.spbstu.ru> section "Authors") by regular post to "Materials Physics and Mechanics" editorial office:

*Periodicals Editorial Office, Institute of Advanced Manufacturing Technologies, Peter the Great St.Petersburg Polytechnic University, Polytechnicheskaya, 29, St.Petersburg 195251, Russia.*

The scanned copy of the signed "Transfer of Copyright Agreement" should be send by e-mail to: [mpmjournal@spbstu.ru](mailto:mpmjournal@spbstu.ru).

### **Filetype:**

Authors are invited to send their manuscripts **as MS Word file with PDF format copy.**

MS Word file should be prepared according to the general instructions bellow; we are kindly asking the authors to look through the detail instruction at: <http://www.mpm.spbstu.ru>.

### **Length:**

Papers should be limited to 30 typewritten pages (including Tables and Figures placed in the proper positions in the text).

### **Structure of the manuscript:**

**PAPER TITLE: CENTERED,**

**TIMES NEW ROMAN 14 BOLD, CAPITAL LETTERS**

**A.B. Firstauthor<sup>1</sup>, C.D. Secondauthor<sup>2\*</sup>** -Times New Roman 12, bold, centered

<sup>1</sup>Affiliation, address, country - Times New Roman 10, centered

\*e-mail: e-mail of the corresponding author - Times New Roman 10, centered

**Abstract.** Times New Roman 12 font, single line spacing. Abstract should not exceed 12 lines.

**Keywords:** please, specify paper keywords right after the abstract.

**Paper organization.** Use Times New Roman 12 font with single line spacing. Use *Italic* font in order to stress something; if possible, please, use **bold** for headlines only.

**Page numbering.** Please, do not use page numbering.

**Tables, Figures, Equations.** Please, see the sample file at <http://www.mpm.spbstu.ru> for more details.

### **References**

References should be subsequently numbered by Arabic numerals in square brackets, e.g. [1,3,5-9], following the sample style below:

[1] A.K. Mukherjee // *Materials Science and Engineering: A* 322 (2002) 1.

[2] C.C. Koch, I.A. Ovid'ko, S.Seal, S. Veprek, *Structural Nanocrystalline Materials: Fundamentals and Applications* (Cambridge University Press, Cambridge, 2007).

[3] A.E. Romanov, V.I. Vladimirov, In: *Dislocations in Solids*, ed. by F.R.N. Nabarro (North Holland, Amsterdam, 1992), Vol. 9, p.191.

[4] C.K. Takemori, T.D. Müller, M.A. De Oliveira, *Numerical simulation of transient heat transfer during welding process*, In: *International Compressor Engineering Conference* (Purdue, USA 2010).

[5] W. Pollak, M. Blecha, G. Specht // *US Patent 4572848*.

[6] <http://www.mpm.spbstu.ru>

### **Правила подготовки статей:**

Рукопись (**английский язык, MS Word и копия PDF**) должна быть направлена в редакцию журнала по электронной почте: [mpmjourn@spbstu.ru](mailto:mpmjourn@spbstu.ru).

После подтверждения принятия статьи в печать, авторы должны отправить подписанные:

1. Соглашение о передаче авторских прав (<http://www.mpm.spbstu.ru>, раздел «Авторам»);
2. Экспертные заключения о том, что материалы статьи не содержат сведений, составляющих государственную тайну, и информацию, подлежащую экспортному контролю; по адресу:

*Россия, 195251, Санкт-Петербург, Политехническая, д. 29, Санкт-Петербургский политехнический университет Петра Великого, Институт передовых производственных технологий, Редакция периодических изданий.*

Скан-копии подписанных документов просим направить по электронной почте: [mpmjourn@spbstu.ru](mailto:mpmjourn@spbstu.ru)

### **Тип файла:**

Редакция принимает **файлы MS Word с копией в формате PDF**. Статья должна быть подготовлена в соответствии с настоящей инструкцией, мы просим авторов также следовать более подробным инструкциям на сайте журнала <http://www.mpm.spbstu.ru> в разделе «Авторам».

### **Длина статьи:**

Статья не должна превышать 30 страниц формата А4, включая Таблицы и Рисунки, размещенные непосредственно в соответствующих местах.

### **Общие правила оформления статьи:**

**НАЗВАНИЕ СТАТЬИ: ВЫРОВНЯТЬ ПО ЦЕНТРУ,**

**ШРИФТ, TIMES NEW ROMAN 14 BOLD, ЗАГЛАВНЫЕ БУКВЫ**

Автор(ы): **А.Б. Первыйавтор<sup>1</sup>, В.Г. Автор<sup>2\*</sup>** - шрифт Times New Roman 12, bold, по центру

<sup>1</sup>Наименование организации, адрес, страна - шрифт Times New Roman 10, по центру

\* e-mail автора, представившего статью - шрифт Times New Roman 10, по центру

**Аннотация.** Аннотация статьи составляет не более 12 строк. Используйте шрифт Times New Roman 12, одинарный межстрочный интервал.

**Ключевые слова:** укажите ключевые слова после аннотации.

**Как организовать текст статьи.** Используйте шрифт Times New Roman 12, одинарный межстрочный интервал. При необходимости выделить какую-либо информацию используйте *курсив*. Используйте **полужирный** шрифт только для заголовков и подзаголовков.

**Номера страниц.** Пожалуйста, не используйте нумерацию страниц

**Таблицы, Рисунки, Уравнения.** Подробные правила оформления данных элементов статьи приведены в инструкции на сайте журнала <http://www.mpm.spbstu.ru>

### **Литература**

Ссылки приводятся в тексте в квадратных скобках [1,3,5-9]. Стиль оформления ссылок:

- [1] A.K. Mukherjee // *Materials Science and Engineering: A* 322 (2002) 1.
- [2] C.C. Koch, I.A. Ovid'ko, S.Seal, S. Veprek, *Structural Nanocrystalline Materials: Fundamentals and Applications* (Cambridge University Press, Cambridge, 2007).
- [3] A.E. Romanov, V.I. Vladimirov, In: *Dislocations in Solids*, ed. by F.R.N. Nabarro (North Holland, Amsterdam, 1992), Vol. 9, p.191.
- [4] C.K. Takemori, T.D. Müller, M.A. De Oliveira, *Numerical simulation of transient heat transfer during welding process*, In: *International Compressor Engineering Conference* (Purdue, USA 2010).
- [5] W. Pollak, M. Blecha, G. Specht // *US Patent 4572848*.
- [6] <http://www.mpm.spbstu.ru>

МЕХАНИКА И ФИЗИКА МАТЕРИАЛОВ

32 (3) 2017

Учредители: Санкт-Петербургский политехнический университет Петра Великого,

Институт проблем Машиноведения Российской Академии Наук

Издание зарегистрировано федеральной службой по надзору в сфере связи,  
информационных технологий и массовых коммуникаций (РОСКОМНАДЗОР),

свидетельство ПИ №ФС77-69287 от 06.04.2017 г.

Редакция журнала

Профессор, д.т.н., академик РАН, А.И. Рудской – главный редактор

Профессор, д.ф.-м.н., член-корр. РАН, Д.А. Индейцев – главный редактор

Профессор, д.ф.-м.н. И.А. Овидько (1961 - 2017) – основатель и почетный редактор

Профессор, д.ф.-м.н. А.Л. Колесникова – ответственный редактор

Доцент, к.т.н. А.С. Немов – ответственный редактор

Е.О. Касяненко – выпускающий редактор

А.И. Хайрутдинова – редактор, корректор

Телефон редакции

+7 (812) 591-65-28

E-mail: [mpmjournal@spbstu.ru](mailto:mpmjournal@spbstu.ru)

Компьютерная верстка А.В. Шимченко

---

Подписано в печать 22.12.2017 г. Формат 60x84/8. Печать цифровая  
Усл. печ. л. 10,0. Тираж 100. Заказ \_\_\_\_.

---

Отпечатано с готового оригинал-макета, предоставленного автором  
в Издательско-полиграфическом центре Политехнического университета Петра  
Великого. 195251, Санкт-Петербург, Политехническая ул., 29.  
Тел.: (812) 552-77-17; 550-40-14.

- Investigation of the influence of strain induced junction disclinations on hardening and nucleation of cracks during plastic deformation of polycrystals.....237-242**  
V.V. Rybin, V.N. Perevezentsev, J.V. Svirina
- Micropolar media with structural transformations – theory illustrated by an example problem.....243-252**  
W. H. Müller, E.N. Vilchevskaya
- Mechanical properties of nanostructured titanium with bioactive titanium-organic nanocoating.....253-257**  
E.G. Zemtsova, N.F. Morozov, B.N. Semenov, R.Z. Valiev, V.M. Smirnov
- Dynamic strength properties of an ultra-fine-grained aluminum alloy under tension conditions.....258-261**  
A.D. Evstifeev, A.A. Chevrychkina, Y.V. Petrov
- Nucleation and growth mechanisms of CdTe thin films on silicon substrates with silicon carbide buffer layers.....262-271**  
A.A. Koryakin, S.A. Kukushkin, A.V. Redkov
- On influence of shear traction on hydraulic fracture propagation.....272-277**  
A. M. Linkov
- Elastomer composites based on filler with negative coefficient of thermal expansion: experiments and numerical simulations of stress-strain behaviour.....278-287**  
S.N. Shubin, A.G. Akulichev, A.B. Freidin
- Fabrication of p-type transparent oxide films with delafossite structure by sol-gel processing.....288-292**  
E.V. Shirshneva-Vaschenko, L.A. Sokura, T.G. Liashenko, E. Podlesnov, V.E. Bougrov, A.E. Romanov
- Application of quantum-chemical modeling results in experimental investigations of silicone composites.....293-297**  
H.H. Valiev, V.V. Vorobyev, Yu.N. Karnet, Yu.V. Kornev, O.B. Yumashev
- Experimental verification of postulate of isotropy and mathematical modeling of elastoplastic deformation processes following the complex angled nonanalytic trajectories.....298-304**  
V.G. Zubchaninov, A.A. Alekseev, E.G. Alekseeva, V.I. Gultiaev
- Testing of steel 45 under complex loading along the cylindrical screw trajectories of deformation....305-311**  
V.G. Zubchaninov, V.I. Gultiaev, A.A. Alekseev, V.V. Garanikov, S.L. Subbotin
- Validation of the mathematical model of isotropic material using parametric optimization of its physical and mechanical characteristics.....312-320**  
A.I. Borovkov, O.I. Klyavin, O.I. Rozhdestvenskiy, M.V. Aleshin, A.N. Leontev, S.P. Nikulina, K.S. Ivanov, A.P. Okunev
- On using quasi-random lattices for simulation of isotropic materials.....321-327**  
Vadim A. Tsaplin, Vitaly A. Kuzkin
- Review of the computational approaches to advanced materials simulation in accordance with modern advanced manufacturing trends.....328-352**  
A.V. Shymchenko, V.V. Tereshchenko, Y.A. Ryabov, S.V. Salkutsan, A.I. Borovkov
- On one class of applied gradient models with simplified boundary problems.....353-369**  
S.A. Lurie, P. A. Belov, Y.O. Solyaev, E.C. Aifantis
- Comparison of adaptive algorithms for solving plane problems of classical and cosserat elasticity....370-382**  
M.A. Churilova, M.E. Frolov
- Finite element modelling of the mitral valve repair using an implantable leaflet plication clip.....383-392**  
M. D. Stepanov, O.S. Loboda, Y. V. Novozhilov, N. V. Vasilyev